

Ultra-Low Phase Noise Atomic Clock using  
Coherent Population Trapping (CPT) in  
Rubidium

Tsvetan Krasimirov Burtichelov

PhD

University of York

October 2017

# Abstract

This thesis describes the design and implementation of a complete atomic clock system from first principles. The system is based on Coherent Population Trapping (CPT) in  $^{85}\text{Rb}$  and incorporates an ultra-low phase noise multi-element local oscillator, consisting of a 10MHz crystal oscillator and 1.5GHz Dielectric Resonator Oscillator (DRO) in a phase locked configuration. It is shown that the crystal oscillator can achieve excellent close to carrier phase noise performance of  $-122\text{dBc/Hz}$  at 1Hz offset and  $-147.7\text{dBc/Hz}$  at 10Hz offset, as well as Allan deviation of  $3 \times 10^{-13}$  at 100ms averaging time. The DRO exhibits excellent medium offset and far from carrier performance with a noise floor of about  $-180\text{dBc/Hz}$ . When phase locked to the crystal oscillator, the phase noise at 1Hz is shown to approach that of the crystal oscillator (scaled up to 1.5GHz).

A frequency synthesis chain, incorporating a Direct Digital Synthesizer (DDS), low noise digital divider, single sideband mixer and notch filter is used to upconvert the 1.5GHz local oscillator frequency to the ground state hyperfine splitting frequency of  $^{85}\text{Rb}$  (1.5178GHz). The DDS is controlled by a microcontroller and used to produce an offset frequency of 17.8MHz, which can be tuned, modulated or swept. The single sideband mixer is used to mix the 1.5GHz and 17.8MHz signals and suppress the lower sideband of the output. The notch filter is used to further suppress the LO feedthrough of the mixer by another  $>30\text{dB}$ .

A Rb CPT physics package incorporates a vertical cavity surface-emitting laser, which is modulated by the output of the synthesizer and used to interrogate the atomic resonance in a  $^{85}\text{Rb}$  vapour cell. The package was built with custom made optical mounts, low noise laser driving electronics and temperature control loops. The parameters affecting the shape, amplitude and stability of the atomic resonance were experimentally investigated and the construction of the physics package was adjusted for the optimal conditions.

A digital frequency locked loop is used to lock the local oscillator to the atomic resonance and the performance of the full system is tested.

# LIST OF CONTENTS

Abstract.....	2
List of Contents.....	3
List of Tables .....	7
List of Figures.....	8
Acknowledgements.....	15
Author’s Declaration.....	16
1 General Introduction.....	17
1.1 Types of Atomic Clocks.....	18
1.1.1 Microwave Atomic Clocks.....	18
1.1.2 Optical Atomic Clocks.....	23
1.2 Motivation for this Project.....	24
1.3 Structure of the Thesis.....	25
2 Rubidium CPT Theory.....	27
2.1 Rb Atomic Structure and Interactions.....	27
2.1.1 Fine Structure.....	27
2.1.2 Hyperfine Structure.....	28
2.1.3 Zeeman sublevels.....	30
2.2 Operation of Rb CPT Physics Package.....	31
2.3 Important conditions for achieving CPT.....	34
2.3.1 Vapour cell temperature.....	35
2.3.2 Laser beam polarization.....	35
2.3.3 Vapour cell magnetic field.....	36
2.3.4 Laser wavelength.....	36
2.3.5 RF modulation index and frequency.....	37

2.4	Parameters affecting the frequency stability. ....	38
2.4.1	Magnetic field. ....	39
2.4.2	Vapour cell temperature coefficient.....	39
2.4.3	Hyperfine resonance linewidth and amplitude. ....	40
2.4.4	Light Shift. ....	42
2.4.5	Detection Noise.....	43
2.4.6	Local Oscillator Phase Noise.....	43
2.5	Summary. ....	44
3	Local Oscillator (LO). ....	45
3.1	Introduction. ....	45
3.1.1	Oscillator Phase Noise Theory.....	46
3.1.2	Considerations for Optimal Phase Noise. ....	50
3.2	10 MHz Ultra-Low Phase Noise Crystal Oscillator.....	53
3.2.1	Differential Amplifier. ....	53
3.2.2	Crystal Resonator.....	56
3.2.3	Spurious Resonance Rejection Filter. ....	58
3.2.4	Electronically Tuned Phase Shifter.....	60
3.2.5	Complete Oscillator Circuit Diagram. ....	63
3.2.6	Crystal Oscillator Phase Noise Measurements. ....	64
3.2.7	Double Oven Temperature Control .....	70
3.3	1.5 GHz Dielectric Resonator Oscillator (DRO). ....	76
3.3.1	Broadband Feedback Push-Pull Amplifiers.....	78
3.3.2	Voltage Tuned Phase Shifter. ....	83
3.3.3	Dielectric Resonators. ....	85
3.3.4	1.5 GHz DRO Phase Noise Measurements.....	87
3.4	Phase Locked Loop Configuration and Measurements.....	92

3.5	Summary .....	99
4	Frequency Synthesizer.....	101
4.1	Direct Digital Synthesizer (DDS). .....	102
4.2	Single Sideband Mixer.....	104
4.3	1.5 GHz Notch Filter.....	115
4.4	Summary .....	120
5	Physics Package.....	121
5.1	Initial CPT Experimental Setup. ....	121
5.1.1	Constant Current Source.....	124
5.1.2	Laser Temperature Controller.....	126
5.1.3	Vapour Cell.....	128
5.1.4	Quarter wave plate and Polarising Beam Splitter (PBS). ....	129
5.1.5	Photodiode and Transimpedance Amplifier. ....	130
5.1.6	RF Signal Generator. ....	131
5.2	Initial Experiments. ....	131
5.2.1	Current Source Noise.....	131
5.2.2	Rb D1 Line Absorption Spectrum .....	133
5.2.3	Laser Modulation and Sidebands.....	135
5.2.4	Detecting the $^{85}\text{Rb}$ Hyperfine Resonance. ....	136
5.2.5	Effects of magnetic field intensity .....	138
5.2.6	Effects of magnetic field polarity and laser beam polarization .....	140
5.2.7	CPT width and amplitude experiments.....	143
5.3	Improved Compact Physics Package. ....	148
5.3.1	Laser Mount and Driving Electronics.....	148
5.3.2	Collimating Lens.....	150
5.3.3	New Rb Vapour Cell.....	151

5.3.4	Wide Area Photodiode.....	154
5.3.5	Laser Centre Frequency Stabilization.....	155
5.4	Testing the Improved Physics Package.....	163
5.5	Summary.....	165
6	Complete Atomic Clock System.....	166
6.1	CPT Resonance.....	166
6.2	Locking to the Atomic Resonance.....	168
7	Conclusions and Future Work.....	179
7.1	Local Oscillator.....	179
7.2	Frequency Synthesizer.....	180
7.3	Physics Package.....	181
7.4	Complete Atomic Clock.....	181
Appendix A: Microcontroller Code.....		183
1.	DDS Sweep through the hyperfine resonance (section 6.1).....	183
2.	DDS Switching frequency around the resonance, sampling ADC and programming DAC (section 6.2).....	186
Appendix B: List of Papers.....		195
References.....		203

# List of Tables

Table 1-1: Atomic clocks specifications and potential of this project.....	25
Table 3-1: Phase noise of oscillator 1 at important offset frequencies.....	66
Table 3-2: Phase noise of oscillator 2 at important offset frequencies.....	67
Table 3-3: Phase noise of XO1 used as reference and XO2 used as input at important offset frequencies.....	69
Table 3-4: Calculated and measured gain of amplifier with BFU690 and BFU790. ....	81
Table 3-5: BFU790 and BFG591 push-pull amplifiers noise figure measurements. ....	83
Table 3-6: Resonator measurements before and after the machining.....	86
Table 3-7: Measurement of dielectric resonator unwanted resonances. ....	87
Table 3-8: DRO measured phase noise.....	91
Table 4-1: AD9912 direct digital synthesizer residual phase noise.....	102
Table 4-2: Sidebands frequency and power from SSM measurement.....	113
Table 4-3: SSM low frequency output harmonics. ....	115
Table 5-1: Measured laser current source noise density.....	133
Table 5-2: Hyperfine shift vs. Magnetic Field and solenoid current. ....	139
Table 5-3: Resonance FWHM and Amplitude vs. Modulation Power.....	143
Table 5-4: Resonance FWHM and Amplitude vs. Coil Current.....	145
Table 5-5: Resonance FWHF and Amplitude vs. Cell temperature. ....	147
Table 5-6: Pressure and temperature coefficients for Rb in Argon and Nitrogen buffer gases. .....	152

# List of Figures

Figure 1-1: Traditional Rb physics package with spectral lamp. Figure drawn based on information from [8].	19
Figure 1-2: Energy diagram of the $^{87}\text{Rb}$ D1 excitation line.	20
Figure 1-3: A simplified 3 level lambda system for $^{85}\text{Rb}$ D1 line. The shown transitions occur when spacing between the two laser sidebands is tuned to the 3.034GHz hyperfine splitting frequency.	21
Figure 1-4: Basic block diagram of a CPT based frequency reference.	22
Figure 1-5: Cs cold atom fountain clock [14].	23
Figure 2-1: Total electron angular momentum J is the sum of L+S. Figure based on [25, p. 72].	28
Figure 2-2: Energy diagram of the $^{85}\text{Rb}$ D1 line hyperfine levels. Figure was drawn with data taken from [26, p. 26].	29
Figure 2-3: Zeeman splitting of the $^{85}\text{Rb}$ ground state hyperfine levels vs. magnetic field intensity. Figure taken from [26, p. 27].	31
Figure 2-4: Basic Rb CPT physics package.	32
Figure 2-5: Rb absorption spectrum calculated (dotted line) and measured (solid line) by the authors in [31]. The 4 absorption dips represent the transitions from ground hyperfine levels to the excited state of each isotope. The spectrum measured by the author of this thesis is shown in Chapter 5.	33
Figure 2-6: Desired laser optical spectrum for $^{85}\text{Rb}$ CPT detection. For optimal operation most of the optical power should be concentrated in the first order sidebands.	34
Figure 2-7: $^{85}\text{Rb}$ hyperfine resonance peak. The horizontal axis corresponds to 1kHz/div. ....	34
Figure 2-8: Quarter wave plate operational diagram. Figure taken from [34].	36
Figure 2-9: Allan Deviation curve example. Figure taken from [37].	38
Figure 2-10: Shift of the hyperfine frequency of Cs vs. cell temperature.	40
Figure 2-11: CPT resonance linewidth and amplitude. In this image the amplitude is about 75mV and the linewidth about 800Hz.	40

Figure 2-12: Light shift coefficients of $^{87}\text{Rb}$ . Figure taken from [43] .....	42
Figure 3-1: Basic atomic clock block diagram. ....	45
Figure 3-2: Equivalent circuit model of an oscillator. ....	46
Figure 3-3: Phase noise degradation as a function of $QLQ0$ [24], [45]. ....	51
Figure 3-4: Phase noise degradation as a function of resonator insertion loss [24]. ....	52
Figure 3-5: Block diagram of the low phase noise 10 MHz crystal oscillator. ....	53
Figure 3-6: Differential amplifier circuit diagram. ....	54
Figure 3-7: Differential amplifier frequency response. ....	55
Figure 3-8: 10MHz amplifier phase shift.....	56
Figure 3-9: Crystal resonator equivalent circuit model. ....	56
Figure 3-10: Crystal resonator frequency response (span=100Hz). ....	57
Figure 3-11: Crystal resonator phase shift (span=100Hz).....	58
Figure 3-12: Spurious resonance filter circuit diagram. ....	58
Figure 3-13: Spurious resonance rejection filter frequency response.....	60
Figure 3-14: Phase noise degradation as a function of open loop phase shift [48]. The degradation in both bipolar and GaAs devices is effectively the same, as they follow the same theoretical line.....	61
Figure 3-15: XO phase shifter circuit diagram. ....	62
Figure 3-16: XO phase shifter measured phase shift and insertion loss vs. varactor voltage..	63
Figure 3-17: Complete crystal oscillator circuit diagram. ....	64
Figure 3-18: Photograph of the crystal oscillator inside metal jig (Oscillator 2). ....	65
Figure 3-19: Measurement configuration used for oscillator 1. ....	65
Figure 3-20: Measured phase noise of oscillator 1. ....	66
Figure 3-21: Measured phase noise performance of oscillator 2. ....	67
Figure 3-22: Measurement configuration using oscillator 1 as reference and oscillator 2 as input. ....	68

Figure 3-23: Measured phase noise plot of oscillator 1 used as reference and oscillator 2 used as input.....	69
Figure 3-24: Photo of the double oven temperature controlled crystal oscillator.....	70
Figure 3-25: Single op amp PID temperature controller. ....	71
Figure 3-26: Example of typical step response with parameters used in Ziegler-Nichols method. Figure taken from [55, p. 569].....	72
Figure 3-27: PID temperature controller for crystal oscillator. ....	73
Figure 3-28: Heating circuit for crystal oscillator.....	74
Figure 3-29: Photo of the completed double oven controlled oscillator with temperature controllers. ....	74
Figure 3-30: Measured phase noise on the double oven controlled crystal oscillator. ....	75
Figure 3-31: Allan Deviation measurement of the double oven controlled crystal oscillator. ....	76
Figure 3-32: Comparison between Pascall [57], Wenzel [58] and NEL [59] 100 MHz low phase noise crystal oscillators and 1.2 GHz DRO [22]. ....	77
Figure 3-33: Block diagram of 1.5 GHz DRO.....	78
Figure 3-34: Circuit diagram of broadband feedback amplifier. ....	79
Figure 3-35: Broadback feedback amplifier PCB layout.....	80
Figure 3-36: Block diagram of 1.5 GHz amplifiers in push-pull configuration. ....	81
Figure 3-37: Layout of push-pull amplifiers.....	82
Figure 3-38: 1.5 GHz DRO phase shifter diagram. ....	84
Figure 3-39: DRO phase shifter insertion loss and phase shift vs. varactor voltage. ....	84
Figure 3-40: 1.2GHz Dielectric Resonator in aluminium cavity. ....	85
Figure 3-41: Photo of 1.5 GHz DRO. ....	88
Figure 3-42: DRO's inside screened metal box. ....	89
Figure 3-43: Block diagram of mixed down 1.5GHz DRO's measurement. ....	90
Figure 3-44: Measured DRO phase noise. ....	90
Figure 3-45: Comparison between measured and theoretical DRO phase noise.....	92

Figure 3-46: Photo of LTC6950 development board.....	93
Figure 3-47: 1.5 GHz DRO phase shifter insertion loss and phase shift vs. varactor voltage (BBY53).....	94
Figure 3-48: DRO oscillation frequency and output power vs. varactor voltage. ....	95
Figure 3-49: ClockWizard phase locked loop design tool.....	96
Figure 3-50: Predicted phase noise plots by ClockWizard design tool. ....	96
Figure 3-51: Local Oscillator phase locked loop configuration. ....	97
Figure 3-52: Phase locked loop noise measurements. The phase locked curves were measured on the R&S FSWP. ....	98
Figure 3-53: Crystal oscillator frequency tuning (x150) vs varactor voltage.....	99
Figure 4-1: Frequency synthesizer basic block diagram.....	101
Figure 4-2: DDS programmed by PIC microcontroller. ....	103
Figure 4-3: PIC microcontroller programming the DDS development board. ....	104
Figure 4-4: Block diagram of SSM (upper sideband).....	105
Figure 4-5: 3dB Wilkinson Splitter with in-phase and quadrature outputs. ....	106
Figure 4-6: 1.5GHz Wilkinson Quadrature Splitter ADS simulation results. ....	107
Figure 4-7: Lumped element 17.868 MHz Quadrature Wilkinson divider circuit diagram. .	108
Figure 4-8: Lumped element Wilkinson Quadrature Divider simulation results. ....	109
Figure 4-9: Complete Single Sideband Mixer layout. ....	110
Figure 4-10: Single Sideband Mixer simulation schematic.....	111
Figure 4-11: SSM harmonic balance simulation results.....	111
Figure 4-12: Photo of the completed SSM. ....	112
Figure 4-13: Block diagram of the SSM test configuration.....	113
Figure 4-14: Output spectrum of the SSM mixer. ....	114
Figure 4-15: 1.5 GHz Notch filter schematic.....	115
Figure 4-16: 1.5 GHz notch filter S-parameters simulation. ....	116

Figure 4-17: Sketch of the notch filter (side and top view). .....	117
Figure 4-18: Photo of the notch filter. ....	118
Figure 4-19: 1.5 GHz notch filter measured frequency response.....	119
Figure 4-20: SSM output spectrum filtered using notch filter. ....	120
Figure 5-1: Rb CPT physics package block diagram.....	122
Figure 5-2: Initial Rb CPT experiment setup (version 1). ....	123
Figure 5-3: Improved CPT experimental setup (version 2). ....	124
Figure 5-4: Low noise constant current source.....	125
Figure 5-5: Aluminium box containing VCSEL, temperature PID controller, current source and Bias Tee (physics package version 2). ....	127
Figure 5-6: Metal enclosure for the vapour cell.....	128
Figure 5-7: Vapour cell with insulation and mu-metal shield. ....	129
Figure 5-8: Mounts for a) Polarising Beam Splitter and b) Quarter wave plate.....	130
Figure 5-9: Measured laser current source noise density.....	132
Figure 5-10: Measured Rb absorption spectrum (D1 excitation lines).....	134
Figure 5-11: Absorption spectrum of Rb detected with laser modulated at 3.417 GHz.....	135
Figure 5-12: Laser optical spectrum without modulation (left) and with modulation at 1.517866 GHz (right).....	136
Figure 5-13: <sup>85</sup> Rb CPT resonance. Channel 1 is the is the ramp signal used to sweep the RF modulation frequency. ....	137
Figure 5-14: Hyperfine shift vs. Magnetic Field. ....	139
Figure 5-15: Hyperfine resonance waveforms for different polarization and magnetic field intensity.....	142
Figure 5-16: Resonance FWHM vs. Modulation Power. ....	144
Figure 5-17: Resonance amplitude vs. Modulation Power.....	144
Figure 5-18: Resonance FWHM vs. solenoid current. ....	145
Figure 5-19: Resonance amplitude vs. solenoid current.....	146

Figure 5-20: Resonance FWHM vs. Cell temperature.....	147
Figure 5-21: Resonance amplitude vs. Cell temperature. ....	148
Figure 5-22: Schematic of the latest laser current source. ....	149
Figure 5-23: Laser assembly Autodesk model.....	150
Figure 5-24: Collimating Lens Mount. ....	151
Figure 5-25: New vapour cell assembly with Helmholtz coils and heating elements. ....	153
Figure 5-26: Wide area photodiode (7.02mm <sup>2</sup> sensitive area) in metal mount.....	154
Figure 5-27: Photo of the latest complete physics package configuration (length=23cm). ..	155
Figure 5-28: Block diagram of laser centre frequency locking to the Doppler-broadened absorption spectrum. ....	156
Figure 5-29: Saturated absorption spectroscopy setup. Figure taken from [79, p. 5].....	158
Figure 5-30: Rb atoms and their velocity components inside the vapour cell.....	158
Figure 5-31: a) Doppler broadened absorption spectrum. b) Saturated absorption spectrum. Figure taken from [80, p. 7]. ....	159
Figure 5-32: DAVLL setup. Figure taken from [82, p. 2]. ....	160
Figure 5-33: DAVLL absorption spectra. (a) Using linear polarized light. (b) Left circularly polarized component. (c) Right circularly polarized component. (d) Error signal (c - b). Figure taken from [82, p. 2]. ....	161
Figure 5-34: Block diagram of the AD835 phase detection circuit. ....	162
Figure 5-35: Photo of the AD835 laser stabilization circuit. ....	163
Figure 5-36: Photo of <sup>85</sup> Rb CPT resonance (~1 kHz/div).....	164
Figure 6-1: Laser centre frequency lock and resonance detection block diagram.....	167
Figure 6-2: Resonance detected using the assembled system with laser centre frequency lock (1kHz/div). ....	168
Figure 6-3: Flowchart of the CPT resonance locking method. ....	170
Figure 6-4: Block diagram of the complete atomic clock configuration. ....	171
Figure 6-5: Block diagram of the digital atomic resonance lock circuit.....	172

Figure 6-6: Circuit diagram of the digital atomic resonance lock circuit (part 1). .....	173
Figure 6-7: Circuit diagram of the digital atomic resonance lock circuit (part 2). .....	174
Figure 6-8: Digital hyperfine locking circuit. ....	175
Figure 6-9: Closed loop step response of the DAC output voltage .....	176
Figure 6-10: Measured Allan deviation of completed CPT system.....	177

## Acknowledgements

I would like to thank Professor Jeremy Everard for his technical and academic support and encouragement, for giving me the opportunity to be part of this project and for his help with getting my studentship.

I would also like to thank the EPSRC and Leonardo MW Ltd. for funding this research and providing the aforementioned studentship. In particular, I thank Professor Robert Lamb, Neil Raphael and Stephen Clark from Leonardo MW for their help with the funding and their technical advice.

I thank Dr. David Iddles for his help with the machining of the dielectric resonators used in this project. Mark Hough, Pete Turner, Andy White and the rest of the technical support staff of the University of York for their help and advice in manufacturing and building components and PCB's for the project, as well as the academic and administrative support staff for their help with non-technical matters.

Last, but not least, I would like to thank my family and friends for their moral support and encouragement. Pratik Deshpande and Simon Bale for also sharing their expertise and helping me with technical matters.

## Author's Declaration

I declare that this thesis is a presentation of original work and I am the sole author. This work has not previously been presented for an award at this, or any other, University. All sources are acknowledged as References.

The theoretical phase noise model was developed by Professor Jeremy Everard and has been referenced accordingly.

The following publications have arisen from this thesis:

1. Tsvetan Burtichelov, Jeremy Everard, "Low Phase Noise 10MHz Crystal Oscillators", *European Frequency and Time Forum 2016*, York, 2016.
2. Tsvetan Burtichelov, Jeremy Everard, "Initial Results on Low Phase Noise Multi-Element Local Oscillator For Use in Atomic Clocks", *International Frequency Control Symposium 2016*, New Orleans, 2016.
3. Tsvetan Burtichelov, Jeremy Everard, "Latest Results in the Development of an Ultra-Low Phase Noise Rb CPT Vapour Cell Atomic Clock", *EFTF/IFCS 2017*, Besancon, 2017

# 1 GENERAL INTRODUCTION.

Atomic clocks are devices, which use the frequency of energy level transitions in atoms as a reference to maintain an accurate and stable frequency output. The development of these devices began in the late 1940's when Harold Lyons and his associates at the U.S. National Bureau of Standards (NBS) demonstrated a clock, using the inversion frequency of ammonia molecules (23.8 GHz) as its stable reference [1]. At the time, that atomic clock could not surpass the stability of quartz oscillators. Several years later, in 1955, Louis Essen and Jack Parry, inspired by the work of I. Rabi built the first Caesium atomic clock at the National Physical Laboratory (NPL) in the UK [2]. Since then the technology has seen great development and has resulted in the re-definition of the second as the duration of 9 192 631 770 periods of the radiation corresponding to the transition between the two hyperfine levels of the ground state of the Caesium 133 atom [3]. This has made time the most accurately measured physical quantity. Atomic clocks have been produced in a variety of sizes and performance grades, ranging from the miniature CSAC [4] to the most stable laboratory optical clocks at NIST, showing stability of parts in  $10^{-18}$  [5]. Multiple different elements have been used in the development of the clocks, as well as different techniques for interrogating the atomic transition frequencies.

The frequency reference that these devices provide has numerous applications beyond time measurement. Global navigation and advanced telecommunication systems, RADAR technology etc. all require very stable and accurate frequency standards. Although there has already been extensive research on atomic clocks, there is still room for improving the short and long-term stability of these devices. The scope of this project is to design an atomic frequency reference using a Rubidium CPT physics package in combination with ultra-low phase noise oscillators.

In this chapter, a brief description will be provided of the most popular materials and methods for developing atomic clocks. To explain the motivation for this research, a comparison will be made of the dimensions and stability performance between several commercially available clocks and the initial target performance of the clock developed in this project. A brief outline of the thesis chapters will be presented.

## 1.1 Types of Atomic Clocks.

Atomic clocks can be generally categorised by the type of atomic transitions used as a reference and the type of methodology used to interrogate those transitions. Currently, there are two main types of transitions used, the microwave and optical atomic transitions.

### 1.1.1 Microwave Atomic Clocks.

Microwave atomic clocks use the frequency of transitions between the ground hyperfine states in the atoms of alkali metals, mainly Caesium (Cs), Rubidium (Rb) and sometimes Sodium (Na). These frequencies are in the microwave domain, ranging from hundreds of MHz, to several GHz. In these clocks, a microwave source (local oscillator) is used to generate a signal matching the frequency of the desired hyperfine transition. By using various methods, this signal probes the atoms and detects a frequency discriminating resonance. The source is then frequency locked to that resonance to achieve the desired stability. The part of the system where the atomic transitions occur is generally referred to as the physics package. The most popular physics package topologies are described below:

#### *1.1.1.1 Using a microwave cavity, spectral lamp and vapour cell.*

In this traditional physics package the atomic resonance is detected by exciting the atoms inside a temperature controlled vapour cell, by using a spectral lamp. This method is generally used with Rubidium, due to the particular transition frequencies of its naturally occurring isotopes. The spectral lamp uses Rubidium to produce light at the wavelengths that correspond to the transitions between energy levels of this element, specifically 780nm and 795nm. The cell itself usually contains a natural mixture of  $^{85}\text{Rb}$  and  $^{87}\text{Rb}$  and is placed inside a microwave cavity. The intensity of light transmitted through the cell is detected by a photodiode (Figure 1-1). The light from the lamp is filtered (usually using a  $^{85}\text{Rb}$  filter cell) [6, pp. 8-10], [7, p. 111] so it mainly excites electrons from one of the ground hyperfine states of  $^{87}\text{Rb}$  and brings them to the excited state (Figure 1-2). After a short time they decay with equal probability into both ground hyperfine states. This process, referred to as optical pumping, shifts the majority of the electron population into one of the hyperfine states where they can no longer interact with the light field (absorb

light) and therefore an increase of light transmission through the cell is detected. At this point, if the frequency of the microwave cavity is tuned to the hyperfine splitting frequency, the electrons redistribute themselves equally between the hyperfine levels and, as a result, more light is absorbed. This produces a small drop in light intensity detected by the photodiode, which means that resonance has been achieved and can be used to provide the feedback to lock the microwave source to the hyperfine reference.

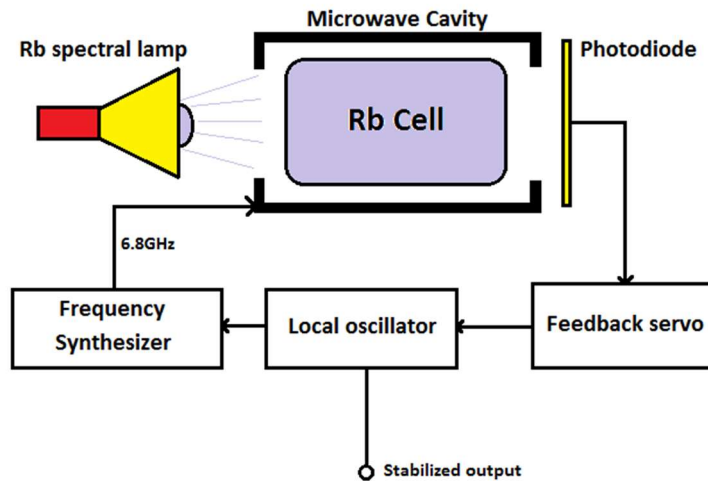


Figure 1-1: Traditional Rb physics package with spectral lamp. Figure drawn based on information from [8].

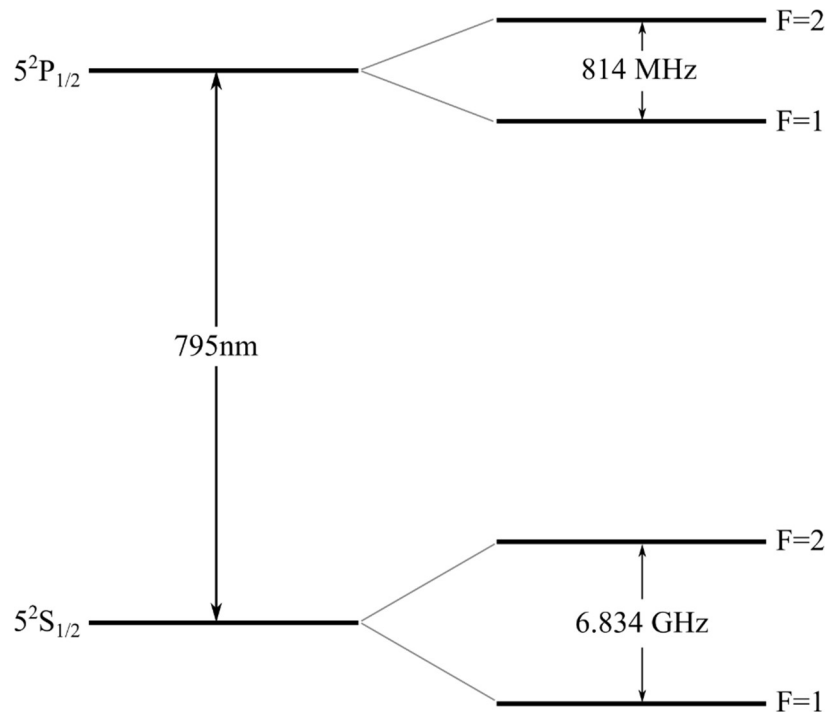


Figure 1-2: Energy diagram of the  $^{87}\text{Rb}$  D1 excitation line.

The main drawback of this configuration is the need for a microwave cavity and spectral lamp, which makes it difficult to produce a compact physics package.

#### 1.1.1.2 *Rb Coherent Population Trapping (CPT) physics package.*

In the case of the CPT method, the spectral lamp is replaced by a Vertical Cavity Surface Emitting Laser (VCSEL) operating at 795nm, the wavelength required for D1 line excitation. It is also possible to use 780nm VCSEL's for D2 line excitation, as the ground state hyperfine splitting for both of them is the same. The laser is modulated at half of the hyperfine splitting frequency (3.417GHz for  $^{87}\text{Rb}$  or 1.517GHz for  $^{85}\text{Rb}$ ) producing two phase coherent light fields (optical sidebands), which are used to excite both hyperfine ground levels simultaneously [9]. The phase coherence means that there is a fixed relationship between the phases of the two optical sidebands. The process that takes place can be explained by a 3-level lambda system (Figure 1-3).

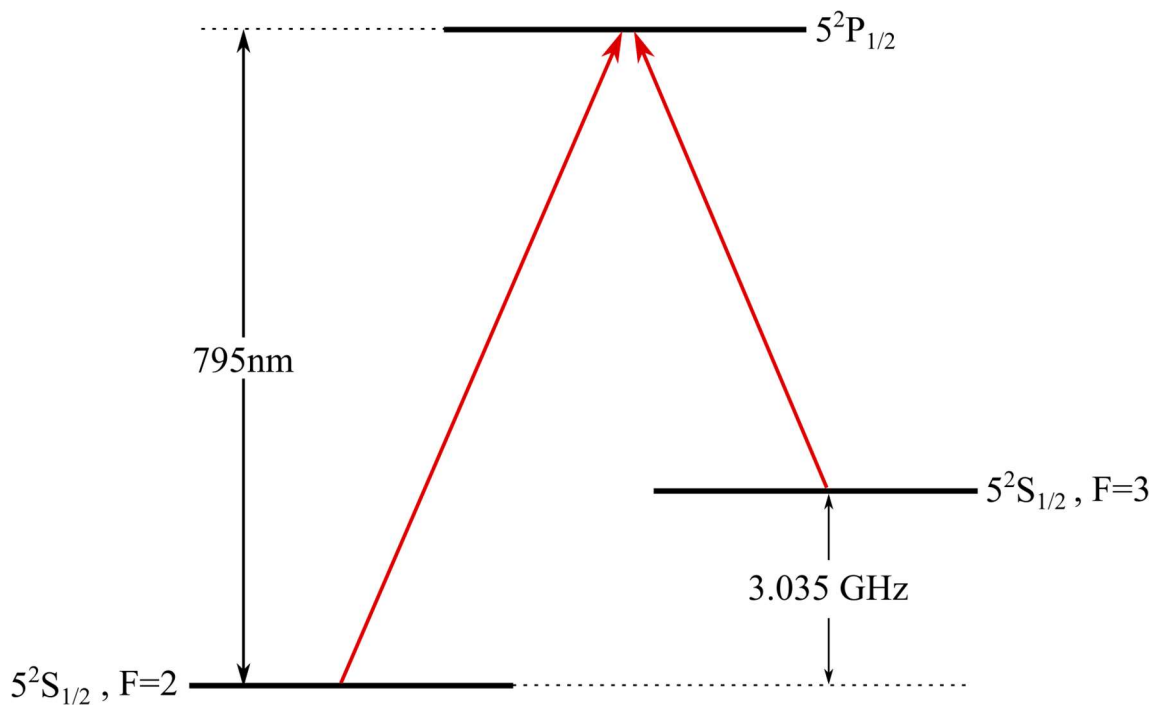


Figure 1-3: A simplified 3 level lambda system for  $^{85}\text{Rb}$  D1 line. The shown transitions occur when spacing between the two laser sidebands is tuned to the 3.034GHz hyperfine splitting frequency.

A 3-level lambda system describes the simultaneous transitions of electrons from 2 separate atomic energy states into one common state. In this case the two hyperfine levels of  $^{85}\text{Rb}$  are excited by the modulated laser light field into a common excited state [10].

When the laser is tuned to the wavelength of the D1 line, transitions are induced between the ground and excited state, absorbing a portion of the light in the process. This is seen as a drop in laser intensity detected by the photodiode.

If a microwave modulation is applied to the laser at a frequency tuned to half of the hyperfine splitting (so that the separation of the two sidebands is the full hyperfine splitting), then both ground hyperfine levels are coupled to a common excited state. As the electrons decay from the excited state, if all conditions are met, they have a probability to enter a quantum superposition state form which they can no longer interact with the light field. This is seen as a small increase of the light intensity detected by the photodiode as absorption is reduced. This only happens for a narrow range of frequencies (in the order of several hundred Hz or a few kHz) and is referred to as the  $^{85}\text{Rb}$  hyperfine resonance [11]. This resonance can then be used to frequency lock the microwave source (local oscillator) (Figure 1-4).

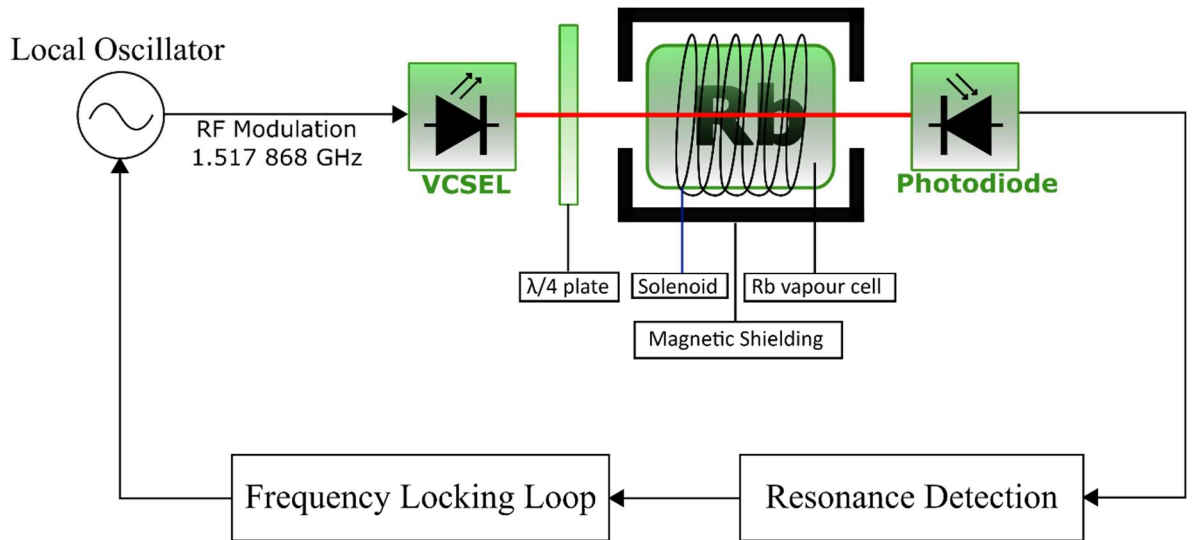


Figure 1-4: Basic block diagram of a CPT based frequency reference.

The main advantage of the CPT physics package is that it does not require a microwave cavity and Rb lamp and therefore can be made much more compact.

#### 1.1.1.3 Atomic fountain clocks.

Currently, the most stable microwave atomic clocks are the atomic fountains, offering frequency stability in the order of parts in  $10^{-16}$ . The most commonly used element in these clocks is Caesium (Cs), however Rubidium (Rb) fountains are also being researched and developed [12]. In this method, a cloud of atoms is laser cooled to a temperature of a few  $\mu K$  and prepared into the desired hyperfine state. Then they are launched through a resonant microwave cavity, where the atomic transitions are induced and populations are measured by probe laser beams using laser-induced fluorescence. This process is known as Ramsey interferometry [13]. This results in the detection of an interference pattern when the microwave interrogation frequency is detuned. The fringes of this interference pattern are much narrower than the resonances of vapour cell based clocks, with a Full Width at Half Maximum (FWHM) in the order of a few Hz [14]. In this case the FWHM is defined as the frequency separation between the points of the central Ramsay fringe where the atomic transition probability is half of the maximum value [15]. This probability is measured as the amplitude of the fluorescent light from the atom cloud. It is because of this narrower structure that these clocks can reach much greater stability. Figure 1-5 shows the construction of a typical cold atom fountain clock.

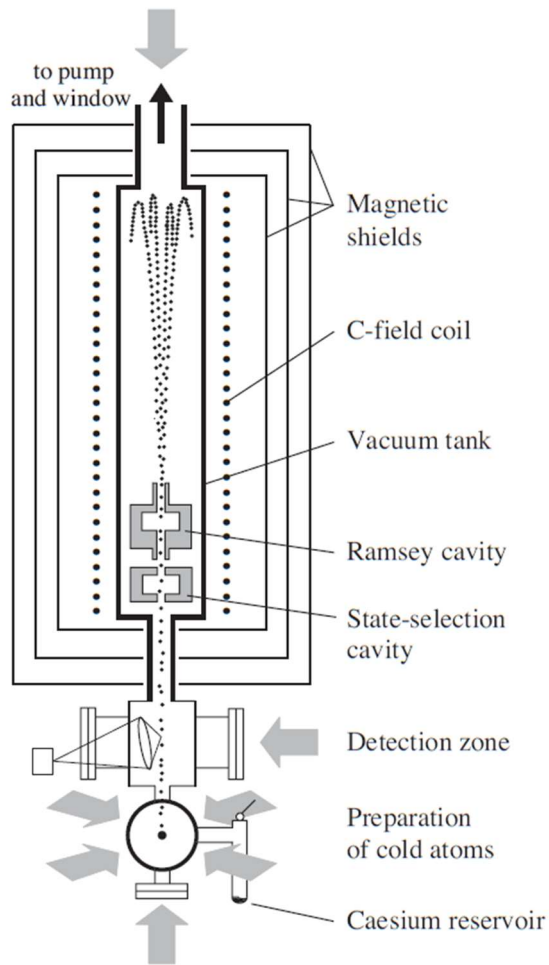


Figure 1-5: Cs cold atom fountain clock [14].

Although these devices offer great stability, their construction requires a large amount of space and comes at a high cost. They are mainly used in major research laboratories around the world.

### 1.1.2 Optical Atomic Clocks.

Currently, the most stable time measuring devices are the optical atomic clocks. Instead of probing the microwave transitions between hyperfine states, these devices are stabilized to the frequency of optical transitions in the atoms. Due to the fact, that these transitions have frequencies in the order of several hundreds of terahertz, their quality factors (ratio of frequency to resonance linewidth) are much higher. In this case, the local oscillator is

replaced by an ultra-stable laser. The atoms are super-cooled and trapped by magnetic fields and/or laser beams to minimize collisions, doppler broadening of the optical lines and thermal effects. Commonly used elements are Strontium (Sr), Ytterbium (Yb) and Mercury (Hg) [16]. Typically, the lasers are stabilised using a high-Q Fabry-Perot cavity to achieve extremely narrow linewidths and stable wavelengths. Then the lasers are used to induce the transitions in the atomic material. The frequency of the laser is then locked to the resonance of the optical atomic transitions. Optical frequency combs are used to downscale the optical frequency to a useable microwave or RF signal. Optical clocks can reach frequency stability in the order of parts in  $10^{-18}$  [17], at least two orders of magnitude greater than that of microwave clocks. For this reason, the scientific community is currently debating the possibility for re-defining the SI second based on the frequency of optical transitions in the  $^{171}\text{Yb}$  atoms [18].

## 1.2 Motivation for this Project.

The frequency stability of an oscillator or atomic clock is typically expressed in two main quantities, phase noise and Allan deviation. In the frequency domain, phase noise is defined as the ratio of the power within a 1Hz bandwidth at a certain offset from the carrier to the power in the carrier. Allan deviation is the equivalent of phase noise in the time domain and is a special form of the statistical standard deviation, which allows for a clearer representation of frequency flicker [19], [20]. The two quantities are closely related and one can be calculated using the data contained in the other. As such, the phase noise of the local oscillator is one of the main factors that define the short to medium-term stability of an atomic clock.

Previous research conducted by Professor Jeremy Everard's research group at the University of York has yielded oscillators with state of the art phase noise performance [21], [22], [23], [24]. The next step to further improve the performance was to develop an atomic clock configuration, which combines a local oscillator based on the techniques that were previously developed with a versatile and flexible frequency synthesis chain and a robust and compact physics package that can significantly improve the long-term stability. The initial goal was to design a system that can be fully automated and integrated into a relatively compact package and therefore be operated as a standalone source or 'black

box’. This is why after an initial research and evaluation of the currently developed physics package topologies, the Rubidium CPT method was selected for its versatility and potential for minimisation.

By utilizing the advantages of a CPT physics package and ultra-low phase noise oscillators, this project aims to produce an atomic clock that can achieve a better frequency stability over volume ratio than the currently available configurations. Table 1-1 shows the phase noise and frequency stability characteristics of several available models and their volume for comparison. It also gives an indication of the characteristics that were the initial aim of this project.

Table 1-1: Atomic clocks specifications and potential of this project.

		Symmetricom SA.45s (SCAC)	Symmetricom SA.22c	Symmetricom SA.22c-LN	Stanford Research PRS10	York Potential
Allan Deviation	$\tau=1\text{sec}$	2.50E-10	3.00E-11	1.40E-11	2.00E-11	$\sim < 2\text{E-}13$
	$\tau=10\text{sec}$	8.00E-11	1.00E-11	8.00E-12	1.00E-11	$\sim < 5\text{E-}13$
	$\tau=100\text{sec}$	2.50E-11	3.00E-12	2.50E-12	2.00E-12	$\sim < 1\text{E-}12$
	$\tau=1000\text{sec}$	8.00E-12				
RF Output Phase Noise at 10MHz O/P	1Hz	<-50dBc/Hz	<-72dBc/Hz	<-100dBc/Hz		<-123dBc/Hz
	10Hz	<-70dBc/Hz	<-90dBc/Hz	<-130dBc/Hz		<-149dBc/Hz
	100Hz	<-113dBc/Hz	<-128dBc/Hz	<-145dBc/Hz	<-130dBc/Hz	<-160dBc/Hz
	1kHz	<-128dBc/Hz	<-140dBc/Hz	<-150dBc/Hz	<-140dBc/Hz	<-163dBc/Hz
	10kHz	<-135dBc/Hz	<-148dBc/Hz	<-155dBc/Hz		<-160dBc/Hz
	100kHz	<-140dBc/Hz				
Volume		<17cc	203cc	640cc	394cc	$\sim < 1000\text{cc}$

Another important aspect of the project is that it aimed to develop most of the main components of the local oscillator and physics package from first principles, rather than using commercially available solutions.

### 1.3 Structure of the Thesis.

This thesis will describe the development of the individual elements of the atomic clock. Chapter 2 will give a general description of the atomic structure of Rubidium and will discuss some of the main factors that affect the stability of the atomic resonance. Chapter 3 will focus on the development of the multi-element ultra-low phase noise local oscillator, along with important design processes and considerations. Chapter 4 will describe the

frequency synthesis chain used for generating a tuneable signal that can interrogate the atomic resonance. Chapter 5 will describe the design and construction of the CPT physics package and important considerations for improving stability. Chapter 6 will focus on the process of assembling the individual elements of the clock and will present stability measurements on the complete system. More detailed introduction and theoretical background will be included as a sub-section in each of these chapters, in order to achieve more coherent flow of information. The final sections of the thesis will include conclusions and plans for continuation of this research.

## 2 RUBIDIUM CPT THEORY.

Rubidium was chosen as the element in the physics package developed in this project. For this reason, the atomic structure, electron energy levels and transition lines were studied extensively in order to understand the CPT resonance transitions and the requirements for building a stable physics package. This chapter contains an overview of the theory describing the Rubidium atoms and their interactions, specifically the ones used in Coherent Population Trapping clocks. It will also give an indication of the important parameters and conditions for detecting the atomic resonance and achieving high frequency stability.

### 2.1 Rb Atomic Structure and Interactions.

The atomic transition frequencies that are used in atomic clocks are the result of interactions between the different angular momenta of the electrons orbiting the atoms. In order to understand the requirements for using particular laser wavelengths and microwave modulation frequencies for detecting the atomic resonance, a basic understanding of the phenomena that determine those electron energy levels is required.

#### 2.1.1 Fine Structure.

Rubidium is an alkali metal and as such its atom has only one electron in its outermost shell. This electron can undergo transitions into discrete quantum states or energy levels provided that it receives enough energy, mainly through electromagnetic radiation. Atomic physics theory states that there is a direct connection between the wavelength or frequency ( $\nu$ ) of the radiation and the energy ( $E$ ) that it carries, as described by the Planck-Einstein relation ( $E = h\nu$ ) where  $h$  is the Planck constant. The energy required to excite the electron of both isotopes of Rb into a higher level is determined by the orbital angular momentum ( $L$ ) of the electron orbiting around the nucleus and the spin angular momentum ( $S$ ) of the electron itself. These momentums can be represented by three-dimensional vectors. If the two vectors point to the same direction, then the total electron angular momentum ( $J$ ) is the sum of the two magnitudes and less energy is required to bring the electron into an excited state. If the vectors point in opposite directions, then  $J$  is the

difference of the two magnitudes and more energy is required (Figure 2-1) [25]. This is shown by the equation:

$$|L - S| \leq J \leq L + S \quad \text{Taken from [26, p. 5]}$$

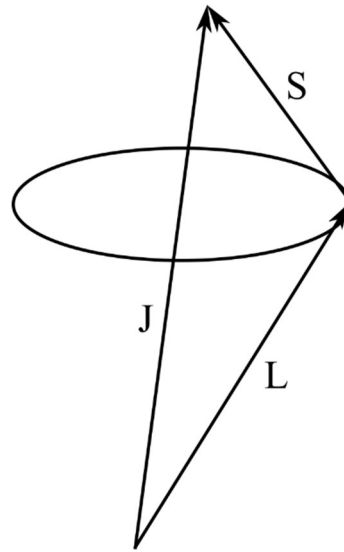


Figure 2-1: Total electron angular momentum  $J$  is the sum of  $L+S$ . Figure based on [25, p. 72].

The values of  $L$  and  $S$  are numbers that represent discrete quantum states of the electron and are characteristic for each isotope and energy level. In particular, for  $^{85}\text{Rb}$  ground state  $L=0$  and  $S=1/2$  and  $J$  can only be  $1/2$ , since  $L + S = 1/2$  and  $|L - S| = 1/2$  as well. However, for the excited state we have  $L=1$  and  $S=1/2$ . Now  $J$  can either be  $L + S = 3/2$  or  $|L - S| = 1/2$ .

This results in two excitation lines with different wavelengths corresponding to the different energy transitions. The D1 line ( $5^2S_{1/2} \rightarrow 5^2P_{3/2}$  transition) at about 795nm and the D2 line ( $5^2S_{1/2} \rightarrow 5^2P_{1/2}$  transition) at about 780nm. The Fine Structure is the splitting of these two excited levels.

### 2.1.2 Hyperfine Structure.

Each of the levels of the fine structure contains hyperfine levels. They are produced from the coupling of the total electron angular momentum ( $J$ ) with the total nuclear angular momentum ( $I$ ). The total atomic angular momentum  $F=J+I$  is the sum of the two. The

coupling of J and I follows the same basic rules as the one of L and S. This results in the splitting of each ground and excited state into several more levels with a certain energy difference between them (hyperfine levels). Since the hyperfine levels are produced by the total nuclear angular momentum, it is expected that for different isotopes these shifts have different energies. This is called the "isotope shift" and is due to the different masses of the nuclei of the isotopes. The splitting between the hyperfine levels of the ground state of  $^{85}\text{Rb}$  is about 3.035GHz and the one for the  $^{87}\text{Rb}$  ground state is about 6.834GHz. In atomic clocks these are used to provide the frequency reference to which the system is locked. The excited state also contains multiple hyperfine levels, the number of which differs for each isotope and excitation line. These levels have smaller energy differences in the order of tens or hundreds of MHz [26, pp. 25-26]. It is noteworthy that in the case of Rb, if the D1 line excitation occurs there are only 2 hyperfine levels of the excited state. If the D2 line excitation occurs there are 4 excited hyperfine levels. This can potentially have an effect on the contrast of CPT resonance, depending on which wavelength is used for excitation. In the current experimental setup, the  $^{85}\text{Rb}$  D1 line is used for excitation. Figure 2-2 shows the energy diagram of the hyperfine levels of that isotope.

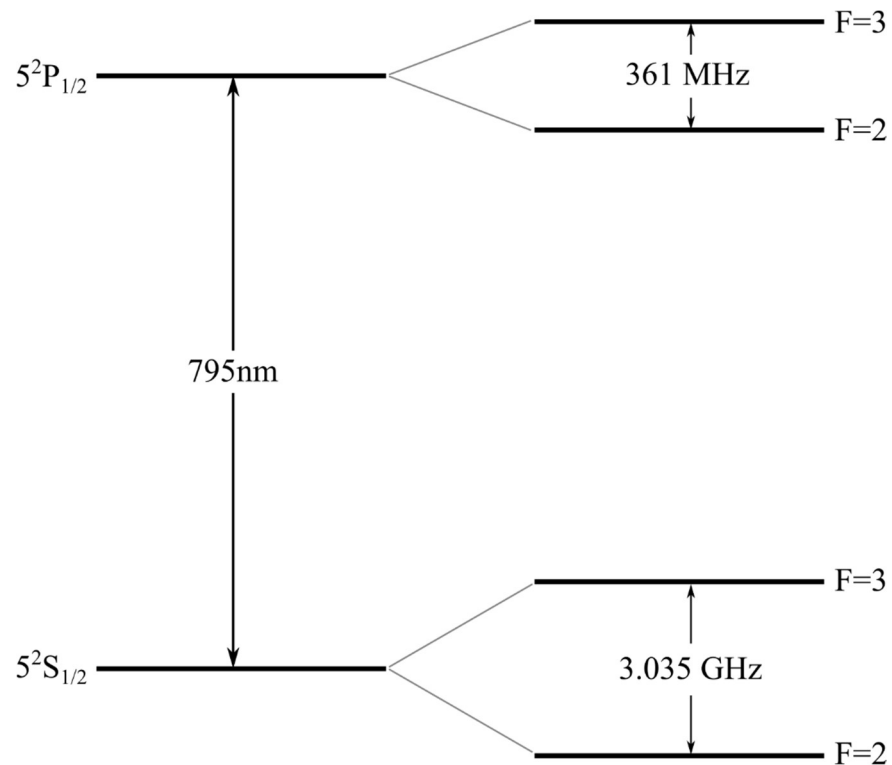


Figure 2-2: Energy diagram of the  $^{85}\text{Rb}$  D1 line hyperfine levels. Figure was drawn with data taken from [26, p. 26].

### 2.1.3 Zeeman sublevels.

When there is no magnetic field applied to the atom there is no further splitting of the hyperfine levels. However, if a static magnetic field is applied, due to Zeeman effects, each hyperfine level is split into several sublevels [27]. This is caused by the electron's magnetic dipole moment being influenced by the magnetic field. The splitting of these sublevels depends on the intensity of the field. Since relatively weak fields are used in CPT experiments, the splitting remains small. These sublevels are rather important for the CPT process, since their population is greatly affected by the polarization of the light being used for excitation. This is because the light transfers its angular momentum to the electron. If the light is circularly polarized to the right or left, the electrons tend to concentrate into the highest or lowest Zeeman sublevel respectively. If linear polarized light is used, then the distribution is more complex and electrons tend to accumulate in the middle sublevel ( $m=0$ ) [26, pp. 13-14]. However, in a CPT physics package a small, uniform, constant magnetic field is required to provide an axis of orientation of the electrons dipole moment. Since the magnetic field lines are typically orientated in a direction parallel to the propagation of the laser beam, circular polarization is required for the beam to transfer its energy to the electrons and achieve resonance. Even though this shifts most of the population to the extreme Zeeman sublevels, the  $m=0$  transition is always used, due to the fact that its frequency is much less sensitive to low intensity magnetic fields, even though the resonance amplitude is low due to the lower electron population. Some more advanced techniques, such as Push-Pull Optical Pumping (PPOP) [28] and modulation of the light polarization [29] are being developed by researchers to circumvent this issue and increase the resonance contrast.

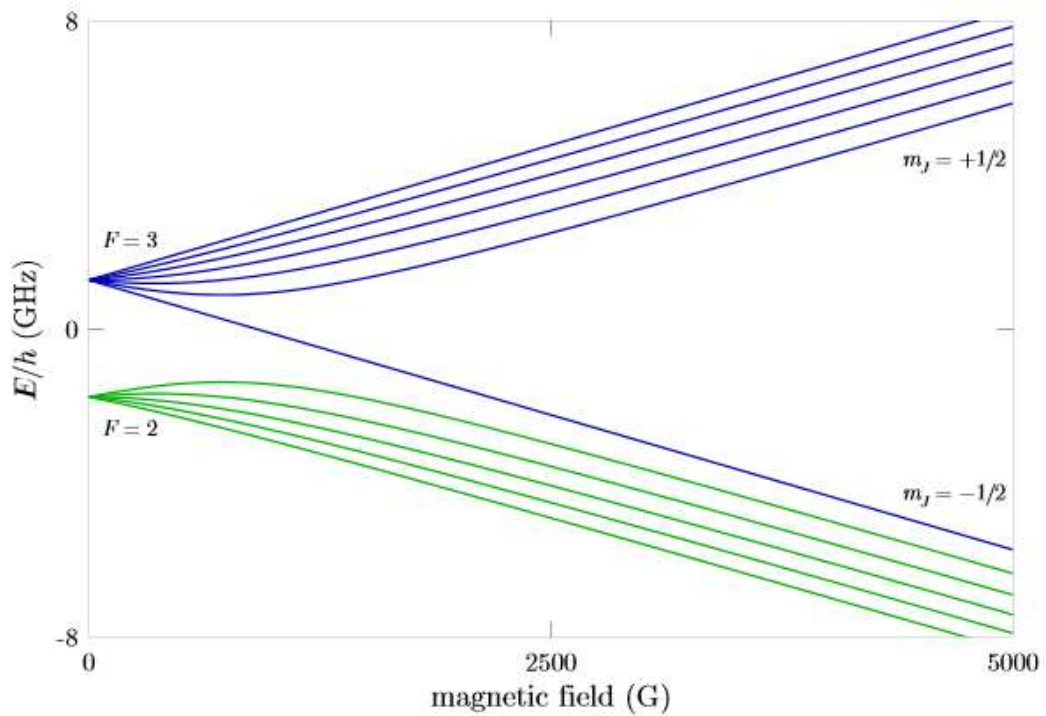


Figure 2-3: Zeeman splitting of the  $^{85}\text{Rb}$  ground state hyperfine levels vs. magnetic field intensity. Figure taken from [26, p. 27].

## 2.2 Operation of Rb CPT Physics Package.

A brief introduction on the principles of operation of a Rubidium CPT physics package was given in section 1.1.1.2. In this section, a more detailed description will be provided, in particular for a clock using a  $^{85}\text{Rb}$  vapour cell. Details on the main conditions required for achieving CPT resonance and the main factors that affect the resonance stability will be discussed.

A basic  $^{85}\text{Rb}$  physics package consists of the following components:

- Laser source. A Vertical Cavity Surface Emitting Laser (VCSEL) is typically used in compact physics package designs. This is a type of semiconductor laser in which the light is emitted vertically from the surface of the semiconductor [30]. The laser is used to induce the electron transitions from the ground states to the excited state. The wavelength is either 780nm, if the D2 line transition is desired ( $5^2S_{1/2} \rightarrow 5^2P_{1/2}$  transition) or 795nm, if the D1 line is desired ( $5^2S_{1/2} \rightarrow 5^2P_{3/2}$  transition).

- Polarizer and quarter wave plate. These are used to produce the circular polarization of the laser beam required to detect the atomic resonance. The linear polarizer can be omitted, if the laser light is already linearly polarized.
- $^{85}\text{Rb}$  vapour cell. The cell can contain either the naturally occurring isotope mixture of Rubidium (72%  $^{85}\text{Rb}$  and 27%  $^{87}\text{Rb}$ ) or just one of the purified isotopes.
- Photodiode detector. Used to detect the intensity of laser light transmitted through the vapour cell.

A diagram of the basic physics package configuration is shown in Figure 2-4.

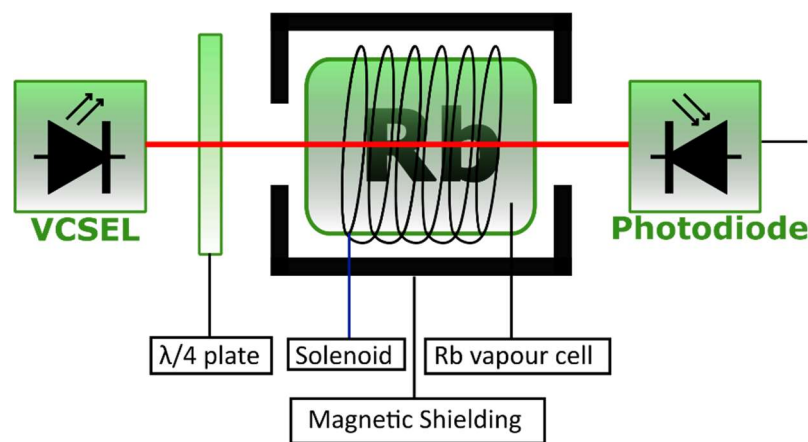


Figure 2-4: Basic Rb CPT physics package.

The cell is heated to a temperature above the melting point of Rubidium (39.3°C). Depending on the contents of the vapour cell, the operating temperature is chosen at a point where there is enough vapour pressure for light absorption to take place. A typical operating point is about 50°C. A coil is used to produce a stable and uniform magnetic field inside the cell in order to provide an axis of polarization for the atoms.

If the laser is tuned to the Rb absorption line and its linewidth is swept over a range of about 10GHz, the full spectrum of the Rb absorption can be observed, which shows the transitions from each of the ground hyperfine levels to the excited state (Figure 2-5) [31]. Transitions between individual hyperfine excited states are masked by doppler broadening in the atoms [32]. This effect and techniques used to deal with it are discussed in another section of this thesis.

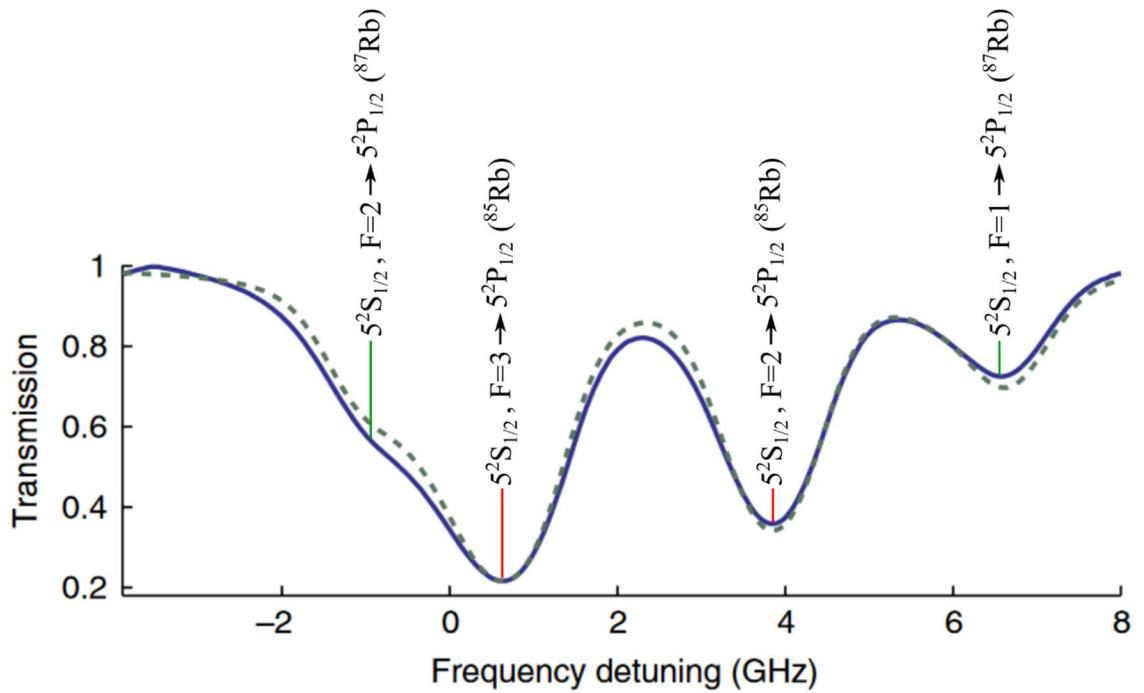


Figure 2-5: Rb absorption spectrum calculated (dotted line) and measured (solid line) by the authors in [31]. The 4 absorption dips represent the transitions from ground hyperfine levels to the excited state of each isotope. The spectrum measured by the author of this thesis is shown in Chapter 5.

In order to trap the electrons in the quantum superposition state and achieve CPT resonance, the laser has to be modulated by a microwave signal at half the frequency of the hyperfine splitting of the Rb ground states. This produces optical sidebands at the exact hyperfine frequency. Figure 2-6 shows the desired optical spectrum for detecting the  $^{85}\text{Rb}$  CPT resonance.

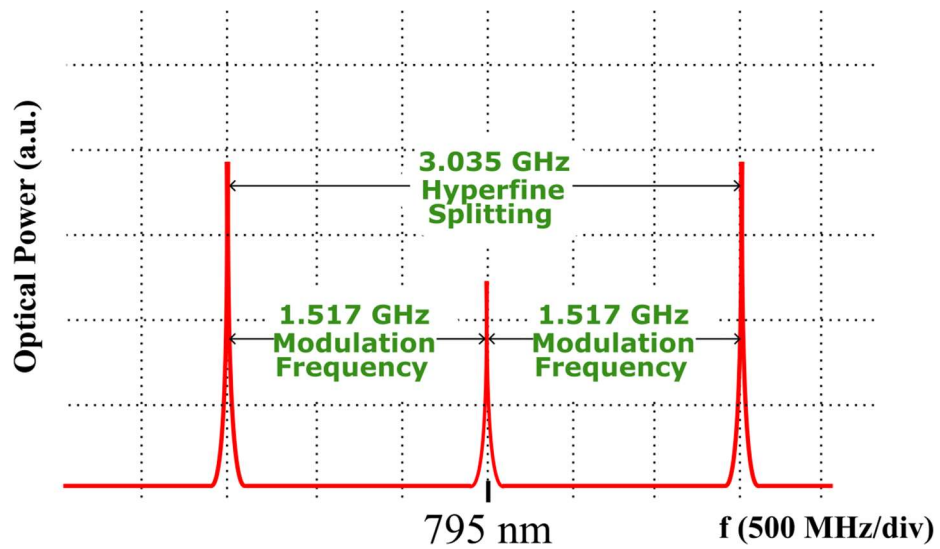


Figure 2-6: Desired laser optical spectrum for  $^{85}\text{Rb}$  CPT detection. For optimal operation most of the optical power should be concentrated in the first order sidebands.

When the RF frequency is scanned over a range of a few kilohertz, the resonance can be seen as a narrow peak on the photodiode's signal (Figure 2-7). This resonance is then used as a frequency discriminator in a feedback loop to lock the frequency of the microwave source (local oscillator) and complete the atomic clock configuration.

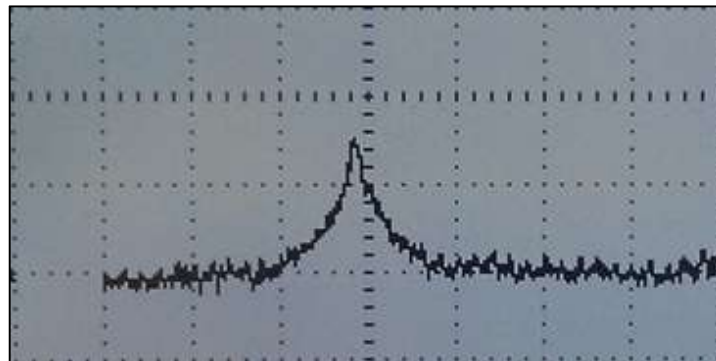


Figure 2-7:  $^{85}\text{Rb}$  hyperfine resonance peak. The horizontal axis corresponds to 1kHz/div.

## 2.3 Important conditions for achieving CPT

In order to achieve Coherent Population Trapping and detect the hyperfine resonances, certain parameters have to be met. This section describes those parameters and the reason why they are critical.

### 2.3.1 Vapour cell temperature.

Rubidium has a melting point of about 39.3°C. Therefore, at room temperature most of the metal condenses on the walls of the cell. However, in order to measure the absorption spectrum or the hyperfine resonances of the element, the laser beam needs to interact with free moving atoms inside the cell. This is why the cell needs to be heated up to a temperature above the melting point. Although this temperature is not nearly high enough to boil the Rubidium, it is enough to vaporize some of it and increase the pressure inside the cell. Depending on parameters such as the cell's dimensions and quantity of Rb and buffer gas inside, the ideal temperature for correct operation may be different for each cell. Typically, CPT resonances can be observed within the range of about 45°C to about 70°C. The cell temperature also has an effect on the amplitude and linewidth of the resonance as well as the clock's stability. By careful selection of the buffer gas pressures inside the cell, a turnover point can be achieved in the temperature coefficient. It is reported in [11] and [33, p. 55] that the resonance frequency vs. temperature coefficients are in the order of  $10^{-10}/^{\circ}\text{C}$  around the turnover point, however these are greatly affected by the dimensions of the cell and the buffer gases.

### 2.3.2 Laser beam polarization.

Another important condition for CPT detection is that the laser beam needs to be circularly polarized. Normally the VCSEL's light is linearly polarized. To change the polarization, a quarter wave plate needs to be inserted in the path of the beam. When the plate's fast axis is aligned at a 45° angle in respect to the plain of polarization of the laser, the component that is parallel to the fast axis gets through the plate unchanged, while the component orthogonal to the fast axis is delayed by 90° phase (1/4 of the wavelength). This causes the vector of polarization to rotate clockwise or counter-clockwise, depending on the direction of the 45° angle (Figure 2-8).

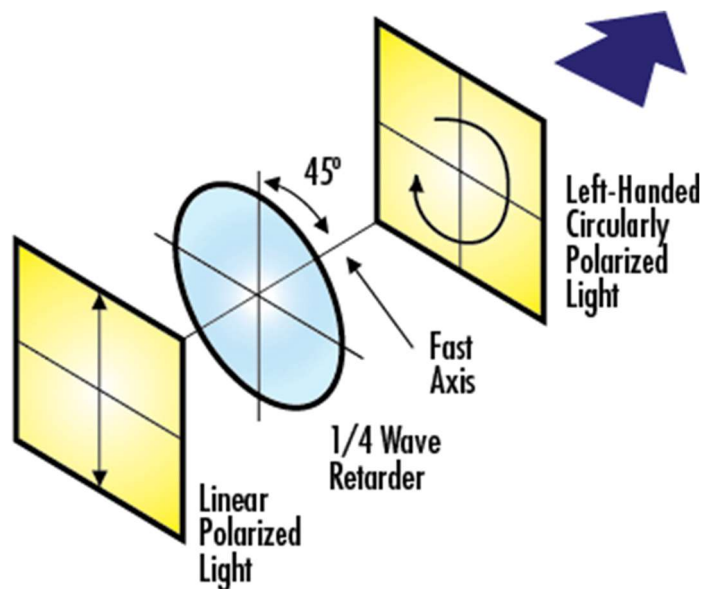


Figure 2-8: Quarter wave plate operational diagram. Figure taken from [34].

Circular polarization is critical mainly because it is required for the light to transfer its angular momentum to the electrons for correct excitation to take place. As described in chapter 3, the hyperfine resonances cannot be detected using linearly polarised light.

### 2.3.3 Vapour cell magnetic field.

Circularly polarized light on its own cannot create the correct conditions for CPT to occur. A constant and stable magnetic field parallel to the direction of propagation of the beam is required inside the vapour cell to align the magnetic dipoles of the Rb atoms and provide an axis of polarization for the beam. This is done by placing the cell inside a solenoid. Then a constant current is passed through the solenoid producing a magnetic field, the intensity of which is proportional to the intensity of the current.

### 2.3.4 Laser wavelength.

As seen in Figure 2-5, absorption by the Rb vapour occurs only over a range of frequencies of about 6.8GHz. This means that the VCSEL's frequency has to be accurate within less than 1GHz in order to detect the hyperfine resonances and even greater accuracy is required to make the atomic reference as stable as possible. The lasers used in this project

were provided by OCLARO Inc. (part number APM2101013300) and are designed especially for use in atomic clocks. Their wavelength can be adjusted by changing either their driving current or their temperature. According to the specifications, the laser should operate at the Rb absorption wavelength at driving current of about 2mA and temperature of about 50°C ( $\pm 3^\circ\text{C}$ ). The linewidth of the laser is specified as 30MHz. The measured coefficients are presented in chapter 5. Keeping the VCSEL's frequency stable requires designing a low noise current source and a stable temperature controller. For optimal stability, the laser frequency can be actively stabilized to the absorption spectrum of Rb.

### 2.3.5 RF modulation index and frequency.

The hyperfine splitting frequency of  $^{85}\text{Rb}$  is 3.035 732 439 GHz (Figure 1-3). However, this can be shifted by the magnetic field, due to the effect of the Zeeman sublevels (see chapter 2.1.3.) The shift can be in the order of hundreds of Hz or even greater, depending on the intensity of the magnetic field. The amplitude of the resonance also depends on the ratio between the laser's carrier and the sidebands created by the RF modulation. It is therefore required to find the correct frequency and modulation index to detect the hyperfine resonance.

## 2.4 Parameters affecting the frequency stability.

The most important feature of an atomic frequency reference is its frequency stability. It is usually presented in terms of Allan Deviation, which is calculated by taking samples of the device's frequency in specific time slots of length  $\tau$ , calculating the difference between each consecutive sample, normalizing to the carrier frequency and averaging all the differences up to a certain point in time. Then the average differences are plotted against the averaging time to produce the Allan Deviation curve (Figure 2-9). A detailed description of how Allan Deviation is calculated is given in [35, pp. 7-8], [36, p. 8].

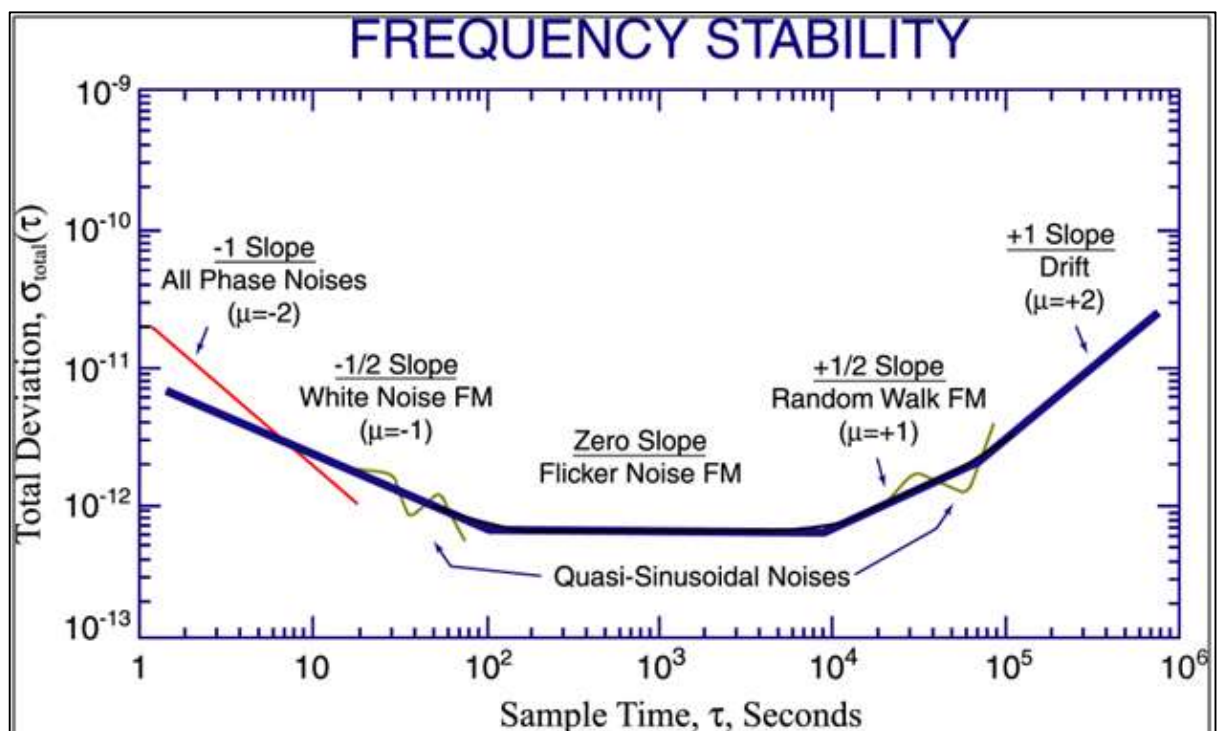


Figure 2-9: Allan Deviation curve example. Figure taken from [37]

This representation is particularly useful, because it can be used to identify different types of noise that degrade the system's stability.

There are several factors that can affect the atomic reference's stability. They are mainly parameters that can change the exact frequency of the hyperfine resonance, but can also be related to electronic noise or mechanical robustness.

#### 2.4.1 Magnetic field.

As described in section 2.3.3, a uniform magnetic field inside the cell, parallel to the propagation of the laser beam is required to achieve hyperfine resonance detection. However, this can also change the resonance's frequency depending on the intensity of the field. Spurious magnetic fields from the environment can also induce shifts and degrade the clock's performance. This issue is addressed by selecting the  $m=0$  Zeeman sublevel transition, as it is significantly less sensitive to magnetic fields, by making sure that the magnetic field generated by the coil is stable and by surrounding the cell with mu-metal shielding to avoid perturbations by spurious external magnetic fields. The Zeeman shift of the desired clock transition in  $^{85}\text{Rb}$  is reported in [26, p. 18] and [38, p. 5] as about  $1294\text{Hz/G}^2$ , which means that in order to achieve frequency stability in the order of parts in  $10^{-13}$  the magnetic field should be stable within about 10mG. For comparison, the average intensity of the earth's magnetic field is about 500mG in the UK.

#### 2.4.2 Vapour cell temperature coefficient.

The temperature of the cell affects the vapour and buffer gas pressure, which in turn changes the frequency of the hyperfine resonance. However small, this change can degrade the systems stability if the cell's temperature changes during operation. It is therefore critical to design a stable temperature controller for the vapour cell and thermally insulate it as best as possible. There is also the possibility to manufacture vapour cells with a mixture of 2 buffer gasses. One that has a positive temperature coefficient (meaning that it shifts the hyperfine resonance to higher values with increasing temperature) and one that has a negative coefficient. By carefully controlling the pressure of these gasses, a temperature region with very low coefficient can be produced (Figure 2-10) [39, p. 111].

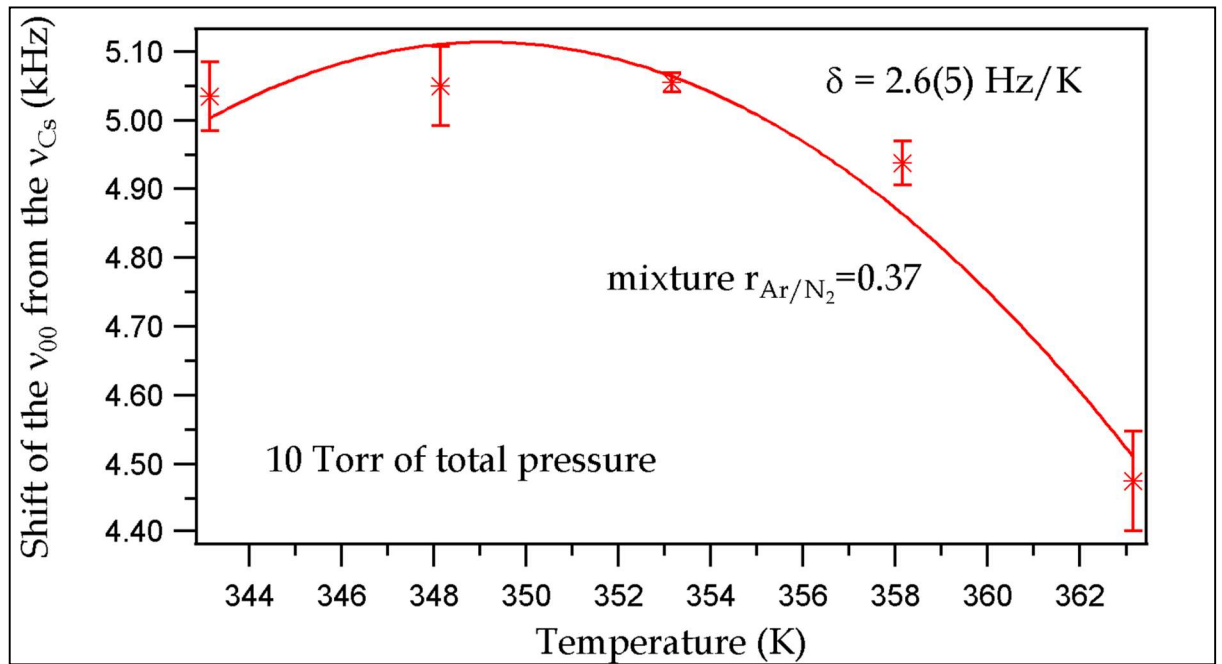


Figure 2-10: Shift of the hyperfine frequency of Cs vs. cell temperature.

Buffer gas mixture of Ar and N<sub>2</sub>. Figure taken from [39, p. 111]

#### 2.4.3 Hyperfine resonance linewidth and amplitude.

The Full Width at Half Maximum of the hyperfine resonance peak in terms of frequency is referred to as linewidth. The amplitude is simply the height of the peak if the base is considered to be the absorption minimum (Figure 2-11).

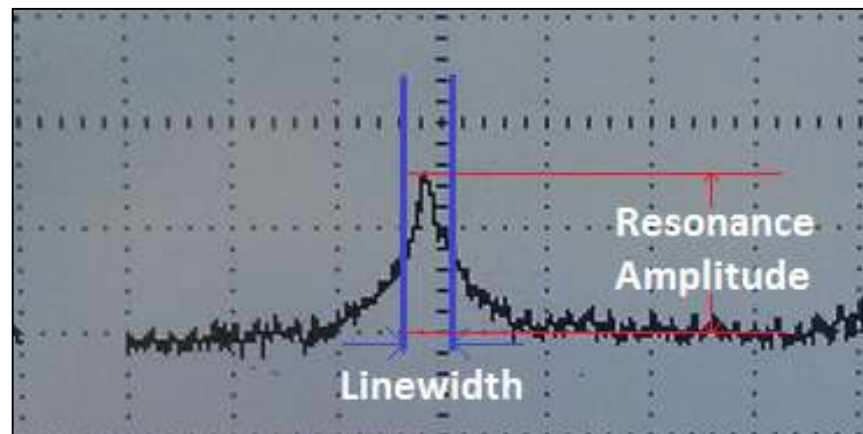


Figure 2-11: CPT resonance linewidth and amplitude. In this image the amplitude is about 75mV and the linewidth about 800Hz.

The ability of the feedback system to stabilize the RF signal source's frequency is improved when the amplitude of the resonance is higher and the linewidth is narrower. These two features are affected by a number of different parameters.

The general equation describing the linewidth of the CPT resonance is:

$$FWHM = \frac{1}{\pi} \left( \gamma_2 + \frac{\omega_R^2}{\Gamma^*} \right) \quad (2.1) [40], [41]$$

Where  $\gamma_2$  is the relaxation rate of the electrons from the coherent superposition state,  $\omega_R$  is the optical Rabi pulsation related to the laser intensity and  $\Gamma^*$  is the decay rate of the electrons from the excited state [40]. It can be seen that the full width at half maximum of the CPT resonance is increased as the relaxation rate from the coherent state increases. The rate  $\gamma_2$  can be expressed as a function of 3 main parameters:

$$\gamma_2 = \gamma_w + \gamma_{se} + \gamma_{bg} \quad (2.2) [40]$$

Where  $\gamma_w$  is the relaxation rate due to collisions of the Rb atoms with the cell walls.

$$\gamma_w = \left[ \left( \frac{2.405}{R} \right)^2 + \left( \frac{\pi}{L} \right)^2 \right] D_0 \frac{P_0}{P} \quad (2.3) [40]$$

This term is inversely proportional to the radius  $R$  and length  $L$  of the vapour cell and the buffer gas pressure  $P$ . Therefore, its contribution is reduced by using a larger size cell and by including the buffer gasses. The term  $\gamma_{se}$  is the relaxation rate due to spin exchange collisions between Rb atoms and is also reduced by the introduction of buffer gasses into the cell. However, if the buffer gas pressure is too great, the linewidth is increased by the term  $\gamma_{bg}$ , which is the rate due to collisions of the Rb atoms with the buffer gas atoms [40].

Another factor that affects the linewidth and amplitude is the cell's temperature. As the temperature increases, the collisions between Rb atoms, cell walls and buffer gasses are also increased. In addition, the increase in the absorption can mask the CPT resonance and reduce its amplitude.

The magnetic field intensity applied by the solenoid can also change the features of the resonance, in addition to changing its frequency. If the intensity is too low, the amplitude

decreases, but if it is too high, it starts to broaden the linewidth. Therefore, it is important to find an optimal intensity setting and keep it constant.

#### 2.4.4 Light Shift.

Light shift is a very important factor that degrades the performance of an atomic clock. It affects the atomic resonance frequency in two different ways. It can either be caused by changes in the light intensity of the interrogating laser beam ( $\alpha$  coefficient) or by changes in its frequency ( $\beta$  coefficient) [42, p. 90]. The beam intensity is reasonably constant while operating the laser with a constant current source, however, changes in the alignment of the optical components may cause it to change. This means that it could be sensitive to vibrations. Figure 2-12 shows the light shift coefficients for  $^{87}\text{Rb}$ . It can be seen that the two ground hyperfine transitions have opposite  $\beta$  coefficients. Since the two laser sidebands are tuned so that they excite both of these levels, it is possible to minimize the frequency coefficient if the power is distributed slightly differently in each sideband [33, pp. 47-49].

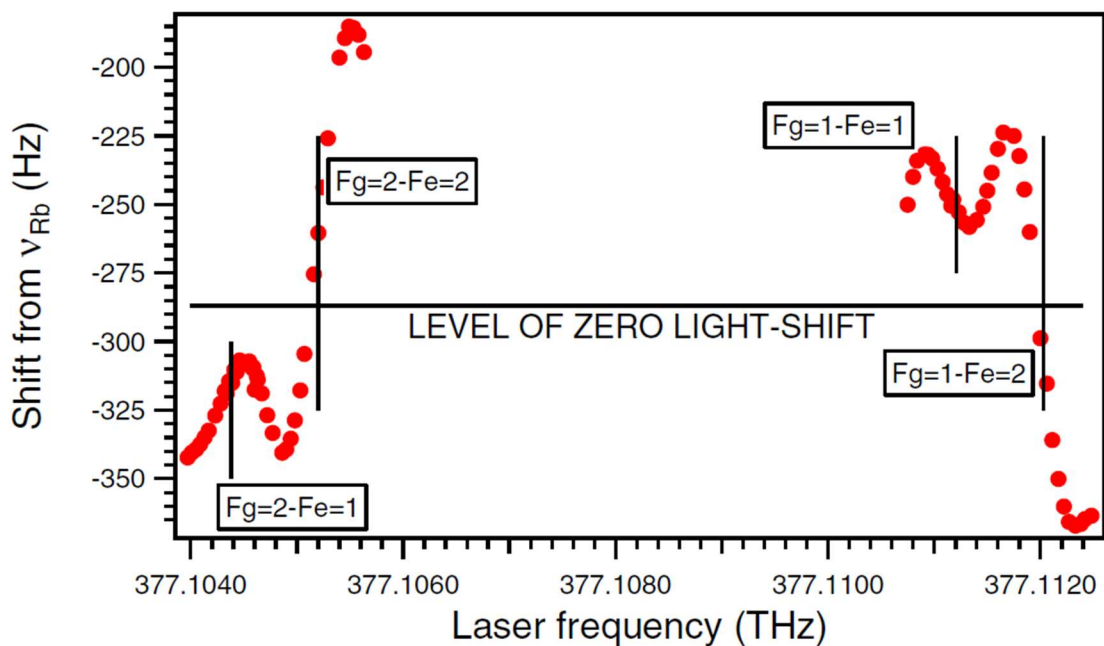


Figure 2-12: Light shift coefficients of  $^{87}\text{Rb}$ . Figure taken from [43]

As described in section 2.3.4. the laser's frequency can shift with changes in temperature and driving current. Although the current to the laser is provided by a constant current source, any noise in these circuits can cause unwanted changes in laser frequency and therefore instability in the final system. This is why, it is important to design these circuits with minimizing the noise as a priority. Ideally, there should be active control of the laser centre frequency. How this is done is described in more detail in section 2.5. Also, the temperature control loop has to be made as stable as possible.

#### 2.4.5 Detection Noise.

The hyperfine resonance is a very small peak in light intensity reaching the photodiode compared to the background light (typically a few percent over the background light). The stability of the atomic clock is directly proportional to the ratio between the Full Width at Half Maximum (FWHM) of the resonance and its contrast. Although there are methods to increase the contrast of the resonance, they require more complex configurations and increase the volume and cost of the physics package. This can also be expressed as a signal to noise ratio (SNR) of the resonance. For optical performance, the amplitude and linewidth of the resonance must be maximized, while the noise in the laser and detection electronics must be minimized. The contribution of the SNR to the stability performance of the clock is described by:

$$\sigma_y(\tau) = \frac{1}{f_c} \frac{\sigma_N}{S_\ell} \sqrt{\frac{1}{\tau}} \quad (2.4) [44]$$

Where  $f_c$  is the clock frequency,  $S_\ell$  is the slope of the frequency discriminator (atomic resonance) and  $\sigma_N$  is the standard deviation of the signal's white noise.

#### 2.4.6 Local Oscillator Phase Noise.

The phase noise of the local oscillator that is being locked to atomic reference is also critical. Lower noise floor and flicker noise corner mean that the short-term stability is greater, while the close to carrier noise affects the medium to long-term stability. One of

the main goals of this project is to use a multi-element local oscillator that will achieve excellent close to carrier and far from carrier performance, while the stable reference of the atomic resonance will further improve the long-term stability. The short-term stability of the clock in terms of Allan Variance can be expressed as:

$$\sigma_y^2(\tau) = \sum_i \sigma_{y,p_i}^2(\tau) + \sigma_{y,LO}^2(\tau) \quad (2.5) [44]$$

Where  $\sigma_{y,p_i}^2(\tau)$  is the variance due to the fluctuations induced in the microwave interrogation signal used to lock to the hyperfine resonance and  $\sigma_{y,LO}^2(\tau)$  is the Allan variance of the local oscillator (LO). For example, the contribution of the LO phase noise in terms of Allan deviation at 1s averaging time can be estimated using:

$$\sigma_{y,LO}(1s) \sim \frac{F_M}{f_c} \sqrt{S_\varphi(2F_M)} \quad (2.6) [44]$$

Where  $S_\varphi(2F_M)$  is the LO phase noise in  $rad^2Hz^{-1}$  and  $F_M$  is the Fourier offset frequency.

## 2.5 Summary.

The atomic transition lines of Rubidium that are used in a CPT physics package and their origins were described. Important effects such as the Zeeman splitting of the hyperfine levels were indicated. The conditions for correct operation of the clock and important parameters that affect the stability were discussed. It was concluded that to achieve optimal frequency stability in the atomic clock, all electronics must be designed with emphasis on low noise operation and the physics package constructed with emphasis on minimizing the FWHM and maximizing the contrast of the atomic resonance. Parameters, such as vapour cell and laser temperature must be optimally stabilized. The phase noise of the local oscillator must be as low as possible to achieve optimal short-term stability.

## 3 LOCAL OSCILLATOR (LO).

### 3.1 Introduction.

A Rubidium CPT atomic clock configuration can be described on a basic level using the 3 main components shown in Figure 3-1.

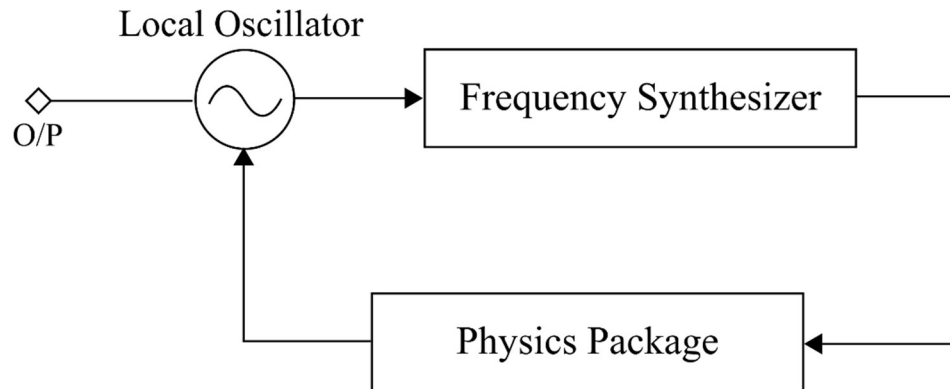


Figure 3-1: Basic atomic clock block diagram.

The local oscillator is the source of the microwave signal that induces the coherent state in a CPT physics package in order to detect the resonance. It is also frequency locked to that resonance and provides the stable frequency output. The frequency synthesizer upconverts, tunes or modulates the LO microwave frequency output, depending on the requirements of the physics package. The physics package is where the atomic transitions take place and the hyperfine resonance is detected. As it was described in section 2.4.6, the phase noise of the local oscillator is one of the main contributors of short and medium-term instability in an atomic clock. It is therefore important to design and construct an LO with the lowest possible phase noise at all offsets. Previous research by Professor Jeremy Everard's group has produced a variety of oscillator designs at different frequency bands, all with state of the art phase noise performance. The general techniques and design methodologies used to produce those oscillators were employed for the construction of the LO used in this project. It was deemed that the best phase noise can be achieved by combining the close to carrier phase noise performance of a crystal oscillator with the medium and high offset performance of a Dielectric Resonator Oscillator (DRO) by placing them in a phase locked

configuration. This chapter includes details on the theoretical models used for designing the oscillators and key design considerations and techniques for achieving optimal phase noise. Details on the construction of the oscillators and completing the phase locked loop are presented, along with phase noise measurements results.

### 3.1.1 Oscillator Phase Noise Theory.

The design of the individual elements of the local oscillator was based on the theoretical model developed by Professor Jeremy Everard and published in [45], [24], [22]. In this model, the oscillator is represented as shown in Figure 3-2.

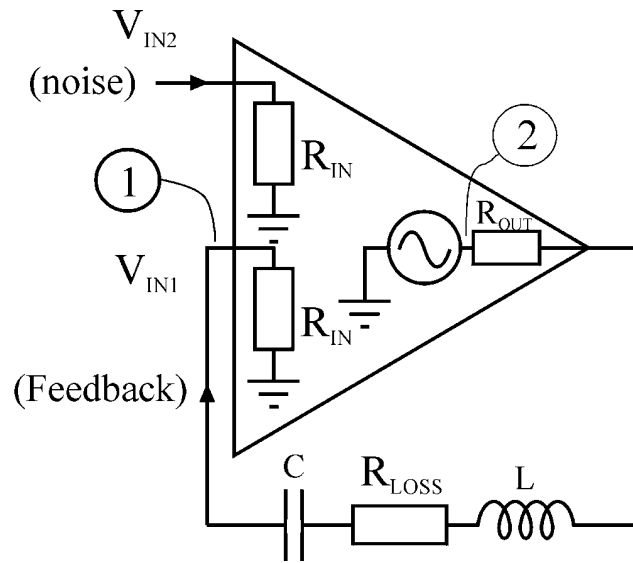


Figure 3-2: Equivalent circuit model of an oscillator.

The oscillator consists of an amplifier with two inputs with equal input impedance  $R_{IN}$ . One of the inputs is used to model the feedback loop including the resonator and one input is used to inject and model the noise. This allows separate modelling of the two parameters. The amplifier also includes an output impedance  $R_{OUT}$ . The resonator is modelled as a series LC circuit with a loss resistance  $R_{LOSS}$ . The unloaded Q of the resonator can therefore be expressed as:  $Q_0 = \omega L / R_{LOSS}$ . The transfer characteristic of this circuit can be described in a similar way to the one of an operational amplifier. Therefore:

$$V_{OUT} = G(V_{IN2} + V_{IN1}) = G(V_{IN2} + \beta V_{OUT}) = V_{IN2} \frac{G}{1 - \beta G} \quad (3.1)$$

Where  $G$  is the amplifier gain and  $\beta$  is the feedback coefficient between nodes 1 and 2. By considering the input and output impedances as well as the resonator model circuit, the feedback coefficient can be written as:

$$\beta = \frac{R_{IN}}{R_{OUT} + R_{LOSS} + R_{IN} + j\left(\omega L - \frac{1}{\omega C}\right)} \quad (3.2)$$

Assuming that the angular frequency  $\omega$  is expressed in terms of a centre frequency  $\omega_0$  and an offset frequency  $\Delta\omega$ , with ( $\Delta\omega \ll \omega_0$ ), the approximation can be made that:

$$\left(\omega L - \frac{1}{\omega C}\right) = \pm 2\Delta\omega L \quad (3.3)$$

And the loaded Q at the centre frequency is:

$$Q_L = \omega_0 L / (R_{OUT} + R_{LOSS} + R_{IN}) \quad (3.4)$$

While the unloaded Q is:

$$Q_0 = \omega_0 L / R_{LOSS} \quad (3.5)$$

Then by solving equation (3.4) for L and substituting into (3.2) the feedback coefficient becomes:

$$\beta = \frac{R_{IN}}{(R_{OUT} + R_{LOSS} + R_{IN})\left(1 \pm 2jQ_L \frac{\Delta\omega}{\omega_0}\right)} \quad (3.6)$$

The ratio of loaded to unloaded Q is:

$$\frac{Q_L}{Q_0} = \frac{R_{LOSS}}{(R_{OUT} + R_{LOSS} + R_{IN})} \quad (3.7)$$

And:

$$1 - \frac{Q_L}{Q_0} = \frac{R_{OUT} + R_{IN}}{(R_{OUT} + R_{LOSS} + R_{IN})} \quad (3.8)$$

Then the feedback coefficient at resonance becomes:

$$\beta_0 = \frac{R_{IN}}{(R_{OUT} + R_{LOSS} + R_{IN})} = \left(1 - \frac{Q_L}{Q_0}\right) \left(\frac{R_{IN}}{R_{IN} + R_{OUT}}\right) \quad (3.9)$$

And therefore, the resonator response is:

$$\beta = \left(1 - \frac{Q_L}{Q_0}\right) \left(\frac{R_{IN}}{R_{IN}+R_{OUT}}\right) \frac{1}{1 \pm 2jQ_L \frac{\Delta f}{f_0}} \quad (3.10)$$

Where  $f_0$  is the centre frequency and  $\Delta f$  is the offset frequency in Hertz. Since at resonance  $\Delta f$  is 0, the last term in the above equation can be omitted. In this case the product of the gain and feedback coefficient is  $G\beta_0 = 1$ , which makes:

$$G = \frac{1}{\left(1 - \frac{Q_L}{Q_0}\right) \left(\frac{R_{IN}}{R_{IN}+R_{OUT}}\right)} \quad (3.11)$$

This means that at resonance the amplifier gain is required to be equal to the insertion loss and the gain of the amplifier is fixed by the operating conditions. Another approximation can be made, considering the sideband noise occurs only in the 3dB bandwidth of the resonator, since the Q multiplication process causes the noise to go down to the noise floor within this bandwidth. This is because the resonator's response has negligible effect on the phase noise beyond the 3dB bandwidth. Considering this, the voltage transfer characteristic can be expressed as:

$$\frac{V_{OUT}}{V_{IN2}} = \frac{G}{\pm 2jQ_L \frac{\Delta f}{f_0}} = \frac{1}{\left(1 - \frac{Q_L}{Q_0}\right) \left(\frac{R_{IN}}{R_{IN}+R_{OUT}}\right) \left(\pm 2jQ_L \frac{\Delta f}{f_0}\right)} \quad (3.12)$$

Now the gain is represented in the equation in terms of the ratio of loaded to unloaded Q ( $Q_L/Q_0$ ), which is set by the insertion loss in the resonator.

Oscillator noise is usually quoted as the ratio of the noise power within a 1Hz bandwidth at a certain offset frequency from the carrier to the power in the carrier. For this purpose, the voltage transfer function needs to be converted into a characteristic proportionate to power and noise needs to be inserted into the model. This is done by squaring the voltage characteristic and adding the equivalent voltage noise source of the input resistance:

$$V_{IN} = \sqrt{4kTB R_{IN}}$$

Where  $k$  is the Boltzmann constant,  $T$  is the absolute temperature and  $B$  is the bandwidth. Since the voltage is squared and  $B=1\text{Hz}$ , the voltage transfer characteristic within 1Hz bandwidth at an offset  $\Delta f$  from the carrier becomes:

$$(V_{OUT}\Delta f)^2 = \frac{FkT_{IN}}{4(Q_0)^2\left(\frac{Q_L}{Q_0}\right)^2\left(\frac{R_{IN}}{R_{IN}+R_{OUT}}\right)^2\left(1-\frac{Q_L}{Q_0}\right)^2}\left(\frac{f_0}{\Delta f}\right)^2 \quad (3.13)$$

Where  $F$  is the noise figure of the amplifier under oscillating operating conditions. Although the unloaded  $Q$  is set by the type and construction of the resonator, the ratio of loaded to unloaded  $Q$  is set by adjusting the insertion loss, which also sets the closed loop gain of the amplifier.

Equation ( 3.13 ) includes the equal contributions of both amplitude modulation noise (AM) and phase modulation noise (PM). However, if the output signal amplitude of the oscillator is limited by a hard limiter (i.e. operating in saturation), the AM noise is suppressed and the equation is divided by a further factor of 2. This is because the AM fluctuations are reduced by the limiter, which does not affect the zero-crossing jitter (PM noise).

Now that the noise within 1Hz bandwidth is described, it can be divided by the total output power and the ratio  $L_{FM}$  can be obtained:

$$\mathcal{L}(f) = \frac{(V_{OUT}\Delta f)^2}{(V_{OUT\ MAX\ RMS})^2} \quad (3.14)$$

$$\mathcal{L}(f) = \frac{FkTR_{IN}}{8(Q_0)^2\left(\frac{Q_L}{Q_0}\right)^2\left(\frac{R_{IN}}{R_{IN}+R_{OUT}}\right)^2\left(1-\frac{Q_L}{Q_0}\right)^2(V_{OUT\ MAX\ RMS})^2}\left(\frac{f_0}{\Delta f}\right)^2 \quad (3.15)$$

If the total RF power is defined either as the power in the oscillating system ( $P_{RF}$ ) or the power available at the output of the oscillator ( $P_{AVO}$ ), equation ( 3.15 ) can be further simplified. Another generalization can be done by assuming the output impedance is either set to 0 (as in the case of high efficiency amplifiers) or equal to the input impedance, which is the most commonly used configuration in RF amplifier design. A general form of the equation can therefore be written as:

$$\mathcal{L}(f) = A \frac{FkT}{8(Q_0)^2\left(\frac{Q_L}{Q_0}\right)^2\left(1-\frac{Q_L}{Q_0}\right)^N P} \left(\frac{f_0}{\Delta f}\right)^2 \quad (3.16)$$

Where:

1.  $N=1$  and  $A=1$  if the power  $P$  is defined as the total power in the oscillating system ( $P_{RF}$ ), excluding the losses in the amplifier and  $R_{OUT} = 0$ .
2.  $N=1$  and  $A=2$  if the power  $P$  is defined as the total power in the oscillating system ( $P_{RF}$ ) and  $R_{OUT} = R_{IN}$ .
3.  $N=2$  and  $A=1$  if the power  $P$  is defined as the power available at the output of the amplifier ( $P_{AVO}$ ) and  $R_{OUT} = R_{IN}$ .

### 3.1.2 Considerations for Optimal Phase Noise.

One of the main variables that influences the phase noise result in equation ( 3.16 ) is the ratio of loaded to unloaded  $Q$  of the resonator. An optimal value of this variable for minimum phase noise can be found by differentiating the equation in terms of  $Q_L/Q_0$  and equating it to 0:

$$\frac{d\mathcal{L}(f)}{d(Q_L/Q_0)} = 0 \quad (3.17)$$

When the power is defined as the total RF power in the oscillating system, this gives an optimal ratio of  $Q_L/Q_0 = 2/3$ , which means that the feedback coefficient needs to be set to 1/3 and the gain of the amplifier should be set to 3.

When the power is defined as the power available at the output of the amplifier ( $V^2/R_{OUT}$ ), then equation ( 3.16 ) becomes:

$$\mathcal{L}(f) = \frac{FkT}{32(Q_0)^2 \left(\frac{Q_L}{Q_0}\right)^2 \left(1 - \frac{Q_L}{Q_0}\right)^2 P_{AVO}} \left(\frac{R_{OUT} + R_{IN}}{R_{OUT} R_{IN}}\right)^2 \left(\frac{f_0}{\Delta f}\right)^2 \quad (3.18)$$

The term including the input and output resistances is minimum when  $R_{IN} = R_{OUT}$  and then the equation simplifies to:

$$\mathcal{L}(f) = \frac{FkT}{8(Q_0)^2 \left(\frac{Q_L}{Q_0}\right)^2 \left(1 - \frac{Q_L}{Q_0}\right)^2 P_{AVO}} \left(\frac{f_0}{\Delta f}\right)^2 \quad (3.19)$$

Applying the same differentiation to this form of the equation now yields an optimal ratio of  $Q_L/Q_0 = 1/2$ , which sets the loss in the resonator to 1/2 and the gain of the amplifier to 2. If this value for the Q ratio is inserted into equation ( 3.19 ), the phase noise performance of the oscillator simplifies to:

$$\mathcal{L}(f) = \frac{2Fk}{(Q_0)^2 P_{AVO}} \left( \frac{f_0}{\Delta f} \right)^2 \quad (3.20)$$

Using this model, a graph can be generated describing the phase noise degradation of the oscillator as a function of the ratio of loaded to unloaded Q and by extension, the resonator insertion loss:

$$S_{21(dB)} = 20 \log \left( 1 - \frac{Q_L}{Q_0} \right) \quad (3.21)$$

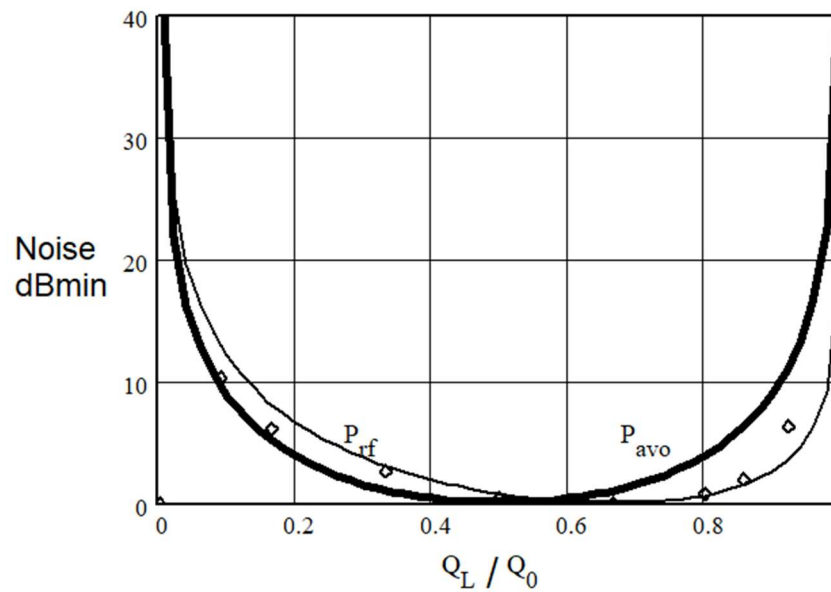


Figure 3-3: Phase noise degradation as a function of  $Q_L/Q_0$  [24], [45].

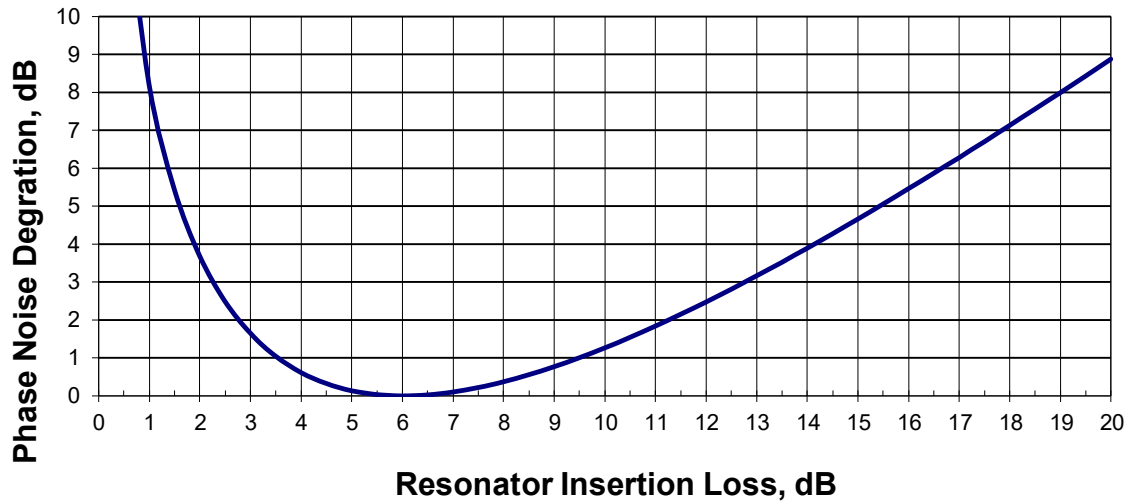


Figure 3-4: Phase noise degradation as a function of resonator insertion loss [24].

It can be seen from the graphs, that the optimal resonator insertion loss is 6dB and within the 3.5dB to 9.5dB margin the phase noise degradation remains lower than 1dB.

The Everard phase noise model [45] is similar to Leeson's model [46] however, it provides a better representation of the effect of the RF feedback power on the total phase noise. Also, it has a better correlation to practical measurements, due to the approximation that the AM component of the noise is suppressed in most oscillator designs, which effectively halves the total measured noise.

## 3.2 10 MHz Ultra-Low Phase Noise Crystal Oscillator.

The first component of the multi-element local oscillator used in the atomic clock is an ultra-low noise crystal oscillator operating at 10 MHz. This oscillator serves three main purposes:

1. To provide excellent close to carrier phase noise performance, within offset frequencies lower than 1Hz, up to about 10Hz.
2. To enable narrow frequency tuning with an electronically tuned phase shifter.
3. To provide a stable, low phase noise 10 MHz output signal.

The block diagram of the low phase noise 10 MHz crystal oscillator is shown in Figure 3-5. The design is based on the methodology described and published in [24], but has been significantly expanded upon. It comprises of a differential amplifier, spurious resonance rejection filter, a voltage tuned phase shifter and the crystal resonator. Details of the design of each of these elements and their circuit diagrams are described in this section.

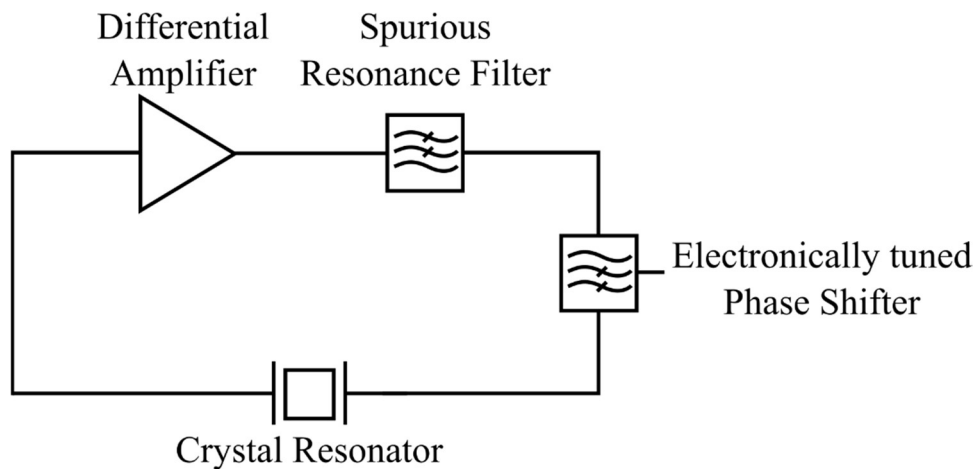


Figure 3-5: Block diagram of the low phase noise 10 MHz crystal oscillator.

### 3.2.1 Differential Amplifier.

The complete circuit diagram of the differential amplifier is shown in Figure 3-6

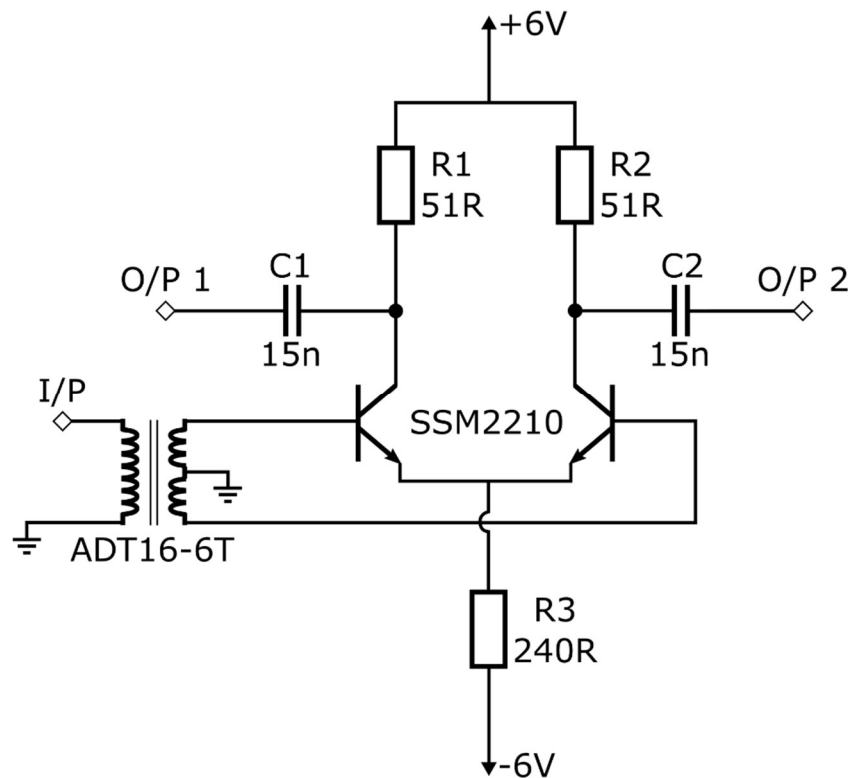


Figure 3-6: Differential amplifier circuit diagram.

The amplifier uses a low noise super matched NPN transistor pair (SSM2210 or SSM2212) to ensure good symmetry and low noise performance. These devices have very low flicker noise corner ( $\sim 5\text{Hz}$ ) and very low noise voltage and current density ( $e_n = 0.8\text{nV}/\sqrt{\text{Hz}}$ ), ( $i_n = 2\text{pA}/\sqrt{\text{Hz}}$ ) [47], which is useful for achieving low close to carrier phase noise. The advantage of the differential configuration is that it offers non-saturated limiting with lower noise, as the voltage swing across R1 and R2 is limited by the maximum current in each leg of the amplifier, which is set by R3 (the collector current was set to about 7.5mA in this case). The non-saturated limiting suppresses the AM noise of the oscillator, while avoiding significant non-linear effects, distortion and high order harmonics in the output signal. Another benefit is the fact that two outputs can be obtained with a phase difference of  $180^\circ$ . One of the outputs can be used to close the feedback loop and complete the oscillator, while the other can be used as the output. This eliminates the need for an output coupler. The bases of the transistors are differentially driven by the transformer ADT16-6T, which has one primary winding and two secondary windings with a centre tap and an impedance transformation ratio of 1:16. This transforms the  $50\Omega$  source impedance of the amplifier to  $800\Omega$ , which is near the optimal source impedance for minimum noise [45, p.

119]. The output impedances are set close to 50 ohm by the collector resistors R1 and R2. The capacitors C1 and C2 are used to couple the outputs of the amplifier and are calculated to have an impedance of about 1 ohm at the operating frequency.

The amplifier was built on Rogers R4003C substrate PCB. This is a low loss, low cost substrate, which has a precise dielectric constant and can be used to produce PCB's using the same process as FR4 boards. The gain and phase shift were measured using the HP8714ES network analyzer. Figure 3-7 shows the measured gain and Figure 3-8 shows the phase shift.

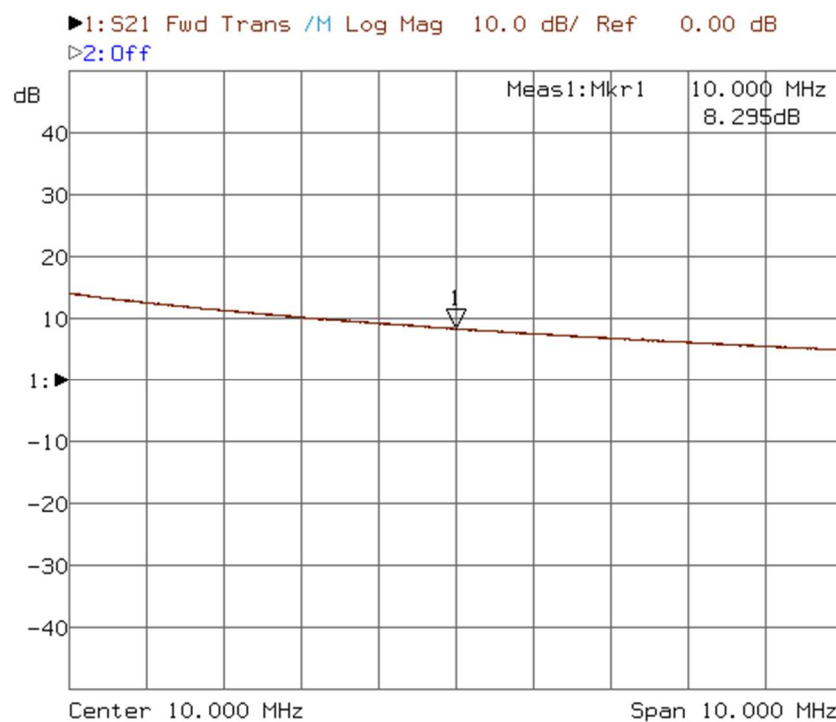


Figure 3-7: Differential amplifier frequency response.

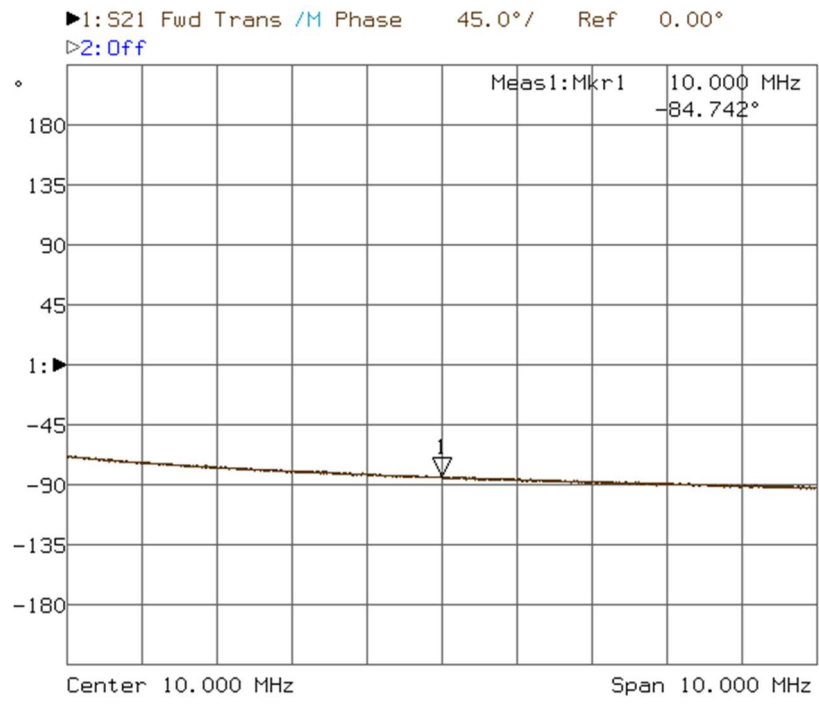


Figure 3-8: 10MHz amplifier phase shift.

The measured gain at 10MHz was 8.3dB, while the phase shift at output 2 (O/P 2) was 84.7°.

### 3.2.2 Crystal Resonator.

The 10 MHz SC cut crystal resonators were purchased from Nofech. Their specified characteristics were approximately: equivalent series resistance at resonance  $RR \sim 53\Omega$ ,  $Q_0 \sim 1.3M$  and turnover temperature,  $TO \sim 82^\circ C$ . Figure 3-9 shows the simple model of the crystal resonator with the series and parallel resonant components. The crystal was soldered on a test board with  $50\Omega$  microstrip transmission lines and its frequency response was measured using a network analyzer. The measurements were done with a slow sweep time to avoid ringing due to the high Q of the resonator.

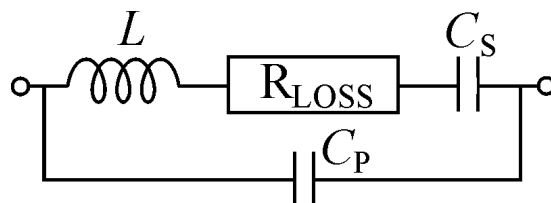


Figure 3-9: Crystal resonator equivalent circuit model.

Figure 3-10 shows the measurement of the series resonance.

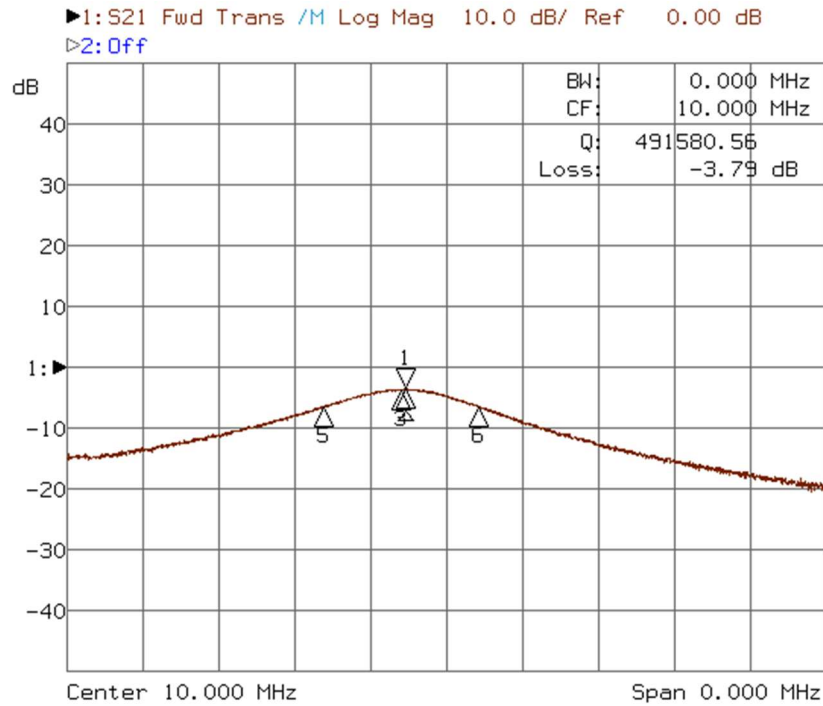


Figure 3-10: Crystal resonator frequency response (span=100Hz).

The measured loaded Q was 491,580 (which corresponds to a bandwidth of about 20Hz) and the insertion loss was 3.79dB. By using these measurements in equation ( 3.21 ), the unloaded Q of the series resonance can be estimated.

$$S_{21(dB)} = 20 \log \left( 1 - \frac{Q_L}{Q_0} \right) \Rightarrow Q_0 = \frac{Q_L}{\frac{S_{21}}{1 - 10^{\frac{S_{21}}{20}}}} = 1.39M \quad (3.22)$$

The estimated unloaded Q is slightly higher than the specified by the manufacturer. Figure 3-11 shows the phase shift response of the crystal resonator at the series resonance.

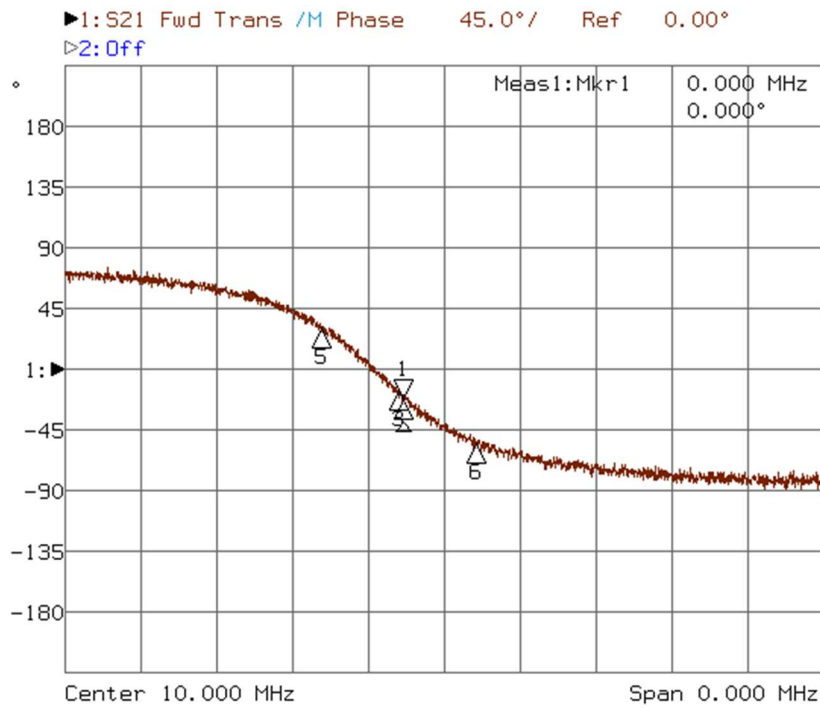


Figure 3-11: Crystal resonator phase shift (span=100Hz).

### 3.2.3 Spurious Resonance Rejection Filter.

Aside from the useful 10 MHz resonance, the crystals exhibit an unwanted spurious resonance mode at about 10.9 MHz. This can cause the oscillator to begin oscillating at the wrong frequency. In order to suppress that resonance, a filter was designed and incorporated into the loop. It is essential that this filter does not interfere with the main resonance, while filtering out the unwanted one. The design that was used in this case is inspired by the equivalent circuit model of the crystal resonator. Figure 3-12 shows the circuit diagram of the filter.

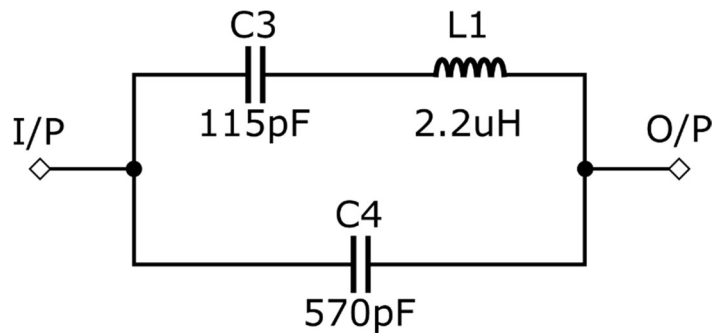


Figure 3-12: Spurious resonance filter circuit diagram.

In this circuit the impedance of the series combination of  $L_1$  and  $C_3$  is  $j\omega L - j\frac{1}{\omega C_3}$ . At resonance this is theoretically 0, making the whole impedance of the filter 0, which gives minimal insertion loss.

$$X_{L_1} + X_{C_3} = 0 \Rightarrow j\omega L_1 - j\frac{1}{\omega C_3} \Rightarrow j\omega L_1 = j\frac{1}{\omega C_3} \Rightarrow \omega^2 L_1 C_3 = 1 \Rightarrow \omega = \frac{1}{\sqrt{L_1 C_3}}$$

$$f_{series} = \frac{1}{2\pi\sqrt{L_1 C_3}} \quad (3.23)$$

The standard series resonance equation. The impedance of the whole filter, including the parallel capacitor is:

$$Z_{filter} = \frac{(X_{L_1} + X_{C_3}) \times X_{C_4}}{(X_{L_1} + X_{C_3}) + X_{C_4}} = \frac{(j\omega L_1 - j\frac{1}{\omega C_3}) \times (-j\frac{1}{\omega C_4})}{j\omega L_1 - j\frac{1}{\omega C_3} - j\frac{1}{\omega C_4}} \quad (3.24)$$

At resonance, the added reactance of all 3 components is theoretically 0, making the denominator 0, which makes the impedance infinite (or in reality very high), making the insertion loss very high.

$$j\omega L_1 - j\frac{1}{\omega C_3} - j\frac{1}{\omega C_4} = 0 \Rightarrow \omega^2 L_1 C_3 C_4 = C_3 + C_4 \Rightarrow \omega = \sqrt{\frac{C_3 + C_4}{L_1 C_3 C_4}}$$

$$f_{parallel} = \frac{1}{2\pi} \sqrt{\frac{C_3 + C_4}{L_1 C_3 C_4}} \quad (3.25)$$

S21 can be calculated using the method from [45, pp. 88-91] by having a voltage source of magnitude 2 in a 50Ω system. Then the magnitude of S21 is equal to the output voltage:

$$|S21| = V_{out} = 2 \frac{50}{50 + 50 + Z_{filter}} \Rightarrow S21_{in\ dB} = 20 \log \left( 2 \frac{50}{50 + 50 + Z_{filter}} \right)$$

Using equations ( 3.23 ) and ( 3.25 ) the component values were calculated by setting the series resonance to 10 MHz and the parallel resonance to 10.9 MHz. This way there is an increased insertion loss in the unwanted resonance, while the loss in the useful resonance is kept to a minimum. Figure 3-13 shows the frequency response of the filter.

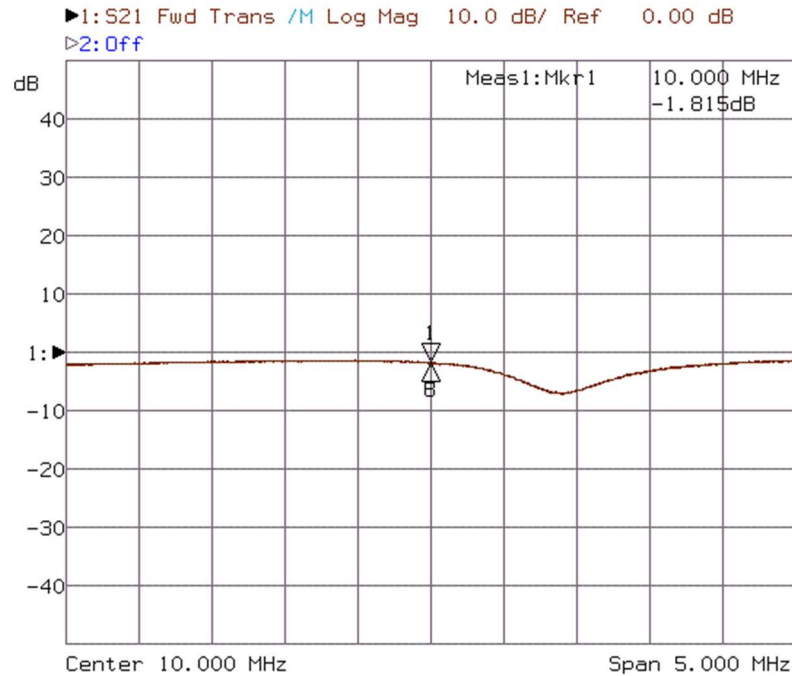


Figure 3-13: Spurious resonance rejection filter frequency response.

### 3.2.4 Electronically Tuned Phase Shifter.

A voltage tuned phase shifter was designed and included in the oscillator loop to enable fine tuning of the operating frequency and phase locking. Frequency tuning can be done by placing varactor diodes either at the resonator or in a separate phase shifter. In this case the separate phase shifter was chosen, as this does not degrade the unloaded Q of the crystal and the phase noise degradation can be estimated using the methods described in [48], [24]. Figure 3-14 shows the degradation of the phase noise performance as a function of the open loop phase shift.

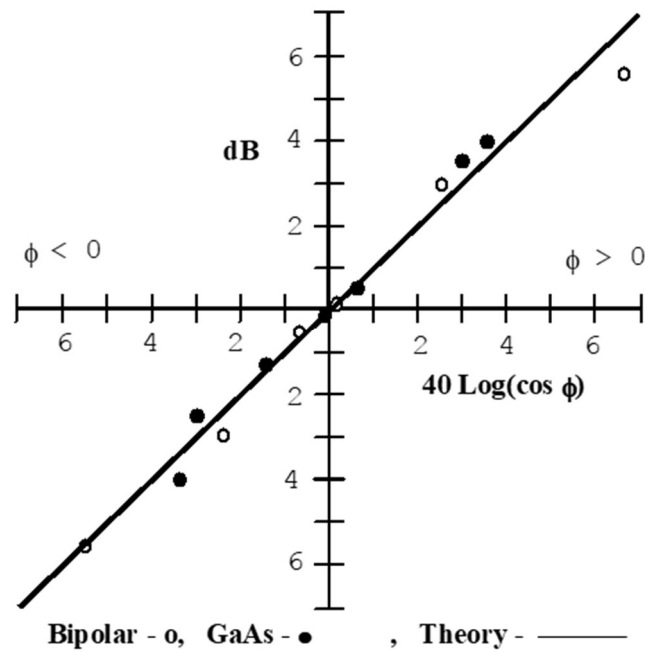


Figure 3-14: Phase noise degradation as a function of open loop phase shift [48]. The degradation in both bipolar and GaAs devices is effectively the same, as they follow the same theoretical line.

The design of the phase shifter is based on a high pass 5th order Butterworth filter. The filter was designed for a cut-off frequency of 6 MHz (0.6x the oscillator operating frequency), which gives optimal phase tuning, while maintaining low insertion loss. The varactor diodes are incorporated into the series capacitances. Figure 3-15 shows the circuit diagram. The component values were calculated by using the filter prototype tables in [49, pp. 404-410], [50, p. 427] to obtain the normalized values for a low-pass Butterworth 5<sup>th</sup> order filter and then transforming it into a high-pass filter and denormalizing the values for 6 MHz frequency and 50Ω characteristic impedance. The 6 MHz frequency was chosen, because it provides a reasonable compromise between relatively low insertion loss and linear phase tuning. Two varactor diode pairs (BB201) were used in parallel in order to have increased tuning capability. Fixed value capacitors C5 and C6 were also added to bring the capacitance up to the filter design specifications (328pF) when the varactors are operated around 1.5V. Capacitor C7 is for decoupling the inductor L3. The inductors chosen were the closest standard values to the calculated ones.

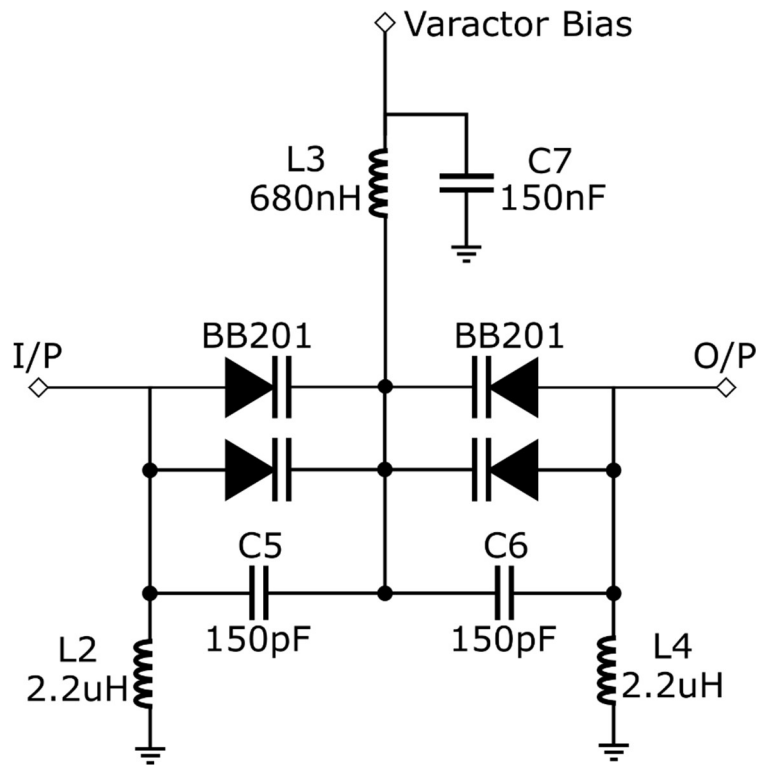


Figure 3-15: XO phase shifter circuit diagram.

It was found, through experimentation with different capacitor and inductor types, that the best phase noise results were achieved with high-Q Coilcraft surface mount inductors and high-quality polystyrene capacitors. Lower quality inductors or small surface mount capacitors appear to degrade the performance of the oscillator by as much as 10dB, possibly due to the piezoelectric properties of the dielectric, non-linearity and/or added flicker noise.

Using this phase shifter, the oscillation frequency can be electronically tuned within a range of a few Hertz. Figure 3-16 shows the measured phase shift and insertion loss as a function of varactor voltage.

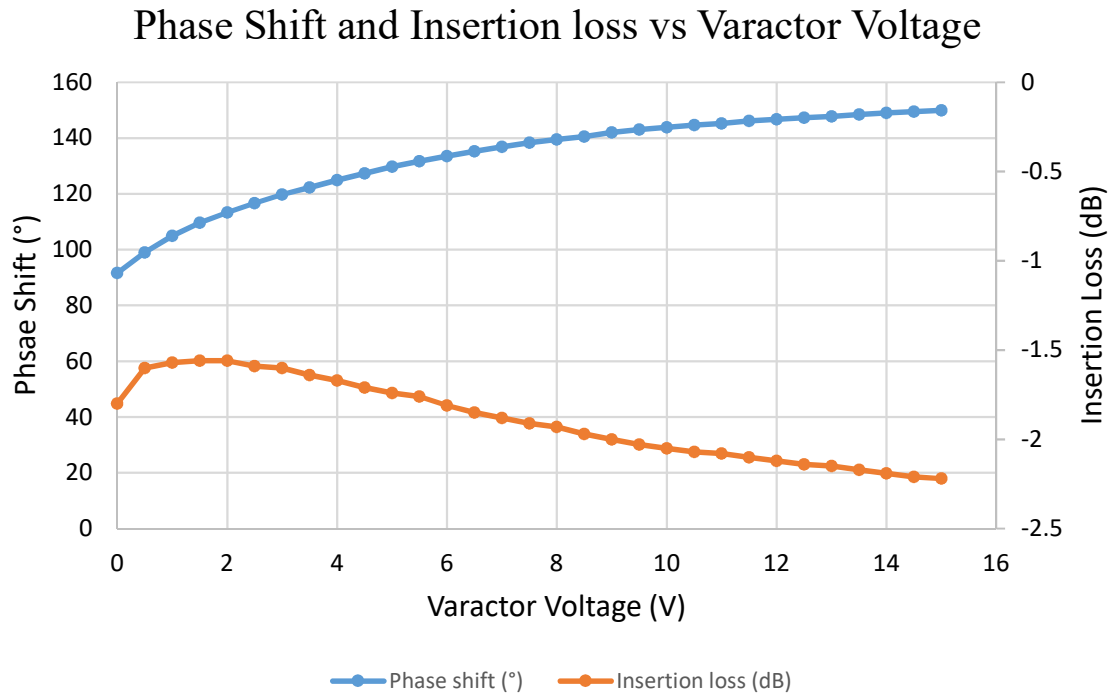


Figure 3-16: XO phase shifter measured phase shift and insertion loss vs. varactor voltage.

### 3.2.5 Complete Oscillator Circuit Diagram.

Figure 3-17 shows the complete diagram of the 10MHz crystal oscillator. The circuit was tested in open loop configuration and the transmission between the input of the transformer and the output of the resonator was measured to ensure that the correct conditions for oscillation were met. With varactor diode bias of 1.5V the phase shift through the complete circuit was about  $3^\circ$  and there was an excess gain of about 0.3dB at 10MHz. These conditions were enough to sustain oscillation at the desired frequency. The gain of the amplifier can be increased by increasing the emitter current to make the gain margin larger. However, it was found through experimentation that if the gain margin was increased to about 2 dB, the phase noise at 1Hz offset showed degradation of about 2-3dB. Therefore, for optimal results, the gain margin was set to 0.3dB. The trade-off in this case is the longer start-up time of the oscillator of up to 5 seconds.

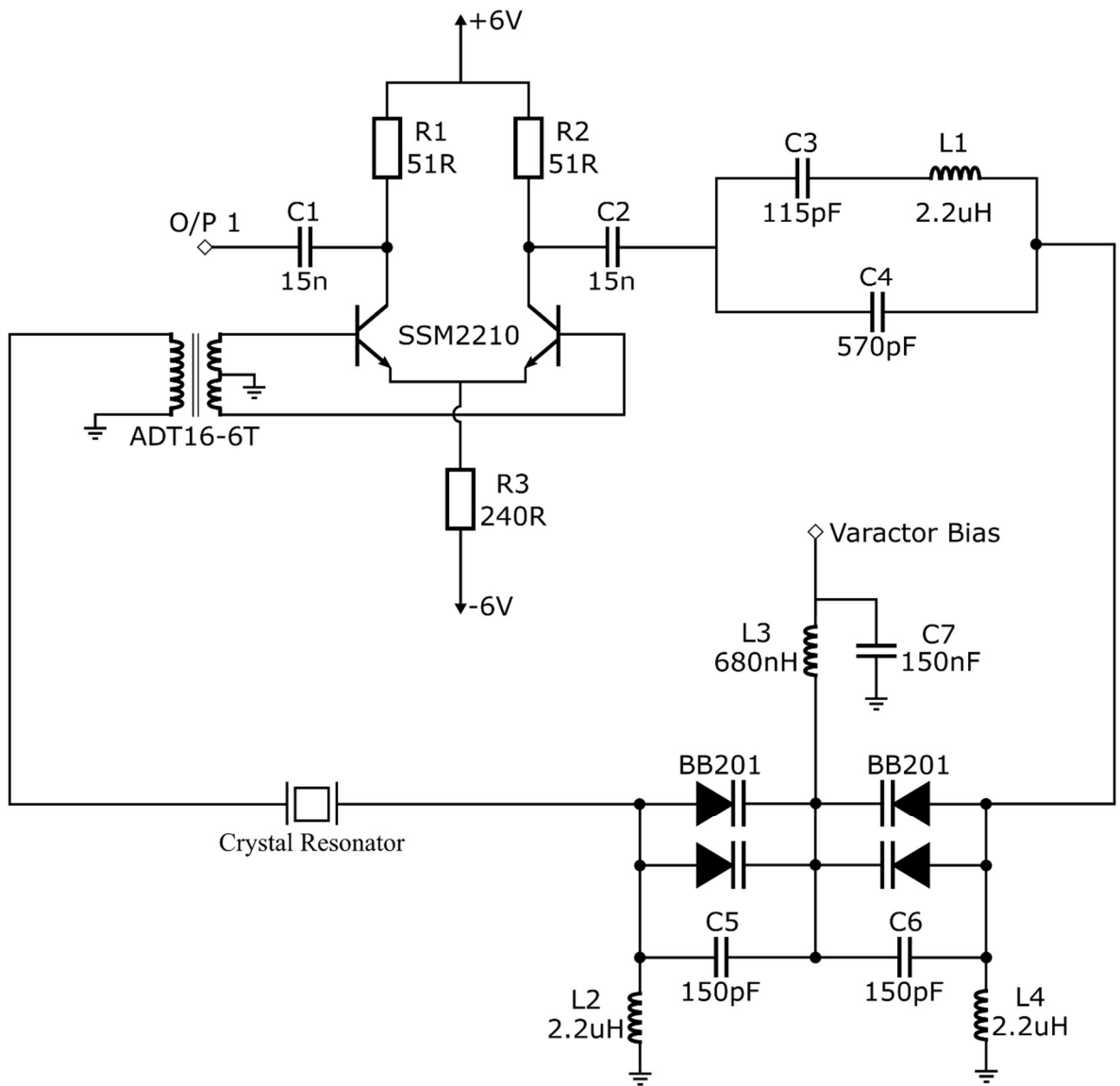


Figure 3-17: Complete crystal oscillator circuit diagram.

### 3.2.6 Crystal Oscillator Phase Noise Measurements.

A prototype crystal oscillator was built and powered by a battery of 4, 1.5V AA cells for both the positive and negative supply. A 1.5V AA cell was used for biasing the phase shifter. The oscillator was then placed inside a metal screened box.

A second, smaller oscillator was also built and placed in a specially machined aluminium jig, which provides screening and heating capabilities for both the circuit board and the crystal resonator. The jig was then covered with a brass lid and feed through pins were used to provide an interface for the bias input, output and power supply to the oscillator (Figure 3-18). This oscillator was also powered by batteries.

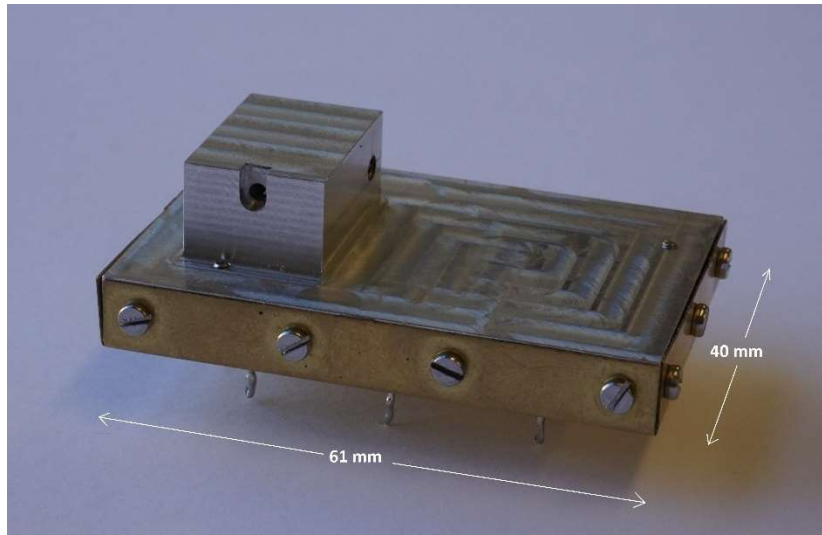


Figure 3-18: Photograph of the crystal oscillator inside metal jig (Oscillator 2).

The phase noise was measured using the Symmetricom 5120A phase noise measurement system. A total of 3 sets of measurements were taken. One for each individual oscillator using the internal reference of the Symmetricom instrument and one in which the two oscillators were measured against each other. The phase noise of the first oscillator was measured using the internal reference of the measurement system. In order to bring the signal level to the value required by the instrument, a Mini Circuits 20dB (ZFL-1000VH) low residual phase noise amplifier was used. Finally, a 10dB attenuator was added to make sure the instrument's input was not overloaded. Figure 3-19 shows a block diagram of the measurement configuration.

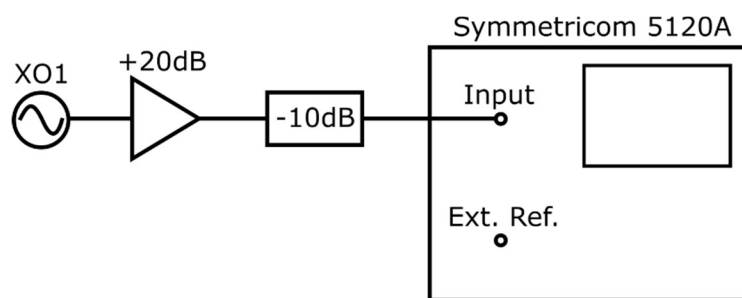


Figure 3-19: Measurement configuration used for oscillator 1.

The measured phase noise performance is shown in Figure 3-20. The exact measured values are tabulated in Table 3-1.

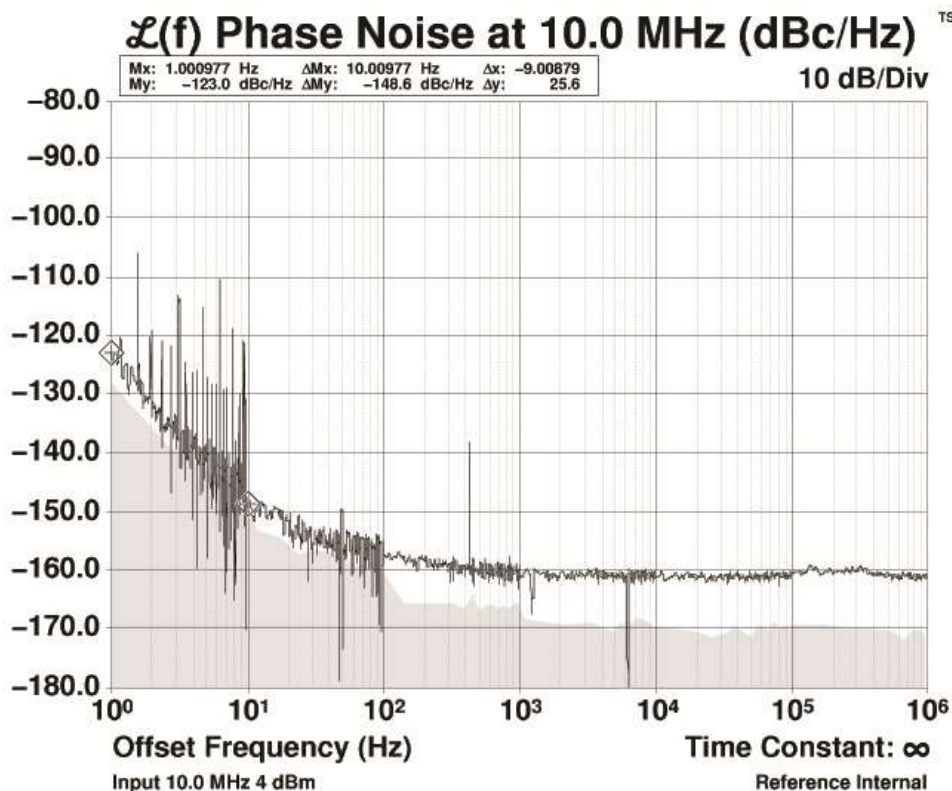


Figure 3-20: Measured phase noise of oscillator 1.

Table 3-1: Phase noise of oscillator 1 at important offset frequencies.

Offset frequency (Hz)	Phase noise (dBc/Hz)
1	-123.0
10	-148.6
100	-157.8
1,000	-161.0
10,000	-161.1

It can be seen that the oscillator shows excellent phase noise performance down to 1Hz offset frequency. There are multiple spurs visible between 1Hz and 10Hz offsets. These could be attributed to insufficient screening or pickup from the interconnecting cables.

The second oscillator was measured using the same configuration as Oscillator 1 (Figure 3-19). The measured phase noise performance is shown in Figure 3-21. The exact values are shown in Table 3-3.

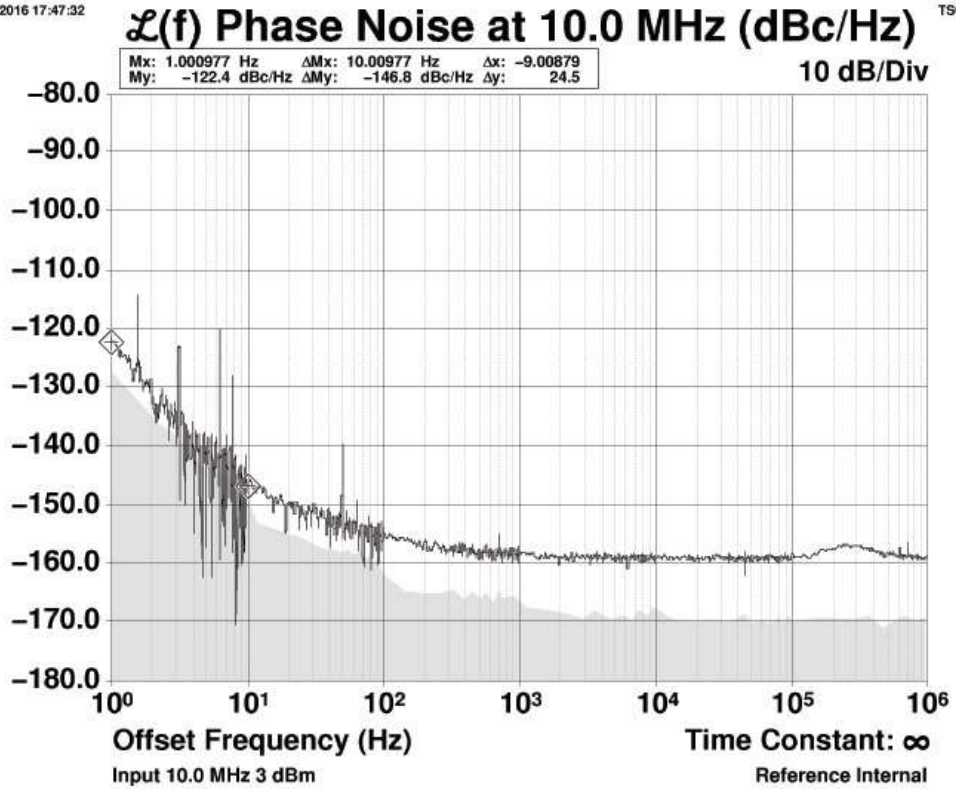


Figure 3-21: Measured phase noise performance of oscillator 2.

Table 3-2: Phase noise of oscillator 2 at important offset frequencies.

Offset frequency (Hz)	Phase noise (dBc/Hz)
1	-122.4
10	-146.8
100	-155.3
1,000	-158.2
10,000	-159.0

It can be seen, that there is a small increase in the phase noise at all offsets. This can be attributed to the differences in the resonators, the tolerance of the components or the smaller volume of Oscillator 2 (when the inductors are placed too close to each other there may be magnetic coupling between them, which could alter the response of the filter and phase shifter). The spurs below 10Hz offset are reduced in this case, possibly because the aluminium jig offers significantly better screening.

Both oscillators exhibit good phase noise performance when measured using the internal reference of the Symmetricom system. However, when using the internal reference, the system’s noise floor is specified as “-120dBc/Hz at 1Hz” by the manufacturer [51]. Therefore, it is unclear whether these results are accurate. In order to confirm them, the two oscillators were measured against each other (one used as reference and the other as the input signal). This brings the noise floor of the measurement at 1Hz offset down significantly (down to -145dBc/Hz according to the datasheet). Another important note about the measured phase noise of the single oscillator against the internal reference is the presence of multiple negative spurs in the plot between 1Hz and 10Hz offsets and a slight “hump” around 250kHz offset. These are very similar to the errors presented by Nelson, Hati and Howe in [52], where they are attributed to cross-correlation collapse, due to anti correlated thermal noise from the power splitters in the measurement system or AM noise leakage [53]. In that case, the phase noise can be underestimated or overestimated, depending on the type of correlation error. This is another reason to confirm the original measurements by measuring the two oscillators against each other. Figure 3-22 shows the block diagram of the measurement setup.

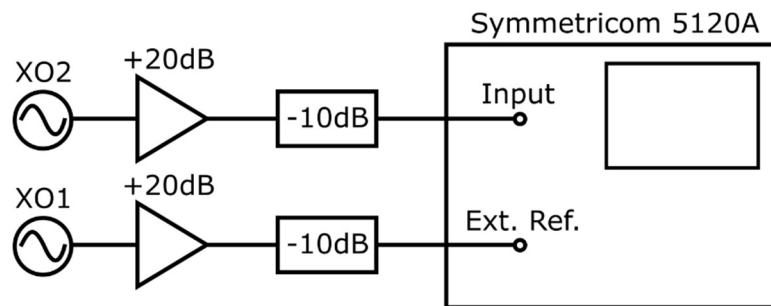


Figure 3-22: Measurement configuration using oscillator 1 as reference and oscillator 2 as input.

The results of the phase noise measurements are shown in Figure 3-23 and the values are tabulated in Table 3-3.

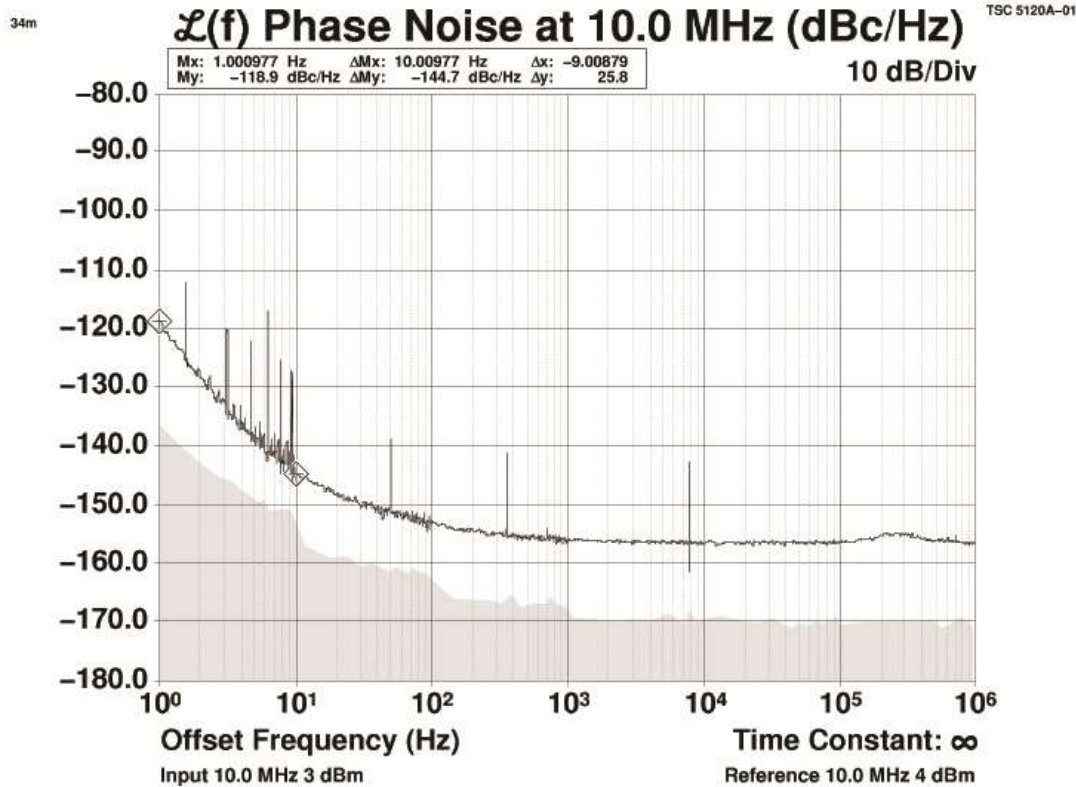


Figure 3-23: Measured phase noise plot of oscillator 1 used as reference and oscillator 2 used as input.

Table 3-3: Phase noise of XO1 used as reference and XO2 used as input at important offset frequencies.

Offset frequency (Hz)	Phase noise (dBc/Hz)	Phase noise -3dB (dBc/Hz)
1	-118.9	-121.9
10	-144.7	-147.7
100	-153.2	-156.2
1,000	-156.2	-159.2
10,000	-156.5	-159.5

The resulting graph shows the added noise of the two oscillators. Therefore, it is safe to estimate that the actual phase noise of one of the oscillators is at least 3dB lower than the displayed graph. This ties in with the measurements taken on each individual oscillator. The total number of spurs has also decreased significantly and the negative spurs have almost completely disappeared.

### 3.2.7 Double Oven Temperature Control

It has to be noted that at this point the oscillator was tested at close to room temperature, because of several issues with heating the to the inversion temperature of the crystal. One of those issues is that the polystyrene capacitors that were initially used have a maximum operating temperature of 85°C, which is very close to the inversion temperature of 82°C. It was also found that the output power of the oscillator drops significantly at higher temperatures and the oscillation may stop altogether. This could be attributed to the capacitors being pushed very close to their maximum specified temperature and also changes in the insertion loss of the resonator and/or filters. For this reason, another version of the same crystal oscillator was built in a significantly more compact package, where the polystyrene capacitors were replaced with high quality ceramic NP0 capacitors from ATC. It was found that out of all tested capacitors, these offer the least degradation to the phase noise of the oscillator. The resonator along with the oscillator circuits were placed in a smaller custom made aluminium jig and heating elements and thermistor were attached to it. A layer of insulation was included and covered with a chemically etched brass box. This box also serves as the second stage of temperature stabilization, as it also includes heating elements and a thermistor. Another layer of insulation was placed and the entire assembly was covered by a second brass box. Figure 3-24 shows a photo of the construction.

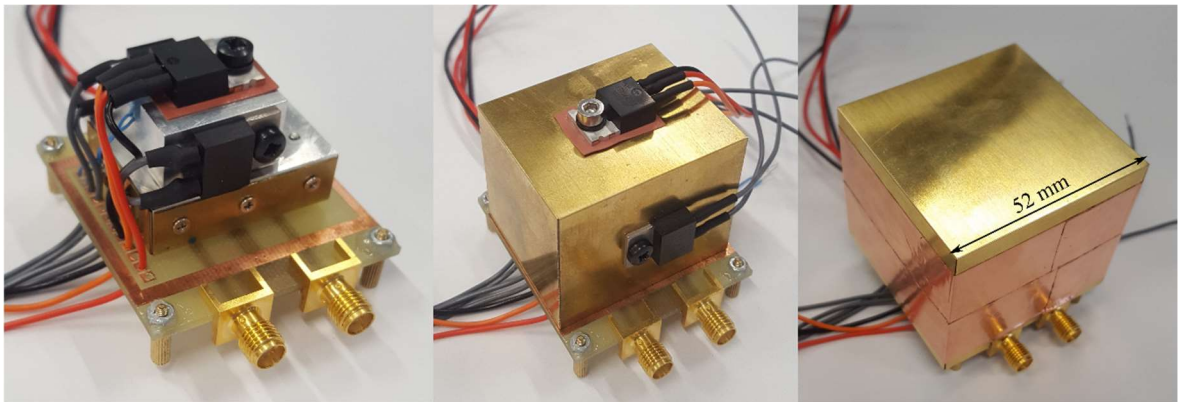


Figure 3-24: Photo of the double oven temperature controlled crystal oscillator.

Temperature controllers were designed for each stage of stabilization. The design of the controllers is based on a single low noise op amp PID controller. It is a simplified design based on [54]. The basic circuit diagram of the controller is shown in Figure 3-25.

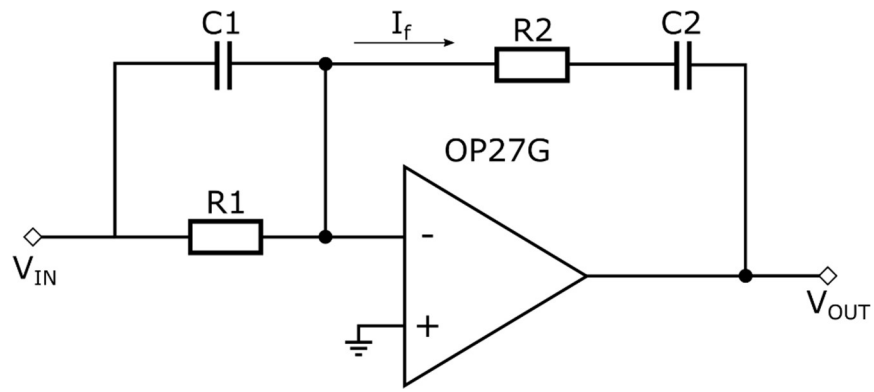


Figure 3-25: Single op amp PID temperature controller.

In this circuit, assuming the op amp is ideal with infinite input impedance, the feedback current can be expressed as:

$$I_f = \frac{V_{IN}}{R_1} + C_1 \frac{dV_{IN}}{dt} \quad (3.26)$$

The output voltage is in turn:

$$V_{OUT} = R_2 I_f + \frac{1}{C_2} \int I_f dt \quad (3.27)$$

Substituting ( 3.26 ) in ( 3.27 ) and separating the resulting proportional, integral and derivative terms results in:

$$V_{OUT} = \underbrace{\left( \frac{R_2}{R_1} + \frac{C_1}{C_2} \right)}_{K_p} + \underbrace{\frac{1}{C_2 R_1}}_{K_i} \int V_{IN} dt + \underbrace{R_2 C_1}_{K_d} \frac{dV_{IN}}{dt} \quad (3.28)$$

Where  $K_p$  is the proportional gain of the controller,  $K_i$  is the integral gain and  $K_d$  is the derivative gain. When the desired PID gains are known, the component values can be calculated by setting one of them to a desired value and solving the system of 3 equations with 3 unknowns.

The initial values for the PID controller parameters can be obtained using the Ziegler-Nichols method for PID tuning described in [55, pp. 568-577]. In this method the controlled system is disturbed with a small step input near the desired set point. The output

of the detector (thermistor voltage in this case) is measured and its step response recorded. In linear systems the response has an exponential curve with some time delay (lag) and a certain time constant in which it reaches the settling point.

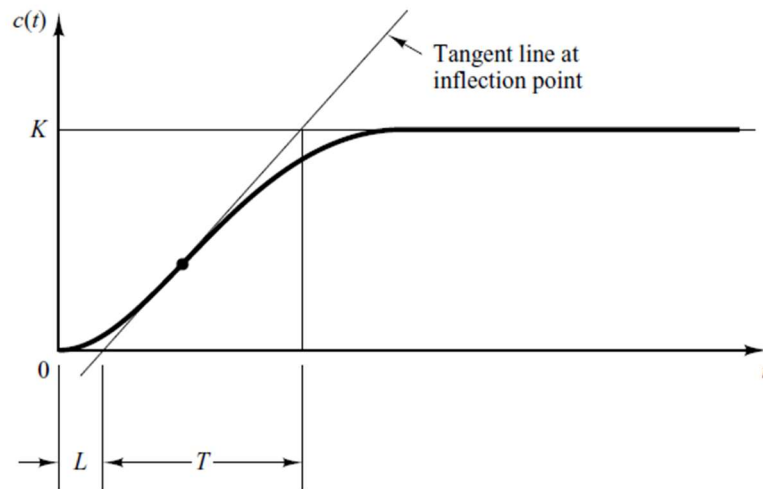


Figure 3-26: Example of typical step response with parameters used in Ziegler-Nichols method. Figure taken from [55, p. 569]

Using the parameters  $L$  and  $T$ , the PID parameters can be estimated as:

$$K_p = 1.2 \frac{T}{L}$$

$$T_i = 2L \Rightarrow K_i = \frac{0.6T}{L^2}$$

$$T_d = \frac{L}{2} \Rightarrow K_d = 0.6T$$

It is important to note that these calculations only give the initial estimate for the correct PID parameters. When the controller is tested, these may need to be adjusted to achieve the optimal stability, low error, settling time and overshoot (if desired).

The circuit diagram of the controllers built for the crystal oscillator is shown in Figure 3-27.

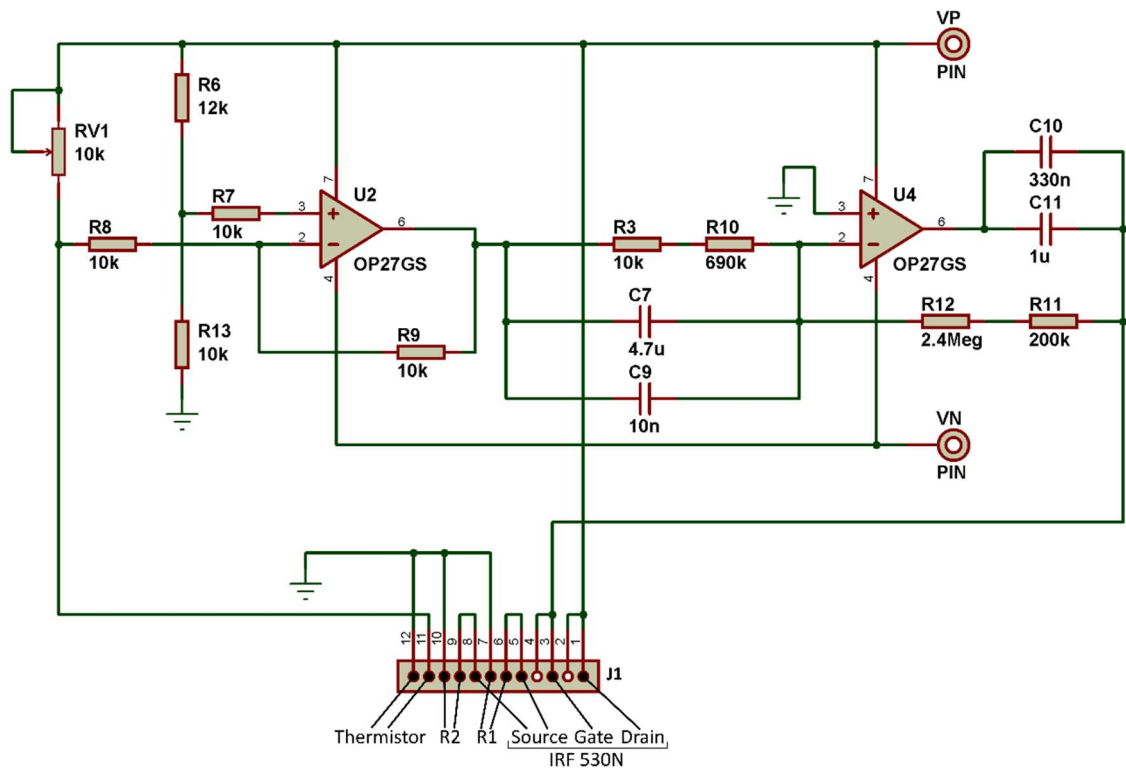


Figure 3-27: PID temperature controller for crystal oscillator.

The first low noise op amp OP27GS (U2) is in a differential amplifier configuration. It computes the difference between the voltages across R13 and the thermistor, which is connected to pins 11 and 12 on the J1 connector. Potentiometer RV1 is used to set the temperature set point. The second op amp (U4) is in a PID controller configuration. X8R capacitors were used when possible, because of their good DC voltage and temperature characteristics [56]. The symmetrical power supply to the op amps is regulated using the ultralow noise TPS7A4700 (positive) and TPS7A3300 (negative) adjustable voltage regulators, capable of sourcing and sinking up to 1A of current respectively. An N-channel MOSFET (IRF530N) with two 51Ω power resistors in parallel at its source were used as the heating elements. These were connected to the controller through pins 1-5 and 6-10 respectively of connector J1 (see Figure 3-27). The MOSFET is driven directly by the output of the PID controller, while the two source resistors bias the transistor and limit the maximum current through the circuit. These power dissipating components were bolted symmetrically around the resonator and second oven boxes for symmetrical heat distribution (Figure 3-24). The circuit diagram of the heating part of the circuit is shown in Figure 3-28.

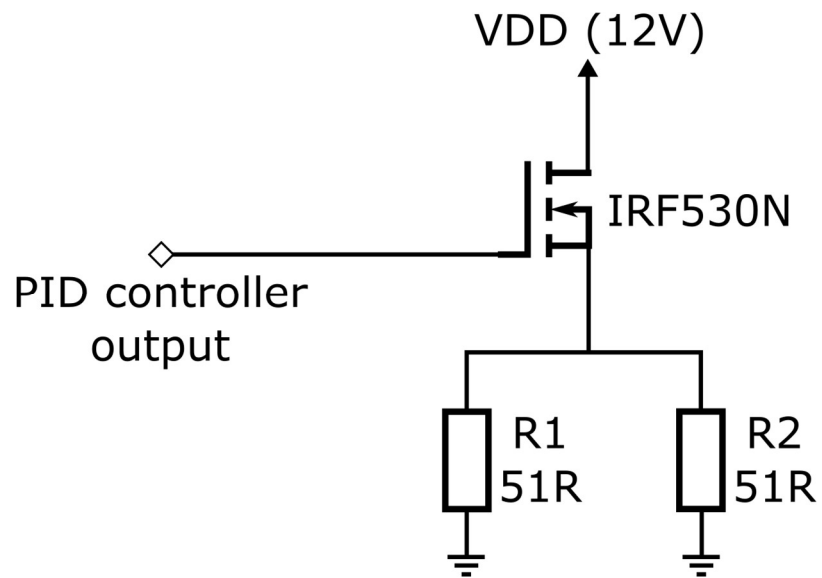


Figure 3-28: Heating circuit for crystal oscillator.

The controllers were built on FR4 printed circuit boards and attached underneath the main box of the oscillator (Figure 3-29).

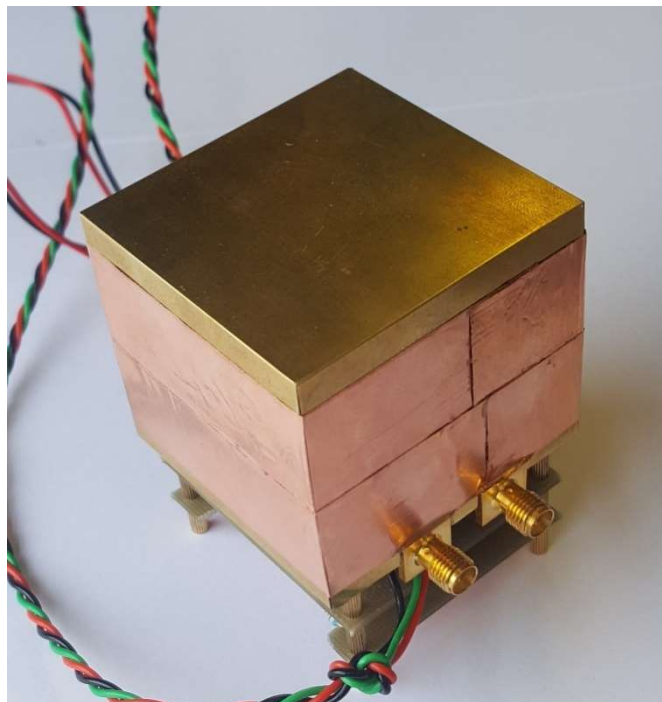


Figure 3-29: Photo of the completed double oven controlled oscillator with temperature controllers.

The temperature controllers were enabled and the phase noise was measured on this version of the oscillator. Figure 3-30 shows the measured phase noise plot and Figure 3-31 shows the measured Allan Deviation.

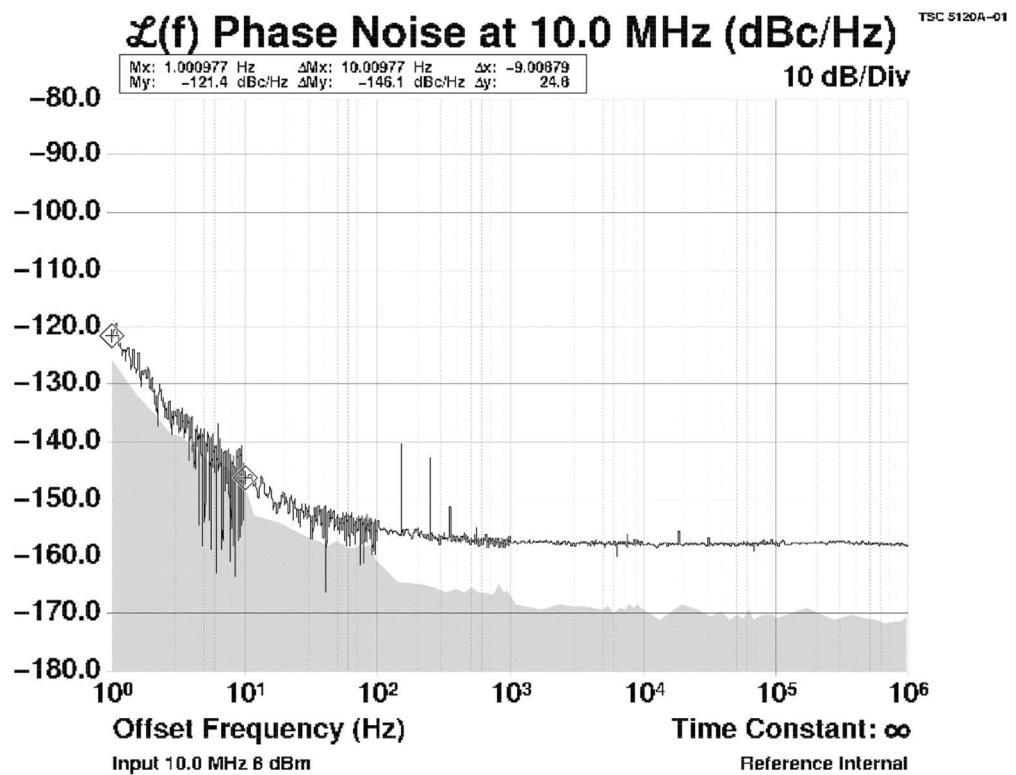


Figure 3-30: Measured phase noise on the double oven controlled crystal oscillator.

The measured phase noise is -121.4dBc/Hz at 1Hz offset and -146.1dBc/Hz at 10Hz offset.

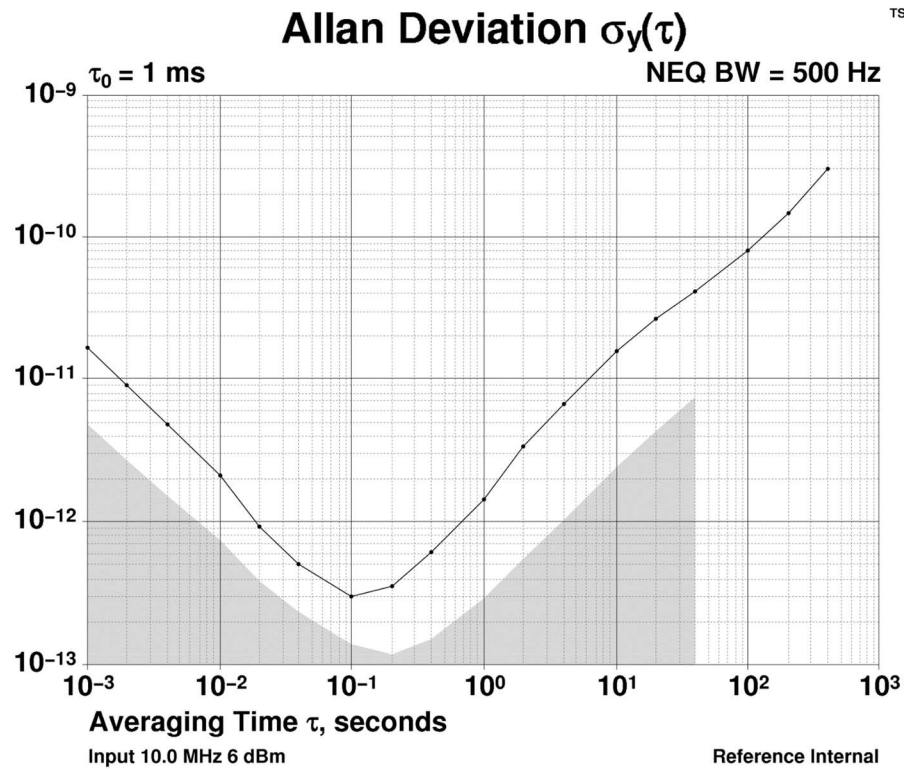


Figure 3-31: Allan Deviation measurement of the double oven controlled crystal oscillator.

The latest phase noise result is higher by about 0.6dB at 1Hz offset. The difference can be attributed to the different components or the even smaller design. With the double oven temperature stabilization enabled the Allan Deviation plot goes down to  $3 \cdot 10^{-13}$  at 100ms averaging time and about  $1.5 \cdot 10^{-12}$  at 1s.

The current required for the initial heating of the oscillator is about 640mA and is reduced to about 200mA when the controller stabilizes to the operating temperature.

### 3.3 1.5 GHz Dielectric Resonator Oscillator (DRO).

The second component of the local oscillator for the atomic clock configuration is the DRO operating at 1.5 GHz. The initial plan for the design of the local oscillator was to include 3 different oscillators: the 10 MHz XO, a 100 MHz XO and the 1.5 GHz DRO in a phase locked loop chain. However, after a comparison was made between the phase noise performance of some of the best commercially available 100 MHz crystal oscillators and the performance of a previously designed DRO at 1.2 GHz [22] (which this design is based

on), it was found that the phase noise of the DRO is the same or better at all offsets down to about 1 Hz. This meant that there would be no significant advantage in incorporating a 100 MHz crystal oscillator into the chain, as the DRO already offers better performance at all offsets. The comparison between the oscillators is shown in Figure 3-32.

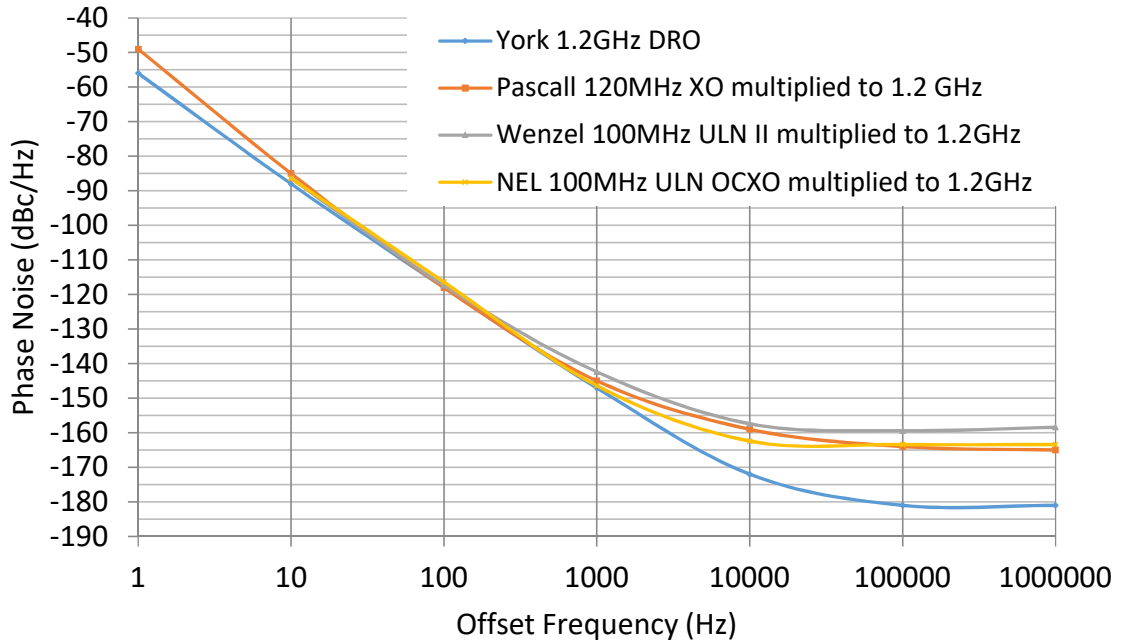


Figure 3-32: Comparison between Pascall [57], Wenzel [58] and NEL [59] 100 MHz low phase noise crystal oscillators and 1.2 GHz DRO [22].

A block diagram of the DRO configuration is shown in Figure 3-33.

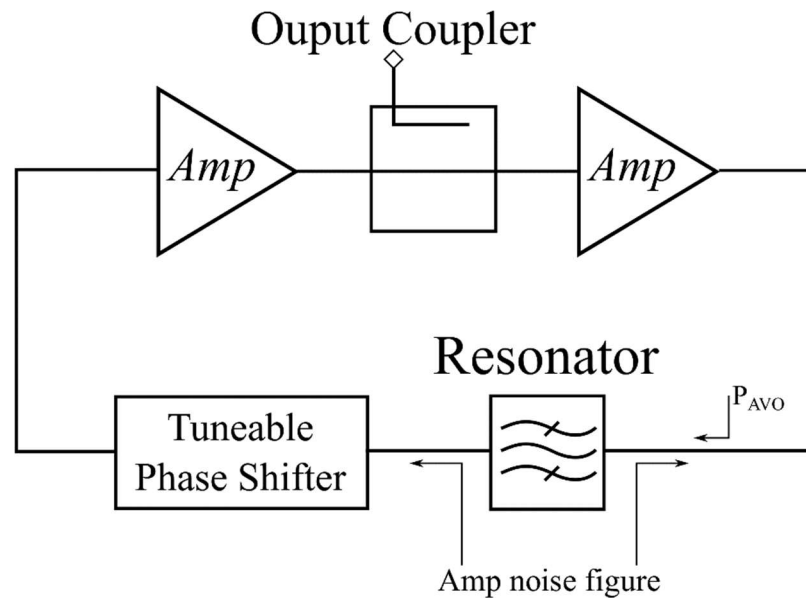


Figure 3-33: Block diagram of 1.5 GHz DRO.

Each amplifier block consists of 2 broadband feedback amplifiers in a push-pull configuration. A 3dB splitter is used as an output coupler and is inserted between the amplifiers to reduce any non-linear saturation effects. The resonator is a Barium Titanate puck mounted on an alumina support and inserted in an aluminium cavity with printed circuit probes. A voltage tuneable phase shifter is also included to enable frequency tuning and phase locking. This section will describe the design and construction of the individual parts of the DRO.

### 3.3.1 Broadband Feedback Push-Pull Amplifiers.

The broadband feedback amplifiers were designed following the methodology described in [45, pp. 156-166]. The circuit diagram of each amplifier is shown in Figure 3-34

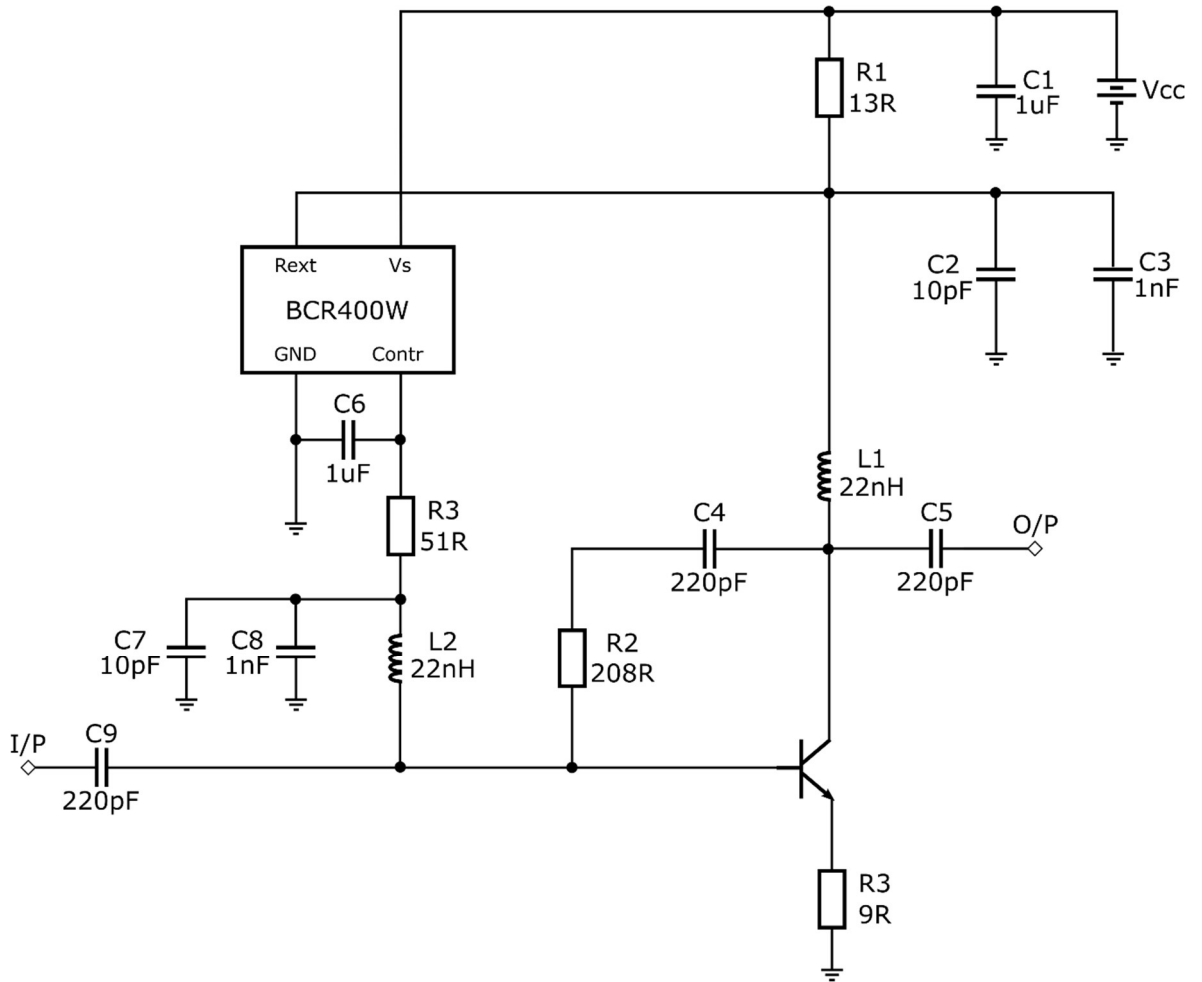


Figure 3-34: Circuit diagram of broadband feedback amplifier.

The BCR400W active bias controller is used to bias the transistor. R1 sets the collector current to about 40mA. By setting the desired power gain as  $(S_{21})^2 = 10dB$  and the input and output impedance to  $Z_0 = 50\Omega$ , The feedback resistor R2 is calculated as:

$$R_2 = 50(1 + \sqrt{10}) = 208\Omega$$

And the emitter resistor is calculated as:

$$R_3 = \frac{Z_0^2}{R_F} - r_E = \frac{Z_0^2}{R_F} - \frac{25mV}{I_E} = \frac{50^2}{208} - \frac{25mV}{40mA} = 11.4\Omega$$

Inductors L1 and L2 are used to decouple the bias voltages from the RF signals. C4, C5 and C9 are used to couple the RF signal to the input, output and feedback path.

Each amplifier was built on R4003C dielectric with  $50\Omega$  impedance microstrip lines at the input and output paths. The feedback path was made slightly thinner for increased inductance, as this was found to give flatter frequency response. Figure 3-35 shows the PCB layout of a single amplifier.

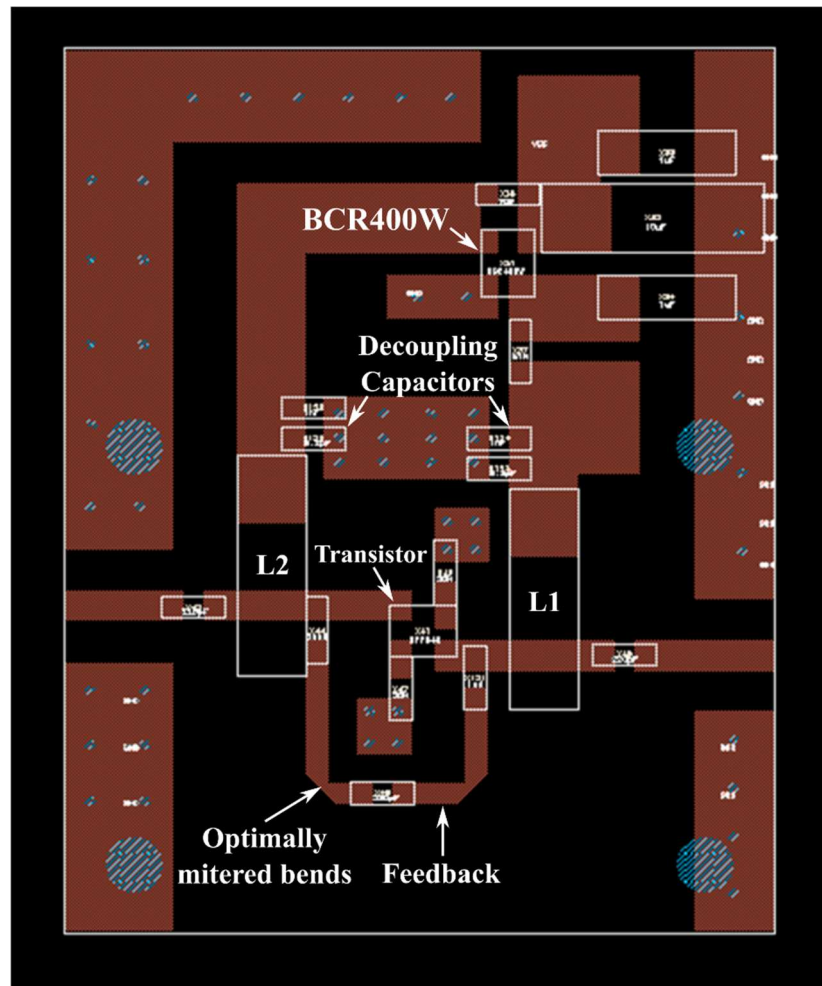


Figure 3-35: Broadback feedback amplifier PCB layout.

The decoupling capacitors and inductors were placed as close as possible to each other to minimize spurious reactances due to the conductor dimensions. It is especially important to avoid parasitic inductances in the transistor's emitter pins, as this can degrade the gain of the amplifier. Originally the BFU690 and BFU790 transistors were used. Since these transistors have 2 emitter pins, the emitter resistor was realized as the parallel combination of 2 resistors with double the originally designed value. These resistors were placed as close to the pin as possible and ground planes with high density of via holes were drawn symmetrically for each resistor. This reduces the parasitic inductance due to the track

lengths, resistor package and via holes. It was found that any inductance larger than about 1.5nH at the emitter can significantly reduce the gain and change the response of the amplifier. Optimally mitered 90° microstrip bends were used where necessary (feedback path), according to the design guidelines in [60].

The amplifiers were built using the BFU690 and BFU790 transistors. The collector current was set to 40mA and the collector-emitter voltage to 2.5V. Their frequency response was measured using the Anritsu 37377C network analyser. Table 5 shows the theoretical and measured gain of these amplifiers at 1.5GHz.

Table 3-4: Calculated and measured gain of amplifier with BFU690 and BFU790.

Transistor	Theoretical Gain (dB)	Measured Gain (dB)
BFU690	10.63	9.177
BFU790	10.63	9.143

The amplifiers were then built again in a push-pull configuration as shown in the block diagram in Figure 3-36. The ADTL2-18 transformers with impedance transformation ratio of 1:2 were used. By using this configuration, the output power of the amplifiers can be increased by 3dB without going into heavier saturation. The typical insertion loss of the transformers at 1.5 GHz is about 1dB.

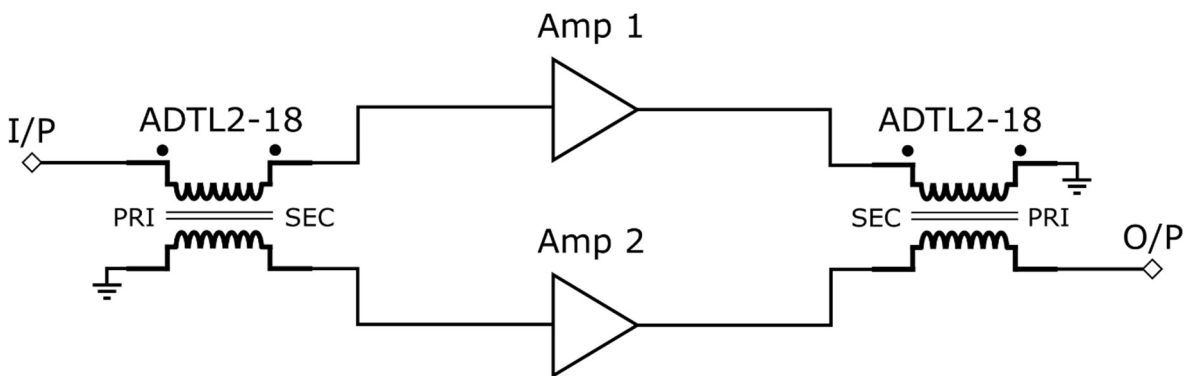


Figure 3-36: Block diagram of 1.5 GHz amplifiers in push-pull configuration.

The layout of the push-pull configuration is shown in Figure 3-37.

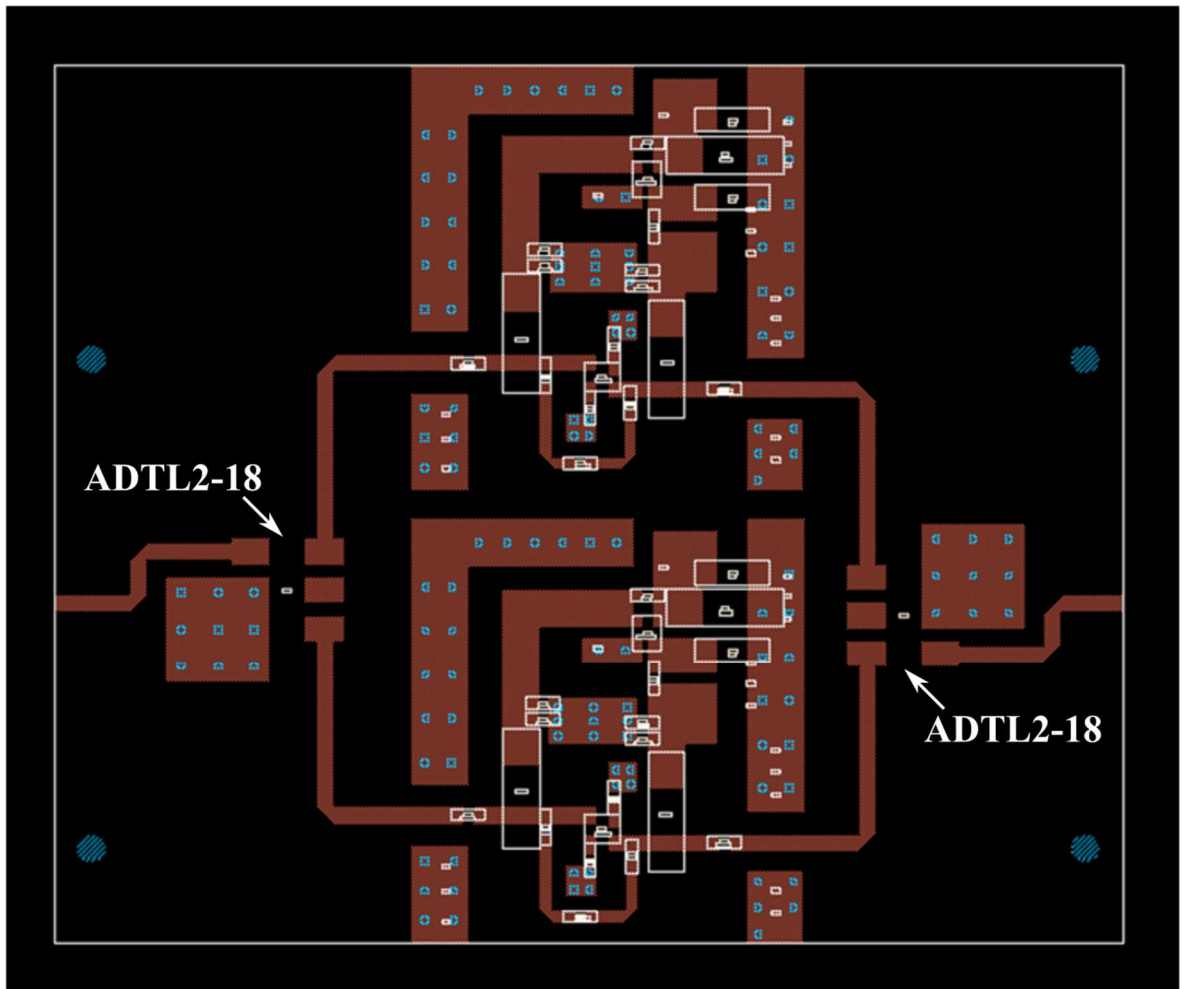


Figure 3-37: Layout of push-pull amplifiers.

It was ensured that the electrical length of each microstrip track between the splitting and re-combining points was kept the same. This ensures an in-phase adding of the power at the output. The  $90^\circ$  bends in the microstrip lines were optimally mitered for minimal losses.

The gain of the amplifiers in this configuration was measured for both the BFU690 and BFU790. The measured gain was in both cases about 6.3dB, which is 2.8dB lower than the measurements on the individual amplifiers. This can be mainly attributed to the losses in the transformers (2x1dB) and possible additional losses in the transmission lines. Some of the components were changed to compensate for the higher insertion loss. The  $11\Omega$  emitter resistor was replaced with a  $9\Omega$ , which increased the gain from 6.3dB to 6.9dB. It was also found that the BFU690 was only conditionally stable, exhibiting oscillations at certain supply voltages. The BFU790 was therefore chosen for the following measurements. A

second, identical push-pull amplifier was built and the gain and noise figure were measured on the HP8970B Noise Figure Meter. A similar version of the amplifier using the BFG591 (which was originally used in the design of the 1.2 GHz DRO [22]) was also measured for comparison (Table 3-5).

Table 3-5: BFU790 and BFG591 push-pull amplifiers noise figure measurements.

Amplifier	Measured Gain (dB)	Noise Figure (dB)
Single BFU790	9	5.6
Push-pull BFU790	6.9	5.3
Push-pull BFG591	4.9	9

The BFU790 transistors exhibit lower noise figure and higher gain. However, the BFG591 has the advantage of higher 1dB suppression point (about 25dBm) and can provide significantly more output power. For this reason, in the final oscillator design, the BFG591 amplifiers were used, as it was found that their higher output power was more beneficial to the overall performance of the resulting oscillator.

### 3.3.2 Voltage Tuned Phase Shifter.

In order to enable tuning of the oscillation frequency and phase locking of the 1.5 GHz DRO, a voltage tuned phase shifter was designed, using similar methodology as described in section 3.2.4 for the crystal oscillator. The phase shifter is again based on a 5<sup>th</sup> order Butterworth high-pass LC filter with cut-off frequency of  $0.6 \times 1.5 \text{ GHz} = 900 \text{ MHz}$ . This time, however, the filter was not designed with a characteristic impedance of  $50\Omega$ . It has been previously found that the high RF voltage swing across the varactor diodes can introduce further unwanted non-linear effects and degrade the response of the phase shifter. To lower the voltage, the filter was designed with a characteristic impedance of  $25\Omega$  and  $\lambda/4$  microstrip impedance transformers were used to transform back to a  $50\Omega$  system. The filter capacitors in this case were completely replaced by the BB831 varactor diodes. The circuit diagram is show in Figure 3-38.

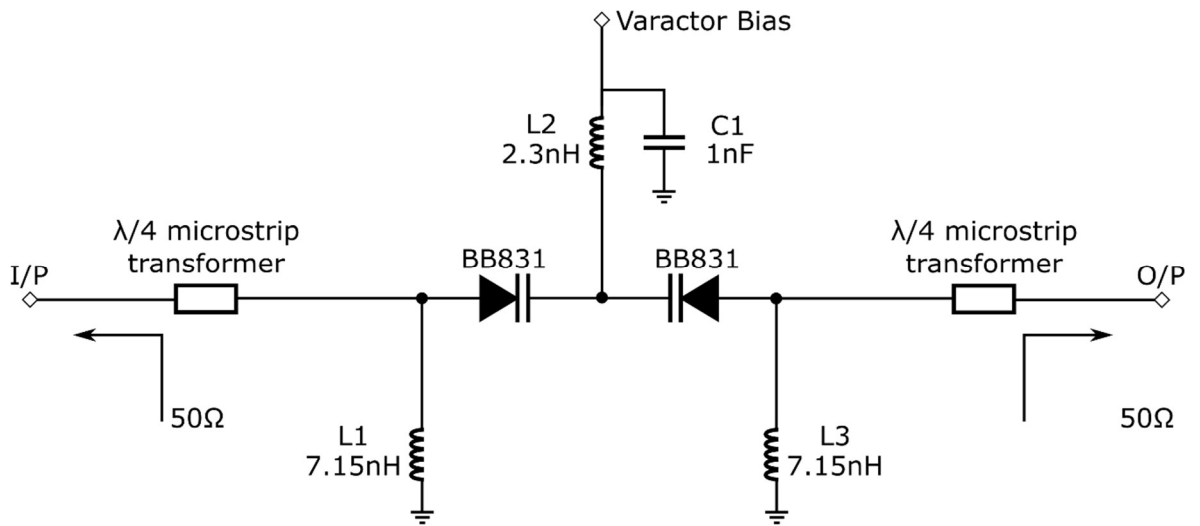


Figure 3-38: 1.5 GHz DRO phase shifter diagram.

Two phase shifters were built and their response was measured over a range of varactor bias voltages. Figure 3-39 shows the measured phase shift and insertion loss as a function of the varactor voltage.

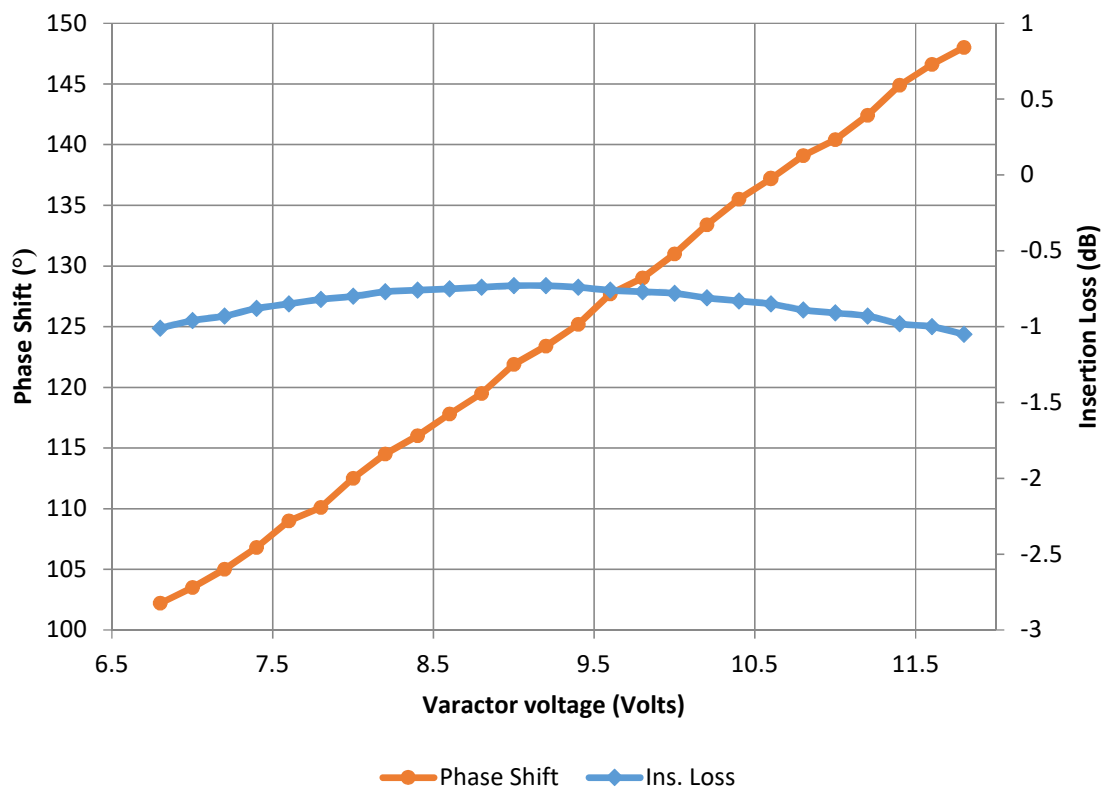


Figure 3-39: DRO phase shifter insertion loss and phase shift vs. varactor voltage.

The insertion loss remains lower than 1dB over a range of about 5V (6.6 – 11.6V). The total phase shift is about 45° within this range and appears relatively linear.

### 3.3.3 Dielectric Resonators.

The resonators used in this DRO were originally manufactured for the 1.2 GHz oscillators. Therefore, it was required that they were machined down to the 1.5 GHz operating frequency. The initial measurements were done in a cylindrical aluminium cavity with 140mm diameter, 90mm depth and printed circuit probes. The resonators themselves were 52mm diameter and 20mm depth. They were placed on a dielectric support with 32mm diameter and 27mm depth (Figure 3-40).

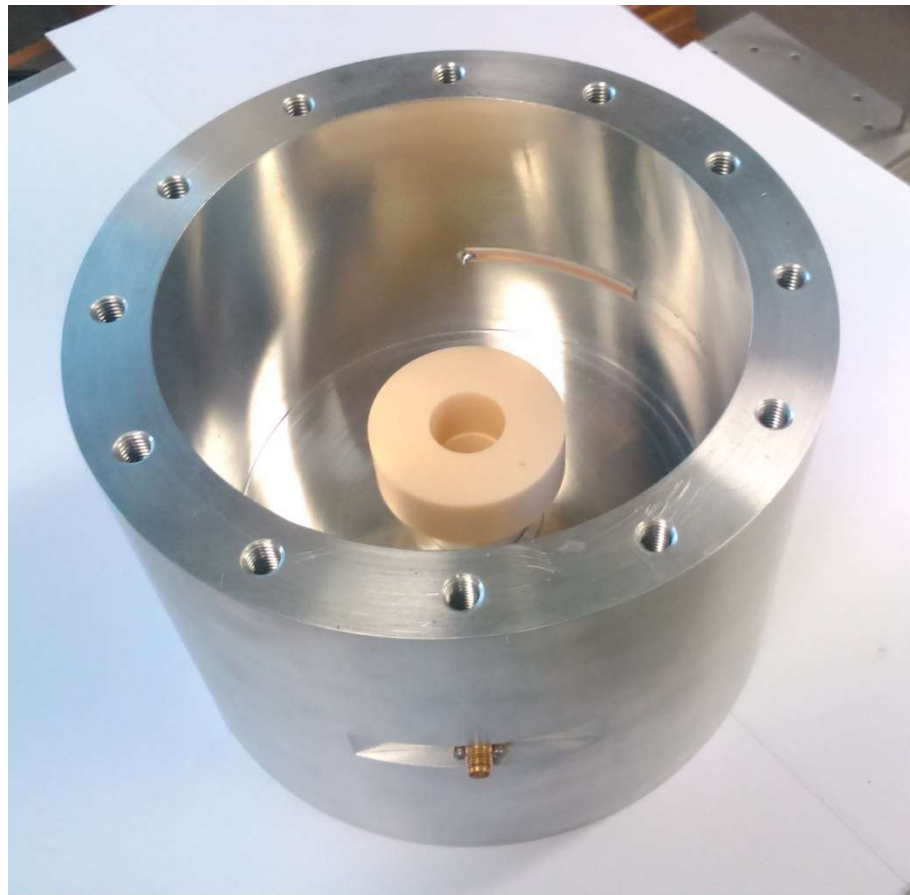


Figure 3-40: 1.2GHz Dielectric Resonator in aluminium cavity.

The resonators' Q, insertion loss and resonance frequency were measured. Then they were shipped to Filtronic Inc. to be machined down to 1.5GHz and have the dielectric supports

glued to them. After the resonators were received back, the measurements were repeated in the same cavity. Their final dimensions were 42mm diameter and 16mm depth. Table 2 shows the data before and after the machining.

Table 3-6: Resonator measurements before and after the machining.

	<b>Before machining</b>		
	Resonance freq.	Q <sub>L</sub>	Ins. Loss
Resonator 1	1.199550 GHz	30362	-6.62 dB
Resonator 2	1.199360 GHz	30381	-6.46 dB
	<b>After machining</b>		
	Resonance freq.	Q <sub>L</sub>	Ins. Loss
Resonator 1	1.487940 GHz	27000	-7.28 dB
Resonator 2	1.487659 GHz	27000	-7.35 dB

It should be noted that the actual resonance frequency of the resonators was purposefully set to be about 12 MHz below the desired 1.5GHz. This was done to avoid going above the desired frequency, as it would not be possible to tune down, while tuning up in frequency is relatively simple, by sanding down the resonator or adjusting the cavity size.

In addition to the main 1.5 GHz high-Q resonance, the dielectric resonators often support other resonance modes at different frequencies. Some of these resonances have even lower insertion loss than the main resonance and can therefore cause oscillations at unwanted frequencies. It was therefore required that the additional resonances of the resonators were measured. The resonators were placed inside the aluminium cavities and the measurements were conducted with the HP8720B network analyser. Several resonances were identified at higher frequency than the main resonance, but none at lower frequencies. The network analyser was then re-calibrated with 1 MHz span, 1601 points and 20s sweep time centred on each resonance individually. Table 1 shows the measured resonance frequency, Q and insertion loss for each resonator. These measurements were made prior to the final adjustment of insertion loss for optimum phase noise.

Table 3-7: Measurement of dielectric resonator unwanted resonances.

Resonator 1		
Resonance Frequency (GHz)	Insertion Loss (dB)	Q <sub>L</sub>
1.48794 (main)	-7.34	27000
1.75277	-5.67	4420
2.0724	-19.6	6724
2.6082	-6.52	7718
Resonator 2		
Resonance Frequency (GHz)	Insertion Loss (dB)	Q <sub>L</sub>
1.48766 (main)	-7.55	26220
1.7527	-5.39	3960
2.073	-21.5	6880
2.608	-6.51	7891

A few more resonances were also found at higher frequencies, but were not individually measured, since the gain of the amplifiers is too low at those frequencies to sustain oscillations. It can be seen that the closest unwanted resonance is at 1.75 GHz. This means that a filter may have been required to prevent oscillation at that frequency.

### 3.3.4 1.5 GHz DRO Phase Noise Measurements.

Two oscillators were built using the configuration shown in Figure 3-33. A 3dB splitter is used as an output coupler. It is inserted between the two amplifiers in order to reduce non-linear saturation effects in the second amplifier. If the amplifiers were connected directly, the increased input power to the second amplifier would drive it harder into saturation. A mechanically tuned phase shifter was originally used to adjust the phase shift and meet the oscillation conditions, but was later replaced by a semi-rigid coaxial line of the appropriate electrical length.

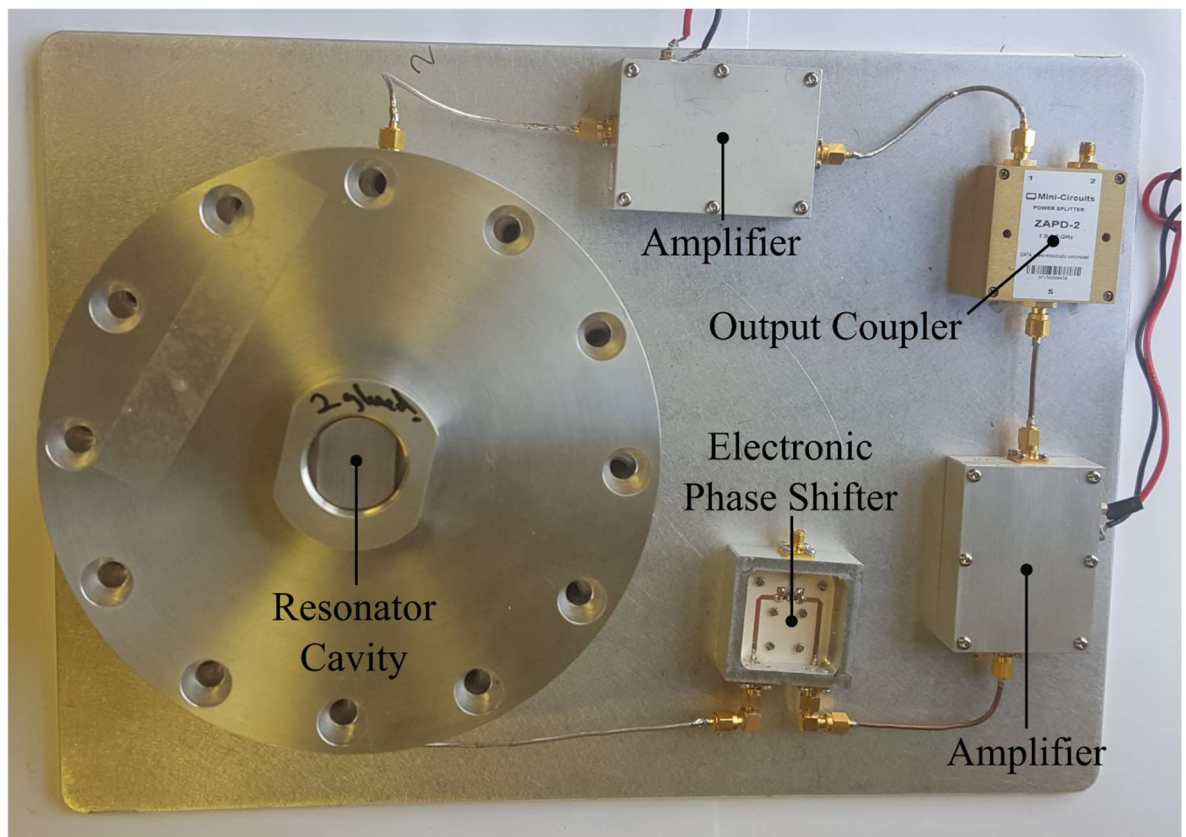


Figure 3-41: Photo of 1.5 GHz DRO.

When this configuration was built, the noise figure of the amplifiers was measured between the points where the resonator cavity is connected. This ensured that both amplifiers, along with the output coupler, phase shifter and all the inter connecting cables and connections were included in the measurement. The measured noise figure with this configuration was 11.5dB. This is used to calculate the theoretical phase noise of the oscillator.

The two oscillators were placed inside a screened metal box and the amplifiers were powered by 12V lead acid batteries (Figure 3-42). After some adjustment of the phase shift, oscillation at the desired frequency was achieved. The output power of both oscillators was about 18dBm. Since the operating frequency is about 1.488 GHz, the phase noise cannot be measured with the Symmetricom 5120A measurement system directly. It was therefore necessary to mix down the frequency of the oscillators to levels acceptable by the measurement system.

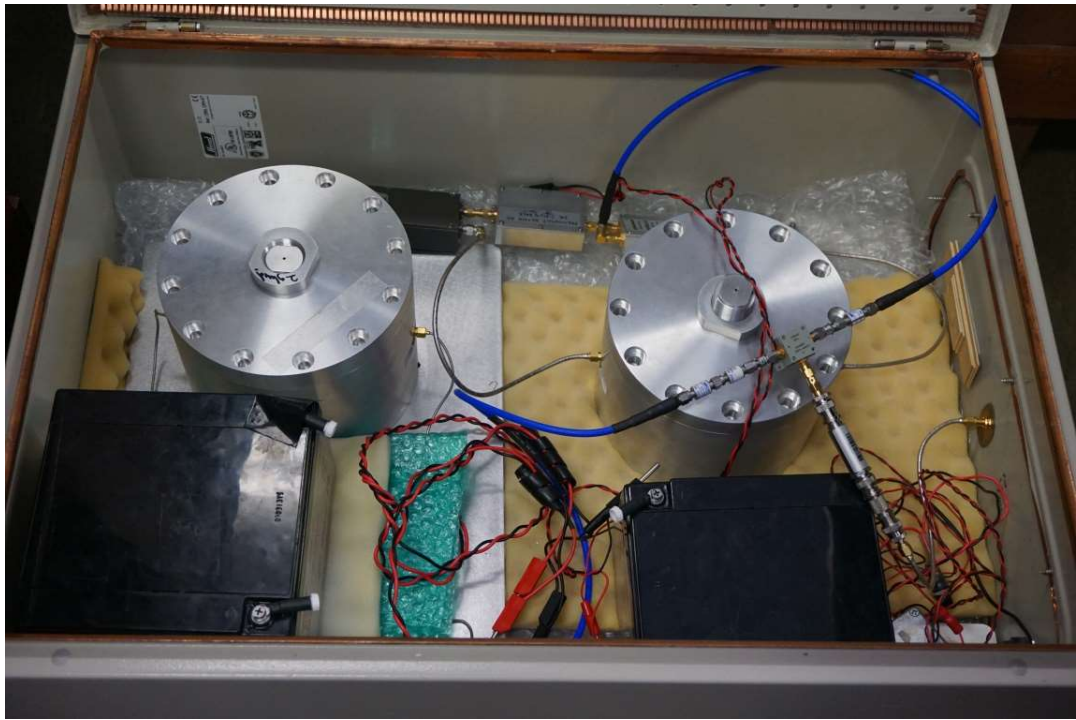


Figure 3-42: DRO's inside screened metal box.

The frequency of the two oscillators was adjusted using the bolts on the lids of the cavities until an offset of about 2.2 MHz was achieved. Both signals were attenuated to the desired signal power and fed into a double balanced mixer (ZEM-4300). This produced a beat note at 2.2 MHz. A 1.9 MHz low pass filter was then used to attenuate the higher order harmonics, which are produced by the mixer. The resulting signal could then be measured using the Symmetricom instrument. Figure 3-43 shows a block diagram of the measurement configuration.

Figure 3-44 shows the measured phase noise of the oscillators. The graph shows the combined phase noise of both DRO's, therefore the phase noise of a single DRO is 3dB lower (assuming they are both identical). Table 3-8 shows the values taken at selected offset frequencies.

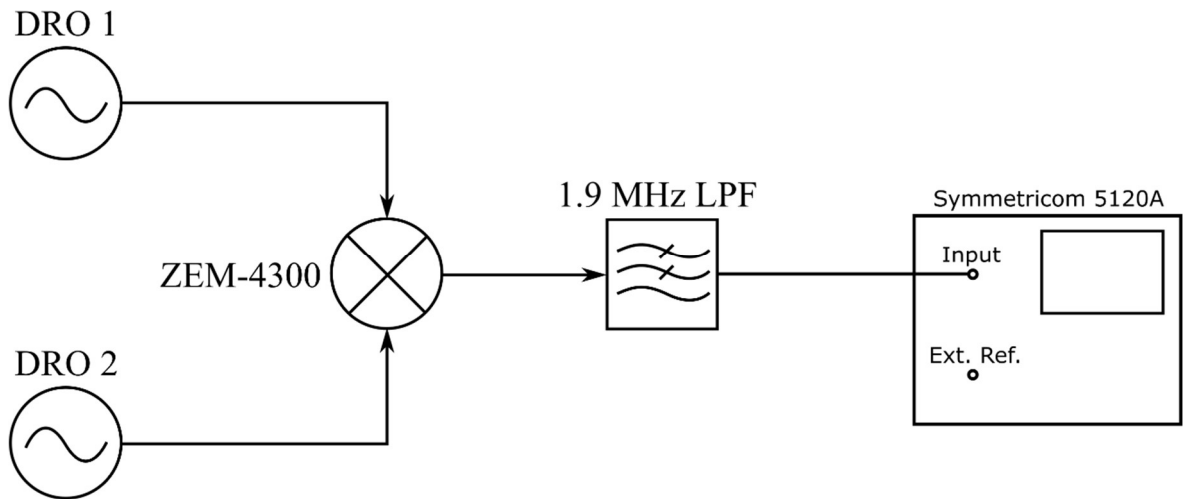


Figure 3-43: Block diagram of mixed down 1.5GHz DRO's measurement.

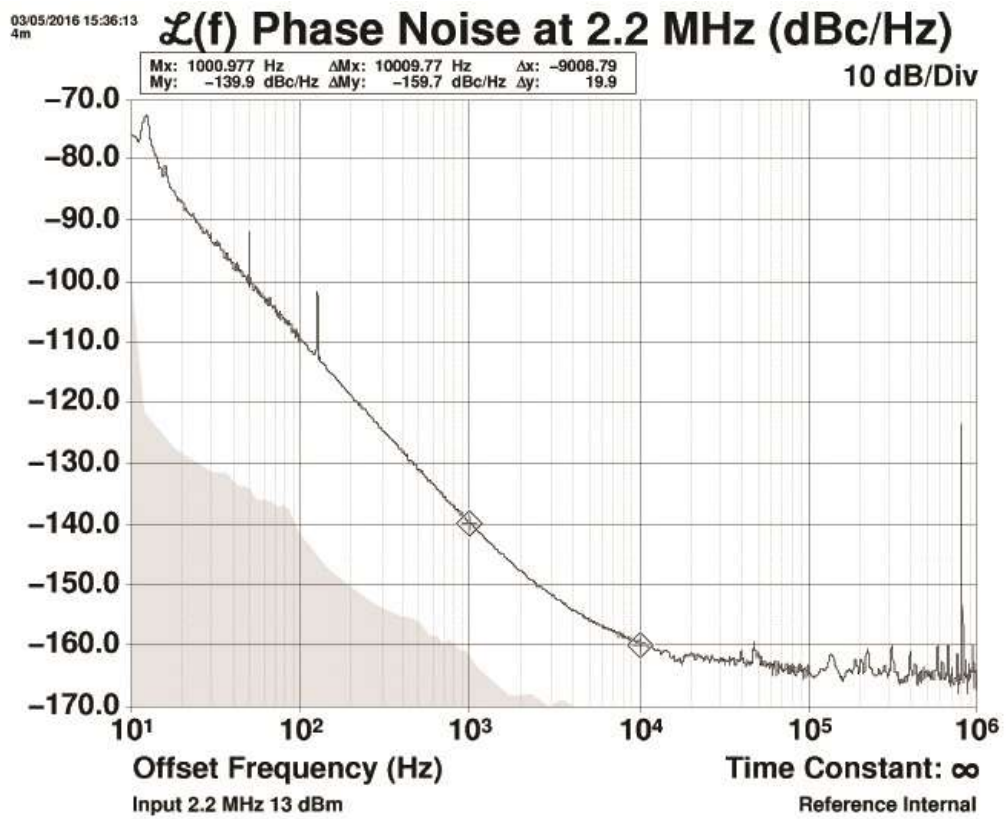


Figure 3-44: Measured DRO phase noise.

Table 3-8: DRO measured phase noise.

Offset frequency (Hz)	Measured Phase noise (dBc/Hz)	Phase noise of a single DRO (-3dB)
10	-76	<b>-79</b>
100	-109.9	<b>-112.9</b>
1,000	-139.9	<b>-142.9</b>
10,000	-159.7	<b>-162.7</b>

It can be seen, that the DRO's offer very good phase noise performance, especially at offsets higher than 100Hz and in terms of noise floor. In order to further evaluate the performance, it was compared with the phase noise predicted by the theory. The theoretical curve was calculated using the model and equations described in section 3.1.1. The general equation is mainly a function of the noise figure of the amplifier (11.5dB in this case), the flicker noise corner (3.5kHz), the power in the oscillator (about 23dBm) and the ratio of loaded to unloaded Q of the resonator (about 1/2).

$$L(f, F1, F2, Q0, QL, P, fc) := 10 \cdot \log \left[ 1 + \left[ \frac{F2 \cdot k \cdot T}{C0 \cdot 2P} + \left( 1 + \frac{fc}{f} \right) \cdot \left[ \frac{F1 \cdot k \cdot T}{2 \cdot P} \cdot \left[ \frac{1}{\left( 1 - \frac{QL}{Q0} \right)^2} \right] + \frac{F1 \cdot k \cdot T}{8 \cdot (Q0)^2 \cdot \left( \frac{QL}{Q0} \right)^2 \cdot \left( 1 - \frac{QL}{Q0} \right)^2 \cdot P} \cdot \left( \frac{f0}{f} \right)^2 \right] \right] \right]$$

A direct comparison between the theoretical and measured phase noise curves is shown in Figure 3-45.

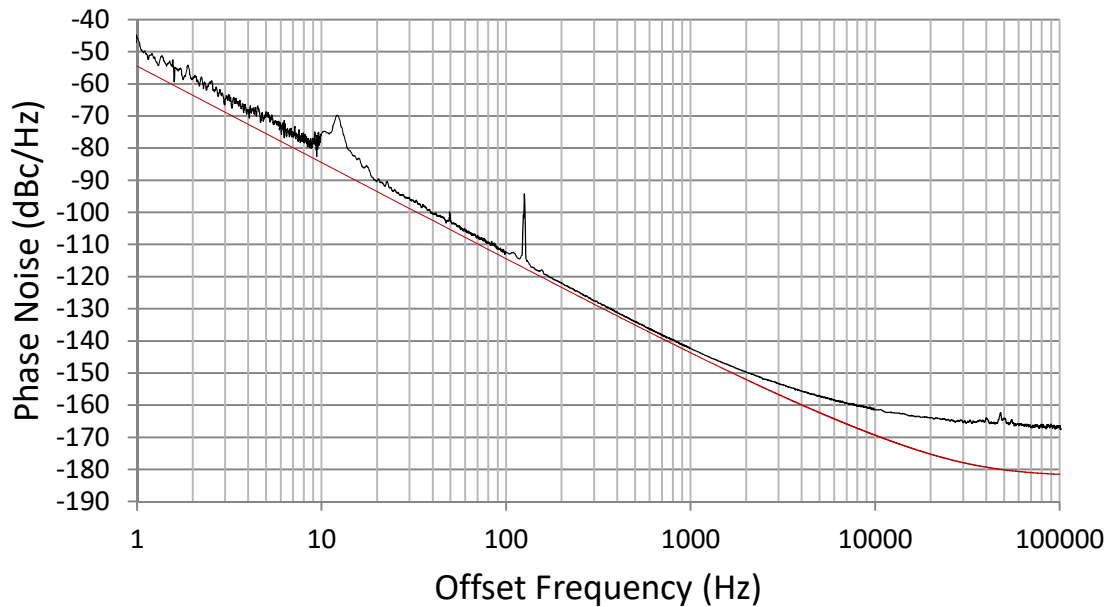


Figure 3-45: Comparison between measured and theoretical DRO phase noise.

At medium offsets the measured phase noise agrees well with the theory. At higher offsets the measurement is limited by the noise floor of the instrument, but the actual performance can be extrapolated from the theoretical curve. At lower offsets (down to 1Hz) there is also some divergence from the theoretical graph. This may be attributed to mechanical vibrations or changes in temperature during the measurement.

### 3.4 Phase Locked Loop Configuration and Measurements.

To complete the local oscillator assembly, the 1.5 GHz DRO was phase locked to the 10 MHz crystal oscillator. The LTC6950, 1.4GHz low phase noise, low jitter PLL chip was chosen for this purpose. This chip was chosen for its low residual phase noise [61]. Although the maximum specified operating frequency of this PLL is specified as 1.4 GHz, after initial testing, it was found that it can be used with the 1.5 GHz DRO, provided that the power at the input of the PLL is sufficient (approximately 2-5dBm). A development board (DC1795A) for the LTC6950 was purchased to simplify setting up and programming the chip. The board comes equipped with a 100 MHz reference crystal oscillator, 1 GHz VCO and loop filter. Therefore, several modifications had to be done to use the demo

board with external oscillators. That involves removing some of the components and adding others in order to enable the external oscillator inputs and the charge pump output of the board. Further modifications were done to the loop filter available on the board to adjust it to the parameters of the DRO. The final modification was the inclusion of low noise voltage regulators for the 3.3V and 5V supply voltages.

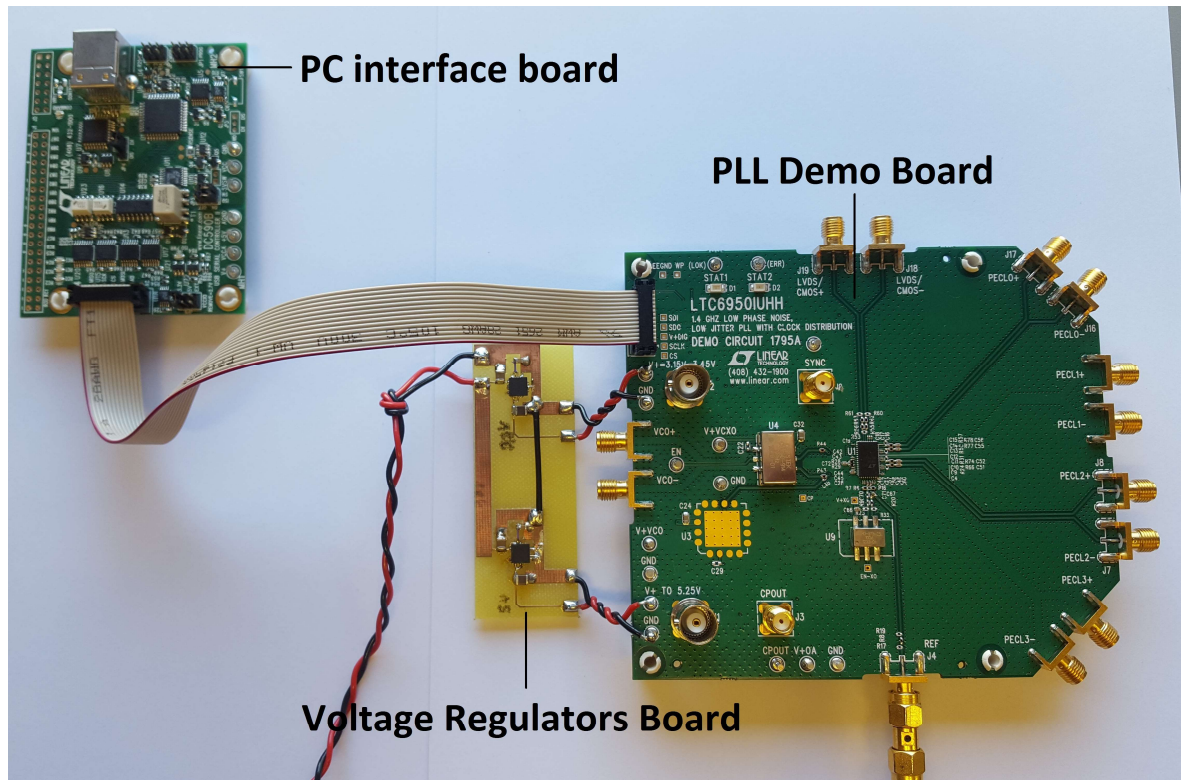


Figure 3-46: Photo of LTC6950 development board.

The board is programmed using the ClockWizard software package from Linear Technologies, which can also be used to calculate the components of the loop filter, based on the parameters of the reference oscillator (10 MHz XO in this case), VCO (1.5 GHz DRO in this case) and desired loop bandwidth. The software also includes a simulation of the predicted phase noise of the reference, VCO and the resulting phase noise in the phase locked configuration.

Since the chip only uses up to 5V power supply, it was found that the varactors used in the original design of the DRO phase shifter were unsuitable for this configuration, as they require 6.6V-11.6V for correct operation (section 3.3.2). It was therefore necessary to replace them with varactors operating at a lower voltage. The BBY53 6V diodes were

chosen. The phase shift and insertion loss of the phase shifter were measured again after the modification (Figure 3-47).

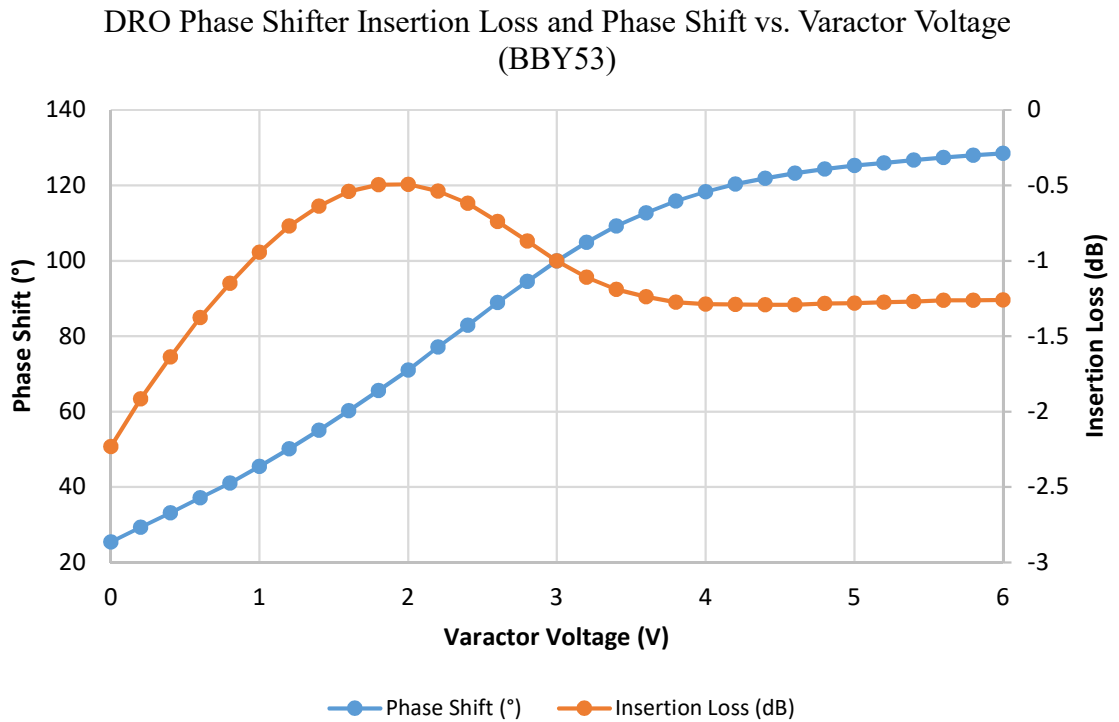


Figure 3-47: 1.5 GHz DRO phase shifter insertion loss and phase shift vs. varactor voltage (BBY53).

In this case the insertion loss remains below 1dB within the range of 1V - 3V of varactor voltage. In this range the phase tuning remains fairly linear with a total phase shift of 54.56°.

One of the main parameters in determining the loop filter for the PLL is the frequency tuning of the VCO vs. varactor voltage. This was measured after the DRO was re-assembled using the new phase shifter and the total phase in the oscillator loop was adjusted to be in the middle of the optimal voltage range (at about 2V). The measured oscillation frequency and output power of the DRO as a function of varactor voltage is shown in Figure 3-48.

DRO Phase Shifter Insertion Loss and Phase Shift vs. Varactor Voltage (BBY53)

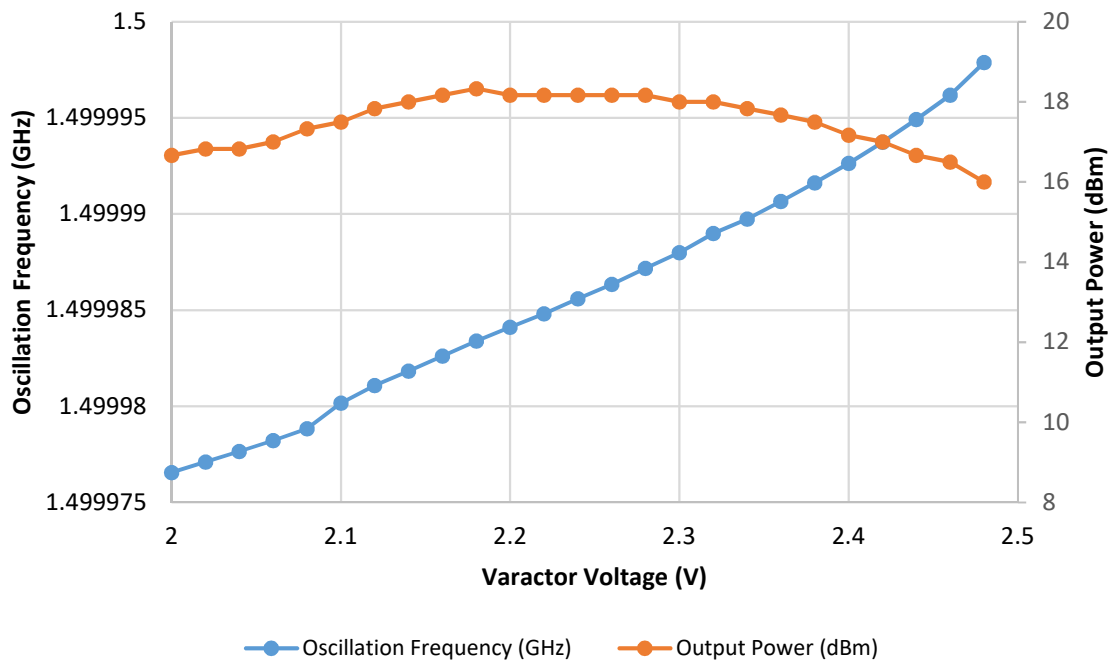


Figure 3-48: DRO oscillation frequency and output power vs. varactor voltage.

The output power remains above 18dBm within the range of 2.1V - 2.34V. The frequency tuning appears linear with a slope of 41.6kHz/Volt.

These parameters, along with the measured phase noise values for both oscillators, such as  $1/f^3$  corner, noise floor and low offset phase noise were entered into the ClockWizard design tool. The loop bandwidth was chosen at 10 Hz and the design tool was used to calculate the loop filter components, which were then soldered to the development board (Figure 3-49). Both the passive (Filter 2) and active (Filter 4) filter options were tested without any significant difference in the resulting phase noise performance. It must be noted that the software does not accept higher VCO frequency than 1.4 GHz, which is why in order to set the dividers to the required 150 division ratio, the frequency values were scaled down, making the frequency of the VCO 1.35 GHz and the frequency of the reference oscillator 9 MHz. As long as the ratio remained the same, the PLL chip was programmed correctly. The predicted phase noise of the reference oscillator, VCO and phase locked configuration is shown in Figure 3-50.

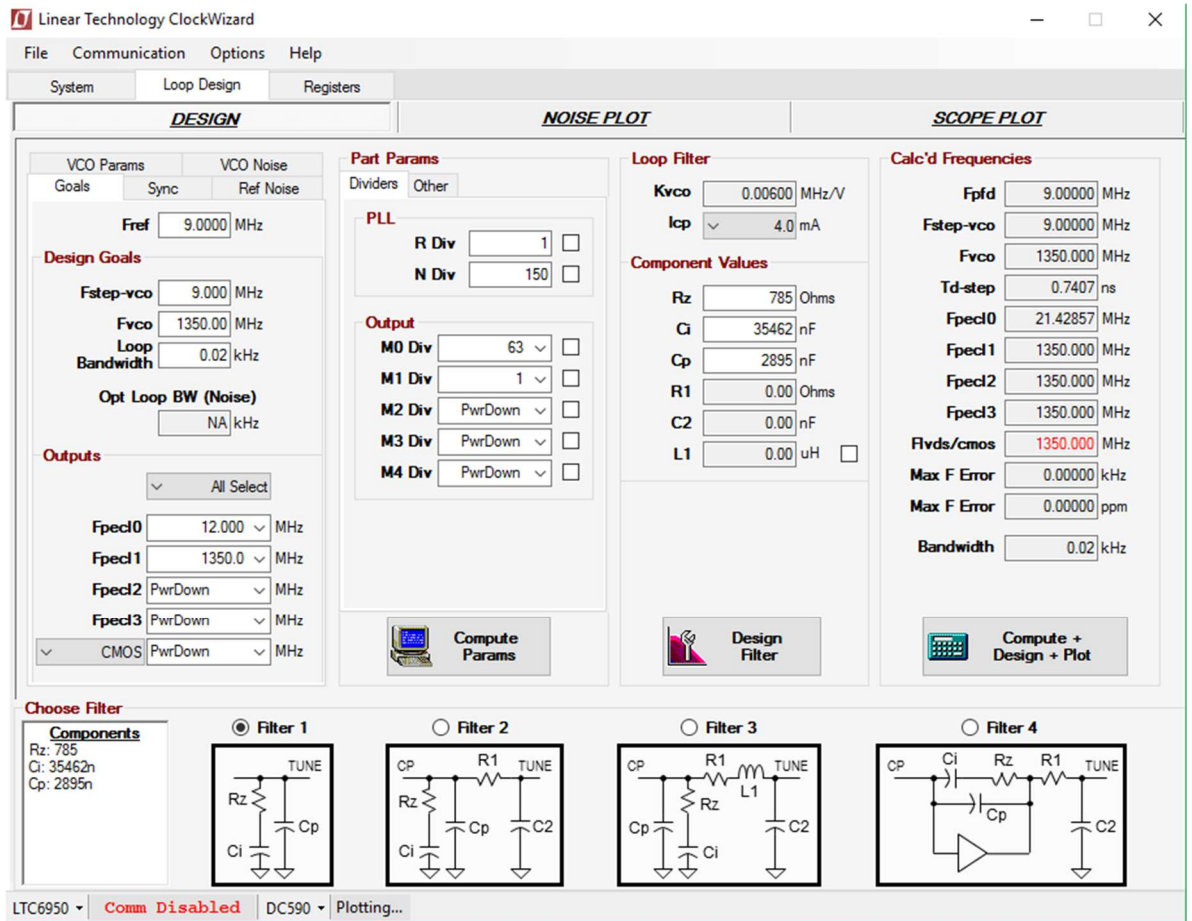


Figure 3-49: ClockWizard phase locked loop design tool.

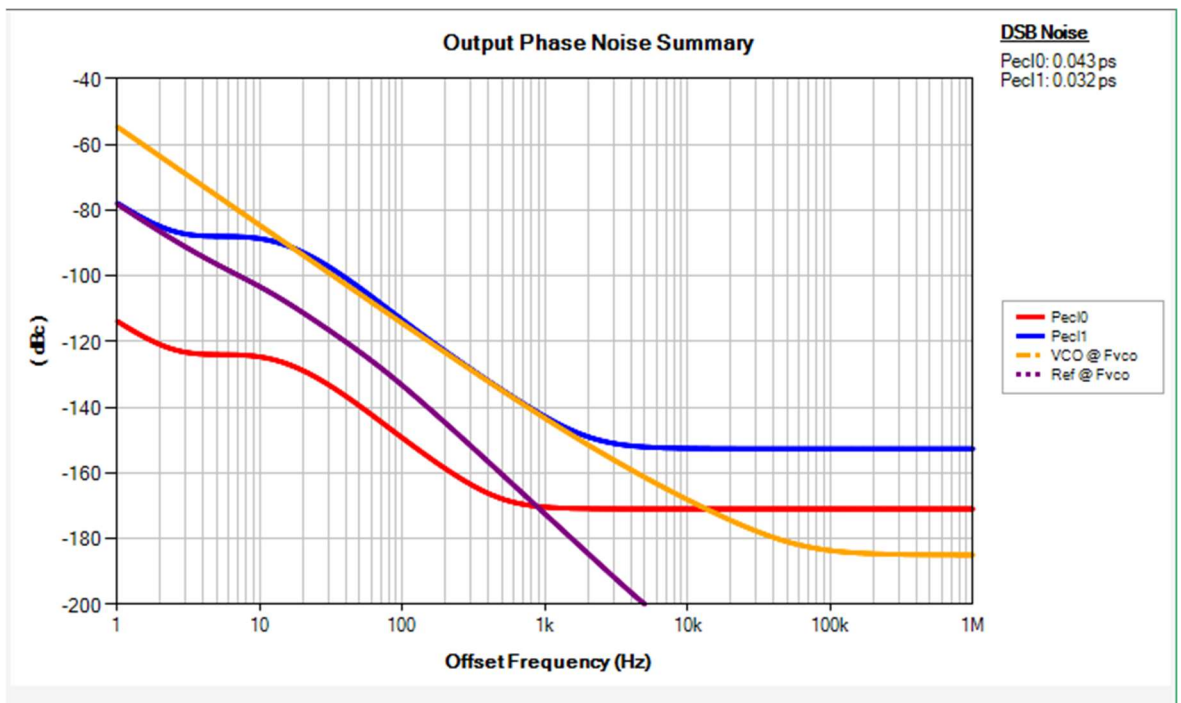


Figure 3-50: Predicted phase noise plots by ClockWizard design tool.

When the modifications to the loop filter were done and the correct division ratio and charge pump current were set, the PLL chip was programmed, the loop was closed and an output was taken directly from the DRO using a 3dB splitter as illustrated in Figure 3-51. The frequency of the DRO was carefully adjusted using the screw on the lid of the cavity until it was an exact multiple of the 10 MHz reference and phase lock was achieved.

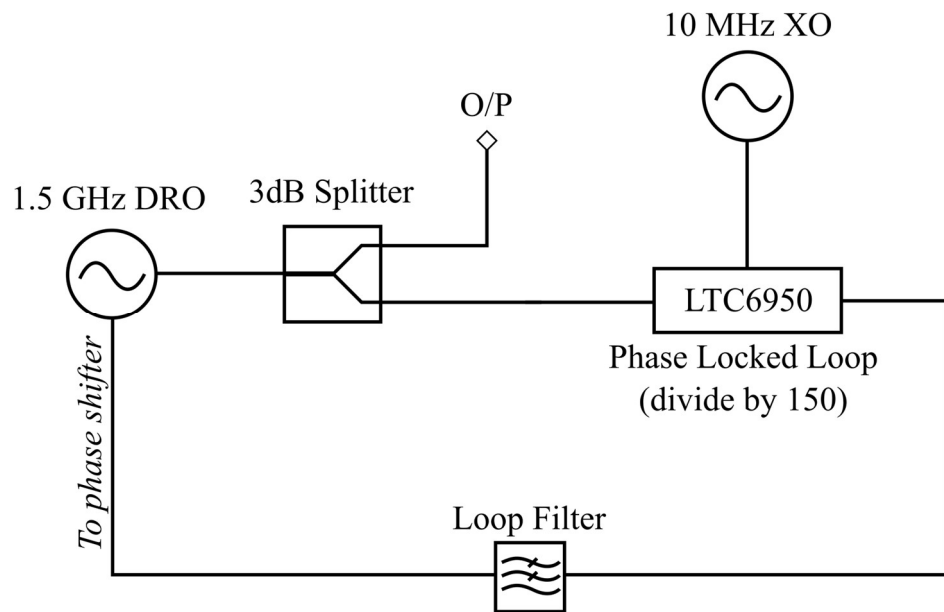


Figure 3-51: Local Oscillator phase locked loop configuration.

The phase noise of this configuration was measured using the R&S FSWP, 26.5 GHz phase noise analyser, which was temporarily borrowed from Rohde & Schwartz. Figure shows a comparison between the measured phase noise of the 10 MHz reference oscillator, the originally measured phase noise of the 1.5 GHz DRO (section 3.3.4) and the performance of the phase locked configuration at two different loop bandwidth settings, 10Hz and 20Hz. The phase noise of the crystal oscillator was scaled up to 1.5 GHz by adding  $20 \log N$  to the original measurement, where  $N$  is the frequency ratio.

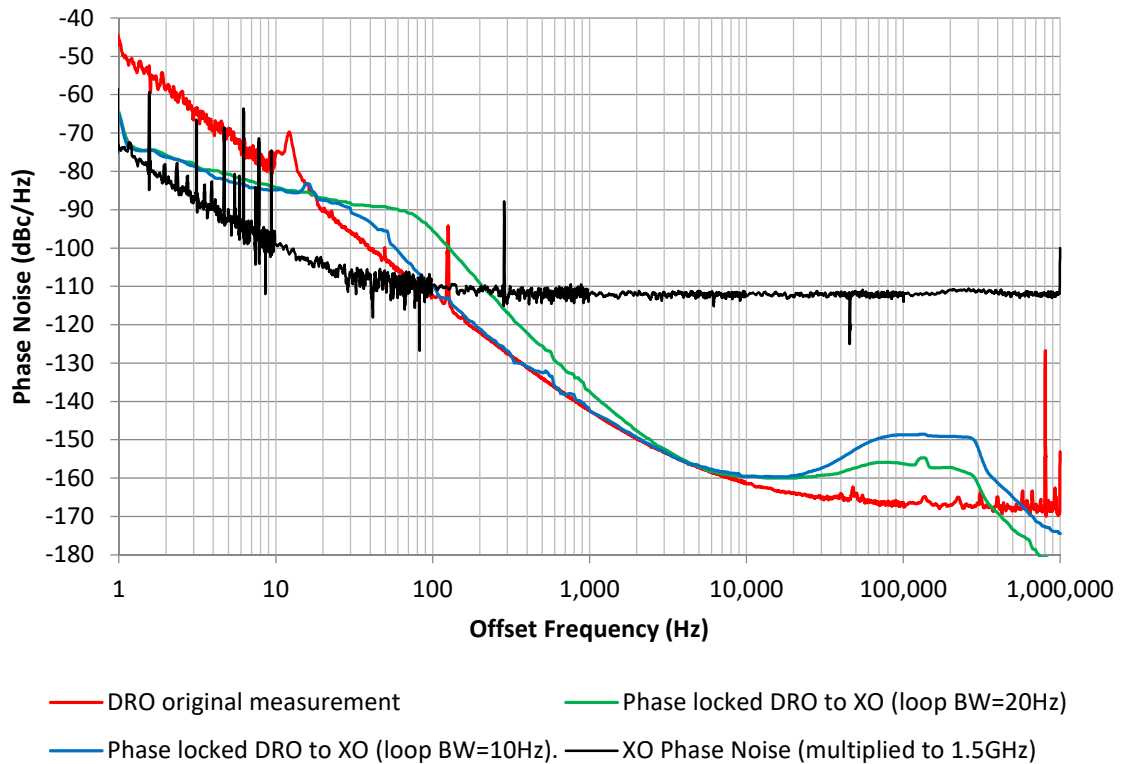


Figure 3-52: Phase locked loop noise measurements. The phase locked curves were measured on the R&S FSWP.

The phase locked graph appears to approach the performance of the crystal oscillator at 1Hz offset. When the loop bandwidth is set to 20Hz, there is significant divergence from the DRO phase noise at medium offsets. By reducing the bandwidth to 10Hz, the plot follows the DRO measurement very closely with only a small overshoot around the 20Hz offset point. It is believed that this can be further improved by further adjusting the loop bandwidth. The noise floor is still believed to be limited by the noise of the measurement instrument. A slight increase in the noise floor is also seen around 100kHz offset. Its origin is not clear, but may be attributed to cross-correlation effects as described in [52] and [53] or high frequency noise from the PLL output, the loop filter or the oscillators.

In the phase locked configuration, the frequency of the 1.5 GHz DRO follows any changes in the frequency of the 10 MHz crystal oscillator multiplied by 150. This means that a more accurate measurement of the crystal oscillator frequency tuning vs. varactor voltage can be achieved. This parameter is particularly important for locking the local oscillator configuration to the atomic resonance. Previous attempts to measure the frequency tuning directly did not yield good results due to the limited resolution bandwidth of the spectrum

analysers available. The crystal oscillator was temperature stabilized at about 82°C (the inversion temperature of the resonator) and the phase locked loop was closed. A precise voltage was provided to the phase shifter input of the XO using the Keithley 2400 SourceMeter. This voltage was varied over a range of about 1.5V and the frequency shift at the output of the 1.5 GHz DRO was measured using the HP8563E spectrum analyser with the minimum resolution bandwidth of 1Hz (Figure 3-53).

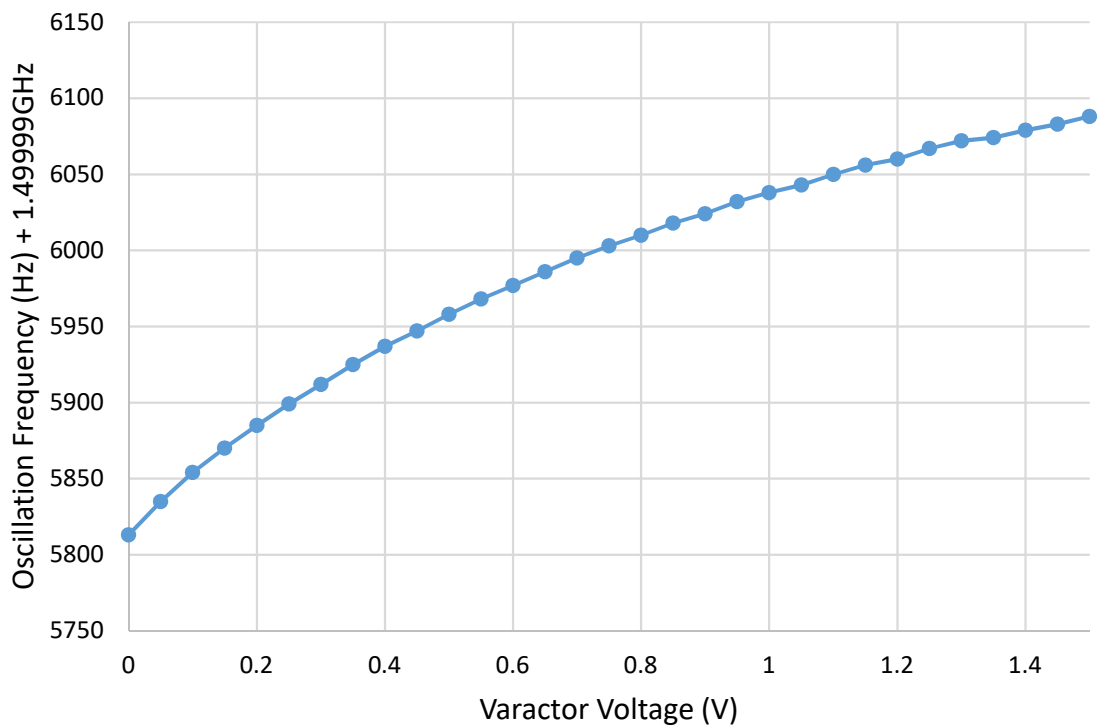


Figure 3-53: Crystal oscillator frequency tuning (x150) vs varactor voltage.

Within the range of 0.4V to 1V the frequency tuning can be considered relatively linear. The frequency at the output of the DRO changes by about 101Hz within this range, which corresponds to about 0.67Hz at the 10 MHz XO. This means that the frequency tuning at this point is about 1.122Hz/Volt.

### 3.5 Summary

An ultra-low phase noise crystal oscillator operating at 10 MHz was designed based on the Everard theoretical phase noise model with a phase noise performance comparable to some of the best available BVA oscillators (-123dBc/Hz at 1Hz offset). Several oscillators were built using the basic design. The current version of the oscillator is built in a compact

package and incorporates double oven temperature stabilization. It was found that this level of performance could only be achieved when high-Q Coilcraft inductors and either polystyrene or high quality ATC ceramic capacitors were used in the oscillator circuit. It was also experimentally found that optimal performance was achieved when the gain margin within the oscillator loop was kept relatively low (about 0.3dB).

An ultra-low phase noise Dielectric Resonator Oscillator operating at 1.5 GHz was designed and built based on the same theoretical model. The measured phase noise agrees with the theoretical prediction at medium and high offsets (-142.9 dBc/Hz at 1kHz offset), however, the noise floor is limited by the noise of the measurement instrument. The DRO is equipped with a voltage tuned phase shifter to enable frequency tuning and phase locking.

The two oscillators were phase locked together using the low residual phase noise PLL chip LTC6950. The loop combines the close to carrier phase noise of the crystal oscillator with the medium offset and noise floor of the DRO, however further improvement can be potentially achieved by optimising the loop parameters. This completes the design of the multi-element local oscillator which can be used to generate the low noise RF excitation signal for use in the Rb atomic physics package, while providing multiple high spectral purity output frequencies.

## 4 FREQUENCY SYNTHESIZER.

One of the main components of the atomic clock, the frequency synthesizer is the one responsible for upconverting, tuning, sweeping and/or modulating the local oscillator signal to the resonance frequency of the atomic transitions. The transition frequency originally selected for this project is the  $^{85}\text{Rb}$  ground hyperfine splitting of 3.035732 GHz, which means that the modulation frequency for the laser in the CPT physics package should be half of that, 1.517866 GHz (Figure 2-2). Therefore, the frequency provided by the 1.5 GHz DRO has to be upconverted with an offset of 17.866 MHz, which should be adjustable. This chapter describes how this was achieved. A direct digital synthesizer in combination with a microcontroller was used to generate the offset frequency, which was then added to the 1.5GHz using a single sideband mixer. The resulting modulated spectrum was further filtered using a high-Q notch filter to reduce the 1.5GHz LO feedthrough component. Figure 4-1 shows a basic block diagram of the synthesizer configuration.

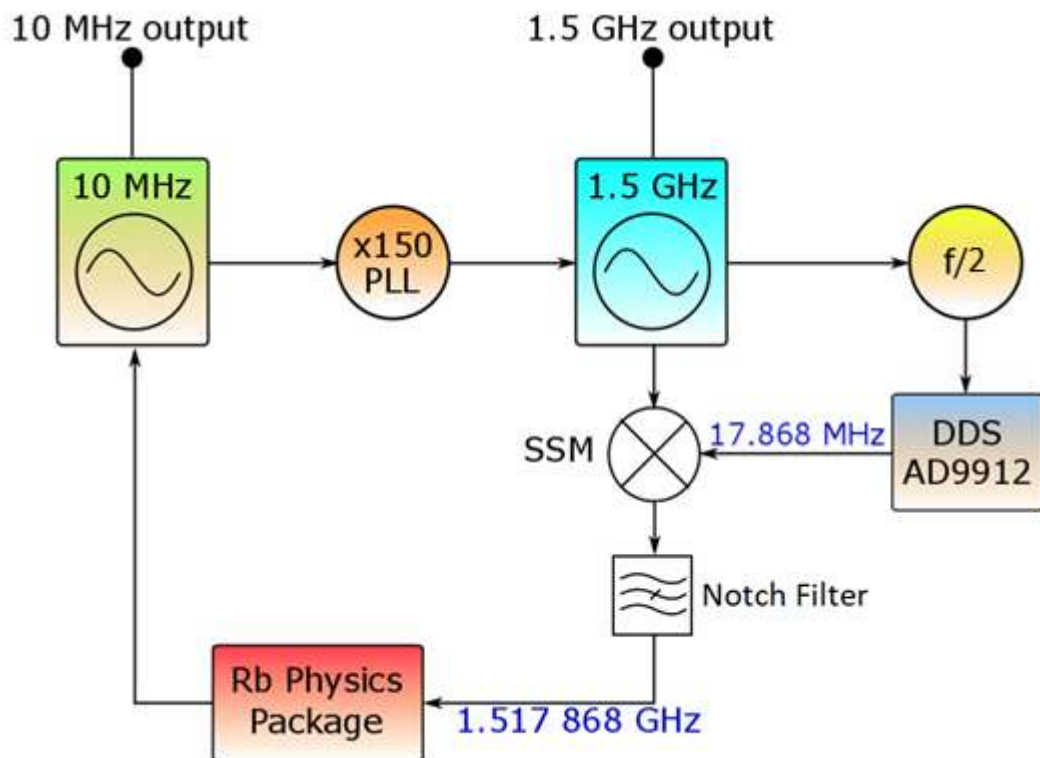


Figure 4-1: Frequency synthesizer basic block diagram.

## 4.1 Direct Digital Synthesizer (DDS).

The only reasonable method to achieve microhertz accuracy and a tuning range of a few kilohertz in the offset signal was to use a DDS with high enough resolution and low residual phase noise. Several different synthesizer datasheets were examined and the AD9912 device from Analog Devices was chosen for its combined low residual phase noise (tabulated in Table 4-1) [62], high resolution frequency tuning (48 bits), high resolution digital to analogue converter (14 bits) and high clock speed (1GHz maximum).

Table 4-1: AD9912 direct digital synthesizer residual phase noise.

Offset frequency (Hz)	Residual phase noise at 250 MHz (dBc/Hz)
10	-113
1000	-133
100,000	-153
40,000,000	-161

This chip offers the best combination of bit resolution, residual phase noise and maximum clock frequency among the Analog Devices DDS solutions. For comparison, the AD9956 has very similar resolution and phase noise, but only supports up to 400MHz clock frequency. When clocked by a 750 MHz signal, the smallest frequency tuning step is about 2.66 $\mu$ Hz. A development board using this device was purchased and tested using the supplied software package. However, this software can only be used to set the output frequency of the DDS to a fixed value, without the capability for continuous tuning or modulation. Another disadvantage is that the DDS resets to its factory default settings when it is powered down, which means that it has to be initialized using a PC each time it's switched on. This was solved by incorporating a PIC microcontroller as an intermediate programming stage. The microcontroller can be used to continuously supply the DDS with data through the serial communication port provided on the development board and adjust the output frequency or apply a sweep or modulation. The instructions are stored in the flash memory of the PIC, which means that the DDS is automatically initialized as soon as the system is powered on. The PIC18F25K20 was initially chosen for this task. Figure 4-2 shows the configuration.

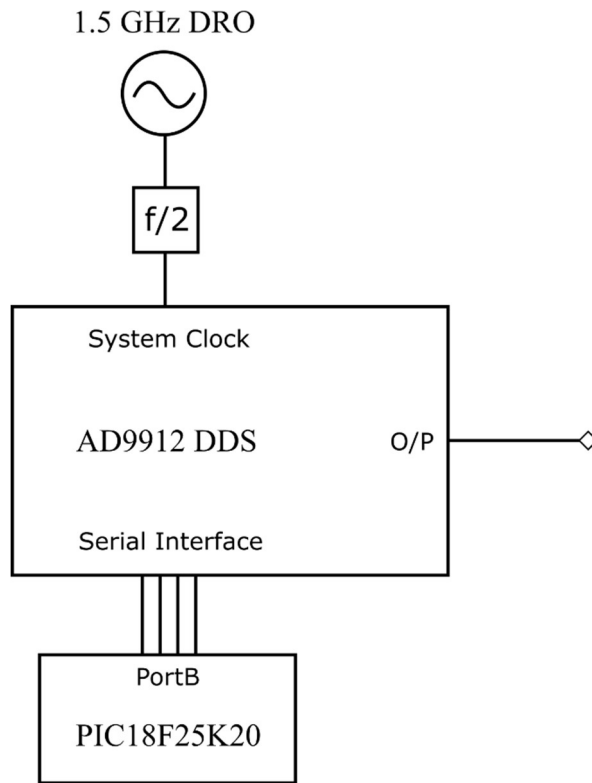


Figure 4-2: DDS programmed by PIC microcontroller.

A low phase noise, low jitter digital divider LTC6954-1 was used to divide down the frequency of the DRO by 2, as the DDS maximum clock frequency is 1 GHz. The code for the PIC was written in the mikroC Pro compiler and the microcontroller was programmed using a PICkit 2. The code incorporates separate dedicated functions and union structures for performing operations on the frequency tuning word and clocking the data into the serial interface of the DDS. This means it can be easily modified to produce switching of the frequency between discreet values, or apply sweep or modulation. It can also be modified to be used with a different PIC model. Figure 4-3 shows the printed circuit board built for the microcontroller feeding data into the DDS development board.

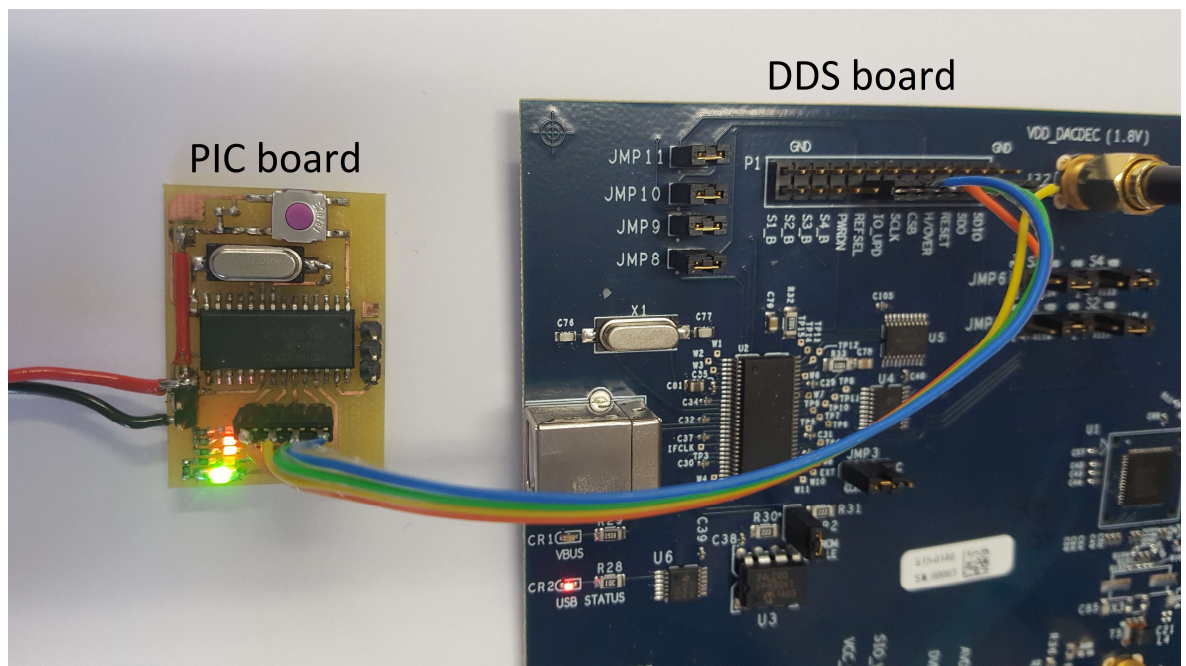


Figure 4-3: PIC microcontroller programming the DDS development board.

For the initial tests, the DDS output frequency was set to 17.866 MHz and was periodically switched by  $\pm 5$  kHz every second.

## 4.2 Single Sideband Mixer.

The next step in generating the signal required for detecting the CPT resonance was to upconvert the 1.5 GHz DRO output to 1.517866 GHz, using the output of the DDS. This can be done by mixing the two signals in a conventional mixer and producing a modulated spectrum. This, however, produces not only the desired upper sideband, but also an unwanted lower sideband at about the same power level, along with significant LO feedthrough and higher order sidebands. Since the frequency difference of those components in this case is very small, filtering them out is especially difficult without affecting the wanted signal. Therefore, it was decided in this case to design a particular type of mixer, known as single sideband mixer (SSM), to upconvert the frequency. These circuits take two frequencies as inputs and generate an output in which only one of the sidebands is dominant, while the other sideband and carrier signals are suppressed. Although there are some commercially available single sideband mixers, their design is usually concentrated to providing suppression of about 20 to 25 dB in a wide range of

frequencies (with very few of them including the desired 1.5GHz frequency) or include active components, which degrade the noise performance. It was therefore decided that designing a passive SSM at the exact desired frequency of operation would provide higher suppression of the unwanted sidebands.

A single sideband mixer operates by splitting the two inputs into an in-phase component and a component with  $90^\circ$  phase shift. The individual components are then mixed separately using two mixers. The resulting modulated signals are then re-combined to provide the single sideband output [63]. The ADE-11X double balanced mixers were used in this case. Figure 4-4 shows the block diagram of the designed SSM.

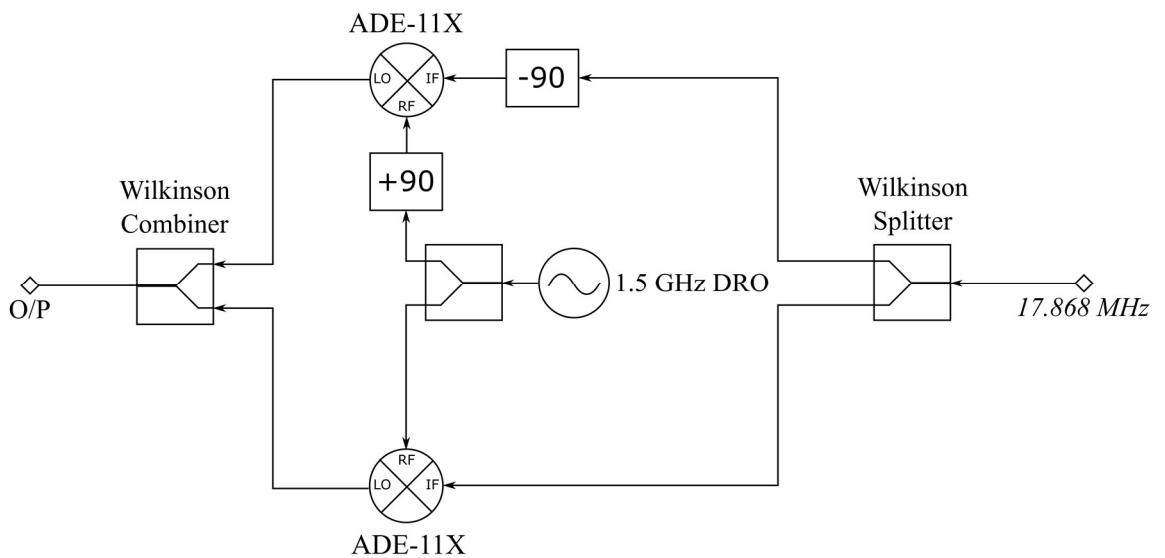


Figure 4-4: Block diagram of SSM (upper sideband).

In this case the phase shifts should be  $-90^\circ$  and  $+90^\circ$ , since the upper sideband is desired. If the lower sideband is desired, then the phase shifts should both have the same sign. Due to the frequency requirements for the ports of these mixers, the IF port was used as the low frequency 17.868 MHz input, while the output was taken from the LO port. The output of the SSM is therefore:

$$\begin{aligned}
V_o(t) &= [\sin(\omega_1 t) \times \sin(\omega_2 t)] + [-\cos(\omega_1 t) \times \cos(\omega_2 t)] \\
&= \frac{1}{2} [\cos(\omega_1 t - \omega_2 t) - \cos(\omega_1 t + \omega_2 t)] - \frac{1}{2} [\cos(\omega_1 t - \omega_2 t) + \cos(\omega_1 t + \omega_2 t)] \\
&= \frac{1}{2} [\cos(\omega_1 t - \omega_2 t) - \cos(\omega_1 t + \omega_2 t) - \cos(\omega_1 t - \omega_2 t) - \cos(\omega_1 t + \omega_2 t)] \\
&= -\cos(\omega_1 t + \omega_2 t)
\end{aligned}$$

Where  $\omega_1 = 2\pi \times 17.868 \text{ MHz}$  and where  $\omega_2 = 2\pi \times 1.5 \text{ GHz}$ . Therefore, the produced output frequency is the  $\omega_1 + \omega_2$  (higher sideband). Of course, in reality, the other frequency components will also be present, due to the finite port isolation and imbalances in the mixers.

Both signals need to be split and the appropriate phase shifts need to be produced for correct operation. In the case of the 1.5GHz signal, this was done by designing a microstrip 3dB Wilkinson Splitter with one of the arms extended by the equivalent  $90^\circ$  electrical length. The splitter is realized using two  $\lambda/4$  lines with an impedance of  $\sqrt{2}Z_0$  ( $70.71\Omega$  for  $Z_0 = 50\Omega$ ) and a resistor with value  $R = 2Z_0 = 100\Omega$ . A detailed analysis of the structure of the splitter is described by Pozar in [49, pp. 328-332]. Figure 4-5 shows the layout of the splitter.

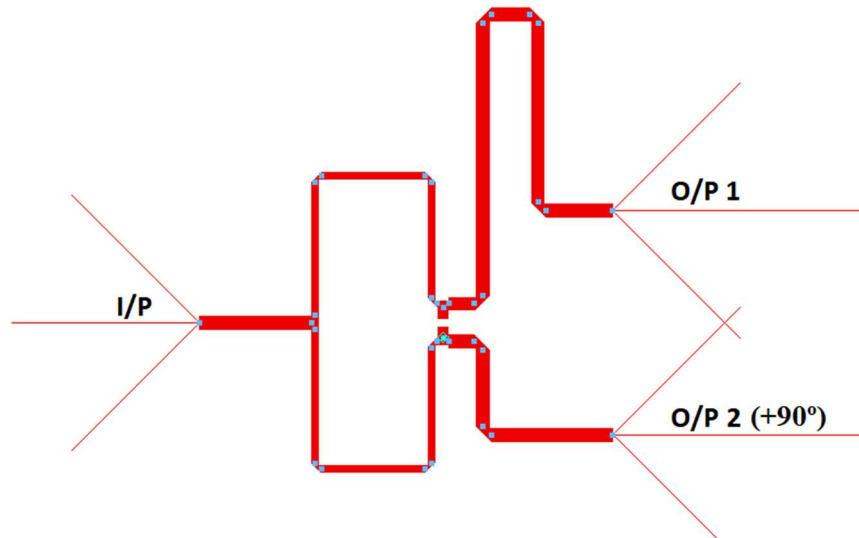


Figure 4-5: 3dB Wilkinson Splitter with in-phase and quadrature outputs.

The Keysight Advanced Design System (ADS) microwave simulation software was used to simulate the microstrip structures and circuits. The  $\lambda/4$  lines were designed with 90° optimally chamfered bends. This was done to conserve space and to align the splitter with the mixers in the final layout. All the lengths in the bends and lines were accounted for in the ADS simulation. The simulated insertion loss in each arm of the splitter was -3.04dB and the phase difference between them was 89.9° (Figure 4-6).

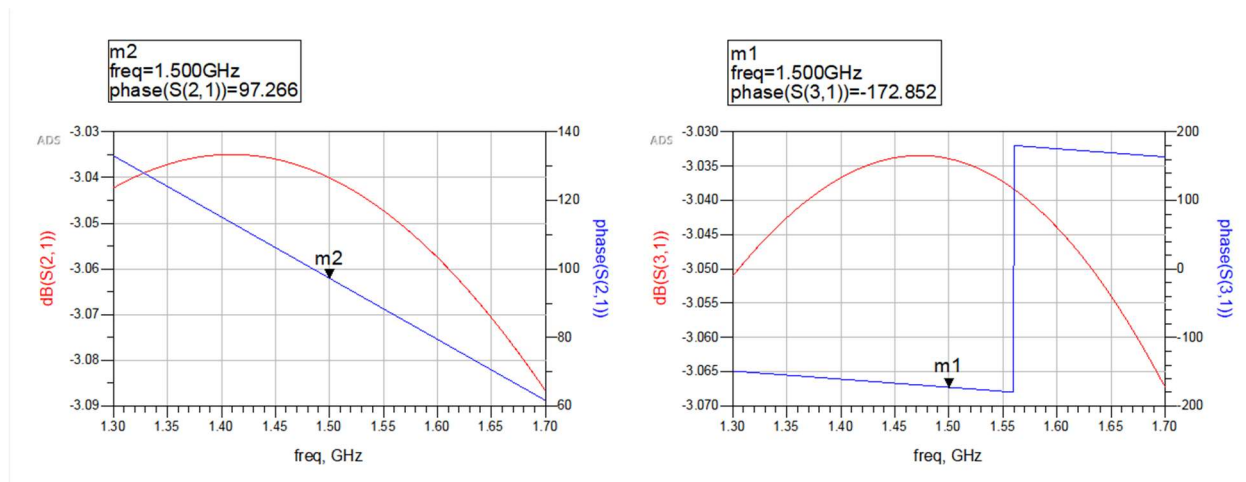


Figure 4-6: 1.5GHz Wilkinson Quadrature Splitter ADS simulation results.

In the case of the 17.868 MHz signal, generating the correct phase shifts is slightly more complicated. The frequency is much lower, so microstrip delay lines are not feasible. Instead, a lumped element Wilkinson Power Divider was designed, based on the design in [64]. The schematic is shown in Figure 4-7. The circuit consists of a power divider and two phase shift networks. The upper phase shift T-network ( $C_7$ ,  $C_8$ ,  $L_5$ ) is designed for  $\theta_1 + 45^\circ$  phase shift, while the lower  $\pi$ -network ( $C_5$ ,  $C_6$ ,  $L_4$ ) was designed for  $\theta_2 - 45^\circ$  phase shift, giving a total of  $90^\circ$  between the two outputs.

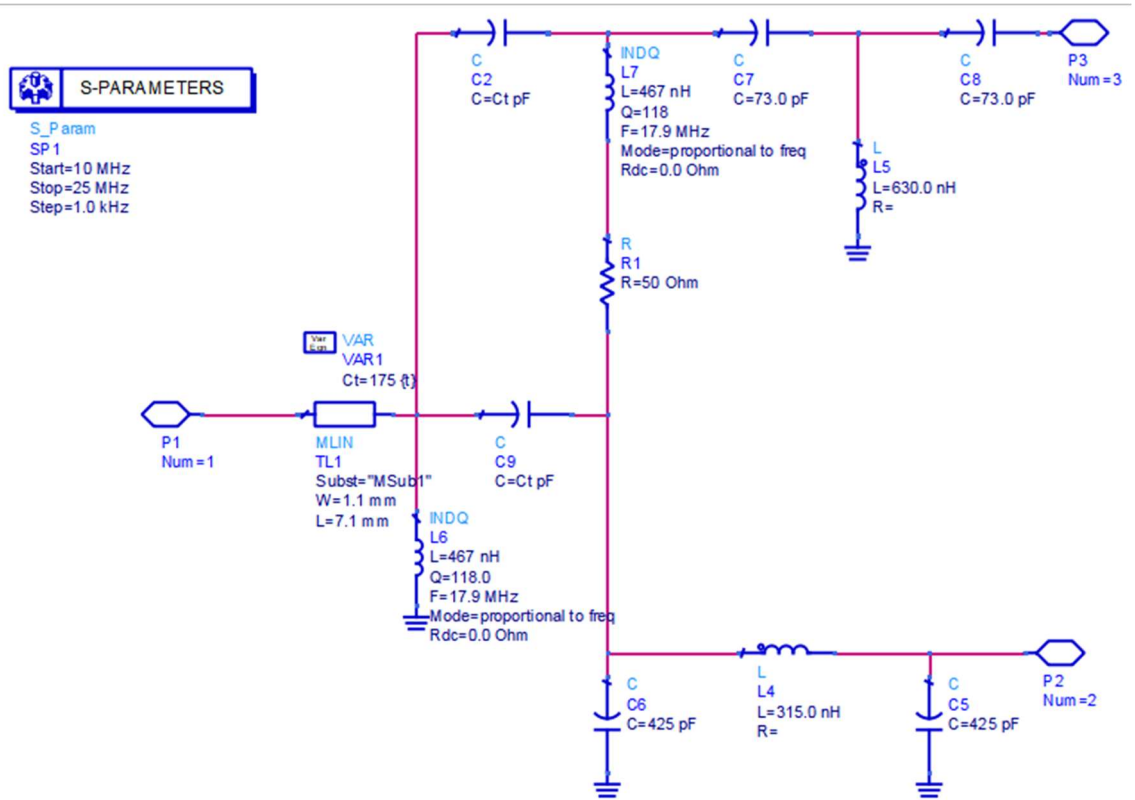


Figure 4-7: Lumped element 17.868 MHz Quadrature Wilkinson divider circuit diagram.

The ideal component values are calculated according to [64] and [65] as:

$$C_2 = C_9 = \frac{1}{2\pi f Z_0} = \frac{1}{2\pi \times 17.868 \times 10^6 \times 50} = 178 \text{ pF}$$

$$L_6 = L_7 = \frac{Z_0}{2\pi f} = \frac{50}{2\pi \times 17.868 \times 10^6} = 446 \text{ nH}$$

$$C_7 = C_8 = \frac{1}{2\pi f Z_0 \frac{-\sin \theta_1}{\cos \theta_1 - 1}} = \frac{1}{2\pi \times 17.868 \times 10^6 \times 50 \frac{-\sin 45}{\cos 45 - 1}} = 73.8 \text{ pF}$$

$$L_5 = \frac{Z_0 \frac{-1}{\sin \theta_1}}{2\pi f} = \frac{50 \frac{-1}{\sin 45}}{2\pi \times 17.868 \times 10^6} = 629 \text{ nH}$$

$$C_5 = C_6 = \frac{1}{2\pi f Z_0 \frac{1 - \cos \theta_2}{\sin \theta_2}} = \frac{1}{2\pi \times 17.868 \times 10^6 \times 50 \frac{1 - \cos(-45)}{\sin(-45)}} = 430 \text{ pF}$$

$$L_4 = \frac{Z_0 \sin \theta_2}{2\pi f} = \frac{50 \sin(-45)}{2\pi \times 17.868 \times 10^6} = 315nH$$

The ideal component values, however are not readily available. Therefore, the closest high-Q air core inductor values available from Coilcraft were selected and the capacitor values were tuned until the desired performance was achieved in the simulation. In the construction of the final circuit the tolerance of the components can alter the response, so low value trimmer capacitors were used in parallel with the fixed ones in order to enable fine tuning of the phase difference. Figure 4-8 shows the simulation results.

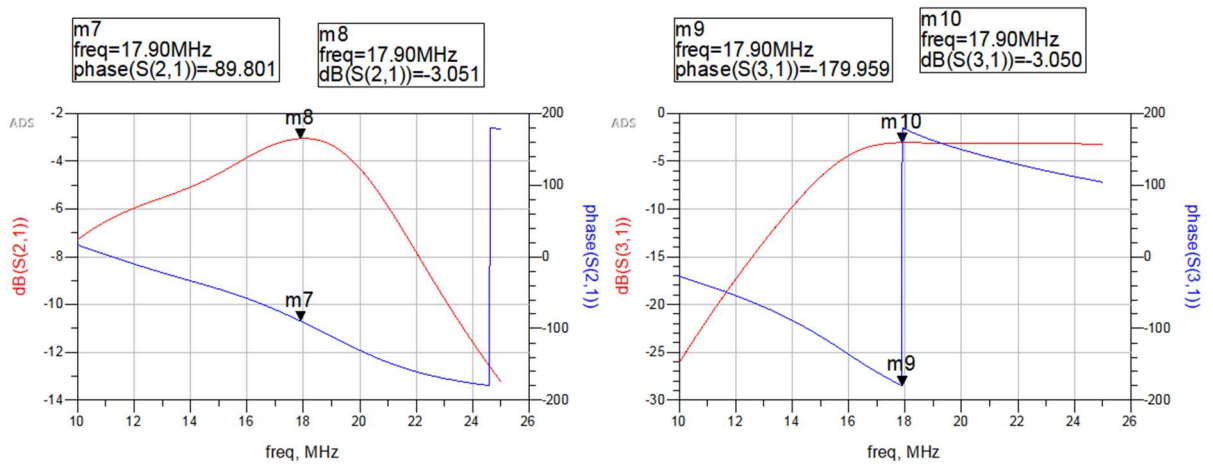


Figure 4-8: Lumped element Wilkinson Quadrature Divider simulation results.

The divider shows simulated insertion loss of about -3.05dB for each output and a phase difference between them of 90.1°.

Another microstrip Wilkinson structure was designed to re-combine the output signals from the two mixers. Figure 4-9 shows the complete SSM layout, including the two dividers, the mixers and the combiner.

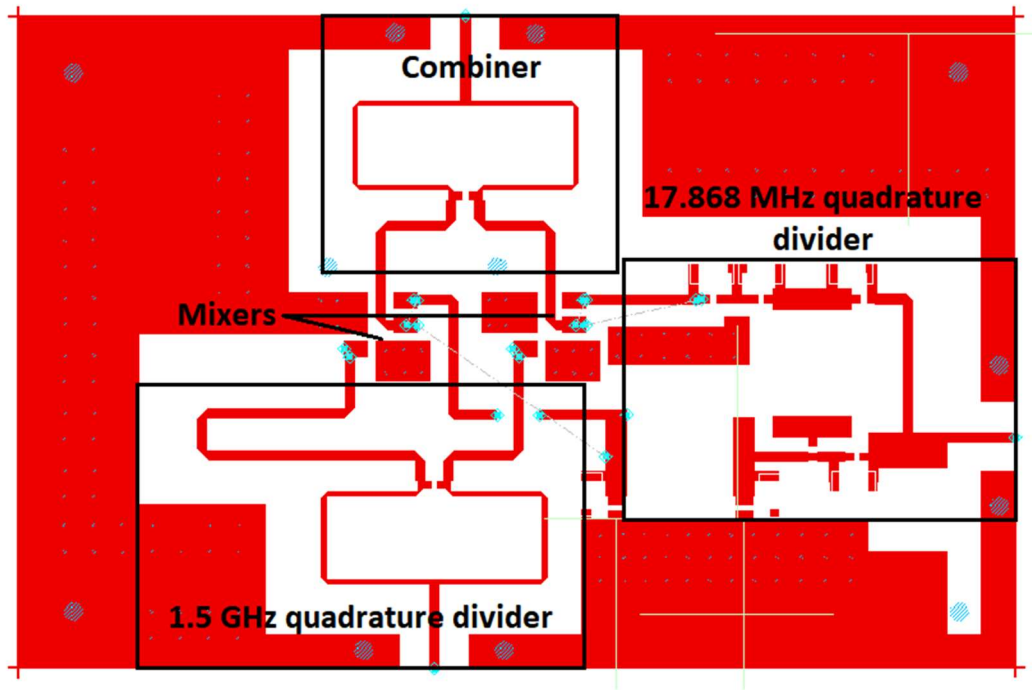


Figure 4-9: Complete Single Sideband Mixer layout.

Once the design of the mixer was completed in ADS, a harmonic balance simulation was conducted on the full circuit. This would give an indication of the amount of suppression of the unwanted sidebands. In order for the simulation to be as accurate as possible, the port isolation and conversion loss parameters of the mixers were inserted into the ADS mixer model (Figure 4-10).

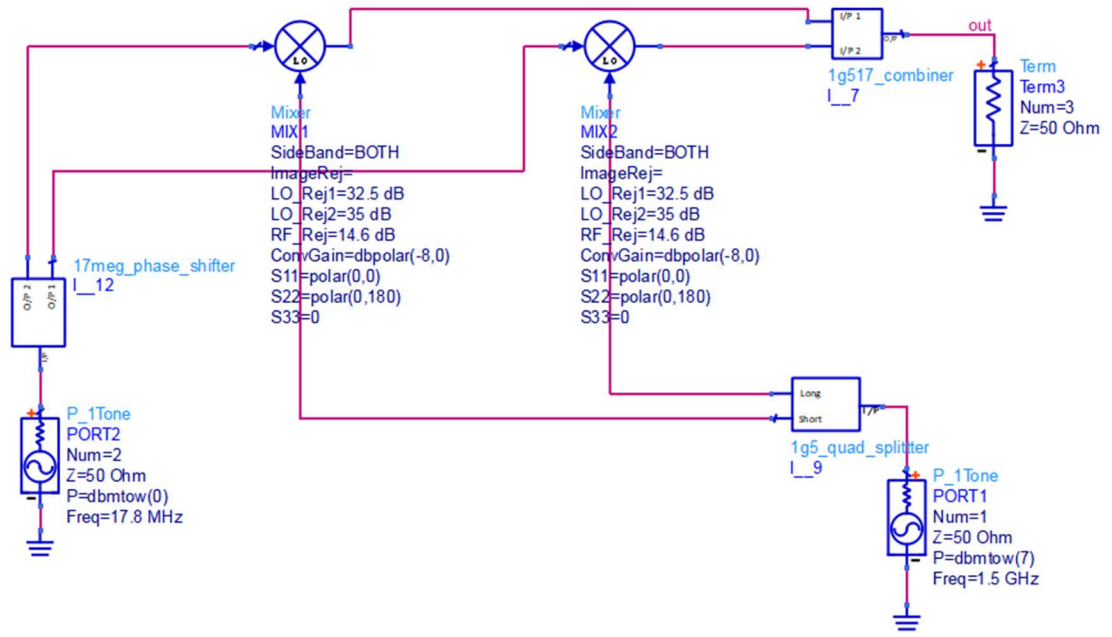


Figure 4-10: Single Sideband Mixer simulation schematic.

The result of the harmonic balance simulation is shown in Figure 4-11.

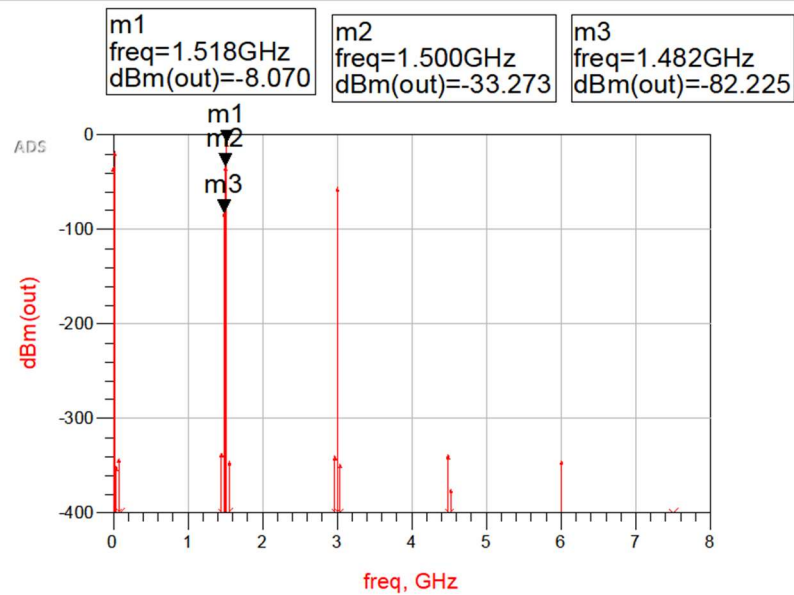


Figure 4-11: SSM harmonic balance simulation results.

It can be seen on the graph that the simulated upper sideband is at -8dBm, while the 1.5GHz carrier is suppressed about 25dB below it and the lower sideband is suppressed about 74dB lower. Even though there are also significant low frequency components (17.868MHz), they can be easily removed with a high pass filter. With the results of this simulation showing acceptable attenuation of the unwanted frequencies, the next step was to construct the circuit and test it. Figure 4-12 shows a photo of the completed Single Sideband Mixer circuit.

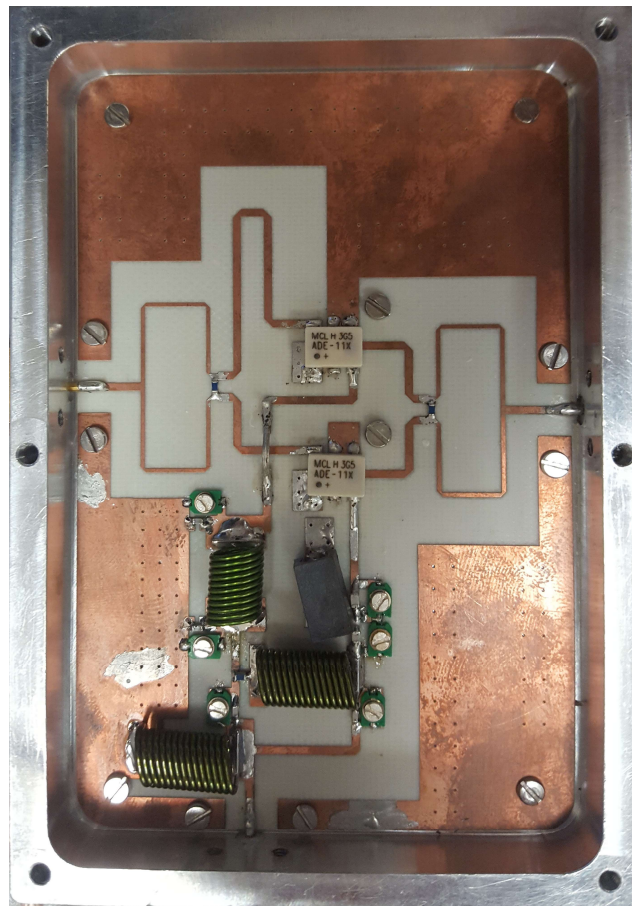


Figure 4-12: Photo of the completed SSM.

To test the mixer, the DDS was clocked by a 750 MHz signal and the microcontroller was used to program it for an output frequency of 17.866 MHz. The measured output of the DDS contained several harmonic components (resembling the spectrum of a square wave in the frequency domain), therefore a low pass filter with a cutoff frequency of 21.5 MHz was used to filter out the higher order harmonics. A low pass 1400 MHz filter was also used at the output of the SSM to remove the higher frequency components. The output was

then viewed on a spectrum analyser. Figure 4-13 shows a block diagram of the test configuration.

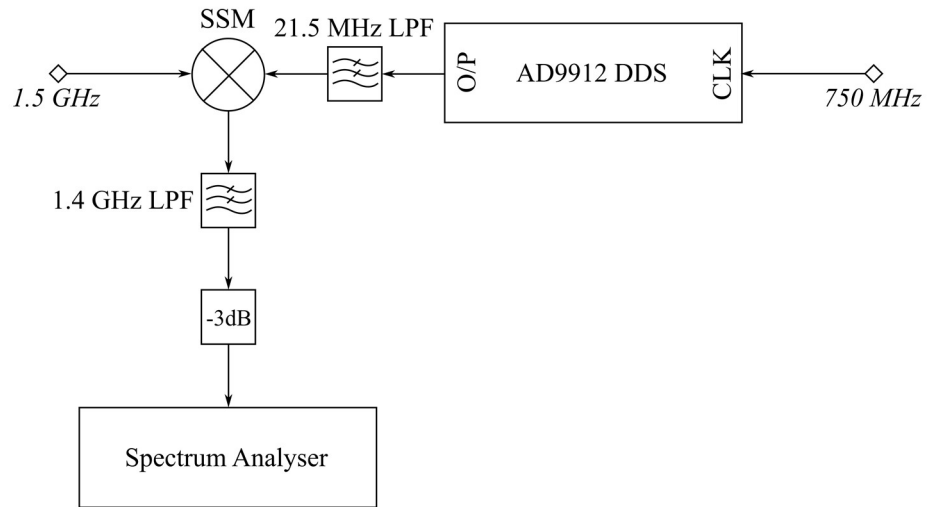


Figure 4-13: Block diagram of the SSM test configuration.

The trimmer capacitors were adjusted until the best possible performance was obtained (best suppression of the unwanted sidebands without affecting the upper sideband). Figure 4-14 shows the measured output spectrum over a span of 200 MHz with centre frequency of 1.5 GHz. Table 4-2 includes the frequency and power of the highest harmonics.

Table 4-2: Sidebands frequency and power from SSM measurement.

Frequency (GHz)	Power (dBm)	
1.5178	-12.83	1st Upper Sideband
1.5	-22	Centre Frequency
1.483	-66.5	1st Lower Sideband
1.4464	-50.17	3rd Lower Sideband
1.4643	-54.33	2nd Lower Sideband
1.5357	-58.5	2nd Upper Sideband
1.5536	-62	3rd Upper Sideband

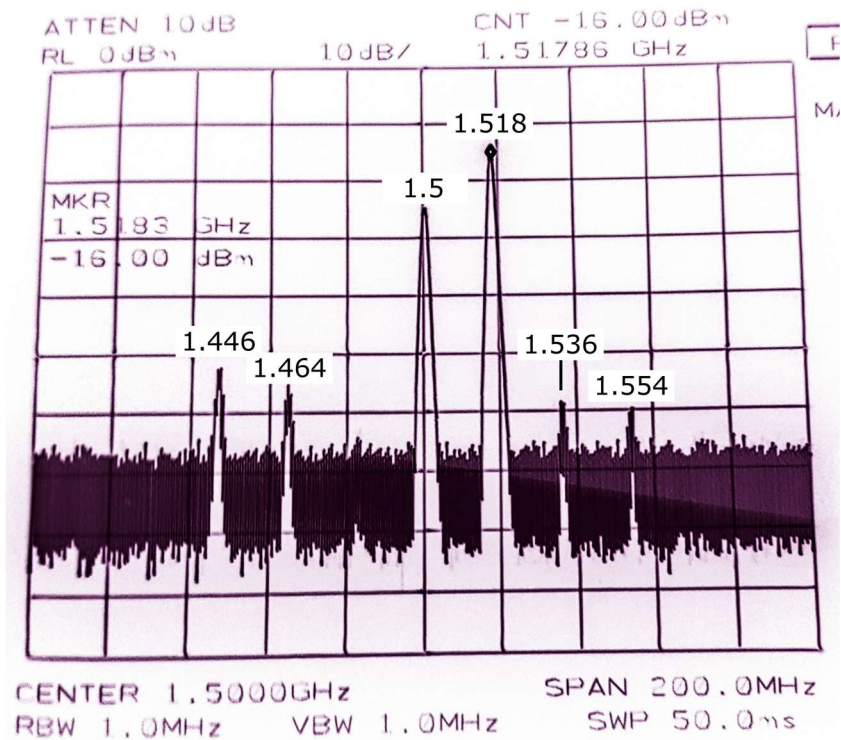


Figure 4-14: Output spectrum of the SSM mixer.

It can be seen, that although the lower sideband is very heavily suppressed, the 1.5 GHz RF frequency is still only about 9dB lower than the wanted upper sideband. There are also several higher order sidebands visible, but their amplitude is still more than 37dB lower than the wanted sideband. If the measured response is compared to the simulation, it can be seen, that the attenuation of the desired sideband is about 5dB higher than predicted (-12.83dBm from measurement and -8dBm from simulation), while the attenuation of the 1.5 GHz component is more than 10 dB lower (-22dBm from measurement and -33dBm from simulation). The high amplitude of the 1.5 GHz component can be attributed to the fact that the mixers being used are double balanced and the isolation between the RF and IF ports is only 14.6dB. It is possible that the suppression of this component can improve if triple balanced mixers (or mixers with higher isolation on all ports) are used. Another solution would be to filter out the undesired frequency by using a very narrow band notch filter.

Some feedthrough from the IF frequency (17.868 MHz) was also seen at the output of the SSM, but their amplitudes were relatively low and can be easily removed using a high pass filter. Table 4-3 shows the low frequency output components with the highest amplitude.

Table 4-3: SSM low frequency output harmonics.

Frequency (MHz)	Power (dBm)
17.87	-40.5
35.73	-53.17
53.63	-59

### 4.3 1.5 GHz Notch Filter

The desired 1.517GHz component at the output of the SSM needed to be filtered further before being used to modulate the laser and interrogate the atomic resonance. It was deemed that the power in the upper sideband (1.517GHz) should be at least 30dB higher than all the other components in the modulated spectrum. This requires that the LO feedthrough (1.5GHz) is suppressed by at least a further 20dB. Since the two signal components are in close proximity to each other, a notch filter with very narrow bandwidth had to be designed. To achieve this, a filter was designed incorporating microstrip  $\lambda/4$  impedance transformers and an open circuit coaxial stub. The stub structure resembles a coaxial cable, with a centre conductor surrounded by an outer (ground) conductor. The impedance of this stub is set by choosing the correct inner to outer diameter ratio. Since the dielectric medium between the two conductors is air, the dielectric constant is 1 and the dielectric losses negligible (Figure 4-17). This enables the resulting structure to have a Q of up to 3400 [66, pp. 163-168]. Figure 4-15 shows the schematic of the notch filter.

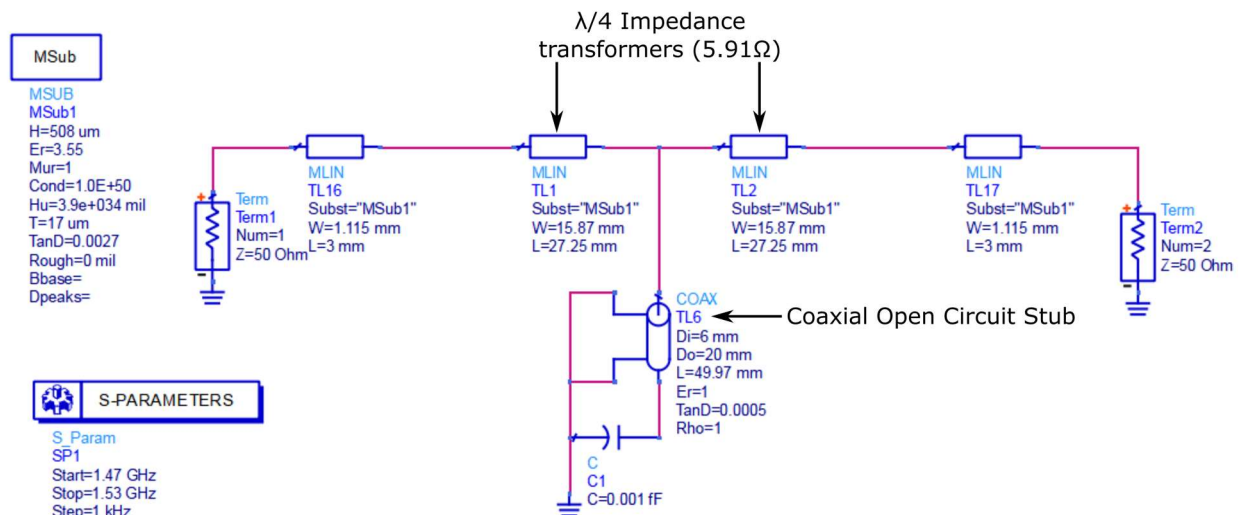


Figure 4-15: 1.5 GHz Notch filter schematic.

TL1 and TL2 are quarter wave impedance transformers. They are designed to transform the impedance from  $50\Omega$  down to  $0.7\Omega$ . Their impedance is therefore set to  $Z_{tr} = \sqrt{Z_0 \times 0.7} = 5.91\Omega$ . By transforming down to  $0.7\Omega$ , the effect of the stub's impedance on the filter's response is limited to a much narrower range of frequencies, therefore producing a narrower stop band notch. The coaxial stub TL6 is designed with inner diameter of 6mm, outer diameter of 20mm and length of 49.97mm ( $\lambda/2$ ). This makes the characteristic impedance  $72.2\Omega$ , which is close to the optimal impedance for highest Q factor [66, p. 167]. Figure 4-16 shows the S-parameter simulation of the filter.

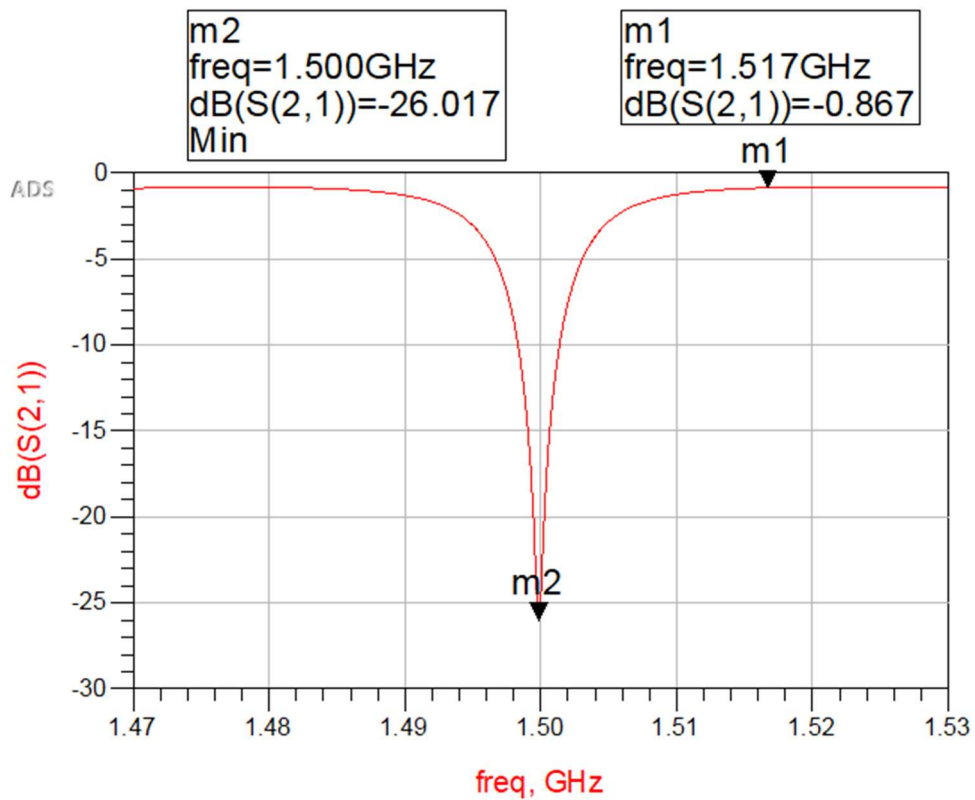


Figure 4-16: 1.5 GHz notch filter S-parameters simulation.

It can be seen from the graph that the filter provides attenuation of about -26dB at the 1.5 GHz frequency, while the attenuation at the desired 1.517868 GHz is about -1dB. The attenuation in the stop band is highly dependent on the copper and dielectric losses. The dielectric losses are minimal in this case (as it is air). The conductor losses  $a_c$  can be calculated using the equation in [66, p. 165].

$$a_c = 1.898 \times 10^{-4} \sqrt{e_r} \sqrt{f_{GC}} \left( \frac{1 + \frac{b}{d}}{b \times \ln \frac{b}{d}} \right) = 1.898 \times 10^{-4} \sqrt{1} \sqrt{1.5} \left( \frac{1 + \frac{0.020}{0.006}}{0.020 \ln \frac{0.020}{0.006}} \right)$$

$$= 0.0418 \text{ dB/m}$$

Where  $e_r = 1$  (dielectric constant of air)  $f_{GC}$  is the frequency in GHz (1.5 in this case),  $b$  and  $d$  are the diameters of the outer and inner conductors respectively.

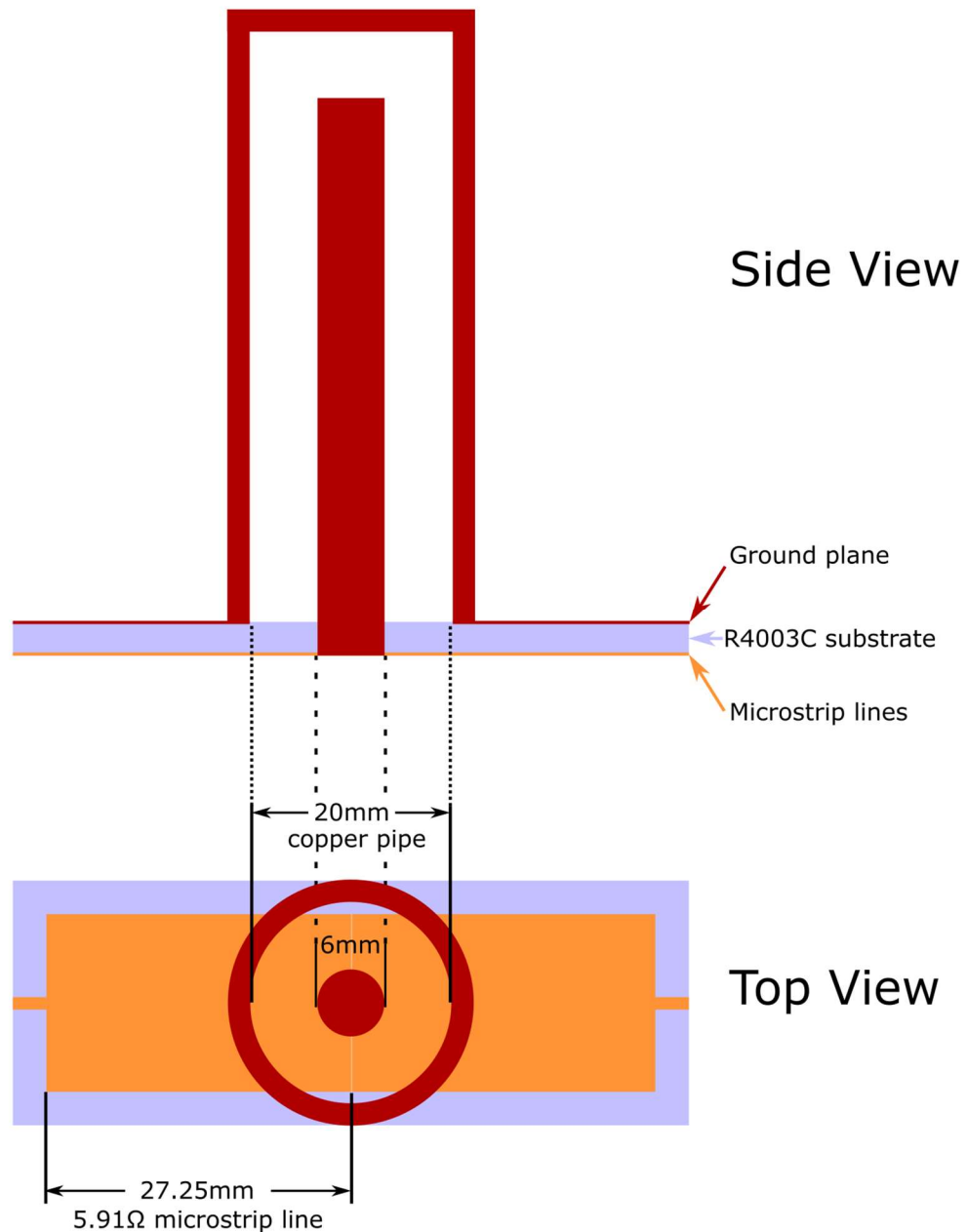


Figure 4-17: Sketch of the notch filter (side and top view).

Previously constructed notch filters at 956MHz have shown a measured response similar to this simulation result [67]. Further attenuation at the stop band or wider bandwidth can be achieved by connecting two of these filters together. Two filters were built using this configuration. A solid copper rod with 6mm diameter was chosen for the inner conductor of the stub and a copper pipe with 20mm inner diameter and 2mm thickness was chosen for the outer conductor.

Because the outer conductor needs to be connected to the ground plane, the inner rod needs to go through the substrate and be soldered to the microstrip lines. The outer pipe is then placed on top and soldered to the ground plane. Because of the large thermal mass of the components, the soldering was done on a hot plate. A cap for the outer conductor was machined out of copper and an M6 brass screw was inserted into it. This screw is used to adjust the capacitive coupling between the inner and outer conductor and fine tune the frequency of the notch. Once assembled, the structure was bolted onto an aluminium jig. A brass lid (that covers the microstrip lines) was made using the same technique used for making the crystal oscillator boxes. Figure 4-18 shows a photo of one of the completed notch filters.

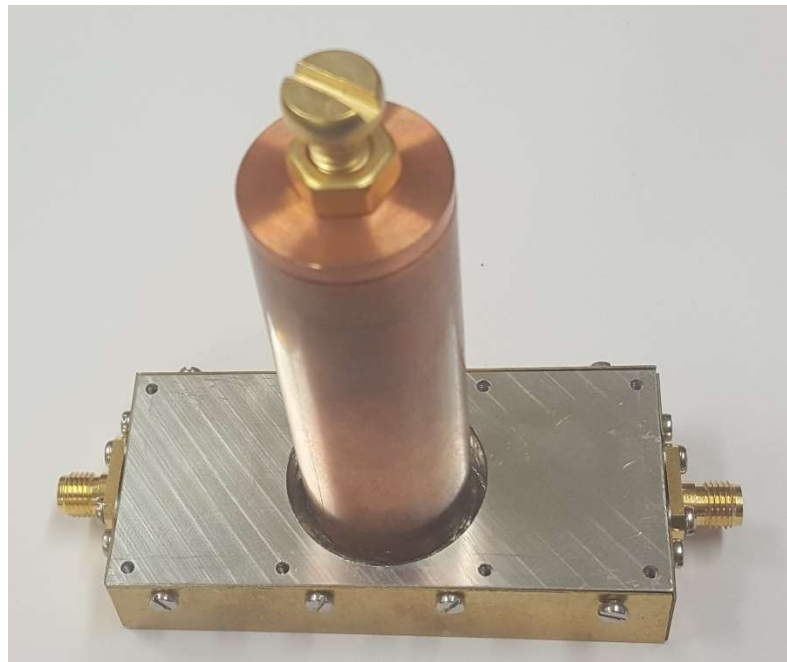


Figure 4-18: Photo of the notch filter.

The filter's frequency response was measured on the Anritsu 37377C network analyser. The frequency of the notch was adjusted to 1.5GHz using the screw. Figure 4-19 shows the measured response.

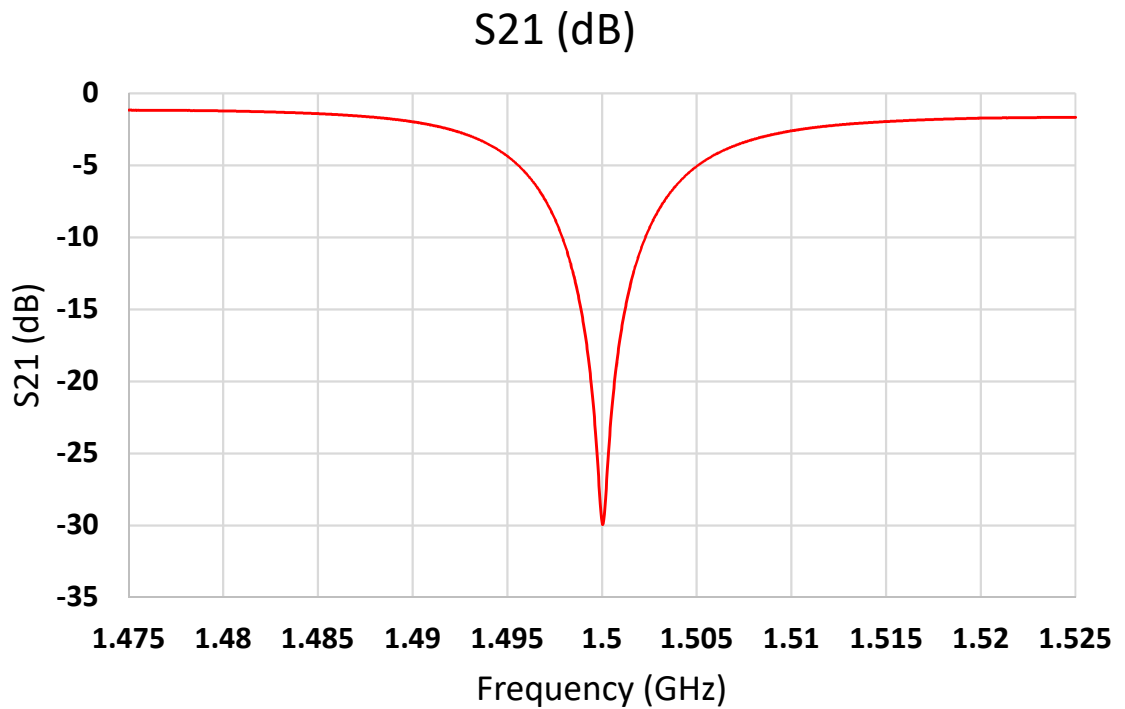


Figure 4-19: 1.5 GHz notch filter measured frequency response.

The attenuation at the centre of the notch is about 30dB, which is 4dB higher than predicted in the simulation. The reason could be that the conductor losses were slightly overestimated or the structure was not modelled completely accurately. The insertion loss at  $\pm 17.9$  MHz away from the notch was measured at about 1.5dB.

The filter was then inserted at the output of the single sideband mixer of the configuration in Figure 4-13 and the output spectrum was viewed again on the spectrum analyser. After some initial fine tuning of the notch frequency, the 1.5 GHz LO feedthrough was suppressed by about 30dB further, while the effect on the wanted sideband was minimal. Figure 4-20 shows the measured spectrum. This spectrum was deemed satisfactory at this point to be used to modulate the laser in the physics package configuration.

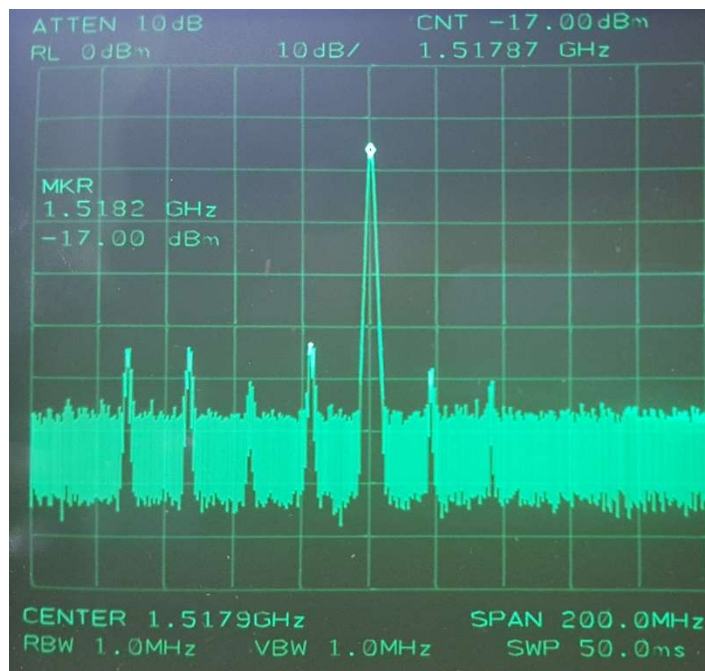


Figure 4-20: SSM output spectrum filtered using notch filter.

#### 4.4 Summary

A Direct Digital Synthesizer was clocked using the local oscillator configuration described in chapter 3. A PIC microcontroller was programmed and used to initialize the DDS on start-up and continuously feed data to adjust the output frequency and apply a sweep or modulation. The DDS was used to generate the 17.866 MHz offset frequency, which is needed to upconvert the 1.5 GHz DRO output to the hyperfine transition frequency of  $^{85}\text{Rb}$ . A Single Sideband Mixer (SSM) was designed and built to achieve this upconversion. The SSM incorporates two double balanced mixers, as well as lumped element and microstrip quadrature Wilkinson dividers. The 1.5 GHz and 17.866 MHz signals were mixed in phase and in quadrature to produce an output spectrum in which the lower sideband is heavily suppressed. A high-Q notch filter was then designed and built to further suppress the LO feedthrough at the output of the mixer. With the filter included in the synthesis configuration, the output spectrum was deemed sufficiently “clean” to be used in the physics package configuration to interrogate the Rb resonance, as the desired sideband was more than 30dB higher than the unwanted frequency components. This completes the design and construction of the frequency synthesizer of the atomic clock.

## 5 PHYSICS PACKAGE.

Perhaps the most important part of the atomic clock, the physics package is where the hyperfine transition frequency of the Rb atoms is detected and used as a frequency discriminator to lock the local oscillator. This part is responsible for the long-term frequency stability of the system. Although the atomic resonance is used as the ultra-stable reference, there are multiple factors that can degrade its stability, as described in section 2.4. It is therefore crucial to design a physics package configuration in which all of the important parameters are closely controlled, noise is minimized and there is sufficient screening from spurious environmental effects. This project was started with the goal to produce a physics package from first principles, although parts from other experiments or malfunctioned commercial atomic clocks were used in the initial tests. The physics package assembly has gone through three different iterations from the start of the project. The first prototype was used to experiment with the basic principles of operation of an atomic clock. The second iteration was designed with emphasis on using more compact vapour cells and optical components. The third version was built as a compact, integrated unit with emphasis on optimal resonance detection and mechanical robustness. Each successive version offered improvements and the ability to investigate different principles of the operation. This section describes the process of constructing these packages and the experiments and measurements that were conducted.

### 5.1 Initial CPT Experimental Setup.

The method of detecting the Rb hyperfine resonance selected for this project is the Coherent Population Trapping (CPT) method described in section 1.1.1.2. This method uses a laser modulated at half the hyperfine transition frequency. The resulting optical sidebands are then tuned to the Rb D1 or D2 absorption lines and the frequency of the RF modulation is swept until the resonance peak is detected. A block diagram of the CPT configuration used in this work is shown in Figure 5-1. A Vertical Cavity Surface Emitting Laser (VCSEL) is used as the coherent light source. The laser's operating current is supplied by a constant current source and its temperature is stabilized at about 50°C. The RF modulation signal from the local oscillator is added to the laser DC current using a broadband bias tee. A beam splitter is used to divert a portion of the emitted light to a

Fabry-Perot spectrometer, which is used to monitor the laser spectrum and modulation index. A quarter wave plate is used to circularly polarize the light, which is required for detecting the hyperfine resonance. The Rb vapour cell is placed in mu-metal shielding and also temperature stabilized. A solenoid is used to produce a small uniform magnetic field inside the cell and align the Rb atoms dipole moment for correct excitation. A photodiode and transimpedance amplifier are used at the end of the configuration to detect the light transmitted through the cell.

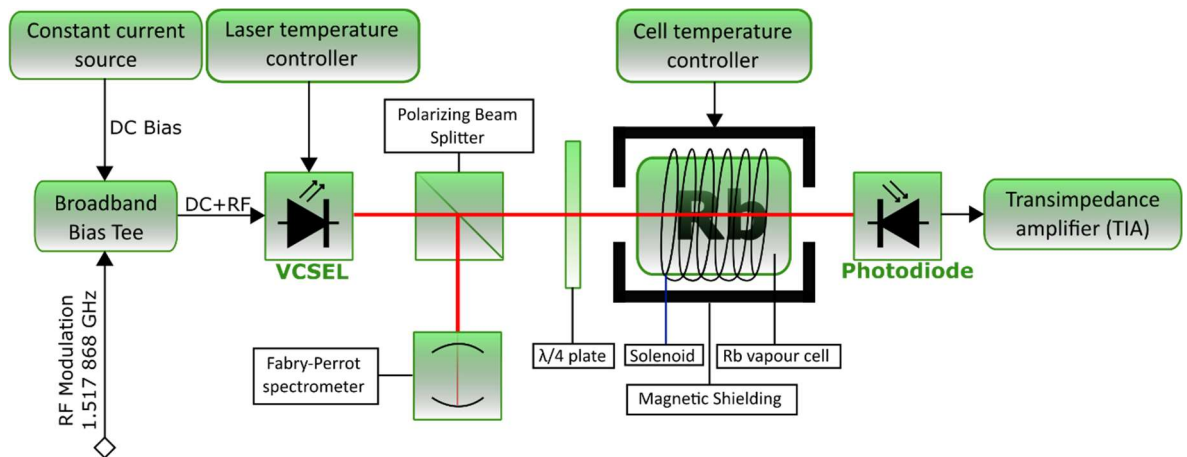


Figure 5-1: Rb CPT physics package block diagram.

The first Rb Coherent Population Trapping (CPT) experimental setup was built using an atomic spectroscopy kit borrowed from the department of physics of the university of York. The kit included a quarter wave plate, a water heated Rb vapour cell and a large area photodiode (Figure 5-2).

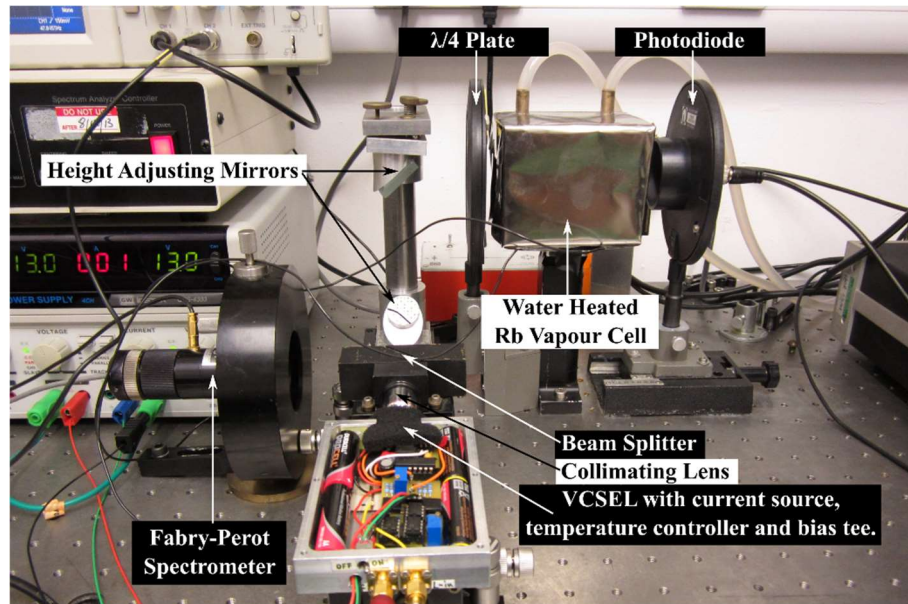


Figure 5-2: Initial Rb CPT experiment setup (version 1).

The vapour cell was modified with a solenoid and magnetic shield. Since the optical mounts used in the physics experiment were higher than the ones used for the laser, the beam height had to be adjusted using a pair of mirrors. The VCSEL, provided by Oclaro Inc., was placed inside an aluminium box along with the battery power supply, current source and bias tee circuits. At the specified operating current and temperature, the wavelength of the laser is about 795nm, which corresponds to the Rb D1 excitation line. An RF signal generator was used to modulate the laser at the time. It must be noted that the construction of this setup began during the course of a BEng project [68]. This setup was used to experimentally investigate some of the basic aspects of the operation of the physics package. However, since the goal of the project is to produce a compact physics package, the cell was soon replaced with a 25x25mm vapour cell extracted from a broken Quartzlock atomic clock. A custom made metal enclosure and temperature controller were designed for the cell. This eliminated the need to use the optical mounts from the physics experiments, so a new polarizing beam splitter and quarter wave plate were purchased from Thorlabs. Custom made optical mounts were designed and manufactured for these components. The photodiode was also replaced with a smaller, better screened one. Figure 5-3 shows a photo of the improved experimental setup (version 2). In this section, the design of the key components and electronic circuits used in this configuration are described.

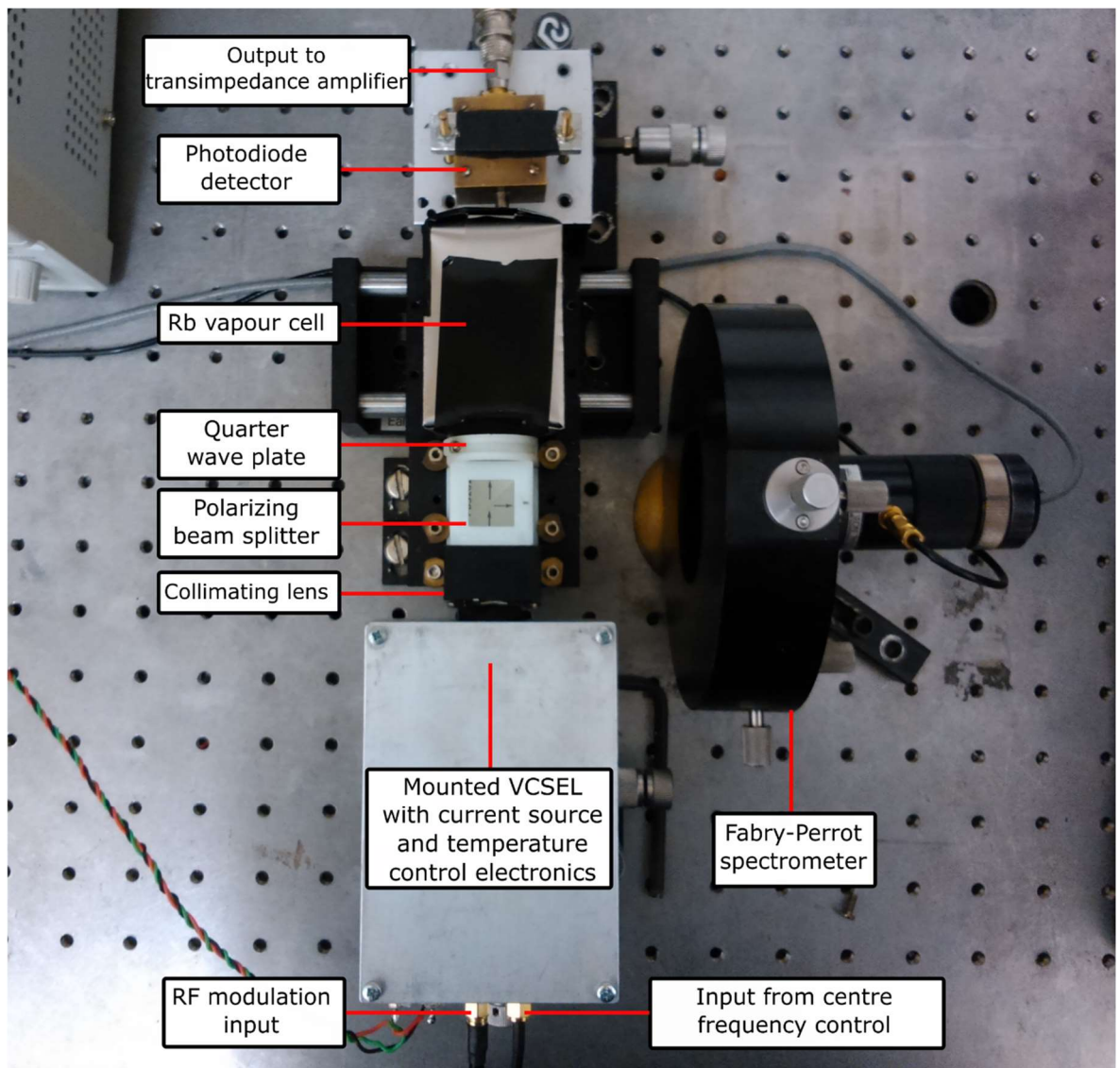


Figure 5-3: Improved CPT experimental setup (version 2).

### 5.1.1 Constant Current Source.

A battery operated current source was designed that provides a constant current through the laser, independent to any change in the load's impedance and with low temperature coefficient. The design of the current source is based on a simplified version of the circuit described in [69]. Low noise operational amplifiers, voltage regulators and transistors were used in the design in a configuration that requires as few resistors as possible, in order to keep the noise to a minimum. The circuit was then placed in an aluminium box for better screening. Figure 5-28 shows a schematic of the current source.



The ADR445 is a low noise voltage regulator with an output of 5V. It also has the capability to source up to 10mA of current. It is used to give a low noise voltage supply to the op-amps and the transistor. The LTC6652 is another low noise voltage regulator, which takes its input from the ADR445 and gives a 2.5V output, which is used as a reference to the first op amp (OP27A). These op amps were chosen for their low noise, low offset and drift characteristics. The first op-amp is in an inverting summing configuration with a gain of 1. It takes an input from the 2.5V regulator and from an external pin (VIN), which goes through two low-pass RC filters. The second op-amp along with the transistor makes the voltage to current conversion. The PNP transistor is one of a super-matched pair, the SSM2220. It was chosen because of its very low input voltage noise (1nV/√Hz at 100Hz). When a voltage is applied to the positive input of the op amp (U2), the amplifier's output will increase the current through the transistor (and effectively through the VCSEL) until the negative input has a voltage equal to the one on the positive input. The fixed resistor R5 is used to limit the maximum current going through the laser. The potentiometer RV1 is used to adjust that current if necessary. When the circuit is enabled there may be some transient effects that can produce a spike in voltage and damage the laser. This is why the switch SW1 was included to ground the collector until these transients have passed and the laser can be enabled. Because of the feedback mechanism and the voltage regulators used in the current source, this circuit has a low temperature coefficient (about 60nA/°C for VCSEL current of 1.8mA) and is practically independent of changes in the VCSEL's impedance.

### 5.1.2 Laser Temperature Controller.

The wavelength of the laser is affected not only by its injection current, but also by its temperature. At a constant current of about 1.8mA, the VCSEL needs to be operated at a temperature of about 50°C, in order to tune to the Rb D1 absorption line. The temperature also needs to be as stable as possible to minimize the changes in the hyperfine resonance's frequency due to light shift effects. The laser was therefore mounted on an aluminium plate along with two heating elements, a power resistor and a transistor. Passing current through these two components causes the dissipated power to increase the temperature of the

mount and by extension of the laser. The VCSEL itself is packaged with a 20k $\Omega$  thermistor, which is used as the temperature sensor. A PID controller was built that detects the voltage drop across the thermistor and regulates the current through the heating elements. After the VCSEL was wrapped in insulating foam it was placed along with the PID controller in the same box as the current source (Figure 5-5).

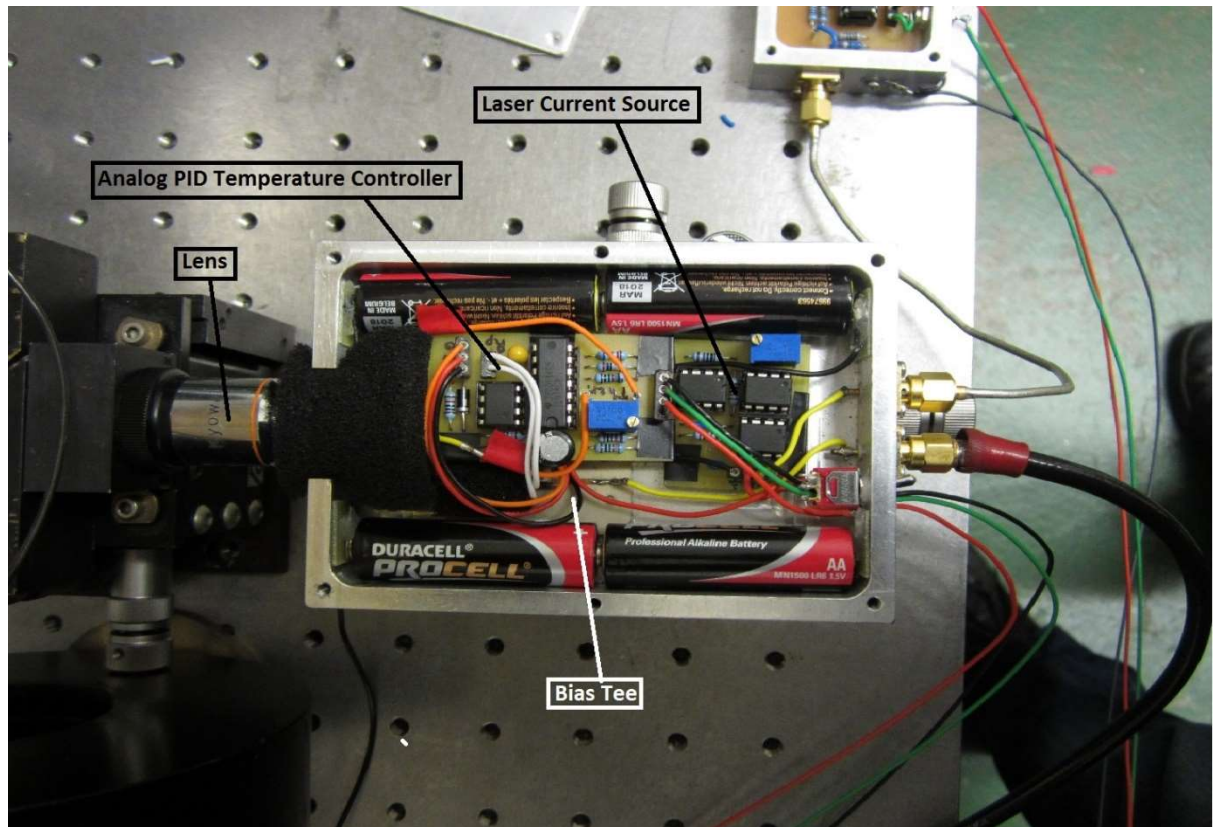


Figure 5-5: Aluminium box containing VCSEL, temperature PID controller, current source and Bias Tee (physics package version 2).

Figure 5-5 also shows the location of the bias tee. This is the component that combines the RF modulation signal with the DC driving current for the laser. The lens in front of the laser is required to collimate the beam, as VCSELS have a relatively high divergence angle. The batteries for the current source are included in the box as well.

### 5.1.3 Vapour Cell.

The vapour cell also needs to be temperature stabilized at about 50-60°C. The temperature controller for it is similar to the one used with the laser, but optimised for the larger thermal mass of the cell. The solenoid used to generate the magnetic field required for CPT resonance is made by winding a thin wire around the walls of the cell. The solenoid along with the cell are inserted into an especially machined metal enclosure to which the heating elements were attached (Figure 5-6). The whole assembly is insulated and covered by two layers of mu-metal foil for shielding against spurious magnetic fields. The two layers were thought to be a reasonable compromise for providing sufficient screening and not increasing the volume of the assembly too much.

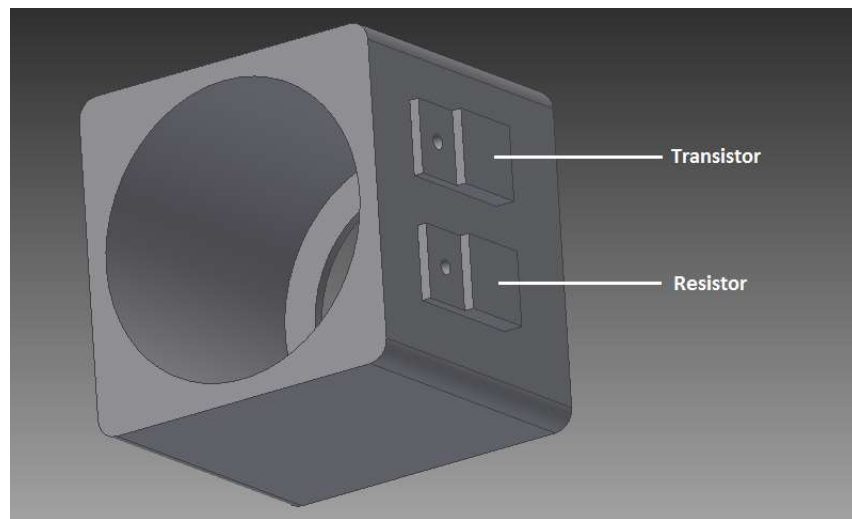


Figure 5-6: Metal enclosure for the vapour cell.

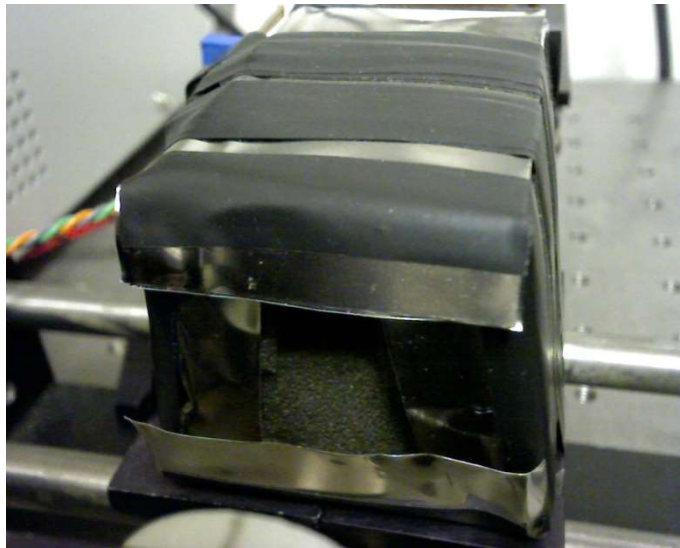


Figure 5-7: Vapour cell with insulation and mu-metal shield.

#### 5.1.4 Quarter wave plate and Polarising Beam Splitter (PBS).

The polarizing beam splitter and quarter wave plate are required to polarize the beam correctly to achieve CPT resonances. The beam splitter also sends a portion of the beam to the Fabry-Perot spectrometer, which is used to display the laser's spectrum on an oscilloscope. A rotating mount was designed in Autodesk Inventor and 3D printed for the wave plate with a scale of the angle of rotation. Another mount was also printed for the PBS (Figure 5-8).

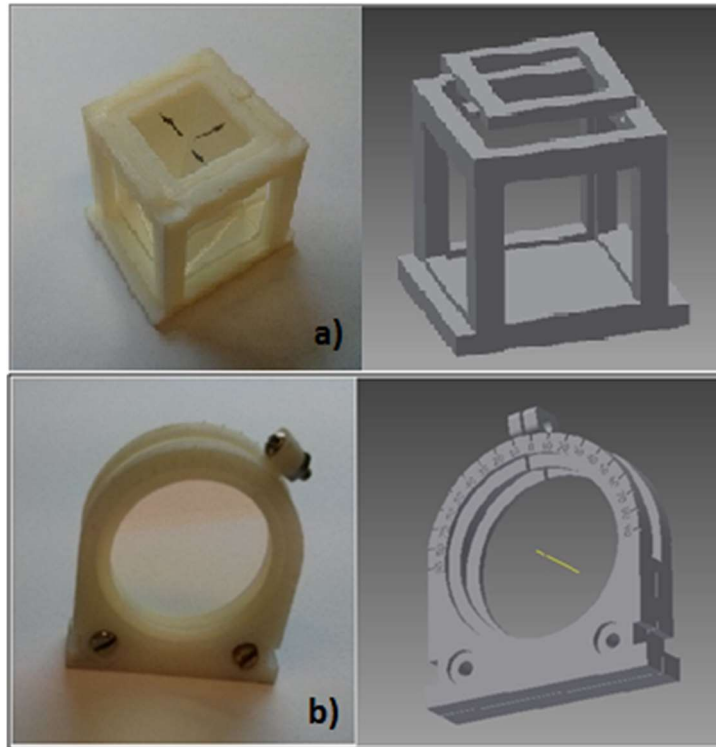


Figure 5-8: Mounts for a) Polarising Beam Splitter and b) Quarter wave plate.

#### 5.1.5 Photodiode and Transimpedance Amplifier.

The physics package is completed by the inclusion of the photodiode. This is used to detect the Rb absorption spectrum and hyperfine resonances. A small area photodiode was initially chosen, because of the lower dark current and shot noise, but was replaced by a larger area one in order to detect as much of the laser light as possible, effectively increasing the signal to noise ratio. The transimpedance amplifier used was a low noise Stanford Research Systems model SR570.

### 5.1.6 RF Signal Generator.

An RF signal generator was initially used to provide the modulation signal to the laser. The Rohde & Schwartz SMB100A has the capability to internally modulate the RF signal output using a low frequency sine wave. It also has the capability to modulate the RF signal's frequency using an external signal into the Mod Ext input. These modulation options were used to detect the hyperfine resonance.

## 5.2 Initial Experiments.

Some initial experimental tests and measurements were conducted using the experimental configuration described in section 5.1. These include:

1. Measuring the current source noise density spectrum.
2. Tuning the laser wavelength to the Rb D1 absorption line.
3. Modulating the laser at 1.517866GHz using the RF signal generator and monitoring the modulation index on the Fabry-Perot spectrometer.
4. Detecting the hyperfine resonance of  $^{85}\text{Rb}$ .
5. Investigating the effects of the laser modulation power, cell temperature and magnetic field intensity on the linewidth and amplitude of the hyperfine resonance.

Some initial attempts were also made to lock the RF signal generator to the atomic resonance, but the stability was compromised by several factors, which were addressed in the following improved design of the physics package.

### 5.2.1 Current Source Noise

The tuning coefficients of the VCSEL with injection current and temperature were previously measured by the author in [68]. It was found that the laser wavelength changes by 101.26 GHz/mA of current and 36.18 GHz/°C. This means that noise in the laser current source can induce changes in its frequency, which can widen the laser linewidth (specified at 30 MHz by the manufacturer) and degrade the stability of the atomic resonance due to light shift effects. The current noise spectral density of the laser current source was calculated using the operational amplifier and transistor noise models described

in [70] and [71]. The theoretical current noise density at 10Hz was calculated at about  $850 \text{ pA}/\sqrt{\text{Hz}}$ . The noise was then measured by plugging the current source directly into the SR570 low noise transimpedance amplifier. The sensitivity of the TIA was set to  $1 \mu\text{A}/\text{V}$ . At this setting, the bandwidth of the amplifier is about 2kHz. At higher sensitivity settings the bandwidth drops significantly, which can filter out the noise under measurement. The output of the TIA was measured on the HP3561A dynamic signal analyser in spectral density mode. The resolution bandwidth was reduced to about 1mHz and the noise was recorded at several key frequencies. Figure 5-9 shows the measured noise density curve and Figure 5-9 shows the tabulated data.

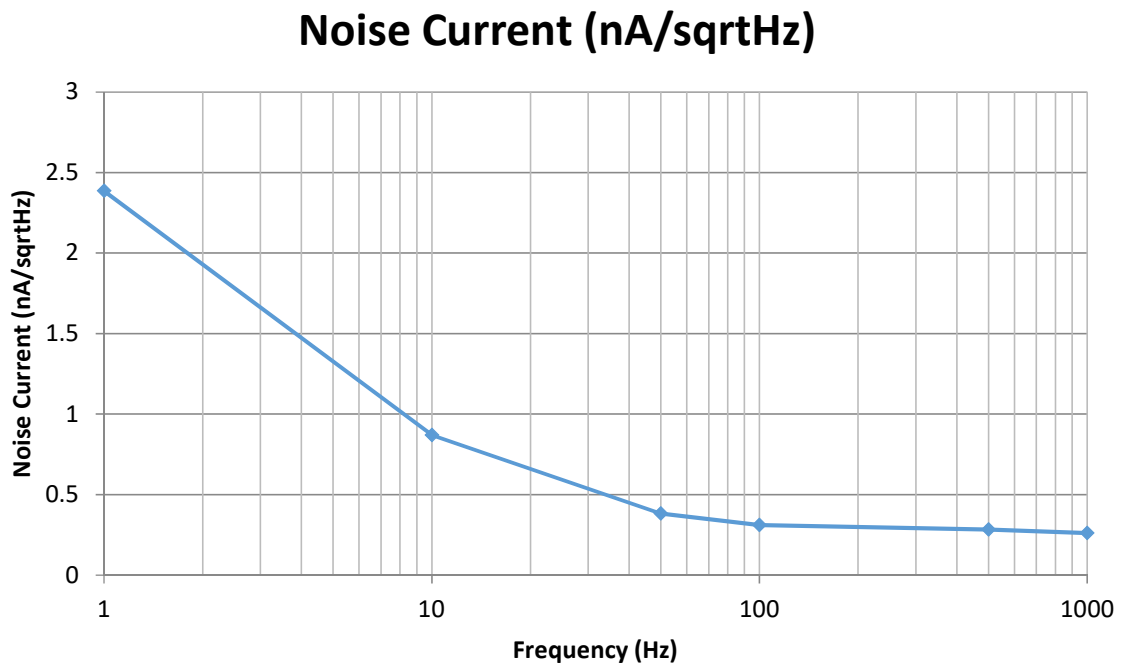


Figure 5-9: Measured laser current source noise density.

Table 5-1: Measured laser current source noise density.

<b>f(Hz)</b>	<b>Noise Current (nA/sqrtHz)</b>
1	2.386
10	0.869
50	0.382
100	0.311
500	0.283
1000	0.261

The current noise at 10Hz was measured at 869pA/sqrtHz. This is fairly close to the calculated value. Since the laser's frequency tuning with injection current is about 101GHz/mA, a current noise of 1nA can cause detuning by about 101kHz, which is less than the laser's specified linewidth, so the performance of the current source was deemed acceptable at this stage.

### 5.2.2 Rb D1 Line Absorption Spectrum

The VCSEL was supplied with about 1.8mA of current and temperature stabilized to about 47°C. The polarizing beam splitter and quarter wave plate were used to circularly polarize the laser beam. The vapour cell was temperature stabilized around 50°C and a small current was supplied through the solenoid to produce a magnetic field of about 50μT. The temperature of the laser was then increased and the output of the photodiode detector was monitored on an oscilloscope. The temperature increase caused the wavelength of the laser to sweep through the Rb transition frequencies and the Rb absorption spectrum was observed on the oscilloscope. This measurement is useful for determining the isotope mixture in the vapour cell and finding the correct laser temperature for tuning to the Rubidium absorption spectrum. The measurement is shown in Figure 5-10.

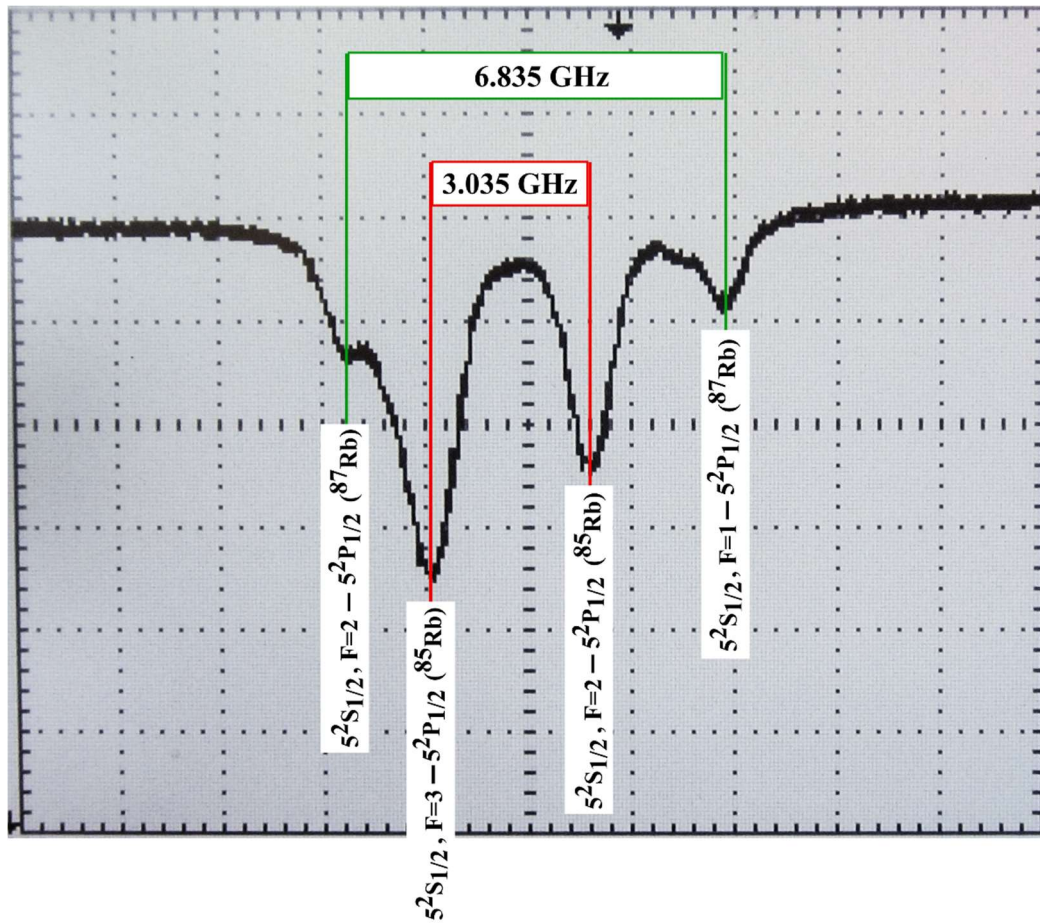


Figure 5-10: Measured Rb absorption spectrum (D1 excitation lines).

When the cell was originally incorporated into the physics package it was unclear what its exact composition was. It can be seen from the spectrum measurement, that the cell contains a natural mixture of Rubidium isotopes (72% of  $^{85}\text{Rb}$  and 28% of  $^{87}\text{Rb}$ ), since the absorption dips corresponding to the  $^{85}\text{Rb}$  transitions are about 2.5-3 times larger than the ones of the  $^{87}\text{Rb}$ . Having detected the absorption lines, the laser was temperature stabilized to the middle of this spectrum. It must be noted that the laser was not modulated in this case, as that would produce a more complex absorption spectrum, which is the result of the superimposed spectra of the carrier and both sidebands of the laser. Figure 5-11 shows an example of the absorption spectrum detected when the laser was modulated at 3.417 GHz.

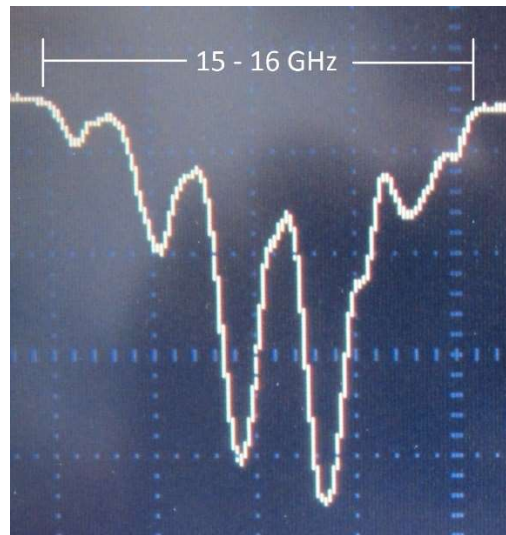


Figure 5-11: Absorption spectrum of Rb detected with laser modulated at 3.417 GHz.

### 5.2.3 Laser Modulation and Sidebands.

The laser is modulated by combining the RF signal from the local oscillator with the DC injection current, using a TCBT-14+ wideband bias tee from Mini-Circuits. The spectrum of the laser was monitored using a Burleigh SA200 Fabry-Perot spectrometer with a free spectral range of 8 GHz and finesse of about 200. The finesse of an optical cavity is defined as the ratio between the free spectral range and the minimum linewidth of its resonances. This means that the Fabry-Perot can measure resonance linewidths of 40MHz or higher. The R&S SMB 100A signal generator was used as a local oscillator in this case. The RF frequency was set to 1.517866 GHz and the output power was slowly increased until the laser spectrum consisted of a carrier and two equal amplitude optical sidebands. Figure 5-12 shows the measured laser spectrum with the applied modulation.

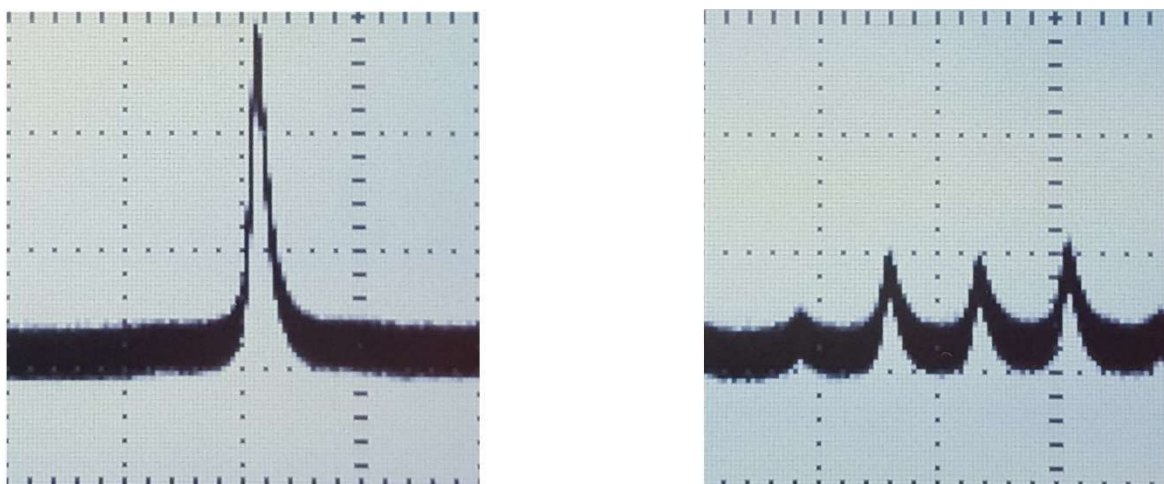


Figure 5-12: Laser optical spectrum without modulation (left) and with modulation at 1.517866 GHz (right).

The peaks in the laser spectrum are not perfectly symmetrical, because the Fabry-Perot cavity was slightly misaligned to avoid reflections back into the laser. The RF power required to produce first order sidebands equal to the carrier in the initial experiments was about -11.5dBm. This was due to the poor coupling of the RF signal into the bias tee and the laser. This issue was addressed in the later improvements of the physics package and the required RF power was significantly reduced. Higher order sidebands can also be seen and their amplitude increases as the RF power is increased.

#### 5.2.4 Detecting the $^{85}\text{Rb}$ Hyperfine Resonance.

The spacing between the two first order laser sidebands in Figure 5-12 is 3.035732 GHz, which is the splitting frequency between the ground hyperfine levels of  $^{85}\text{Rb}$ . In order to achieve Coherent Population Trapping and detect the atomic resonance, the laser centre frequency was tuned to the middle of the Rb absorption, such as the sidebands simultaneously excite both  $^{85}\text{Rb}$  transitions. The correct polarization, cell temperature and magnetic field conditions were also applied (as in section 5.2.2). The modulation frequency was then swept over a range of 10kHz, using the modulation option of the RF signal generator. When the hyperfine splitting frequency is exactly matched (within a range of a few hundred hertz), the atoms enter the coherent superposition state and a slight increase (peak) in the transmitted light is observed. The measured CPT resonance is shown in Figure 5-13.

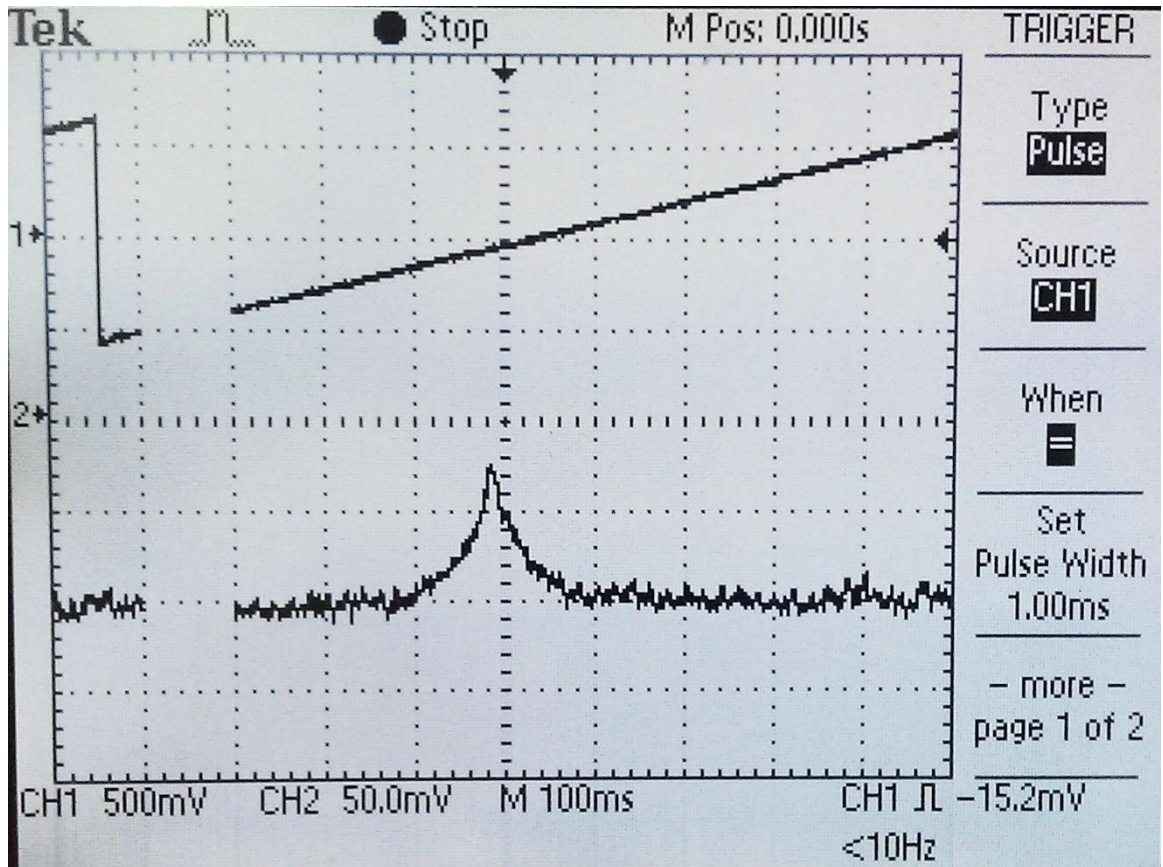


Figure 5-13:  $^{85}\text{Rb}$  CPT resonance. Channel 1 is the is the ramp signal used to sweep the RF modulation frequency.

The full width at half maximum (FWHM) of the detected resonance was about 800 Hz. Therefore, it can be deduced knowing the cell dimensions (25x25mm), that the cell contains some form of buffer gas, however the exact mixture and whether it has been optimised for a minimal temperature coefficient is unknown. In the future improvements of the physics package this issue is also addressed.

Having detected the hyperfine resonance, some further investigations were conducted on the parameters that affect its shape and frequency stability. These include:

1. Effects of magnetic field intensity.
2. Effects of the magnetic field polarity and laser light polarization.
3. Effects of the laser modulation index, cell temperature and magnetic field intensity on the FWHM and amplitude of the resonance.

### 5.2.5 Effects of magnetic field intensity

The effects of changes in the magnetic field intensity through the Rb vapour cell were investigated. The dimensions of the cell used at the time of this experiment only allowed for a solenoid with up to 11 turns to be constructed around it (mainly because of the shape of the cell's mount and the thickness of the wire). This means that a relatively large change in current was required in order to change the magnetic field noticeably. The current through the solenoid was then varied in several small steps and the shift of the CPT peak was recorded. The approximate magnetic field flux density was then calculated using a simplified solenoid formula:

$$B = \mu_0 \frac{NI}{l}$$

Where “ $\mu_0$ ” is the magnetic permeability, “N” is the number of turns, “I” is the current flowing through the solenoid and “l” is the length of the solenoid. Table 5-2 shows the recorded data [72].

Table 5-2: Hyperfine shift vs. Magnetic Field and solenoid current.

Hyperfine Shift (Hz)	Current (mA)	Magnetic Field (uT)
0	101	26.85
4	120	31.9
14	145	38.545
21	173	45.99
29	195	51.836
45	225	59.81
59	254	67.52
65	266	70.71
81	287	76.29
95	329	87.46
132	357	94.9
Starting RF frequency: 1.517 868 612 GHz		
$\lambda/4$ plate at 45° left (best contrast)		
Vapour temperature: 55°C		
RF modulation power: -15.20dBm		

Figure 5-14 shows that for the measured values, the curve remains reasonably linear. Further values were not measured at this point, because of the high current required to obtain them.

### Hyperfine Shift vs. Magnetic Field

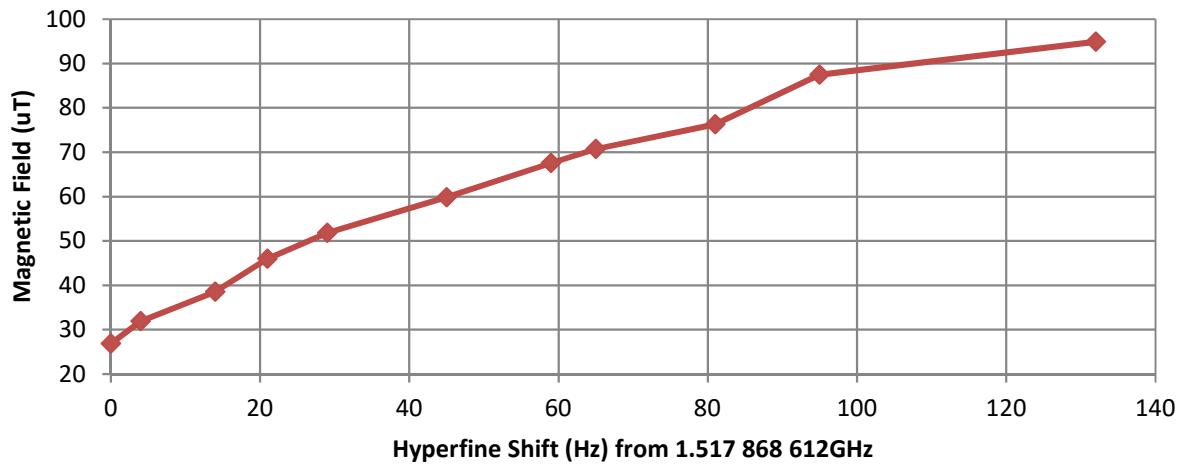


Figure 5-14: Hyperfine shift vs. Magnetic Field.

Although the changes in hyperfine frequency seem small, they can significantly degrade the system's stability if spurious magnetic fields or noise into the solenoid current are present.

#### 5.2.6 Effects of magnetic field polarity and laser beam polarization

As described in section 2.1.3, different Zeeman sublevels interact with different polarizations of the laser beam, producing multiple resonances. It was therefore deemed necessary to conduct some measurements with different polarizations and obtain a better understanding of these phenomena. The same setup was used as in the case of simple hyperfine resonance detection (section 5.2.4). This time, however, the RF frequency was swept through a much wider range (1 MHz) in order to detect all the Zeeman resonances between the ground hyperfine states of  $^{85}\text{Rb}$ . By rotating the quarter wave plate, it was possible to switch between plain, elliptical, left circular or right circular polarized light and observe the effects on the oscilloscope. The intensity and direction of the magnetic field through the cell was also altered using a potentiometer.

Figure 5-15 a) shows the resonances with left circular polarized light and magnetic field of approximately 10uT (calculated using the dimensions of the solenoid and the 4mA current) applied in the same direction as the beam. There are multiple peaks that correspond to resonances caused by the different Zeeman sublevels (refer to Figure 2-3). It is noticeable that the resonances on the left side have the highest amplitude. If the polarization of the light is changed to right circular, it can be seen that the resonances on the right side now have the highest amplitude (Figure 5-15 b). Reversing the magnetic field, instead, also makes the resonances to the right side stronger, although it does not appear equivalent to changing the polarization (Figure 5-15 c). If the magnetic field intensity is increased to about 50uT (20mA of solenoid current), the resonances shift further apart from each other (Figure 5-15 e). This is expected, because of the nature of the Zeeman sublevels and their dependency on magnetic fields. It is also seen that the middle resonance remains relatively in the same position and appears to have the highest amplitude at higher magnetic field intensity. This is the resonance that was detected in the initial experiments (shown in Figure 5-13). If the light is changed to plain polarized, the resonances practically disappear (Figure 5-15 g). Although plain polarized light can be considered as the combination of left and right circular polarized, it appears that it does not have the same effect on the

hyperfine resonances. The reason may be that the interaction occurs with the same group of atoms, since there is a single beam and the light cannot transfer its angular momentum to the free electrons, because the left and right circular components are equal and cancel each other out. It is possible that if two beams are co-propagated in parallel, so they interact with different groups of atoms, waveforms like the ones in Figure 5-15 a) and b) can be detected at the same time. Decreasing the solenoid current to 0 makes the resonances group close together. It is important to note that even with 0 solenoid current, there is still magnetic field inside the cell, since it is not completely surrounded by the magnetic shield, which cannot provide absolute insulation.

The fact that the middle resonance does not shift as much with magnetic field is an advantage, since the clock needs to have the lowest possible sensitivity to external factors.

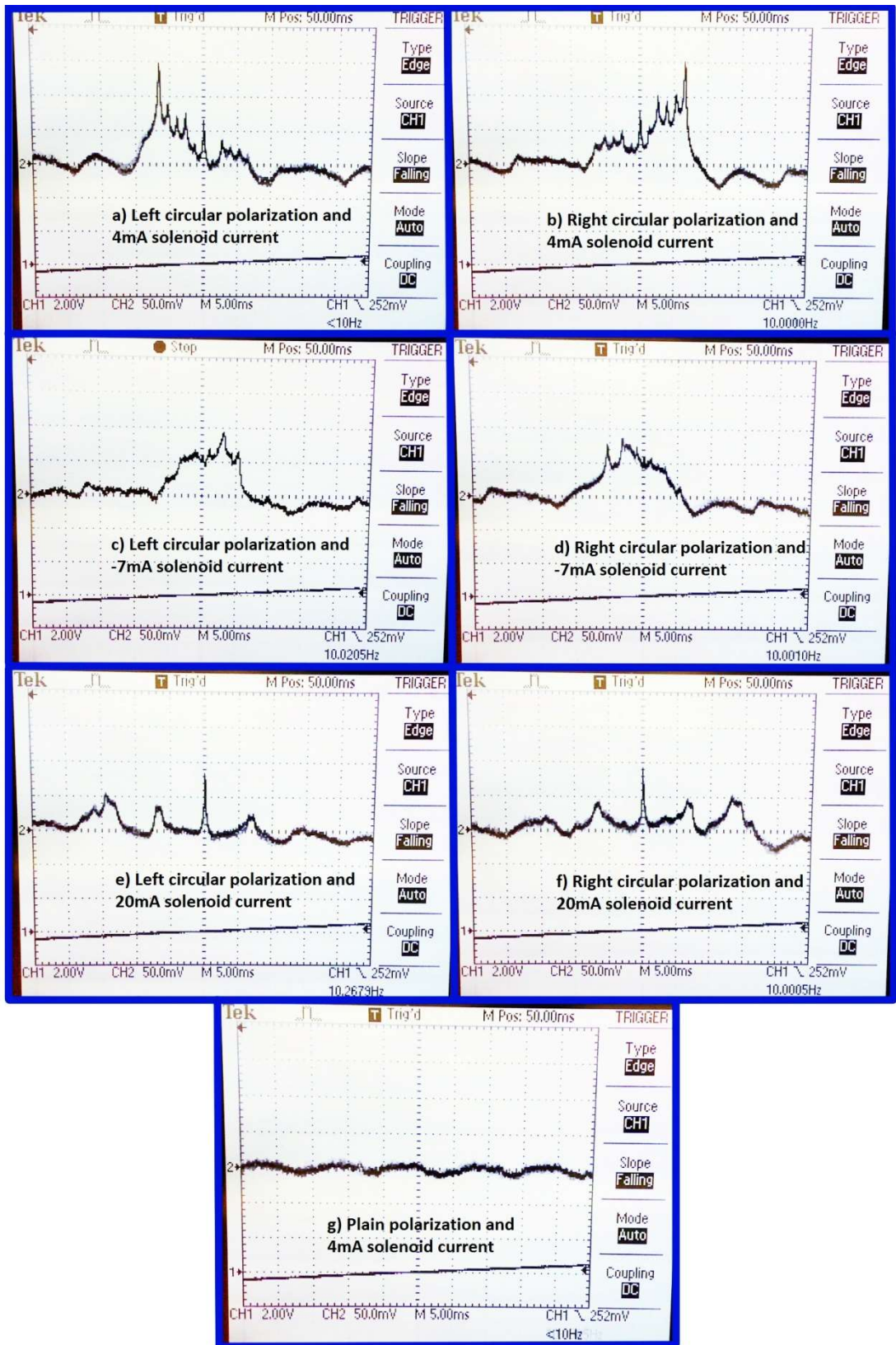


Figure 5-15: Hyperfine resonance waveforms for different polarization and magnetic field intensity.

### 5.2.7 CPT width and amplitude experiments.

Some experiments were conducted on the effects of different parameters on the CPT resonance's full width at half maximum (FWHM) and amplitude. The laser centre frequency was tuned close to the Doppler broadened absorption minimum and the RF frequency was tuned to the  $^{85}\text{Rb}$  resonance and swept across 10kHz around the CPT peak using a 1Hz ramp signal. The shape of the peak was observed and recorded using the oscilloscope. Then one of the parameters (modulation power, magnetic field or cell temperature) was changed while keeping the rest constant and the changes on the CPT peak's shape were recorded. This section includes the results of these experiments.

#### 5.2.7.1 Modulation Power.

Table 5-3 shows the measured FWHM and amplitude of the CPT resonance for different modulation power values. The carrier/1st order sideband ratio as measured through the Fabry-Perot spectrometer is also included.

Table 5-3: Resonance FWHM and Amplitude vs. Modulation Power.

Modulation Power (dBm)	FWHM (Hz)	Amplitude (mV)	Carrier/1st order Sidebands Ratio (div)
-7.00	920.00	60.00	0.3/0.8=0.375
-7.50	920.00	64.00	0.4/0.9=0.44
-8.00	920.00	66.00	0.4/0.8=0.5
-8.50	1000.00	68.00	0.4/1=0.4
-9.00	1040.00	68.00	0.5/0.9=0.55
-9.50	1040.00	66.00	0.5/0.9=0.55
-10.00	1040.00	60.00	0.6/1=0.6
-10.50	1080.00	56.00	0.8/1=0.8
-11.00	1000.00	54.00	0.8/0.9=0.89
-11.50	1000.00	56.00	1/1=1
-12.00	1160.00	48.00	1.2/1=1.2
-12.50	1200.00	40.00	1.3/0.9=1.44
-13.00	1280.00	36.00	1.5/0.8=1.875

Figure 5-16 and Figure 5-17 show the data in graphs.

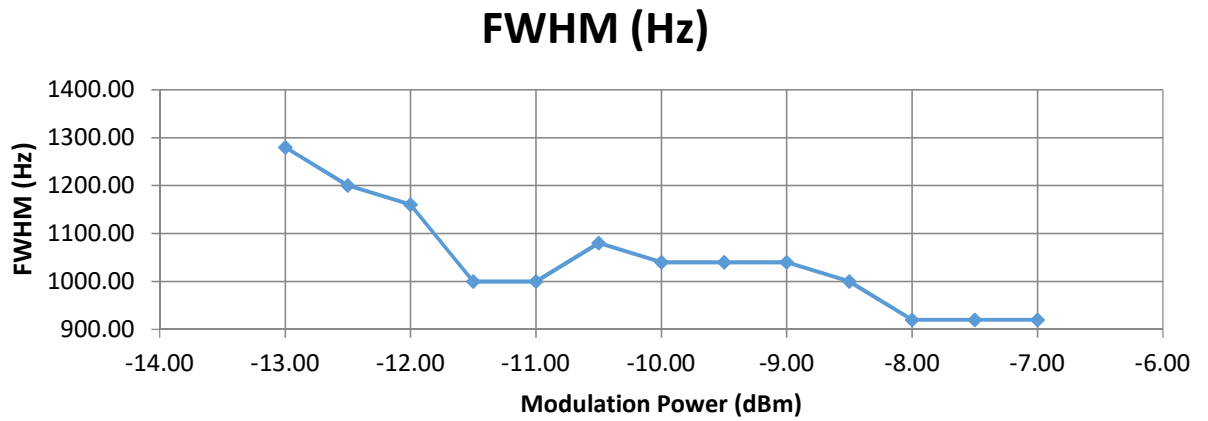


Figure 5-16: Resonance FWHM vs. Modulation Power.

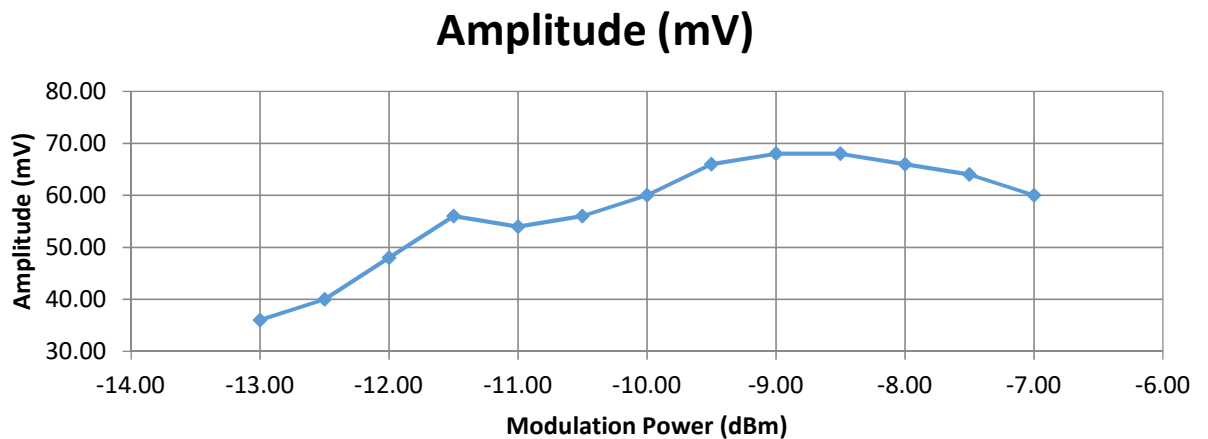


Figure 5-17: Resonance amplitude vs. Modulation Power.

The optimal point of operation in this case is a region where the FWHM is low and the amplitude is high. In particular at -8.00 dBm modulation power there seems to be no significant reduction in amplitude, but the FWHM appears at its minimum. the ratio between carrier and 1st order sidebands is about 0.5 (1st order sidebands are twice as large as the centre frequency). Higher order sidebands are also visible in this case, but they are quite small in size. If higher laser intensity is used, then higher modulation power would be needed to achieve the same modulation index.

### 5.2.7.2 Magnetic Field.

For this experiment the cell's temperature was kept constant, as well as the modulation power (at the optimal point of -8.00dBm) and the solenoid's current (effectively the magnetic field) was varied. The results are shown in Table 5-4.

Table 5-4: Resonance FWHM and Amplitude vs. Coil Current.

Coil Current (mA)	FWHM (Hz)	Amplitude (mV)
0.00	800.00	40.00
2.00	800.00	50.00
4.00	800.00	52.00
6.00	800.00	56.00
8.00	840.00	56.00
10.00	880.00	58.00
12.00	880.00	60.00
14.00	880.00	60.00
16.00	1000.00	60.00
18.00	960.00	60.00
20.00	880.00	60.00
22.00	960.00	64.00
24.00	880.00	60.00
26.00	800.00	60.00
28.00	880.00	64.00
30.00	880.00	60.00
40.00	960.00	60.00
50.00	960.00	64.00

The data is presented in graphs in and Figure 5-19.

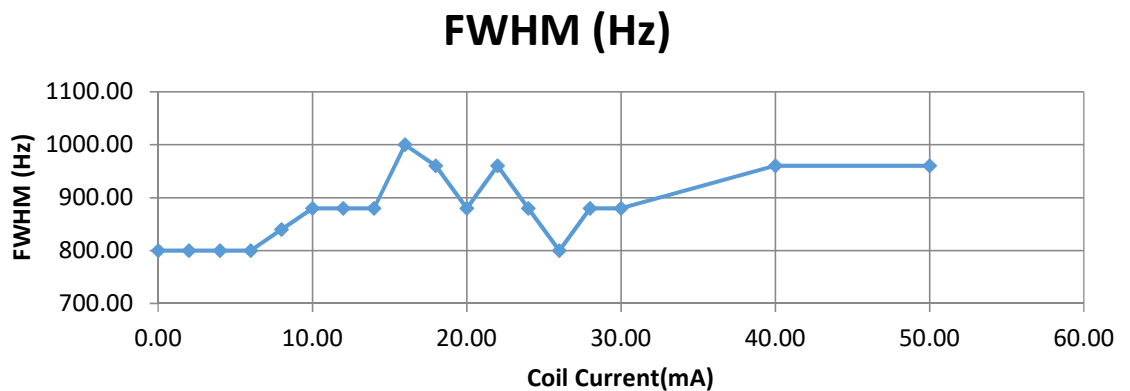


Figure 5-18: Resonance FWHM vs. solenoid current.

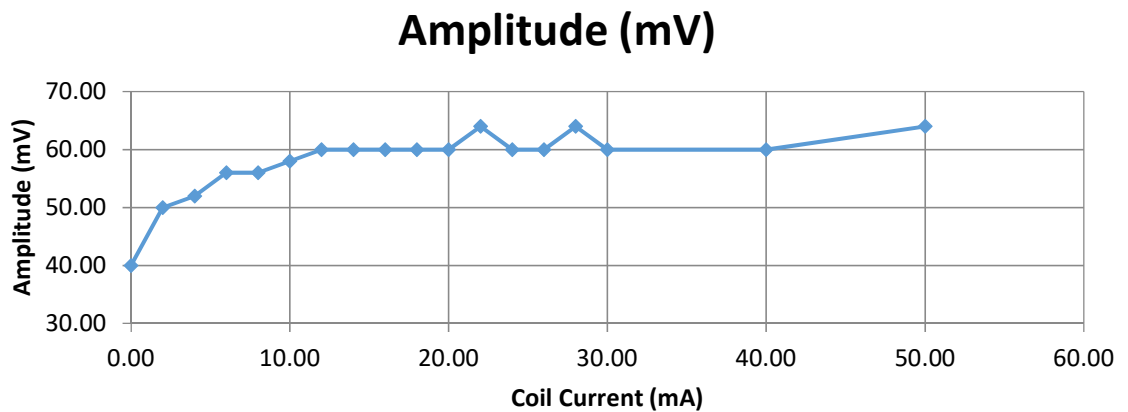


Figure 5-19: Resonance amplitude vs. solenoid current.

Again, the optimal point is where the FWHM is as low as possible without major reduction in amplitude. In this case this would be around 6 or 8mA coil current. Also at very high current values the CPT peak appears a bit asymmetrical. The horizontal axis of the graphs is expressed in Coil Current, instead of magnetic field. This is because the magnetic field inside the sealed glass cell cannot currently be measured. The field is proportional to the intensity of the coil current and can be approximately calculated using the solenoid's dimensions. However, even at 0mA of current, there is still magnetic field inside the cell, since it is not completely covered by the mu-metal shield, because there is a small clear area for the laser beam to get through the cell. At this stage it was more critical to know the appropriate amount of current that will give the best possible results. In other words, the magnetic field is the parameter that changes the resonance, but the coil current is the parameter that can be controlled and needs to be optimal.

### 5.2.7.3 Cell Temperature.

This experiment was conducted while keeping the modulation power at -8.00dBm and the coil current at 6mA. Changing the cell's temperature gave the results in

Table 5-5.

Table 5-5: Resonance FWHF and Amplitude vs. Cell temperature.

Cell Temperature (°C)	FWHM (Hz)	Amplitude (mV)
66	680	18
65	720	26
62	880	32
60	880	38
58	920	42
55	880	44
53	880	46
50	920	40
47	880	40
45	920	32
43	920	28
40	960	26

The data is presented in graphs in Figure 5-20 and Figure 5-21.

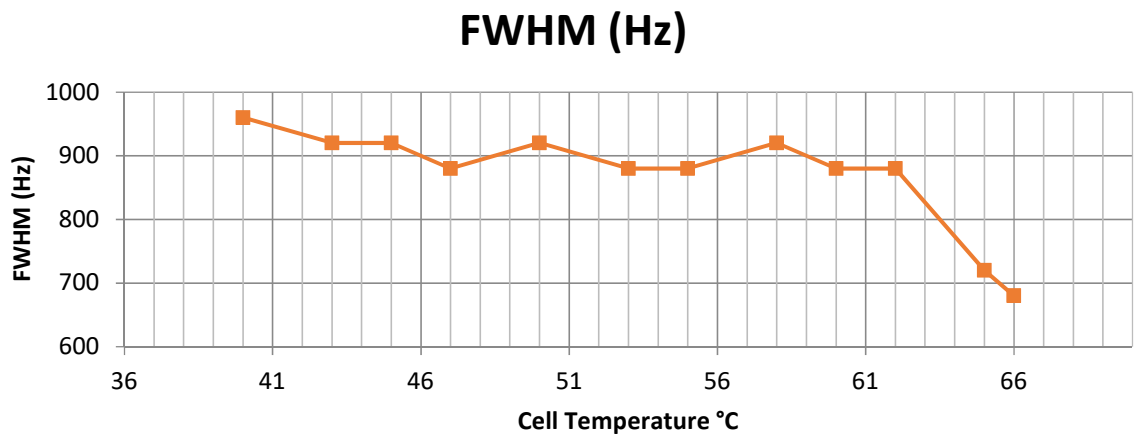


Figure 5-20: Resonance FWHM vs. Cell temperature.

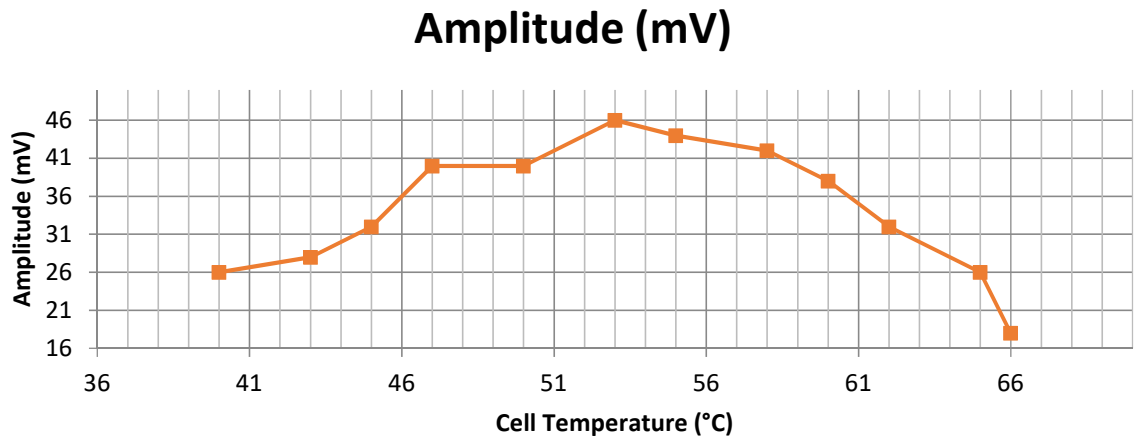


Figure 5-21: Resonance amplitude vs. Cell temperature.

There is not much variation in FWHM with temperature in this case. At very high temperature the amplitude of the resonance reduces too much. Therefore the optimal point can be considered at about 53 °C, where the amplitude is maximum. For different cells with different buffer gas mixture and vapour pressure this data would not be the same.

Making sure that these parameters are at their optimal points can improve the quality of future experiments.

### 5.3 Improved Compact Physics Package.

After the initial experiments on the physics package were completed, it was deemed necessary to design and build a more compact, integrated and robust version with better screening and better control over the operating parameters. This section will describe the modifications made and the complete latest version of the physics package.

#### 5.3.1 Laser Mount and Driving Electronics.

The original design of the laser driving circuits had the bias tee and RF modulation input on a different board than the current source. Therefore, there were significant losses in the interconnections between the boards. The grounding of the electronics could also be

improved. For this purpose, a new mount for the laser and the current source was designed in Autodesk Inventor and machined out of aluminium. A new PCB was designed for both the current source and bias tee on R4003C substrate. The connections to the bias tee were designed as coplanar waveguides according to the recommendations in the device datasheet. The voltage regulators for the current source were replaced with the ultra-low noise TPS7A4700 and the operational amplifiers were replaced with the LT1128 ultra-low noise precision op amps. These have significantly lower noise specs ( $e_n = 1nV/\sqrt{Hz}$  at 10Hz as oppose to the  $3.5nV/\sqrt{Hz}$  of the OP27). Figure 5-22 shows the schematic of the new laser current source.

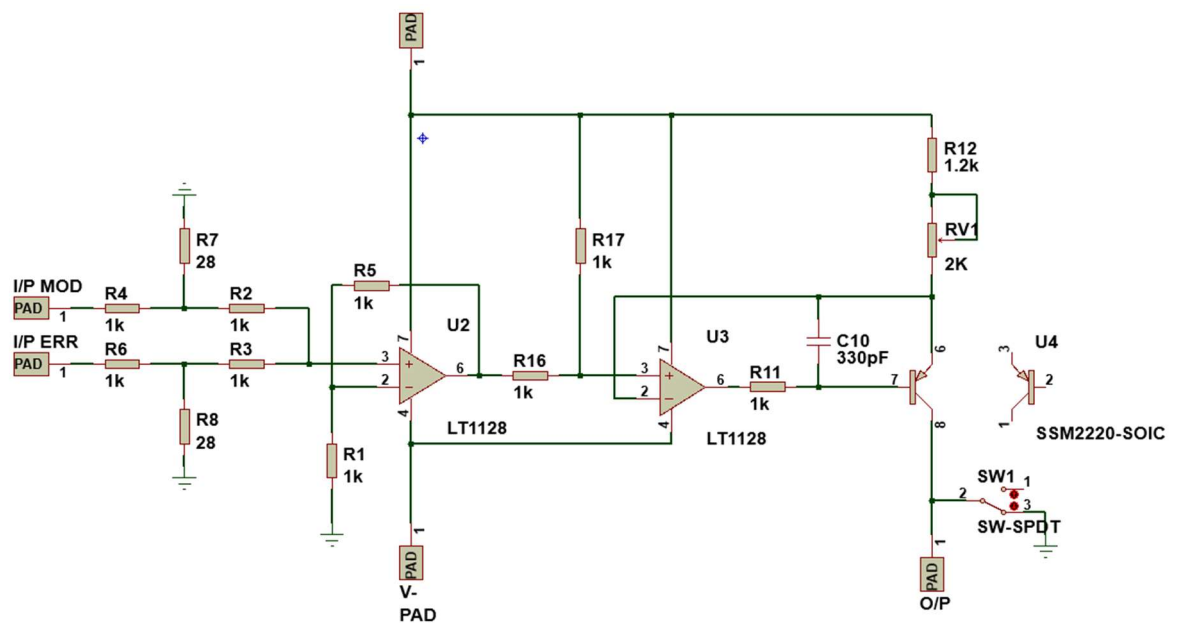


Figure 5-22: Schematic of the latest laser current source.

Two extra voltage tuning inputs were included in the current source for signals that would later be used in locking the laser centre frequency to the Rb absorption lines. T-pad attenuators were included at those inputs to serve two purposes. They reduce the maximum voltage swing on the inputs, which protects the laser from being overdriven and effectively ground the inputs when they are disconnected.

A metal plate was made for heating the laser. It was bolted to the mount using nylon screws for improved temperature insulation. The temperature controller for the laser was also improved and latest design is almost identical to the one used with the crystal

oscillator (section 3.2.7) with low noise voltage regulators and op amps. Figure 5-23 shows the Autodesk model of the complete laser assembly.

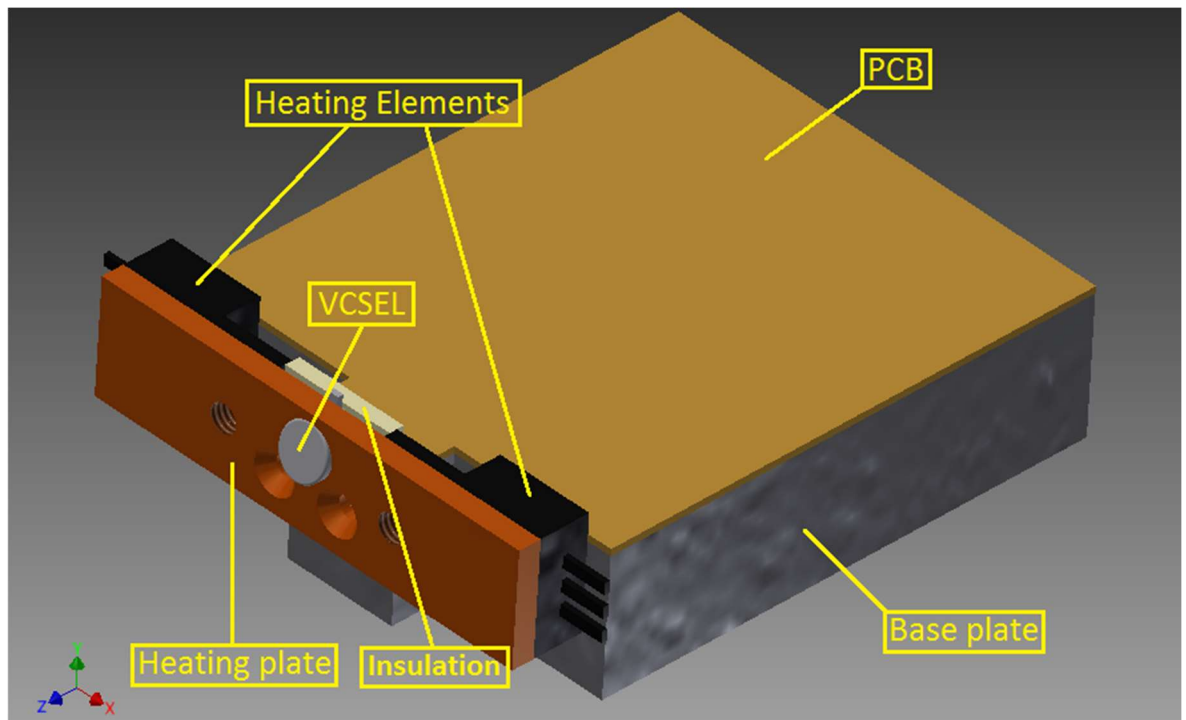


Figure 5-23: Laser assembly Autodesk model.

### 5.3.2 Collimating Lens.

To improve the collimation and alignment of the laser beam, a collimating lens with a diameter and focal length of 3mm was purchased from Thorlabs (part number APL0303-B). A mount was designed on Autodesk and initially 3D printed. In the latest design, however, it has been machined out of aluminium. The vertical position of the lens can be fine adjusted using this mount.



Figure 5-24: Collimating Lens Mount.

### 5.3.3 New Rb Vapour Cell.

The vapour cell used so far was obtained from old malfunctioned atomic clocks. It contains a natural abundance isotope mixture of about 28%  $^{87}\text{Rb}$  and 72%  $^{85}\text{Rb}$ . Since the hyperfine resonance frequency is different for each isotope, only one at a time can be used for CPT. In the case of this cell, the resonance in  $^{87}\text{Rb}$  is relatively difficult to detect and has a much lower amplitude than the  $^{85}\text{Rb}$  one, due to the lower isotope contents. The walls of the cells are also not flat, which distorts the laser beam as it passes through, making it more difficult to focus on a photodiode detector at the end of the physics package. For these reasons, new vapour cells were purchased from Photonics Technologies Ltd. Two cells with pure  $^{87}\text{Rb}$  and two cells with pure  $^{85}\text{Rb}$  were purchased, all including a buffer gas mixture of Argon and Nitrogen. The cells are made of fused silica and have optically flat walls. The dimensions of the cells are 25mm diameter and 25mm length.

In sections 2.4.2 and 2.4.3, it was described that the buffer gas used in a Rb vapour cell has an important impact on several of the cell's properties. The most important of those are the cell's temperature coefficient and the shape of the hyperfine resonance. In a cell containing only atomic vapour, the resonance's linewidth is mainly affected by the collisions between the alkali atoms and the cell's walls. Spin exchange collisions between within the alkali vapour atoms also have an effect. The addition of a buffer gas reduces the number of collisions of Rb atoms with the cell's walls and increases the lifetime of the electrons in the

coherent superposition state, which is manifested as a narrowing of the resonance's linewidth. However, if the buffer gas pressure is too high, then the collisions between the Rb atoms and the buffer gas atoms can cause broadening of the linewidth. It was estimated, based on information from [40], [41] and [33], that a total buffer gas pressure of about 20 torr is sufficient for having a narrow resonance linewidth.

The cell's temperature coefficient describes how the hyperfine resonance's frequency is shifted by changes in the cell's temperature. One way to minimize that shift, in addition to temperature stabilization, is to use a mixture of buffer gases with opposite temperature coefficients. By choosing a certain ratio of buffer gas pressures, an inversion point can be obtained at a desired temperature. This means that the frequency shift with temperature is minimized at that particular point [73], [74].

Since the operating temperature of the laser in the current physics package is about 50°C, it can be beneficial if the cell's inversion temperature is about the same. A commonly used combination of buffer gases for that purpose is Argon and Nitrogen. In order to calculate the correct buffer gas ratio for the desired inversion temperature, the temperature coefficient for each gas in that particular alkali vapour are required. An extensive search was conducted to find the correct coefficients. However, there is slight variation in the coefficients presented by different sources. There also appears to be more information available on the Cs coefficients and less on the ones for Rb (especially for the quadratic temperature coefficient) [74], [75], [76], [77], [78]. The coefficients that were chosen in this calculation are shown in Table 5-6.

Table 5-6: Pressure and temperature coefficients for Rb in Argon and Nitrogen buffer gases.

<b>Coefficients for <sup>87</sup>Rb</b>			
	<b><math>\beta</math></b>	<b><math>\delta</math></b>	<b><math>\gamma</math></b>
Argon	-60.3	-0.35	-0.00035
Nitrogen	560	0.54	0.0013
<b>Coefficients for <sup>85</sup>Rb</b>			
	<b><math>\beta</math></b>	<b><math>\delta</math></b>	<b><math>\gamma</math></b>
Argon	-26.78	-0.1555	$155.5 \times 10^{-6}$
Nitrogen	248.733	0.2399	$577.42 \times 10^{-6}$

The coefficients for <sup>85</sup>Rb were calculated by taking those for <sup>87</sup>Rb and multiplying by the ratio of the hyperfine frequencies, as was done in [74].

The pressure ratio for inversion temperature of 50°C can now be calculated using the following equation [73]:

$$\frac{P_{Ar}}{P_{N_2}} = a = -\frac{\delta_{N_2} + 2 \times \gamma_{N_2}(T_{inv} - T_0)}{\delta_{Ar} + 2 \times \gamma_{Ar}(T_{inv} - T_0)} = -\frac{0.54 + 2 \times 0.0013 \times 50}{-0.35 - 2 \times 0.00035 \times 50} = \frac{0.67}{0.385} = 1.74$$

Where P is the pressure of each buffer gas,  $\delta$  is the linear temperature coefficient,  $\gamma$  is the quadratic temperature coefficient,  $T_{inv}$  is the desired inversion temperature and  $T_0$  is the reference temperature of 273K [5]. Since the coefficients for  $^{85}\text{Rb}$  were scaled down from the ones for  $^{87}\text{Rb}$ , they return the same result for either isotope.

The cells were therefore ordered with buffer gas pressures of 12.7 torr Ar and 7.3 torr  $\text{N}_2$ . A new metal heating enclosure was designed and machined for these cells. However, because of the manufacturing process used with these cells, there is a small glass protrusion on the side of each cell. This means that a single solenoid coil can no longer be used to generate the magnetic field. Therefore, the coil was split into two parts separated by the a distance equal to their radii, effectively making a pair of Helmholtz coils (Figure 5-25).

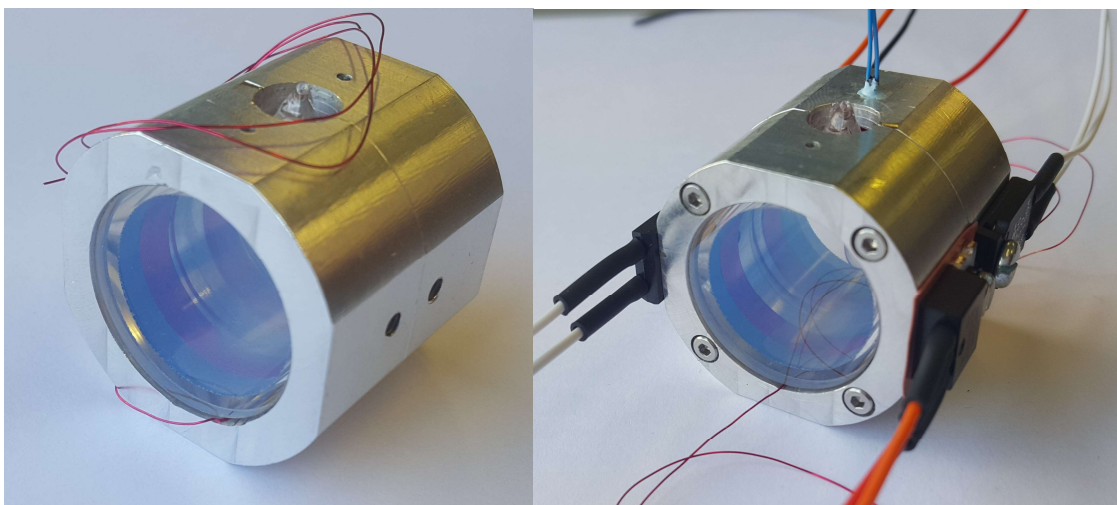


Figure 5-25: New vapour cell assembly with Helmholtz coils and heating elements.

The heating elements were attached symmetrically on the two sides of the cell and a thermistor was glued in a small hole in the jig using a thermal bonding compound. The temperature controller for the cell was also designed using the method described in section 3.2.7, but with parameters adjusted for this particular thermal system.

The outside of the cell was then covered with a layer of thermal insulation and three layers of mu-metal foil. An outermost enclosure was also made for it to allow for more precise and secure alignment in the physics package configuration (Figure 5-27).

#### 5.3.4 Wide Area Photodiode.

The inclusion of a better collimation lens was meant to increase the amount of incident light on the photodiode at the end of the physics package and effectively improve the signal to noise ratio of the detected resonance. Another way to further improve this was to use a wider area photodiode. Therefore, the physics package was equipped with a photodiode with a sensitive area of  $7.02\text{mm}^2$ . An aluminium mount was also designed and machined for the photodiode Figure 5-26.

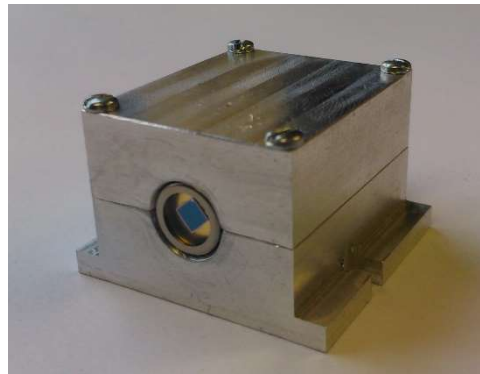


Figure 5-26: Wide area photodiode ( $7.02\text{mm}^2$  sensitive area) in metal mount.

The inclusion of the photodiode completed the improvements on the optical parts for the physics package. All of the optical mounts and components were then fixed onto a main aluminium rail, which was specifically designed for them. Figure 5-27 shows a photo of the latest physics package configuration with all the components labelled.

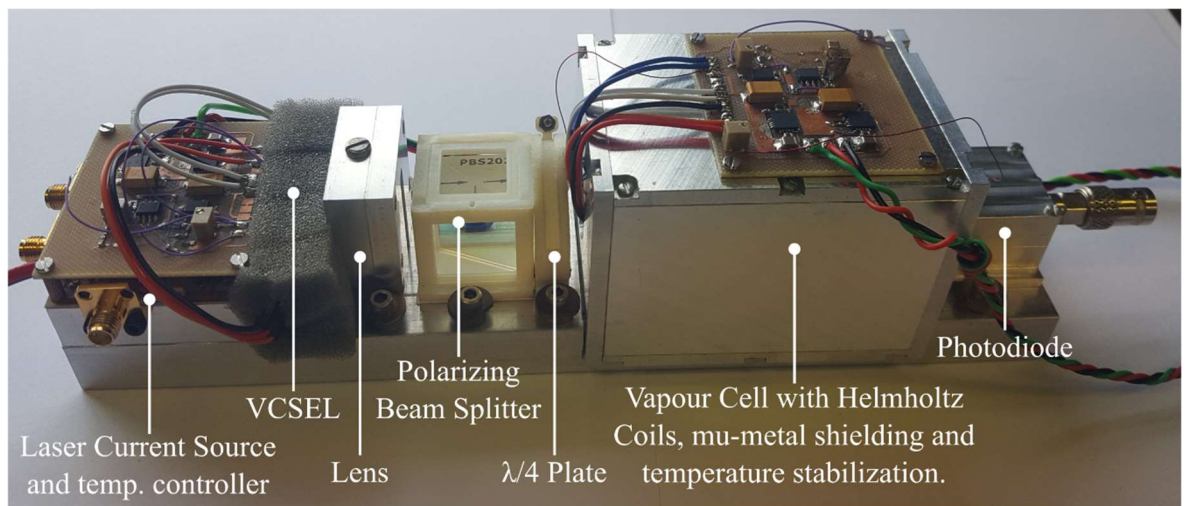


Figure 5-27: Photo of the latest complete physics package configuration (length=23cm).

The main rail was designed so that the height of the cell along with all of the components attached to it was the same as the height of the laser beam. It was also designed, so that the optical mounts can be easily removed or replaced and their position can be aligned accurately.

### 5.3.5 Laser Centre Frequency Stabilization.

As described in section 2.4.4, changes in the laser centre frequency can cause instability in the final system due to the effects of Light Shift [33], [42]. It is therefore important to stabilize the centre frequency of the laser as best as possible. The two main factors that can change the laser frequency are the injection current and temperature. The constant current source provides a stable, low noise current with very low temperature coefficient and independent on small changes in the laser diode impedance. The temperature controller can stabilize the laser's temperature to well within 0.1°C accuracy. However, it is still susceptible to disturbances in the thermal system, such as sudden changes in the ambient temperature. It is therefore required that an active form of stabilization of the laser centre frequency is incorporated for optimal performance. A common way to further stabilize the laser is to use the absorption spectrum of Rb as a reference and lock the laser to that transition. Several techniques were identified, which can be used to achieve that, all with their advantages and drawbacks. This section discusses the most commonly used ones and proposes which are more appropriate for this project.

### 5.3.5.1 Using the Doppler-broadened spectrum of Rb

In this technique, a small, low frequency AC signal is added to the DC injection current. This same signal is also used as a reference to a phase detector (typically a lock-in amplifier). The input to the amplifier is the signal from the photodiode detector. When the laser centre frequency is swept through the Doppler broadened absorption of Rb (Figure 5-10), the AC modulation component at the output of the photodiode will have a different phase depending on the position of the laser's frequency inside the absorption dip. This phase difference is then detected by the lock-in amplifier and converted into a DC error signal, which can be used to lock the laser to the middle of the absorption (Figure 5-28).

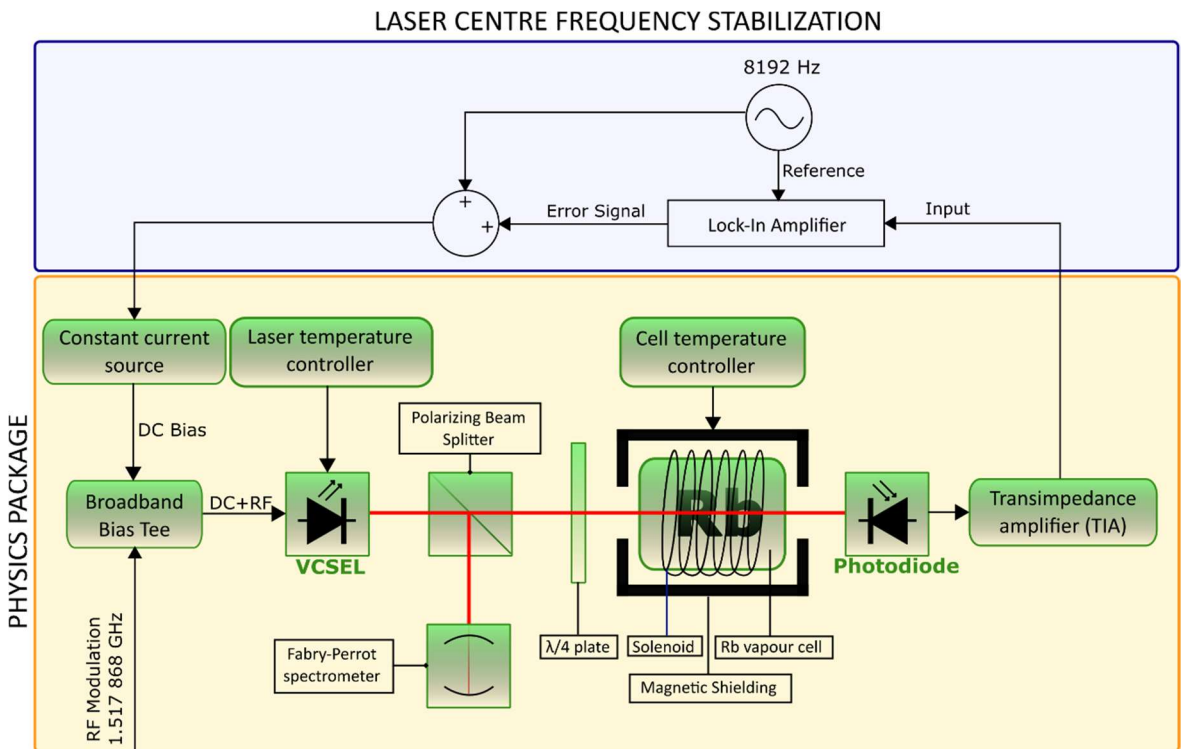


Figure 5-28: Block diagram of laser centre frequency locking to the Doppler-broadened absorption spectrum.

The advantage of using this technique is mainly its simplicity. It only requires minor modifications to the basic CPT setup. It utilizes the ability of the VCSEL to have its frequency tuned by adjusting the injection current. Small changes also have to be made to the laser's current driver, so that the two extra signals (low frequency AC modulation and lock-in error signal) can be introduced. This was already shown in section 5.3.1.

The main disadvantages are that modulating the laser's current can degrade the system's short term stability. It would also introduce extra noise to the injection current along with the error signal. In addition, the shape of the Doppler broadened spectrum is not very narrow (depending on the absorption line, the width is in the order of a few hundred MHz) and that limits the accuracy of the stabilization loop.

#### 5.3.5.2 Locking to the Doppler-free absorption spectrum of Rb

The Doppler broadening in the Rb absorption spectrum is the result of the random movement of the atoms in all directions inside the vapour cell. Let's assume we have the configuration with a single laser beam passing through a Rb vapour cell. In the ideal case, transitions in atoms can only occur when the laser beam exciting them is at exactly the resonance frequency. However, if the atoms have different velocity components along the axis of propagation of the light, because of the Doppler effect, they will interact with light which has a slightly different frequency, effectively shifting the resonance. The shifted resonance frequency is given by the following equation:

$$f'_0 = f_0 \left( 1 + \frac{V_z}{c} \right) \quad (5.1)$$

Where  $f_0$  is the resonance frequency,  $V_z$  is the velocity component along the axis of propagation of the light and  $c$  is the speed of light. [79, p. 2]

This causes absorption to occur for a wider range of frequencies, broadening the spectrum. The way to obtain absorption spectra free of any Doppler broadening is to only detect atoms with zero velocity component along the laser propagation axis. The most common method of doing this is by passing a second laser beam through the cell, along the same axis (for example the Z axis), but in the opposite direction (Figure 5-29).

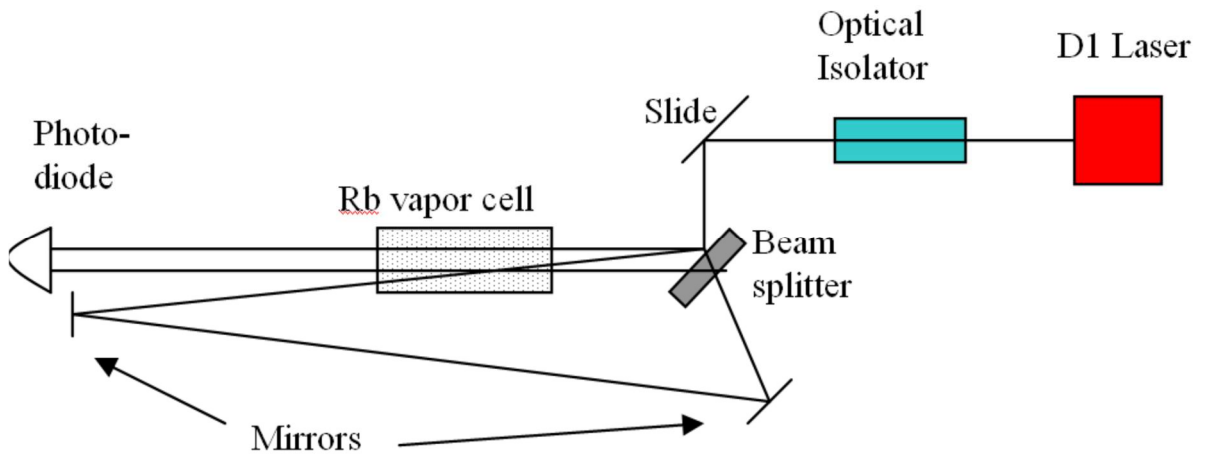


Figure 5-29: Saturated absorption spectroscopy setup. Figure taken from [79, p. 5].

The second beam is called the “pump” beam and the first one is the “probe” beam. The pump beam is usually made significantly more powerful than the probe one. Since light is passing twice through the cell in opposite directions, when the laser frequency is slightly off resonance it interacts with two groups of atoms at the same time. The pump beam interacts with atoms with velocity component  $V_z$  along the Z axis and the probe beam interacts with those with velocity component  $-V_z$  (Figure 5-30).

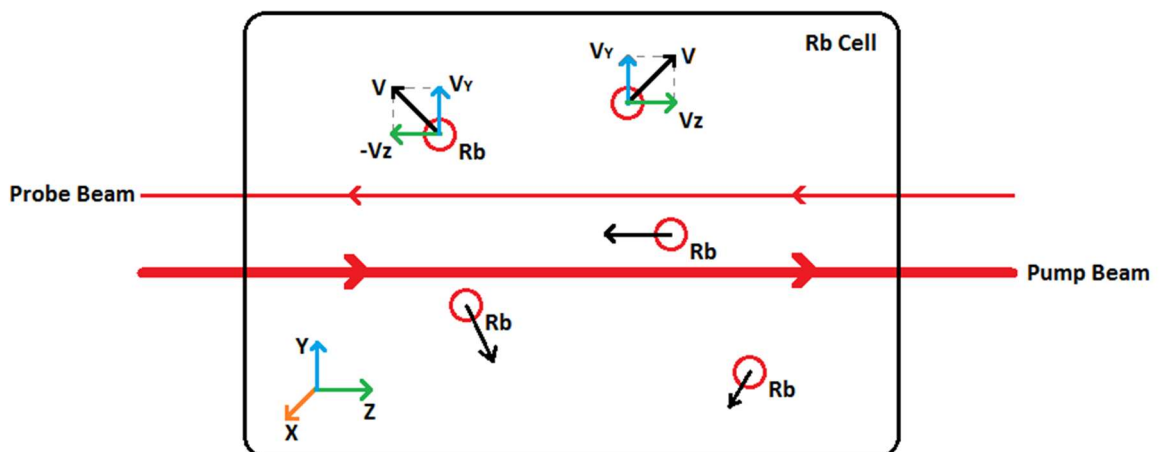


Figure 5-30: Rb atoms and their velocity components inside the vapour cell.

This means that the light from the probe beam will still be absorbed as previously. When the laser is on resonance, however, both beams can only interact with atoms with 0

velocity along the Z axis. Since the pump beam is stronger, it excites the majority of the atoms and the probe beam can no longer interact with them. This results in an increase of light intensity when on resonance and the detection of the saturated spectrum (Figure 5-31).

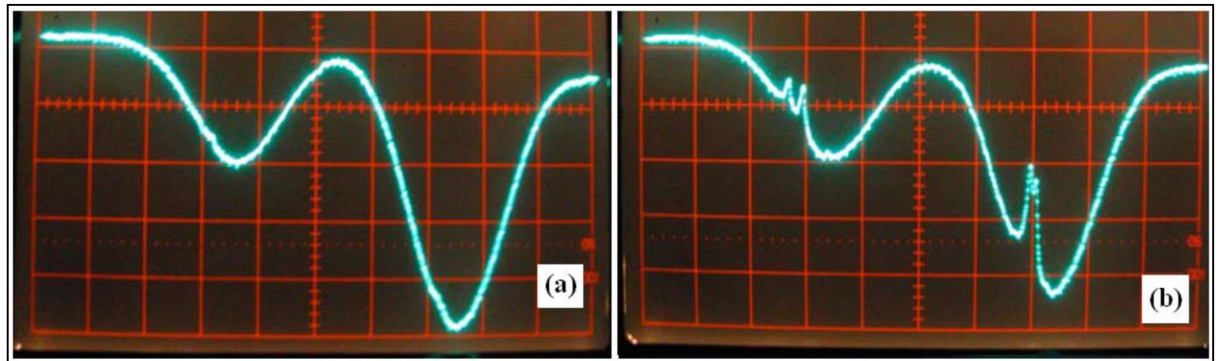


Figure 5-31: a) Doppler broadened absorption spectrum. b) Saturated absorption spectrum. Figure taken from [80, p. 7].

Subtraction of signal a) from signal b) will result in obtaining only the narrow substructure peaks corresponding to the hyperfine transitions in Rb. That is the Doppler-free saturated absorption spectrum. In addition to the peaks that occur when the laser is resonant at the hyperfine transitions, there are also peaks that occur when the laser is half way between two consecutive hyperfine resonances. These are referred to as crossover resonances and the physics behind them are a bit more complex.

The Doppler-free spectrum's peaks are much narrower than the broadened ones and therefore can be used to control the laser's centre frequency with greater accuracy. However, the main disadvantage is that a vapour cell containing no buffer gas is required to achieve saturated absorption. This is why a second vapour cell is usually included in setups using this method. Another one is that in order to achieve the required waveforms, the laser's linewidth needs to be relatively narrow (within about 100MHz). Narrowing the laser's linewidth can be done by including a diffraction grating into the laser assembly, but would result in loss of some of the laser power. The VCSEL currently used has a specified linewidth of about 30MHz, which is theoretically narrow enough for such an experiment. The complexity, volume and component count of the optical setup also increases.

### 5.3.5.3 Dichroic Atomic Vapour Laser Lock (DAVLL). [81], [82]

This configuration goes back to using the Doppler broadened spectrum of Rb. The DAVLL setup consists of the VCSEL, a linear polarizer, the vapour cell in a weak magnetic field, a quarter wave plate, a polarizing beam splitter and two photodiodes (Figure 5-32).

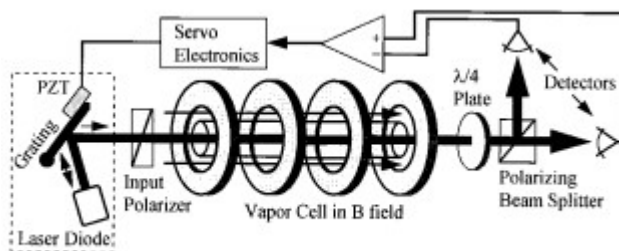


Figure 5-32: DAVLL setup. Figure taken from [82, p. 2].

It is possible that linewidth reduction of the laser may still be necessary, even though the method uses the broadened spectrum. In this figure, the diffraction grating is also used to adjust the laser's frequency using the error signal. The same can be done by adjusting the laser injection current.

In this case the laser beam is linearly polarized and sent through the vapour cell. When a constant magnetic field is applied, the centre absorption frequency changes due to Zeeman effects. This change is in one direction if the light is circularly polarized to the left and in the opposite direction if the light is polarized to the right. If the light is linearly polarized the resulting absorption is the superposition of the two circular light fields, since linear polarization is the combination of 2 circularly polarized components of opposite rotation. The quarter wave plate is used after the cell to split the linearly polarized beam into two perpendicular components. These components are then separated using a polarizing beam splitter. Then they are measured separately by the two photodiodes and one is subtracted from the other. This produces the error signal that can be used to lock the laser's centre frequency (Figure 5-33).

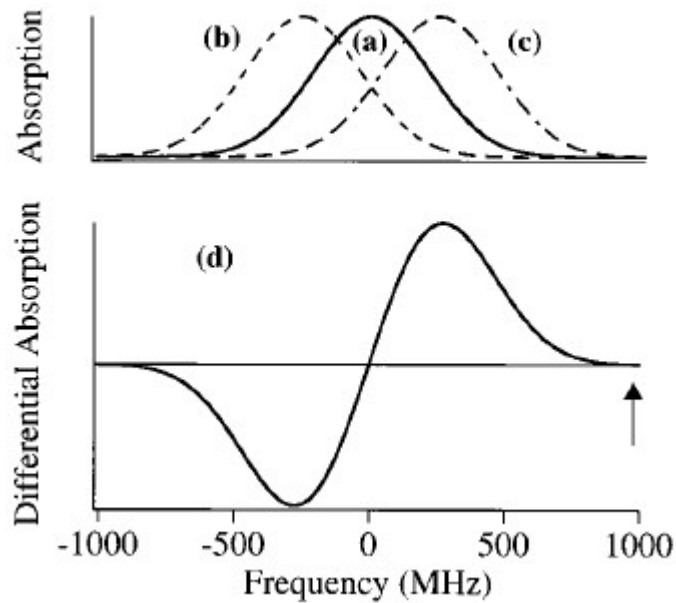


Figure 5-33: DAVLL absorption spectra. (a) Using linear polarized light. (b) Left circularly polarized component. (c) Right circularly polarized component. (d) Error signal (c - b). Figure taken from [82, p. 2].

One disadvantage of using this technique is that the magnetic field has to be significantly more powerful than the one used to detect the CPT resonance. The optical setup is also significantly different. Therefore, it may be required to have a separate optical setup dedicated to the DAVLL mechanism.

After consideration of the available methods, it was decided that the best current option was to lock the laser centre frequency to the Doppler broadened absorption spectrum, because it requires no major modifications or additions to the physics package configuration and doesn't add complexity and volume to the system. Original tests were performed by modulating the laser injection current with an audio frequency sinewave and using a lock-in amplifier as the phase sensitive detector. As the physics package was upgraded to its more compact version, it was deemed necessary to design a laser locking circuit, which is also compact and integrated. Originally, a Gilbert cell analogue multiplier was designed, which replaced the lock-in amplifier. In the latest design, however, this was replaced by the AD835 low-noise, 4-quadrant analogue multiplier. For the purpose of integration, a miniature MEMS oscillator at 8192 Hz was used as the source of the audio frequency modulation signal. The block diagram of the circuit is shown in Figure 5-34.

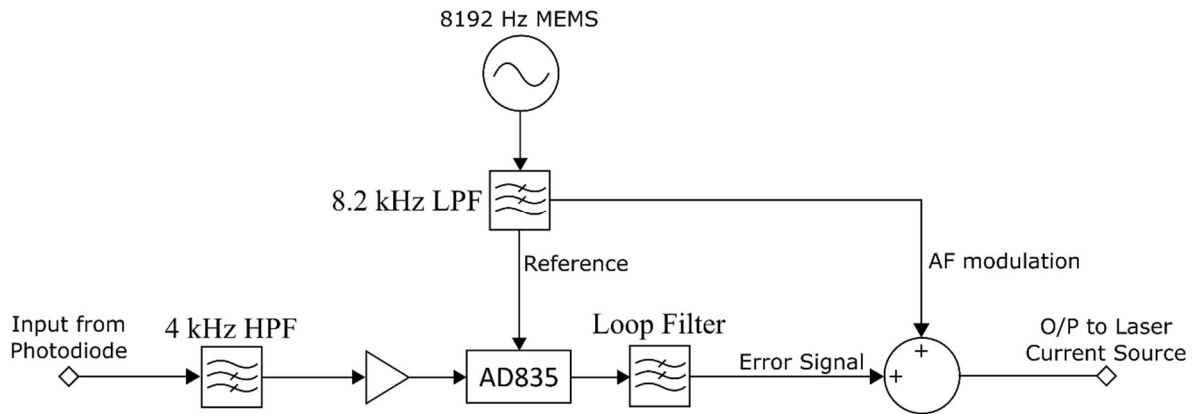


Figure 5-34: Block diagram of the AD835 phase detection circuit.

The reference signal to the AD835 and modulation signal to the laser current source is generated by the 8.192kHz MEMS oscillator. Since the output of the MEMS is a square wave, an 8<sup>th</sup> order Sallen-Key low-pass filter is used to filter it into a sine wave. The second input into the multiplier is from the photodiode at the end of the physics package configuration. It is also filtered by a high-pass filter to only obtain the 8.192 kHz component of interest and amplified for increased sensitivity. The DC component of the AD835, which is proportional to the phase difference between the multiplied signals is then filtered by the loop filter to produce the error signal that stabilizes the laser. All the high order filters were realized with the LT1125 low-noise, high-precision quad op amps. It must be noted that the summing of the error signal and audio frequency modulation signals is done on the current source board incorporated into the physics package. The active components were supplied by low-noise voltage regulators. The board was built on R4003C. Figure 5-35 shows a photo of the laser stabilization circuit.



Figure 5-35: Photo of the AD835 laser stabilization circuit.

The circuit was enabled and the audio frequency modulation signal was applied to the laser current source. The amplitude of the modulation signal was attenuated to about  $2\text{mV}_{\text{p-p}}$ , which produces a modulation in the laser centre frequency of about  $\pm 100\text{ MHz}$ . The response of the circuit was confirmed to produce an error signal dependent on the position of the laser centre frequency inside the Rb absorption dip. The loop was then closed and the loop filter parameters were fine adjusted until a lock of the laser centre frequency was achieved. The lock was confirmed by introducing a disturbance to the laser temperature and making sure that the laser centre frequency remains in the centre of the absorption.

#### 5.4 Testing the Improved Physics Package.

The inclusion of the laser centre frequency stabilization circuit completed the improvements on the physics package and a test was conducted on its operation. The laser current source and temperature controller were powered up and its frequency was tuned to the Rb absorption lines. A modulation was applied using the RF signal generator. Thanks to the incorporation of the bias tee onto the main current source PCB, the RF power required to reach 1/1 ratio of carrier and first order sidebands was reduced to  $-25\text{ dBm}$

(from -11.5dBm previously). The alignment of the lens was adjusted until the beam was well collimated into a small (about 3mm diameter) circular spot at the end of the physics package configuration. The wide area photodiode was included and the alignment was fine adjusted until the maximum signal from the photodiode was detected. The cell was also temperature stabilized at 50°C and the magnetic field of about 50 $\mu$ T was applied using the Helmholtz coils. The laser was then fine tuned to the bottom of the superimposed  $^{85}\text{Rb}$  absorption dip. The RF modulation frequency was set to 1.517866410 GHz and swept over a range of 10 kHz. The photodiode signal was amplified using the transimpedance amplifier with a sensitivity of 0.1 $\mu$ A/V and monitored on an oscilloscope. The CPT hyperfine resonance was detected as shown in Figure 5-36.

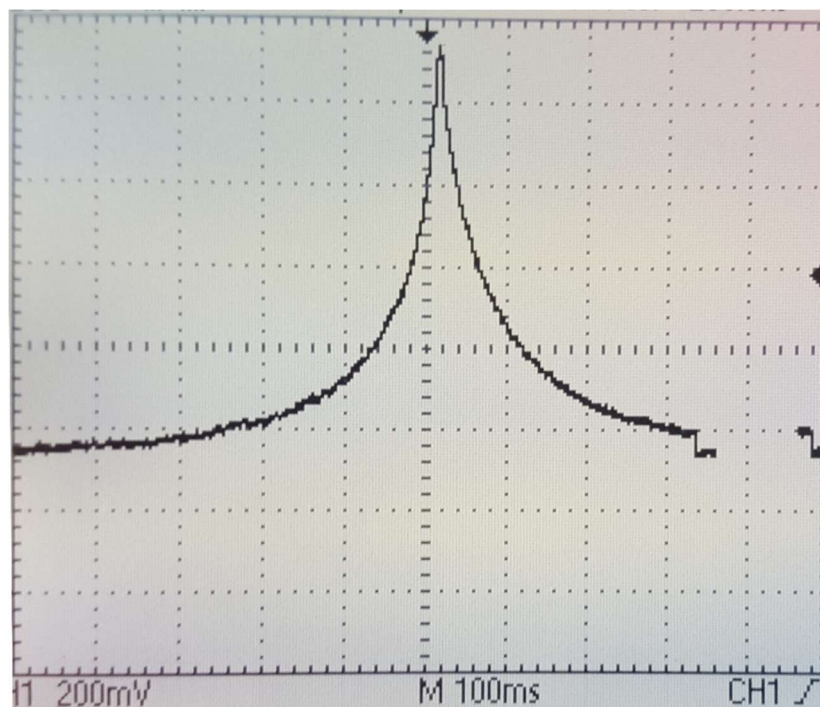


Figure 5-36: Photo of  $^{85}\text{Rb}$  CPT resonance ( $\sim 1$  kHz/div).

The FWHM of this resonance is about 800 Hz and the amplitude is about 1V or 0.1 $\mu$ A of photodiode current. Considering that the background light of the photodiode is about 3 $\mu$ A, this means that the contrast of the resonance is about 3.3%. When this figure is compared to Figure 5-13, it can be seen, that the resonance amplitude and signal to noise ratio are significantly improved. The FWHM is similar to the one detected in the old vapour cell.

It must be noted that this measurement was taken using a signal generator as the local oscillator and without the laser active centre frequency stabilization, to establish a baseline for comparison. When the full system, including the designed local oscillator and synthesizer was assembled, the resonance was measured again and compared to Figure 5-36.

## 5.5 Summary.

A Rubidium 85 coherent population trapping physics package was built from first principles. The basic operating parameters were initially investigated and the atomic resonance was detected using a setup assembled on an optical bench. A series of measurements were conducted investigating the resonances corresponding to the different Zeeman sublevels. The optimal magnetic field, vapour cell temperature and RF modulation power for achieving the best resonance shape and amplitude were also experimentally found. The latest version of the physics package was designed in a more compact and integrated form with lower noise circuitry, better screening and higher resonance detection sensitivity. All the optical mounts, enclosures, laser and vapour cell assemblies were designed and built in-house. The latest vapour cell was manufactured according to the specified buffer gas ratios and containing only the isolated  $^{85}\text{Rb}$  isotope. The new physics package contains all the components needed for detecting the Rb resonance, including the laser and vapour cell temperature stabilization electronics and the laser current source. The construction is mechanically robust and can be moved as a unit without compromising the alignment of the components. An active laser centre frequency stabilization circuit was also designed and built. The latest measured atomic resonance exhibits a FWHM of 800 Hz and contrast of 3.3% and significant improvement on the signal to noise ratio.

## 6 COMPLETE ATOMIC CLOCK SYSTEM.

The design and construction of the local oscillator (Chapter 3), frequency synthesizer (Chapter 4) and physics package (Chapter 5) were completed. These main elements were then combined into the complete atomic clock system. The laser centre frequency was locked to the Doppler broadened Rb absorption and the atomic resonance was detected again using the designed system components (without the use of external signal sources, such as signal generators). A digital resonance detection and frequency locking system was designed and implemented to lock the local oscillator to the CPT resonance. This chapter describes the atomic resonance detected using the low phase noise local oscillator and frequency synthesizer while locking the laser centre frequency. Phase noise and Allan deviation measurements on the full system locked to the atomic resonance are also presented.

### 6.1 CPT Resonance.

The frequency synthesizer was clocked by the phase locked local oscillator. The DDS was programmed to produce the 17.866 MHz offset signal, which was then used to upconvert the 1.5 GHz output of the DRO to the 1.517866 GHz hyperfine transition frequency. This signal was then attenuated to -25dBm and plugged into the RF input of the bias tee. The VCSEL was therefore modulated, so the power of the two optical sidebands was equal to the carrier. The physics package was prepared for detecting the atomic resonance. The PIC microcontroller was then used to program the DDS to produce a continuous frequency sweep within a range of about  $\pm 5$  kHz around the 1.517866 GHz hyperfine. This configuration is illustrated in Figure 6-1.

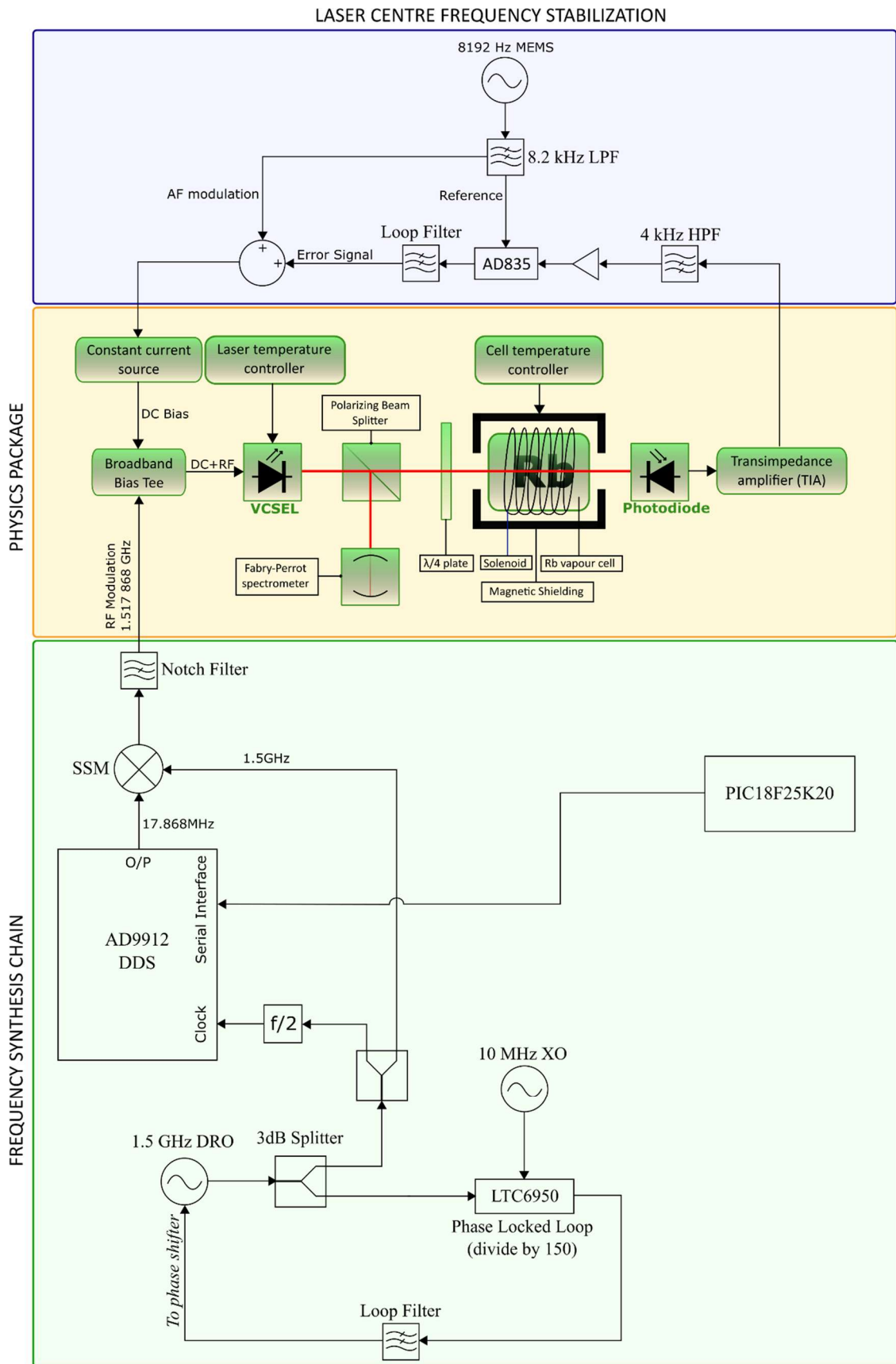


Figure 6-1: Laser centre frequency lock and resonance detection block diagram.

The atomic resonance was measured using this configuration (Figure 6-2).

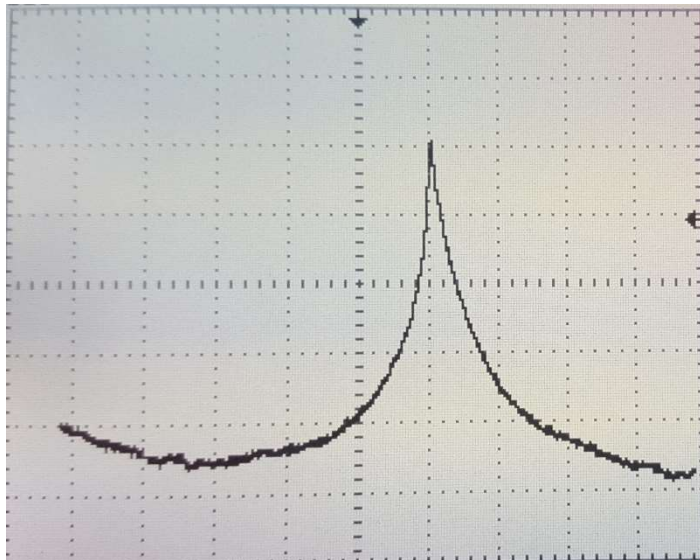


Figure 6-2: Resonance detected using the assembled system with laser centre frequency lock (1kHz/div).

The resonance appears nearly identical to the one previously measured in section 5.4. The audio frequency modulation of the laser centre frequency cannot be seen on the oscilloscope.

## 6.2 Locking to the Atomic Resonance.

With the CPT resonance detected, the next step was to design a mechanism for locking the local oscillator to it. It was described in section 3.2, that the 10 MHz crystal oscillator incorporates a voltage tuned phase shifter, which would be used for this purpose. Since there was already a digital control scheme implemented for the DDS, it was decided to take advantage of its versatility and also digitally generate the resonance locking feedback signal. Therefore, a system was designed that uses the following algorithm to lock the local oscillator:

1. The PIC microcontroller is used to set the DDS frequency to the lower-frequency slope of the CPT resonance.
2. An analogue to digital converter (ADC) is used to acquire a sample of the photodiode DC output and store it as a variable in the microcontroller (sample 1).
3. The DDS is then set to the higher-frequency slope of the CPT resonance.
4. The ADC is used to acquire a second sample and also store it in the PIC (sample 2).

5. The microcontroller compares the two samples. If sample 1 > sample 2, then the frequency is too low. If sample 1 < sample 2, then the frequency is too high. If the two samples are equal, then the frequency is matched to the centre of the Rb hyperfine transition.
6. Depending on the result of the operation in step 5, the PIC adjusts the output of a digital to analogue converter (DAC), which is connected to the phase shifter of the crystal oscillator.

This is illustrated in a flowchart in Figure 6-3. The block diagram of the full configuration, including the converters is shown in For maximum sensitivity, the samples must be taken at the points in the resonance where the frequency discriminating slope is maximum. The switching is applied through the DDS, so there is no disturbance or degradation of the DRO output. The stability that can be achieved using this method is limited by the resolution of the converters. Therefore, high resolution converters must be used. In section 3.4 the frequency tuning of the crystal oscillator vs. varactor voltage was measured at about 1.122 Hz/V within the range of 0.4V to 1V. If the full-scale output of a 20-bit DAC is set to 1V, then this would result in a frequency tuning step of:

$$\Delta f_{LSB} = \frac{1.122}{2^{20}} = 1.07 \mu Hz$$

At the 10 MHz operating frequency, this corresponds to 1.07 parts in  $10^{13}$ , which should be sufficient to meet the target stability set at the start of the project.

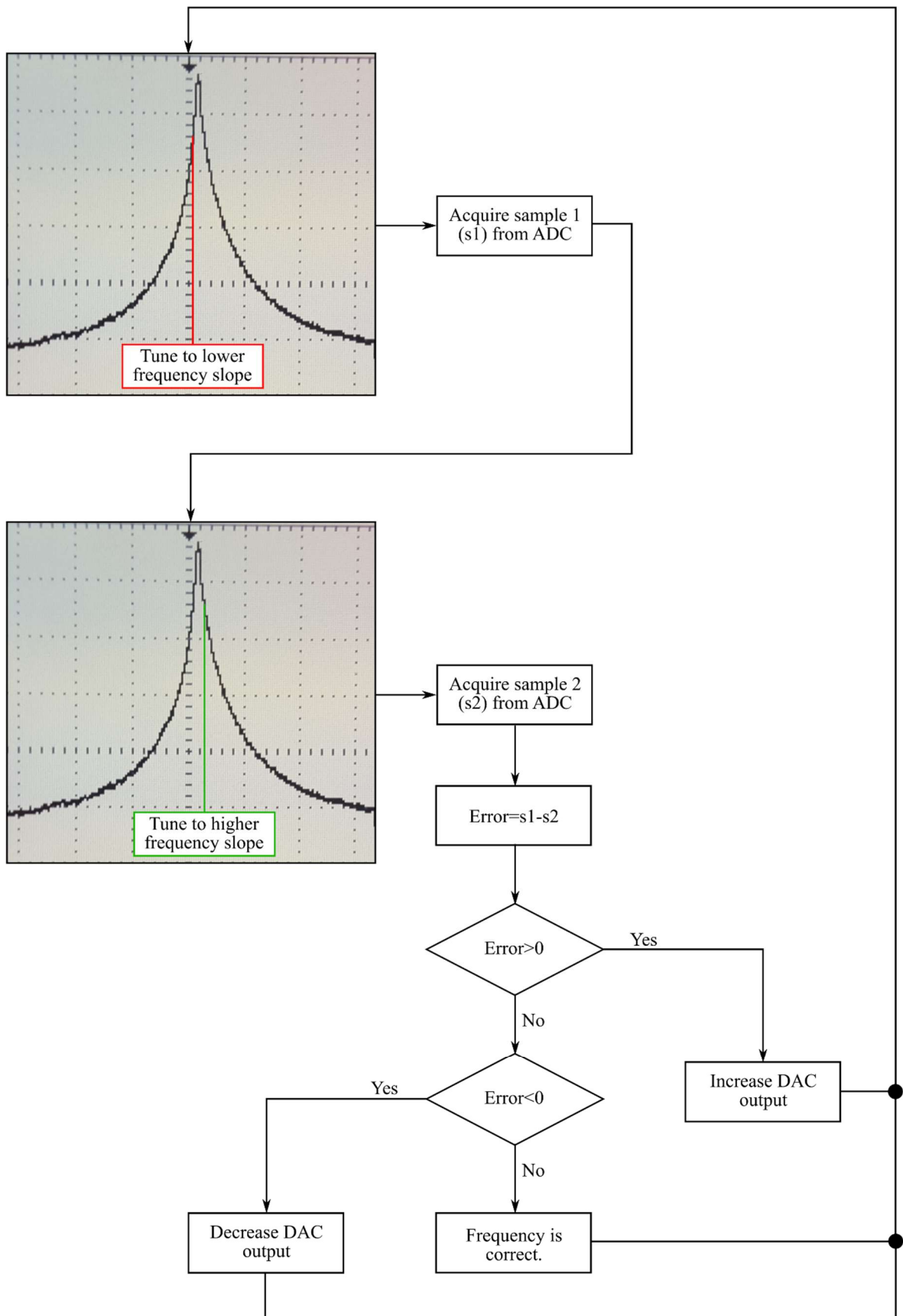


Figure 6-3: Flowchart of the CPT resonance locking method.

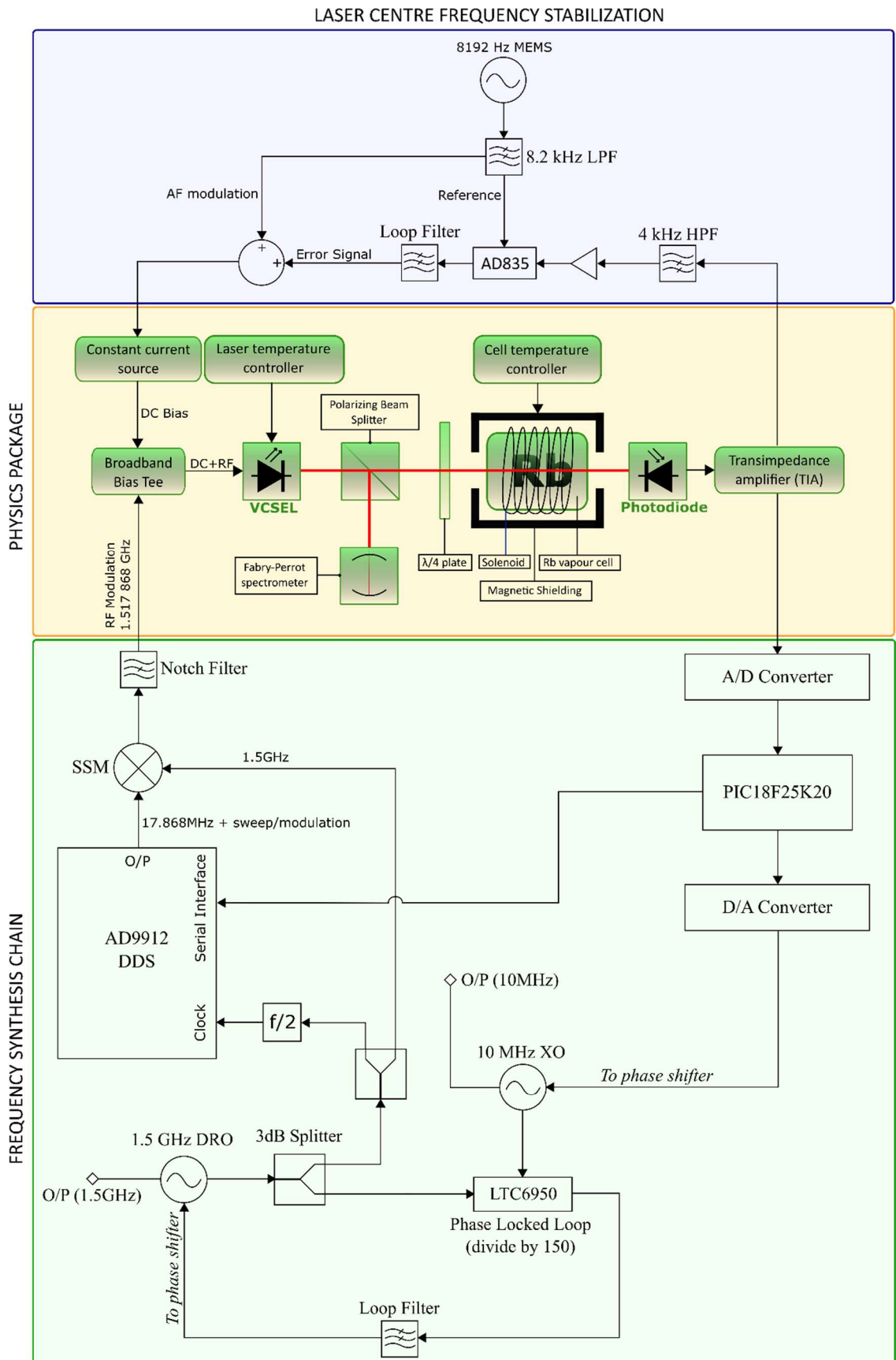


Figure 6-4: Block diagram of the complete atomic clock configuration.

The AD7195 ultra-low noise, 24-bit, delta-sigma A/D converter was chosen in combination with the AD5791 low noise, 20-bit, voltage output D/A converter from Analog Devices. The AD420 (2.048V) and AD425 (5V) voltage references were used, as recommended in the converters datasheets. The recommended op amps (AD8676) were also used as buffers for the references and output of the DAC. It must be noted that, because the minimum reference voltage specified for the AD5791 is 5V, the output had to be attenuated to 1V (full scale) using a potential divider, in order to achieve the 1uHz resolution at the crystal oscillator. The converters were interfaced with and controlled by the PIC18F25K20 microcontroller. Figure 6-5 shows the block diagram of the circuit configuration.

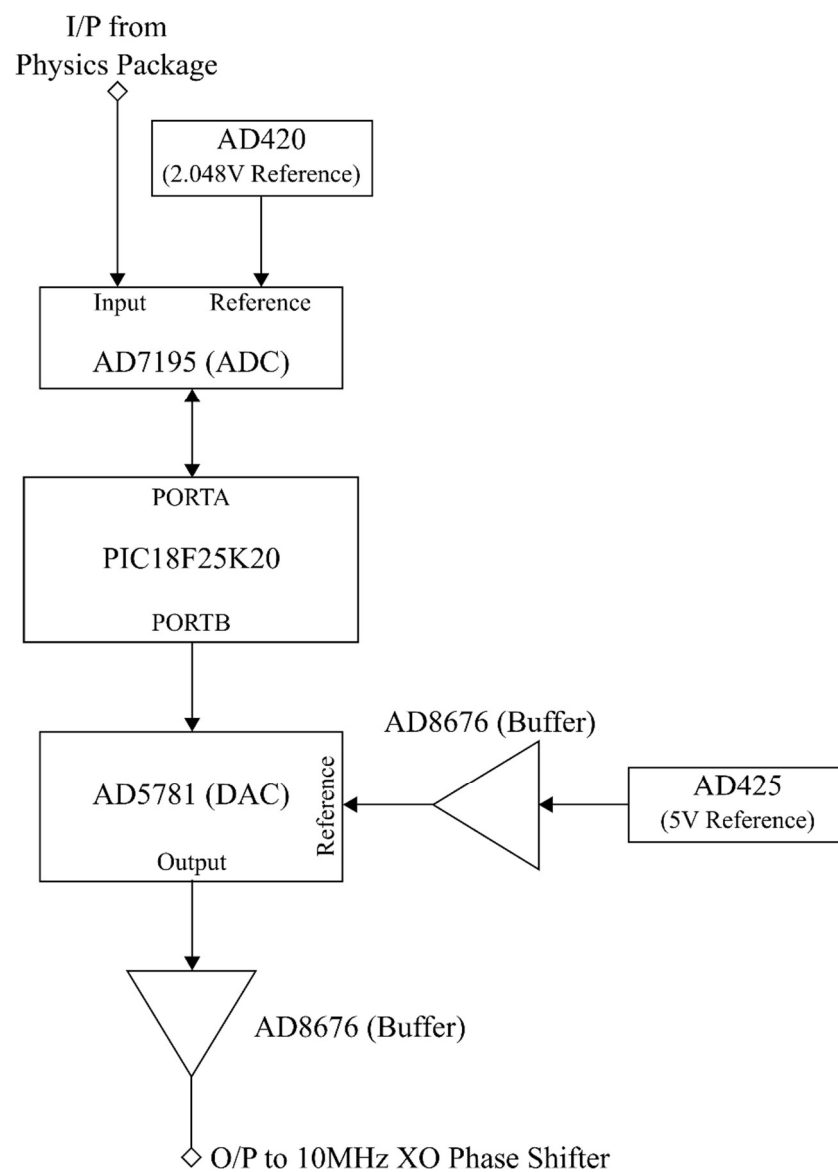


Figure 6-5: Block diagram of the digital atomic resonance lock circuit.

Figure 6-6 and Figure 6-7 show the circuit diagram.

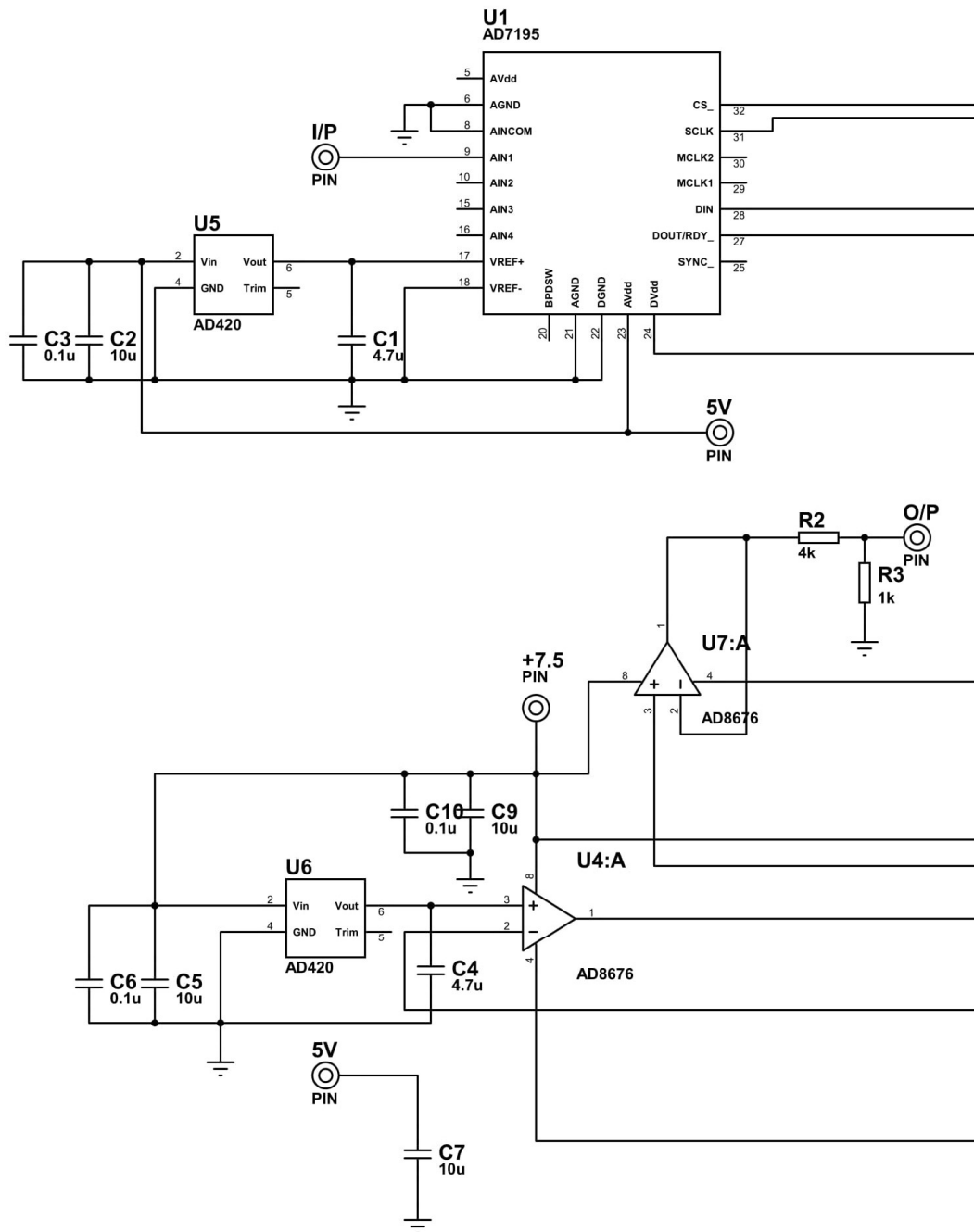


Figure 6-6: Circuit diagram of the digital atomic resonance lock circuit (part 1).

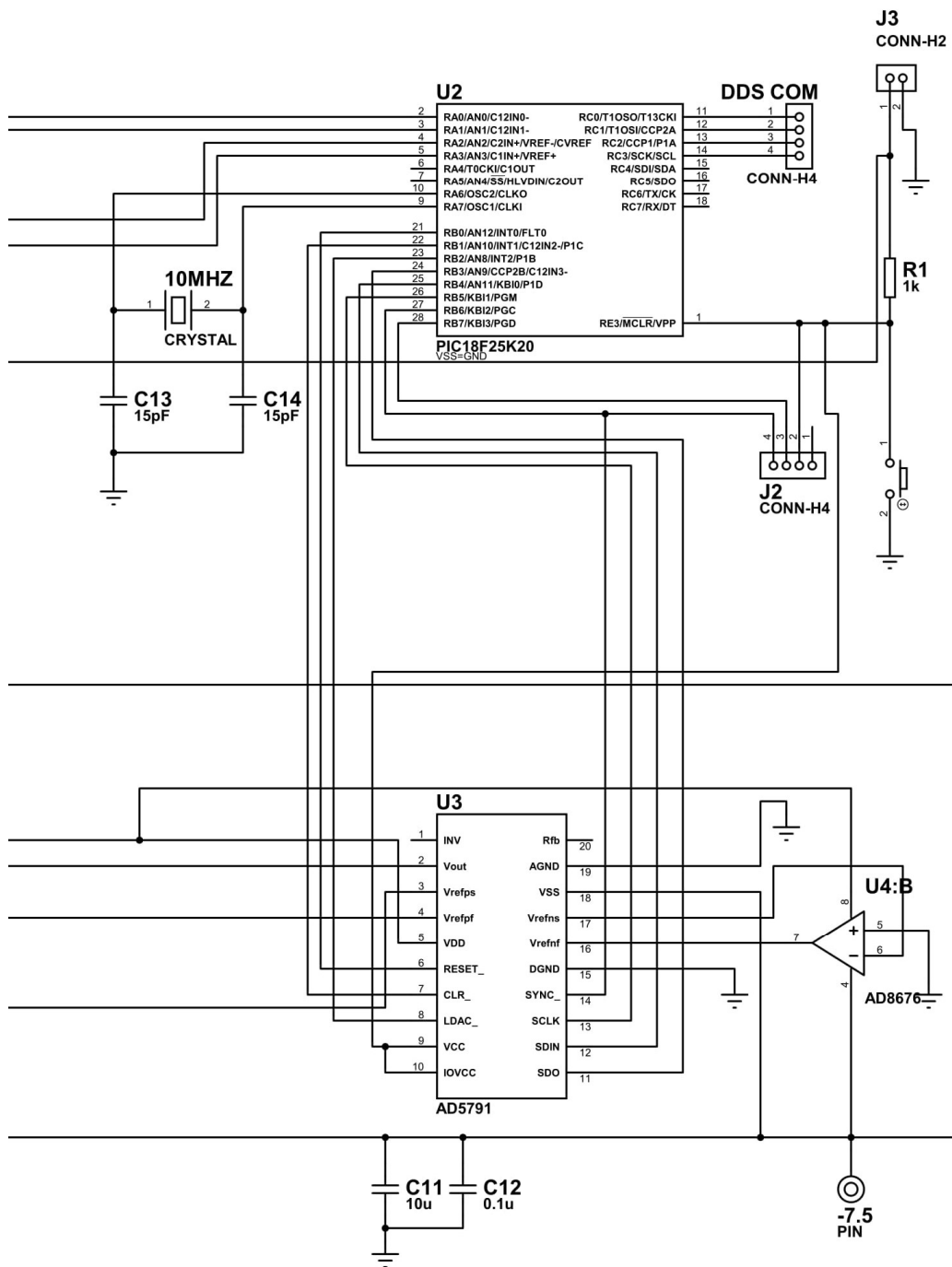


Figure 6-7: Circuit diagram of the digital atomic resonance lock circuit (part 2).

Note: The J2 and J3 connectors are used to connect the PICKit2 for in-circuit programming and debugging of the microcontroller. The “10MHz CRYSTAL” part is a surface mount crystal used to clock the microcontroller (not to be confused with the ultra-low phase noise crystal oscillator of the synthesizer). Resistors R2 and R3 are the potential divider used to reduce the DAC full scale voltage to 1V.

The circuit was designed and built (Figure 6-8). The microcontroller code was written in MikroC Pro compiler and it is included in Appendix A of this thesis. The data must be communicated to and from the converters through the serial interface in individual bytes, however operations must be done on the full 24-bit ADC samples. For this reason, the data was organized in unions. This enables the declaration of variables of different types that share the same memory and data. One long unsigned integer variable holds the full samples, while an array of 3 char variables hold the individual bytes. Any operations done on the integer are automatically assigned to the individual bytes as well. The processes of reading and writing data to the converters were organized in separate functions that were called from the main program.

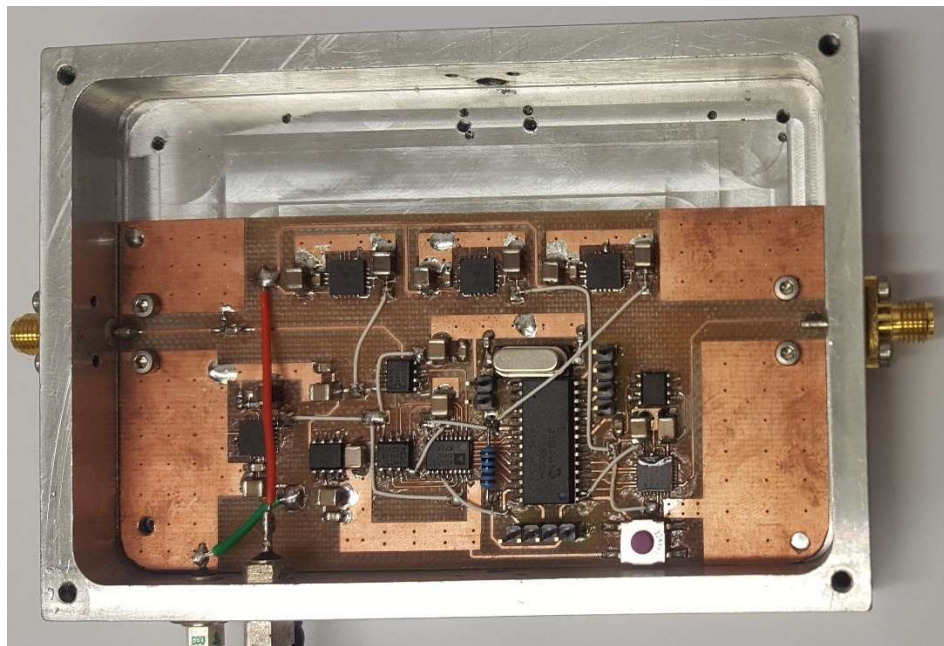


Figure 6-8: Digital hyperfine locking circuit.

Once the circuit was implemented and the microcontroller was programmed with the correct algorithm, the system was enabled and the output of the transimpedance amplifier was monitored. The DDS frequency was switched by about 300Hz around the CPT resonance. A square waveform was observed at the output of the photodiode amplifier

indicating that the synthesizer frequency is not in the middle of the CPT resonance (sample 1 and 2 have different amplitudes). The loop was then closed by connecting the DAC output to the phase shifter of the crystal oscillator. The DAC output voltage then stabilized around 0.45V and the square waveform disappeared, indicating that the system has locked to the middle of the hyperfine peak (the two samples have the same amplitude). This was confirmed by introducing a step in the DAC's output voltage and observing how the loop compensates for the deviation in frequency. This step response is shown in Figure 6-9.

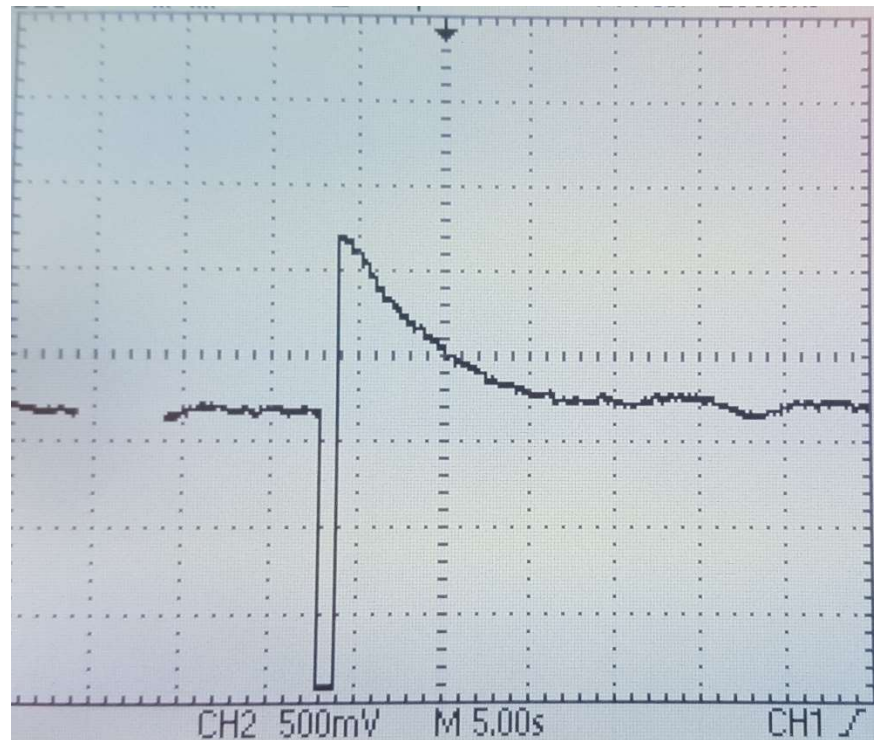


Figure 6-9: Closed loop step response of the DAC output voltage

A series of Allan deviation measurements were taken to evaluate the performance of the locked system. To optimize the loop, its parameters were tuned digitally within the microcontroller code, using delay functions and operations. Unfortunately, the expected improvement in the long term stability was not seen by the time of submission of this thesis. The Allan deviation measurements of the closed loop system were nearly identical to those taken on the free running double oven crystal oscillator. This can be seen in the comparison shown in Figure 6-10.

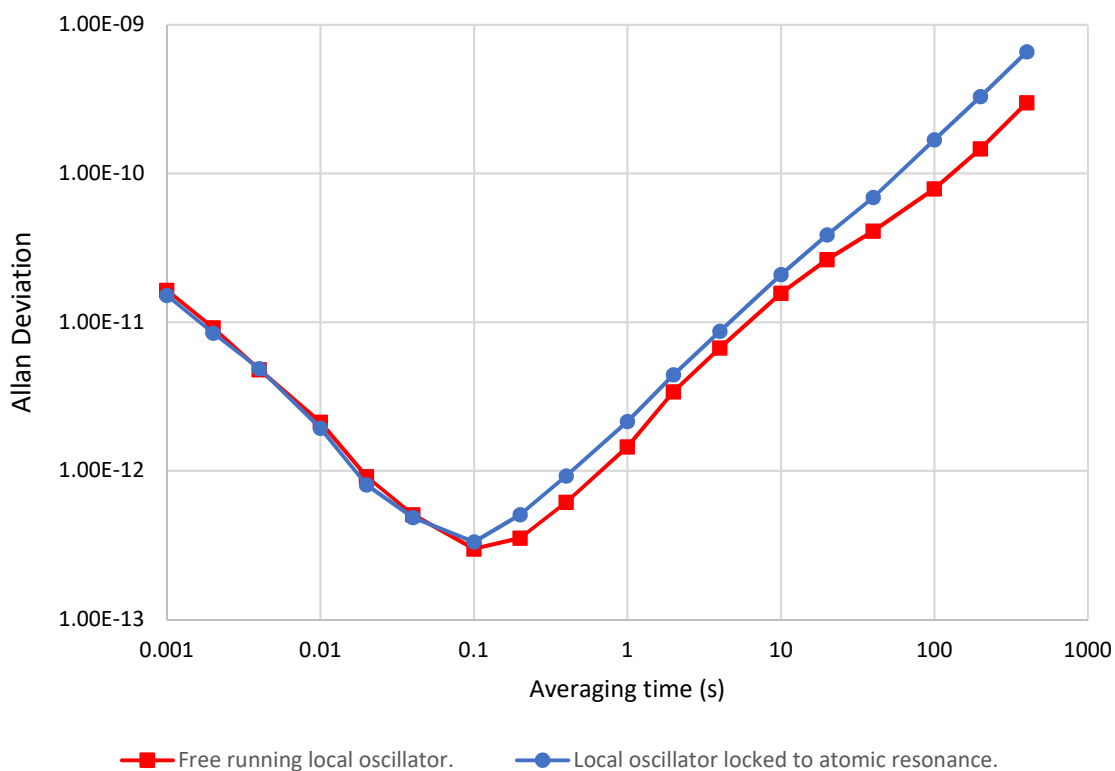


Figure 6-10: Measured Allan deviation of completed CPT system.

A rise in the Allan deviation plot of about one order of magnitude per decade can be observed above 100ms averaging time. The performance up to this point can be attributed mainly to the crystal oscillator. The small difference in the plots can be attributed to the measurements being taken at different times and using the internal reference of the 5120A measurement instrument, which is not temperature stabilized. The atomic resonance lock is supposed to provide better performance at higher averaging times (1s and above), but this was not achieved within the time frame of the project. Possible reasons for this can be:

1. The internal reference of the Symmetricom 5120A measurement instrument was used in these measurements. According to the specifications shown in the device’s manual,  $1 \times 10^{-13}$  is the lowest Allan deviation that can be measured at averaging times of 1s and 10s using the internal reference at the time of purchase. At higher averaging times the Allan deviation floor rises at the same rate as measured. The instrument has been used for several years since the last calibration and the internal reference may not be stable enough to measure the actual long term performance of the CPT clock. This problem can be solved by building a second, identical system

to use as an external reference or by using a reference signal which is more stable than the atomic clock under test, such as a hydrogen maser.

2. The output noise of the DAC or the detection noise from the transimpedance amplifier may be degrading the performance of the system, despite using high precision and low noise components.
3. The atomic resonance is not stable enough. This can be caused by instability in one of the parameters influencing the hyperfine transition frequency. Further evaluation and optimization of the control loops in the physics package, as well as better screening may be required to improve the stability of the resonance.
4. Clock noise in the digital stabilization loop. Noise from the microcontroller can couple into the control loop and degrade the stability of the locked system. An investigation of the noise in the loop is required.

Attempts were made to optimise the system and determine the actual reason for the measured performance, however better measurement results were not obtained within the deadline for submission of this thesis. The steps that can be taken to improve the quality of the measurements and properly evaluate the system's performance are discussed in the future work section.

## 7 CONCLUSIONS AND FUTURE WORK.

This thesis described the design and implementation of a complete atomic clock system from first principles. A multi-element, ultra-low phase noise local oscillator was designed and built, which was combined with a digitally controlled synthesis chain incorporating microcontrollers, direct digital synthesizers and dividers. The resulting system shows a phase noise performance comparable or better than the commercially available oscillator configurations, capable of producing the microwave signal required for interrogating the  $^{85}\text{Rb}$  hyperfine atomic resonance. The system is also has the versatility of applying modulation, frequency switching and sweeping to the output signal.

The resonance interrogation was achieved in a custom built, compact physics package based on coherent population trapping. This section discusses the conclusions drawn from the development and testing of each major component of the system, as well as suggestions for the future development and optimization.

### 7.1 Local Oscillator.

The 10MHz crystal oscillator design has gone through multiple iterations, gradually reducing its size, while maintaining a level of performance similar to the original prototype. It was found that the quality of the components used in the oscillator electronics has a major impact on the phase noise performance. The best performance was achieved with high Q inductors, thin film resistors and polystyrene capacitors. This is one of the main challenges of miniaturizing the design, as the components had to be replaced with smaller ones with similar quality. The latest version of the oscillator has dimensions of about 52x52x55mm, which includes the oscillator electronics, resonator and two stages of temperature stabilization. The oscillator exhibits close to carrier phase noise of about  $-122\text{dBc}/\text{Hz}$  at 1Hz offset, which is similar to the performance of the best commercially available crystal and BVA oscillators. Further improvement of the performance can potentially be achieved by designing vacuum enclosures for the crystal resonator and electronics for improved thermal insulation, a more precise measurement and stabilization to the resonator's inversion temperature and improved electromagnetic screening. The design can also be modified to use a single voltage power supply (symmetrical  $\pm 6\text{V}$  power

supply is currently used). The design of the active stage, phase shifter and filter can also be modified and used with a 5MHz BVA resonator, which can further improve the phase noise and stability performance.

The 1.5GHz Dielectric Resonator Oscillator was built using broadband feedback push-pull amplifiers. The PCB layout and choice of components were found to have significant impact on the amplifier's gain, noise figure and stability and should therefore be considered carefully during the design process. Electronic tuning of the DRO's frequency was achieved using a varactor based phase shifter. The phase shifter incorporates a quarter wave microstrip transformer, which reduces non-linearities in the phase tuning characteristics caused by the increased RF voltage swing across the varactor diodes. The measured phase noise performance of the DRO is in good agreement with the theoretical prediction as shown in Figure 3-45. Further improvement can be achieved by reducing the noise figure of the amplifiers and increasing the oscillator power. The oscillator can also be re-designed in a more compact, integrated package. The cavity can be made smaller and the amplifiers and phase shifter can be incorporated into a single PCB.

The 1.5GHz DRO was phase locked to the 10MHz crystal oscillator. The phase noise of the phase locked configuration approached the performance of the crystal oscillator at close to carrier offsets and the noise floor of the DRO at high offsets. This can be potentially improved further by incorporating the phase locked loop chip into the oscillator PCB and optimization of the loop parameters. An alternative phase locked loop can also be designed with improved dividers and phase detectors.

## 7.2 Frequency Synthesizer.

The output of the 1.5 GHz DRO was divided by 2 using a low-noise divider (LTC6954) and used to clock the AD9912 direct digital synthesizer. A PIC microcontroller was used to control, tune and modulate the output frequency of the DDS, while simultaneously sampling and processing the resonance signal from the physics package. A single sideband mixer was designed that upconverts the DRO signal by the offset provided by the DDS and a high-Q notch filter was designed to suppress the unwanted LO feedthrough by more than 30dB. An advantage of the digital control is that the resonance detection method, loop parameters and signal processing can be altered simply by editing the code executed by the

microcontroller. A disadvantage is the added digital circuit and quantization noise. Future work can investigate potential analogue methods of generating the required signals or optimization of the microcontroller code to improve the performance of the system. Similar synthesizer topology can also be used to produce the 3.417GHz frequency required for interrogation of the  $^{87}\text{Rb}$  atomic resonance.

### 7.3 Physics Package.

The  $^{85}\text{Rb}$  CPT physics package was designed and constructed from first principles. It went through multiple iterations, which enabled experimental investigation of the main factors affecting the stability, contrast and shape of the atomic resonance. Experiments were conducted on the influence of magnetic fields, vapour cell temperature, light polarization, laser modulation power, light shift, etc. These experiments provided a better understanding of the processes involved. The latest version of the physics package was built as a compact unit with interchangeable parts. The low-noise, regulated laser current source and temperature controllers were designed and incorporated into the package. Custom made optical mounts and photodiode assembly were designed for better control over the alignment, collimation and polarization of the laser beam. It was shown that the latest version of the physics package can achieve significantly better resonance amplitude and signal to noise ratio than the initial iterations. Further miniaturization of the physics package is still possible. If easy replacement of components is no longer required for the purpose of experimentation, all the optical components and enclosures can be integrated into a single block. The insulation of the temperature controlled components can also be improved.

### 7.4 Complete Atomic Clock.

The local oscillator, frequency synthesizer and physics package were combined to complete the atomic clock. Although the local oscillator performed as expected, the latest Allan deviation measurements only showed satisfactory performance up to 100ms averaging times. Although frequency lock to the atomic resonance was confirmed by monitoring the feedback signals, no significant improvement in the long term stability was

observed and attempts to optimize the frequency control loop and find any source of instability haven't been successful at the time of submission of this thesis. The measurement could be limited by the stability of the internal reference of the instrument (Symmetricom 5120A). In this case a more stable external reference or the construction of a second, identical system will be required to obtain a valid measurement. It is planned to perform further long-term stability measurements at NPL using a variety of reference clocks, including a hydrogen MASER with Allan deviation of parts in  $10^{-15}$ . A thorough investigation of the noise in the feedback loops and sources of instability in the atomic resonance can also indicate ways for future improvement. Possible sources of noise that need to be investigated include:

- Microcontroller clock noise, which can be coupled into the feedback loop and compromise the stability.
- Digitization noise and sampling uncertainty added by the digital stabilization loop.
- Noise in the photodiode detector. Including shot noise due to the light intensity reaching the photodiode.
- Noise or instability in the laser centre frequency stabilization circuit.
- Instability in the temperature controllers used in the physics package (laser or vapour cell).
- Instability caused by spurious magnetic fields. The effectiveness of the mu-metal shielding should be investigated in more detail.

The instabilities coming from these parameters should be quantified, normalized and expressed in terms of resonance frequency stability. It should be determined whether these parameters are stable enough to achieve frequency stability in the order of a few parts in  $10^{-13}$ , which was the initial goal for this project.

More advanced algorithms for stabilizing to the atomic resonance should also be investigated as a means for improving performance. Better statistical analysis of the samples taken from the resonance may also be required.

# APPENDIX A: MICROCONTROLLER CODE

## 1. DDS Sweep through the hyperfine resonance (section 6.1)

```
unsigned long int freq_word=0;
union U32_
{
    unsigned long int instr;    // For accessing the whole 32-bit
    unsigned int
        unsigned char byte[4]; // For accessing 32-bits as individual bytes
}mu, *mup;
void prog_dds(char instrbyte1, char instrbyte0, char freqtune1, char
freqtune0)
//Function for programming the DDS through the serial com port
{
LATB.B2=0;           //Set CSB to 0 to start the transfer
LATB.B0=0;
LATB.B1=instrbyte1.B7; //Send first bit to the output register
LATB.B0=1;           //Clock in the bit to the DDS
LATB.B0=0;
LATB.B1=instrbyte1.B6;
LATB.B0=1;
LATB.B0=0;
LATB.B1=instrbyte1.B5;
LATB.B0=1;
LATB.B0=0;
LATB.B1=instrbyte1.B4;
LATB.B0=1;
LATB.B0=0;
LATB.B1=instrbyte1.B3;
LATB.B0=1;
LATB.B0=0;
LATB.B1=instrbyte1.B2;
LATB.B0=1;
LATB.B0=0;
LATB.B1=instrbyte1.B1;
LATB.B0=1;
LATB.B0=0;
LATB.B1=instrbyte1.B0;
LATB.B0=1;
LATB.B0=0;
LATB.B1=instrbyte0.B7;
LATB.B0=1;
LATB.B0=0;
LATB.B1=instrbyte0.B6;
LATB.B0=1;
LATB.B0=0;
LATB.B1=instrbyte0.B5;
LATB.B0=1;
LATB.B0=0;
LATB.B1=instrbyte0.B4;
LATB.B0=1;
LATB.B0=0;
LATB.B1=instrbyte0.B3;
LATB.B0=1;
LATB.B0=0;
LATB.B1=instrbyte0.B2;
```

```

LATB.B0=1;
LATB.B0=0;
LATB.B1=instrbyte0.B1;
LATB.B0=1;
LATB.B0=0;
LATB.B1=instrbyte0.B0;
LATB.B0=1;
LATB.B0=0;
LATB.B1=freqtune1.B7;
LATB.B0=1;
LATB.B0=0;
LATB.B1=freqtune1.B6;
LATB.B0=1;
LATB.B0=0;
LATB.B1=freqtune1.B5;
LATB.B0=1;
LATB.B0=0;
LATB.B1=freqtune1.B4;
LATB.B0=1;
LATB.B0=0;
LATB.B1=freqtune1.B3;
LATB.B0=1;
LATB.B0=0;
LATB.B1=freqtune1.B2;
LATB.B0=1;
LATB.B0=0;
LATB.B1=freqtune1.B1;
LATB.B0=1;
LATB.B0=0;
LATB.B1=freqtune1.B0;
LATB.B0=1;
LATB.B0=0;
LATB.B1=freqtune0.B7;
LATB.B0=1;
LATB.B0=0;
LATB.B1=freqtune0.B6;
LATB.B0=1;
LATB.B0=0;
LATB.B1=freqtune0.B5;
LATB.B0=1;
LATB.B0=0;
LATB.B1=freqtune0.B4;
LATB.B0=1;
LATB.B0=0;
LATB.B1=freqtune0.B3;
LATB.B0=1;
LATB.B0=0;
LATB.B1=freqtune0.B2;
LATB.B0=1;
LATB.B0=0;
LATB.B1=freqtune0.B1;
LATB.B0=1;
LATB.B0=0;
LATB.B1=freqtune0.B0;
LATB.B0=1;
LATB.B0=0;

LATB.B2=1; //Raise CSB to complete the transfer.
LATB.B3=1; //Raise I/O Update to apply the changes.
LATB.B3=0; //Clear I/O Update again.

```

```

}

void main() {
TRISB=0x00;
LATB.B4=1; //LED on.
//Set the CSB, SCLK, SDIO, I/O Update pins with initial values to prepare
for transfer.
LATB.B2=1; //CSB
LATB.B1=0; //SDIO
//LATB.B0=1; //SCLK
LATB.B3=0; //I/O Update
mup=&mu; //Assign a pointer to the union.
while(1)
{
mu.instr=0x21AB0619; //Instruction to set the DDS to about
17.866MHz
prog_dds(mu.byte[3], mu.byte[2], mu.byte[1], mu.byte[0]);
for (mu.instr=0x21A9AB00; mu.instr<0x21A9AD00; mu.instr+=1)
//Perform sweep of about 10kHz around the 17.866MHz
{
prog_dds(mu.byte[3], mu.byte[2], mu.byte[1], mu.byte[0]);
delay_ms(1);
}
//prog_dds(0x21, 0xAB, 0x06, 0x19);
//delay_ms(500);
//prog_dds(0x21, 0xAB, 0x06, 0x1A);
//delay_ms(500);
}
}

```

## 2. DDS Switching frequency around the resonance, sampling ADC and programming DAC (section 6.2).

```
unsigned long int dds_word=0;
unsigned long int adc_sample1;
unsigned long int adc_sample2;
int i;
union Udds_
{
    unsigned long int dds_instr;        // For accessing the whole 32-bit
unsigned int
    unsigned char dds_byte[4]; // For accessing 32-bits as individual
bytes
}ddsu, *ddsup;
union Uadc_
{
    unsigned long int adc_data;        // For accessing the whole 24-bit
unsigned int
    unsigned char adc_byte[4]; // For accessing 24-bits as individual
bytes
}adcu, *adcup;
union Udac_
{
    unsigned long int dac_data;        // For accessing the whole 24-bit
unsigned int
    unsigned char dac_byte[4]; // For accessing 24-bits as individual
bytes
}dacu, *dacup;
void prog_dds(char instrbyte1, char instrbyte0, char freqtune1, char
freqtune0)
//DDS serial communication function
{

LATC.B2=0;        //Set CSB to 0 to start the transfer
LATC.B0=0;
LATC.B1=instrbyte1.B7;
LATC.B0=1;
LATC.B0=0;
LATC.B1=instrbyte1.B6;
LATC.B0=1;
LATC.B0=0;
LATC.B1=instrbyte1.B5;
LATC.B0=1;
LATC.B0=0;
LATC.B1=instrbyte1.B4;
LATC.B0=1;
LATC.B0=0;
LATC.B1=instrbyte1.B3;
LATC.B0=1;
LATC.B0=0;
LATC.B1=instrbyte1.B2;
LATC.B0=1;
LATC.B0=0;
LATC.B1=instrbyte1.B1;
LATC.B0=1;
LATC.B0=0;
LATC.B1=instrbyte1.B0;
LATC.B0=1;
```

```

LATC.B0=0;
LATC.B1=instrbyte0.B7;
LATC.B0=1;
LATC.B0=0;
LATC.B1=instrbyte0.B6;
LATC.B0=1;
LATC.B0=0;
LATC.B1=instrbyte0.B5;
LATC.B0=1;
LATC.B0=0;
LATC.B1=instrbyte0.B4;
LATC.B0=1;
LATC.B0=0;
LATC.B1=instrbyte0.B3;
LATC.B0=1;
LATC.B0=0;
LATC.B1=instrbyte0.B2;
LATC.B0=1;
LATC.B0=0;
LATC.B1=instrbyte0.B1;
LATC.B0=1;
LATC.B0=0;
LATC.B1=instrbyte0.B0;
LATC.B0=1;
LATC.B0=0;

LATC.B1=freqtune1.B7;
LATC.B0=1;
LATC.B0=0;
LATC.B1=freqtune1.B6;
LATC.B0=1;
LATC.B0=0;
LATC.B1=freqtune1.B5;
LATC.B0=1;
LATC.B0=0;
LATC.B1=freqtune1.B4;
LATC.B0=1;
LATC.B0=0;
LATC.B1=freqtune1.B3;
LATC.B0=1;
LATC.B0=0;
LATC.B1=freqtune1.B2;
LATC.B0=1;
LATC.B0=0;
LATC.B1=freqtune1.B1;
LATC.B0=1;
LATC.B0=0;
LATC.B1=freqtune1.B0;
LATC.B0=1;
LATC.B0=0;
LATC.B1=freqtune0.B7;
LATC.B0=1;
LATC.B0=0;
LATC.B1=freqtune0.B6;
LATC.B0=1;
LATC.B0=0;
LATC.B1=freqtune0.B5;
LATC.B0=1;
LATC.B0=0;
LATC.B1=freqtune0.B4;
LATC.B0=1;

```

```

LATC.B0=0;
LATC.B1=freqtune0.B3;
LATC.B0=1;
LATC.B0=0;
LATC.B1=freqtune0.B2;
LATC.B0=1;
LATC.B0=0;
LATC.B1=freqtune0.B1;
LATC.B0=1;
LATC.B0=0;
LATC.B1=freqtune0.B0;
LATC.B0=1;
LATC.B0=0;

LATC.B2=1; //Raise CSB to complete the transfer.
LATC.B3=1; //Raise I/O Update to apply the changes.
LATC.B3=0; //Clear I/O Update again.

}
void init_adc(char com_reg, char mode_reg2, char mode_reg1, char
mode_reg0)
//Serial communication function for initializing the ADC
{
    LATA.B1=0;
    LATA.B2=com_reg.B7;
    LATA.B1=0;
    LATA.B1=1;
    LATA.B2=com_reg.B6;
    LATA.B1=0;
    LATA.B1=1;
    LATA.B2=com_reg.B5;
    LATA.B1=0;
    LATA.B1=1;
    LATA.B2=com_reg.B4;
    LATA.B1=0;
    LATA.B1=1;
    LATA.B2=com_reg.B3;
    LATA.B1=0;
    LATA.B1=1;
    LATA.B2=com_reg.B2;
    LATA.B1=0;
    LATA.B1=1;
    LATA.B2=com_reg.B1;
    LATA.B1=0;
    LATA.B1=1;
    LATA.B2=com_reg.B0;
    LATA.B1=0;
    LATA.B1=1;
    LATA.B2=mode_reg2.B7;
    LATA.B1=0;
    LATA.B1=1;
    LATA.B2=mode_reg2.B6;
    LATA.B1=0;
    LATA.B1=1;
    LATA.B2=mode_reg2.B5;
    LATA.B1=0;
    LATA.B1=1;
    LATA.B2=mode_reg2.B4;
    LATA.B1=0;
    LATA.B1=1;
    LATA.B2=mode_reg2.B3;

```

```

LATA.B1=0;
LATA.B1=1;
LATA.B2=mode_reg2.B2;
LATA.B1=0;
LATA.B1=1;
LATA.B2=mode_reg2.B1;
LATA.B1=0;
LATA.B1=1;
LATA.B2=mode_reg2.B0;
LATA.B1=0;
LATA.B1=1;
LATA.B2=mode_reg1.B7;
LATA.B1=0;
LATA.B1=1;
LATA.B2=mode_reg1.B6;
LATA.B1=0;
LATA.B1=1;
LATA.B2=mode_reg1.B5;
LATA.B1=0;
LATA.B1=1;
LATA.B2=mode_reg1.B4;
LATA.B1=0;
LATA.B1=1;
LATA.B2=mode_reg1.B3;
LATA.B1=0;
LATA.B1=1;
LATA.B2=mode_reg1.B2;
LATA.B1=0;
LATA.B1=1;
LATA.B2=mode_reg1.B1;
LATA.B1=0;
LATA.B1=1;
LATA.B2=mode_reg1.B0;
LATA.B1=0;
LATA.B1=1;
LATA.B2=mode_reg0.B7;
LATA.B1=0;
LATA.B1=1;
LATA.B2=mode_reg0.B6;
LATA.B1=0;
LATA.B1=1;
LATA.B2=mode_reg0.B5;
LATA.B1=0;
LATA.B1=1;
LATA.B2=mode_reg0.B4;
LATA.B1=0;
LATA.B1=1;
LATA.B2=mode_reg0.B3;
LATA.B1=0;
LATA.B1=1;
LATA.B2=mode_reg0.B2;
LATA.B1=0;
LATA.B1=1;
LATA.B2=mode_reg0.B1;
LATA.B1=0;
LATA.B1=1;
LATA.B2=mode_reg0.B0;
LATA.B1=0;
LATA.B1=1;
//LATA.B0=1;
}

```



```

LATA.B1=1;
adcu.adc_byte[2].B5=PORTA.F3;
LATA.B1=0;
LATA.B1=1;
adcu.adc_byte[2].B4=PORTA.F3;
LATA.B1=0;
LATA.B1=1;
adcu.adc_byte[2].B3=PORTA.F3;
LATA.B1=0;
LATA.B1=1;
adcu.adc_byte[2].B2=PORTA.F3;
LATA.B1=0;
LATA.B1=1;
adcu.adc_byte[2].B1=PORTA.F3;
LATA.B1=0;
LATA.B1=1;
adcu.adc_byte[2].B0=PORTA.F3;
LATA.B1=0;
LATA.B1=1;
adcu.adc_byte[1].B7=PORTA.F3;
LATA.B1=0;
LATA.B1=1;
adcu.adc_byte[1].B6=PORTA.F3;
LATA.B1=0;
LATA.B1=1;
adcu.adc_byte[1].B5=PORTA.F3;
LATA.B1=0;
LATA.B1=1;
adcu.adc_byte[1].B4=PORTA.F3;
LATA.B1=0;
LATA.B1=1;
adcu.adc_byte[1].B3=PORTA.F3;
LATA.B1=0;
LATA.B1=1;
adcu.adc_byte[1].B2=PORTA.F3;
LATA.B1=0;
LATA.B1=1;
adcu.adc_byte[1].B1=PORTA.F3;
LATA.B1=0;
LATA.B1=1;
adcu.adc_byte[1].B0=PORTA.F3;
//LATA.B1=0;
//LATA.B1=1;
//LATA.B0=1;
//return adcu.adc_data;
}
void prog_dac(char dac2, char dac1, char dac0)
//Serial communication function for programming the DAC
{
    LATB.B2=1;
    LATB.B6=0;

    LATB.B4=dac2.B7;
    LATB.B5=1;
    LATB.B5=0;
    LATB.B4=dac2.B6;
    LATB.B5=1;
    LATB.B5=0;
    LATB.B4=dac2.B5;
    LATB.B5=1;
    LATB.B5=0;
}

```

```
LATB.B4=dac2.B4;  
LATB.B5=1;  
LATB.B5=0;  
LATB.B4=dac2.B3;  
LATB.B5=1;  
LATB.B5=0;  
LATB.B4=dac2.B2;  
LATB.B5=1;  
LATB.B5=0;;  
LATB.B4=dac2.B1;  
LATB.B5=1;  
LATB.B5=0;  
LATB.B4=dac2.B0;  
LATB.B5=1;  
LATB.B5=0;  
LATB.B4=dac1.B7;  
LATB.B5=1;  
LATB.B5=0;  
LATB.B4=dac1.B6;  
LATB.B5=1;  
LATB.B5=0;  
LATB.B4=dac1.B5;  
LATB.B5=1;  
LATB.B5=0;  
LATB.B4=dac1.B4;  
LATB.B5=1;  
LATB.B5=0;  
LATB.B4=dac1.B3;  
LATB.B5=1;  
LATB.B5=0;  
LATB.B4=dac1.B2;  
LATB.B5=1;  
LATB.B5=0;  
LATB.B4=dac1.B1;  
LATB.B5=1;  
LATB.B5=0;  
LATB.B4=dac1.B0;  
LATB.B5=1;  
LATB.B5=0;  
LATB.B4=dac0.B7;  
LATB.B5=1;  
LATB.B5=0;  
LATB.B4=dac0.B6;  
LATB.B5=1;  
LATB.B5=0;  
LATB.B4=dac0.B5;  
LATB.B5=1;  
LATB.B5=0;  
LATB.B4=dac0.B4;  
LATB.B5=1;  
LATB.B5=0;  
LATB.B4=dac0.B3;  
LATB.B5=1;  
LATB.B5=0;  
LATB.B4=dac0.B2;  
LATB.B5=1;  
LATB.B5=0;  
LATB.B4=dac0.B1;  
LATB.B5=1;  
LATB.B5=0;  
LATB.B4=dac0.B0;
```

```

    LATB.B5=1;
    LATB.B5=0;

    LATB.B6=1;
    LATB.B2=0;
}

void main() {
ADCON0=0x00;
ANSEL=0x00;
TRISA=0x08;
TRISB=0x00;
TRISC=0x00;

delay_ms(100);

//SBt the CSB, SCLK, SDIO, I/O Update pins with initial values to prepare
for transfer.
LATC.B2=1; //CSB
LATC.B1=0; //SDIO
LATC.B0=1; //SCLK
LATC.B3=0; //I/O Update
ddsup=&ddsu;
PORTA=0xFE;
init_adc (0x10, 0x00, 0x10, 0x18);
//delay_ms(10);

LATB=0b01100111;
delay_ms(100);
prog_dac (0x20, 0x00, 0x10); //Initialize configuration register of
DAC
delay_ms(100);
prog_dac (0x3F, 0xFF, 0xFF); //Set DAC clear code.
delay_ms(100);

dacup=&dacu;
//adcup=&adcu;
//prog_dac(0x18, 0x00, 0x00);

ddsu.dds_instr=0x21AB0619; //Set the DDS frequency to about 17.866MHz
prog_dds(ddsu.dds_byte[3], ddsu.dds_byte[2], ddsu.dds_byte[1],
ddsu.dds_byte[0]);
dacu.dac_data=0x18000000;

while(1)
{
//delay_ms(100);
dds_word=0x21A9A900;
ddsu.dds_instr=dds_word-0x0400; //Set frequency to about 150Hz below
the resoannce
prog_dds(ddsu.dds_byte[3], ddsu.dds_byte[2], ddsu.dds_byte[1],
ddsu.dds_byte[0]); //Program DDS
delay_ms(80);
init_adc (0x08, 0x28, 0x00, 0x00); //Initialize ADC
read_adc(); //Read ADC sample 1
adc_sample1=adcu.adc_data;
delay_ms(80);

    ddsu.dds_instr=dds_word+0x0400; //Set frequency to about 150Hz
above the resonance

```

```

prog_dds(ddsu.dds_byte[3], ddsu.dds_byte[2], ddsu.dds_byte[1],
ddsu.dds_byte[0]); //Program DDS
delay_ms(80);
init_adc (0x08, 0x28, 0x00, 0x00); //Initialize ADC
read_adc(); //Dear ADC sample 2
adc_sample2=adcu.adc_data;
delay_ms(80);

if (adc_sample1>adc_sample2) //Compute difference
dacu.dac_data+=adc_sample1/16-adc_sample2/16; //Reduce or increase the
DAC output depending on the error
else if (adc_sample1<adc_sample2)
dacu.dac_data-=adc_sample2/16-adc_sample1/16;

prog_dac(dacu.dac_byte[3], dacu.dac_byte[2], dacu.dac_byte[1]);
//Program DAC
}
}

```

## APPENDIX B: LIST OF PAPERS

The papers submitted and presented at conferences during this project include:

- [1] Tsvetan Burtichelov, Jeremy Everard, "Low Phase Noise 10MHz Crystal Oscillators", *European Frequency and Time Forum 2016*, York, 2016.
- [2] Tsvetan Burtichelov, Jeremy Everard, "Initial Results on Low Phase Noise Multi-Element Local Oscillator For Use in Atomic Clocks", *International Frequency Control Symposium 2016*, New Orleans, 2016.
- [3] Tsvetan Burtichelov, Jeremy Everard, "Latest Results in the Development of an Ultra-Low Phase Noise Rb CPT Vapour Cell Atomic Clock", *EFTF/IFCS 2017*, Besancon, 2017

# Low Phase Noise 10MHz Crystal Oscillators

Tsvetan Burtichelov, Jeremy Everard

Department of Electronics, University of York, Heslington, York, UK

Email: [tkb502@york.ac.uk](mailto:tkb502@york.ac.uk), [jeremy.everard@york.ac.uk](mailto:jeremy.everard@york.ac.uk),

**Summary:** This paper describes the design and implementation of low phase noise 10MHz Crystal Oscillators which are being used as part of the chain of a local oscillator for use in compact atomic clocks. The design considerations and phase noise measurements are presented. This paper is based on a previous design [1] but now demonstrates significantly improved phase noise performance and now includes the key circuit descriptions.

**Introduction:** The short and medium term phase noise and Allan deviation of the local oscillator is one of the limiting factors of the performance of most systems including vapour cell atomic clocks. Extremely low phase noise can be achieved by combining the close to carrier performance of crystal oscillators with the medium offset and the low noise floor of a DRO [2] and the narrow band digitally controlled tuning of a Direct Digital Synthesiser [3]. The resulting system is highly versatile in terms of tuning and locking the frequency to the atomic resonance and in terms of providing multiple highly stable output signals at both RF and Microwave frequencies.

**Design:** The design of the crystal oscillators (the main concentration of this paper) is based on a feedback configuration which incorporates an amplifier, an electronic phase shifter for narrowband frequency tuning and a spurious oscillation rejection filter. The broadband amplifier includes a transformer coupled differential amplifier which simultaneously offers non-saturated limiting, noise matching and low flicker noise performance. The electronically tuned phase shifter is based on a 5th order high pass Butterworth filter incorporating varactor diodes and the spurious resonance rejection filter has a similar circuit to the model of the crystal resonator. The oscillator's output signal can be obtained directly from one of the amplifier's outputs without the use of an output coupler.

**Initial Results:** The latest measurements of the 10MHz crystal oscillator's performance show a promising  $-123\text{dBc/Hz}$  phase noise at 1 Hz and  $-148\text{dBc/Hz}$  at 10 Hz. Further improvement in longer term stability is expected through improved temperature stabilization at the turnover temperature of the resonator. These results demonstrate close correlation with the theory [1] [4].

**Acknowledgements:** The authors would like to thank SELEX-ES Ltd. and the UK Engineering and Physical Sciences Research Council (EPSRC) for providing a PhD studentship for Tsvetan Burtichelov.

## References

- [1] Jeremy Everard and Keng Ng, "Ultra-Low Phase Noise Crystal Oscillators", 2007 Joint European Frequency and Time Forum and the IEEE Frequency Control Symposium, Geneva, Switzerland, 29th May to 1st June 2007, pp. 1246-1250.
- [2] Jeremy K.A. Everard and Konstantinos Theodoropoulos 'Ultra-Low Phase Noise Ceramic based Dielectric Resonator Oscillators', IEEE Frequency Control Symposium, Miami USA, June 2006, pp. 869-874.
- [3] See for example the RB-1 and CS-1 produced by Spectra Dynamics ([www.spectradynamics.com](http://www.spectradynamics.com))
- [4] J. Everard, "Fundamentals of RF Circuit Design with Low Noise Oscillators" ISBN 0 47149793 2, Wiley - Dec 2000, reprinted in 2002.

# Initial Results on Low Phase Noise Multi-Element Local Oscillator For Use in Atomic Clocks

Tsvetan Burtichelov and Jeremy Everard

Department of Electronics

University of York

Heslington, York, UK

tkb502@york.ac.uk, jeremy.everard@york.ac.uk

**Abstract**—This paper describes the initial design and implementation of a low phase noise local oscillator for use in compact atomic clocks. The design considerations and initial phase noise measurements are presented. The system consists of a low phase noise Crystal Oscillator operating at 10 MHz and a Dielectric Resonator Oscillator (DRO) operating at 1.5 GHz. Additional components include phase lock loops, dividers, direct Digital Synthesizers and mixers. It is shown that L Band DROs can have better performance than the very best multiplied up 100MHz crystal oscillators at offsets beyond 1Hz (and probably below this). The crystal oscillator demonstrates  $-123\text{dBc/Hz}$  phase noise at 1 Hz and  $-148\text{dBc/Hz}$  at 10 Hz. These results compare well with the phase noise of the best 5MHz BVA oscillators when 6dB ( $\div 2$ ) is subtracted. The 1.5GHz DRO resonator unloaded Q is around 56,000 which is about half the unloaded Q of a typical 100MHz crystal resonator.

**Keywords**—Low noise oscillators, noise, phase noise, crystal oscillators, dielectric resonator oscillators

## I. INTRODUCTION

The short and medium term phase noise and Allan deviation of the local oscillator are some of the limiting factors of the noise performance of most systems including vapour cell atomic clocks. Extremely low phase noise can be achieved by combining the close to carrier performance of crystal oscillators with the medium offset and the low noise floor of a DRO [2] and the narrow band digitally controlled tuning of a Direct Digital Synthesiser [3]. The resulting system is highly versatile in terms of tuning and locking the frequency to the atomic resonance and in terms of providing multiple highly stable output signals at both RF and Microwave frequencies.

## II. DESIGN

The design of the crystal oscillator is based on a previous design [1] but now demonstrates improved phase noise performance and this paper now includes the key circuit descriptions. The oscillator is based on a feedback configuration which incorporates an amplifier, an electronic phase shifter for narrowband frequency tuning and a spurious oscillation rejection filter. The broadband amplifier includes a transformer coupled differential amplifier which simultaneously offers non-saturated limiting, noise matching, low flicker noise performance and crystal power control. The electronically tuned phase shifter is based on a 5th order high

pass Butterworth filter incorporating varactor diodes. The spurious resonance rejection filter has a similar circuit to the equivalent circuit model of the crystal resonator. The oscillator's output signal can be obtained directly from one of the amplifier's outputs without the use of an output coupler.

The 1.5 GHz dielectric resonator used in the DRO has an unloaded Q of  $\sim 56000$  which is about half the unloaded Q of a typical 100MHz crystal. It is mounted inside an aluminium cavity with adjustable height for fine tuning the resonance frequency. A medium power (few 100mW) active bias low flicker noise amplifier is used in the oscillator sustaining stage. Previous DROs operating at 1.25GHz developed by this group [2] have demonstrated a noise performance of  $-173\text{dBc/Hz}$  at 10kHz offset and  $-56\text{dBc/Hz}$  at 1Hz. Similar/significantly better results are expected in the new design due to lower NF, lower flicker noise corner and higher power.

## III. INITIAL PHASE NOISE RESULTS

The latest measurements of the 10MHz crystal oscillator's performance are  $-123\text{dBc/Hz}$  phase noise at 1 Hz and  $-148\text{dBc/Hz}$  at 10 Hz. These results compare well with the phase noise of the best 5MHz BVA oscillators when 6dB ( $\div 2$ ) is subtracted. These results demonstrate close correlation with the theory [1] [4].

## ACKNOWLEDGMENTS

The authors would like to thank Selex-ES Ltd. and the UK Engineering and Physical Sciences Research Council (EPSRC) for providing a PhD studentship for Tsvetan Burtichelov and Dr. David Iddles from Filtronic plc. for his help with the dielectric resonators.

## REFERENCES

- [1] Jeremy Everard and Keng Ng, "Ultra-Low Phase Noise Crystal Oscillators", 2007 Joint European Frequency and Time Forum and the IEEE Frequency Control Symposium, Geneva, Switzerland, 29th May to 1st June 2007, pp. 1246-1250.
- [2] Jeremy K.A. Everard and Konstantinos Theodoropoulos 'Ultra-Low Phase Noise Ceramic based Dielectric Resonator Oscillators', IEEE Frequency Control Symposium, Miami USA, June 2006, pp. 869-874.
- [3] See for example the RB-1 and CS-1 produced by Spectra Dynamics ([www.spectradynamics.com](http://www.spectradynamics.com)).
- [4] J. Everard, "Fundamentals of RF Circuit Design with Low Noise Oscillators" ISBN 0 47149793 2, Wiley - Dec 2000, reprinted in 2002.

This work was supported by: Selex-ES, The UK Engineering and Physical Sciences Research Council (EPSRC) and the University of York.

# Latest Results in the Development of an Ultra-Low Phase Noise Rb CPT Vapour Cell Atomic Clock

Tsvetan Burtichelov and Jeremy Everard

Department of Electronics  
University of York  
York, United Kingdom

[tkb502@york.ac.uk](mailto:tkb502@york.ac.uk), [jeremy.everard@york.ac.uk](mailto:jeremy.everard@york.ac.uk)

**Abstract**— This paper describes the latest progress and results, at the University of York, UK, in the development of an atomic clock based on Coherent Population Trapping (CPT). The clock uses Rubidium and a flywheel local oscillator consisting of an ultra-low phase noise Crystal Oscillator (XO), Dielectric Resonator Oscillator (DRO) and Direct Digital Synthesiser. Aspects of the design and construction of the oscillators, phase locked loop, frequency synthesizer and physics package are presented, along with phase noise and stability measurements.

**Keywords**—Atomic clocks; CPT; Rubidium; Local Oscillator; Phase Noise; Phase Locked Loops.

## I. INTRODUCTION

Recently atomic clocks have been developed to offer high performance in very small packages. See, for example, the chip scale atomic clocks. There is usually a size/performance trade-off in terms of short and long term stability.

The aim of this work is to develop the best performance available in a volume of around a  $\frac{1}{2}$  to a full-size shoe box. Both RF (5/10MHz) and Microwave outputs (1.25 to 1.5GHz) should be provided. The key aims here are to produce ultra-low phase noise and excellent long term stability (ADEV).

To achieve this, almost every element of the clock was developed in house from first principles. The key elements are the frequency synthesiser, the physics package and the locking electronics.

This paper will discuss the key aspects of the:

- 1) Flywheel Local Oscillator
  - a) Single/double oven Crystal oscillators
  - b) Temperature stabilisation
  - c) Dielectric resonator oscillators
  - d) Direct Digital Synthesisers
  - e) Single sideband mixers
- 2) Physics Package
  - a) Vapour cells:
    - i) The Ar/N<sub>2</sub> buffer gas pressures are optimised for low temp. coefficient for the hyperfine lines
    - ii) AR coated to minimise reflections

- b) Ultra low noise laser drive electronics and microwave modulation
  - c) Magnetic screening and magnetic biasing
- 3) Laser centre frequency locking
  - 4) Optical sideband/microwave locking to the hyperfine transitions

## II. SYNTHESIZER DESIGN

The LO in the current system uses an ultra-low phase noise crystal oscillator operating at 10 MHz and a DRO operating between 1.25 to 1.5 GHz with a DDS offset loop incorporating a single sideband mixer. Figure 1 shows a block diagram of the configuration.

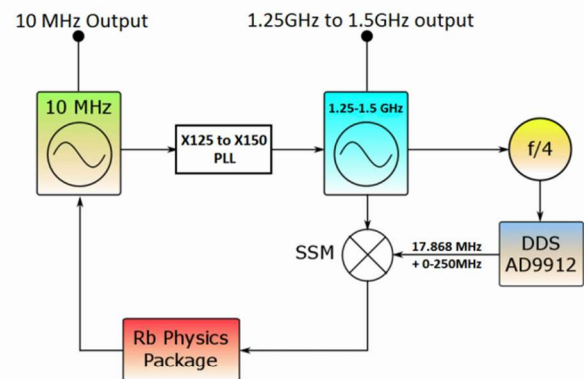
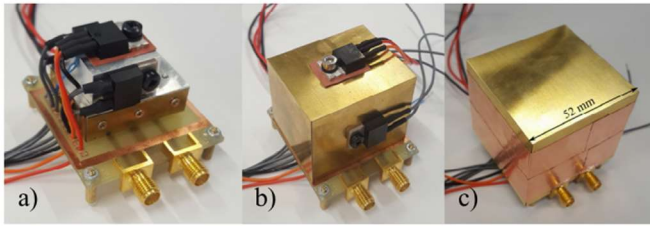


Figure 1: Atomic Clock block diagram.

### A. 10 MHz Double Oven Controlled Crystal Oscillator

The Crystal Oscillator (XO) is based on the design described in [1] and [2], but is now constructed in a significantly more compact package and incorporates a two-stage temperature stabilization. Figure 2 shows the layers of temperature stabilization (double oven) and screening.



**Figure 2: 10 MHz XO. a) Oscillator circuit and resonator enclosure. b) Second enclosure with temperature control. c) Complete oscillator.**

The resonator, along with the oscillator circuit is inserted in a custom made aluminium enclosure. A power transistor and resistors are used as heating elements (figure 1.a). The second and outermost enclosures (figures 1.b and 1.c respectively) are made of chemically etched brass plates. The temperature controllers are designed with low-noise voltage regulators and op amps and high-quality passive components.

The circuit diagram of the oscillator is shown in Figure 3. This was presented in [2], but not included as a proceedings paper.

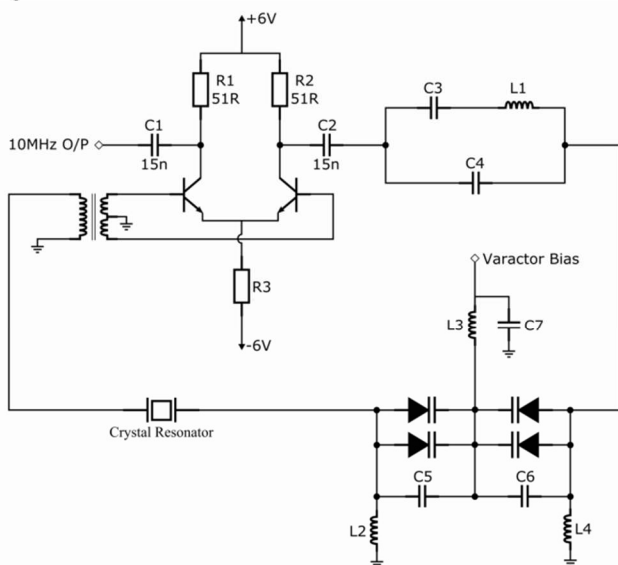


**Figure 3: Circuit diagram of the 10 MHz crystal oscillator.**

The circuit incorporates:

- A transformer coupled differential amplifier with low flicker noise,
- A notch filter designed to avoid oscillation at the 10.9 MHz mode in the crystal.
- An electronically tuned phase shifter for frequency tuning using varactor diodes.

A full journal paper is currently being written, describing in detail the design and operation of the circuit.

### B. 1.5 GHz Dielectric Resonator Oscillator

The design of the DRO is based on the theory and methodology described in [3] and [4]. The microwave output frequency can be preset between 1.25GHz-1.5GHz by changing the Barium Titanite dielectric resonator. The active stage of the oscillator consists of 2 push-pull broadband feedback amplifiers. The output coupler is inserted between the amplifiers to limit saturation effects. An electronic phase shifter is used to phase lock the DRO to the XO. Figure 4 shows the prototype DRO configuration. The resonator enclosure is oversized in this prototype, however the whole oscillator will be made significantly smaller in the final design.

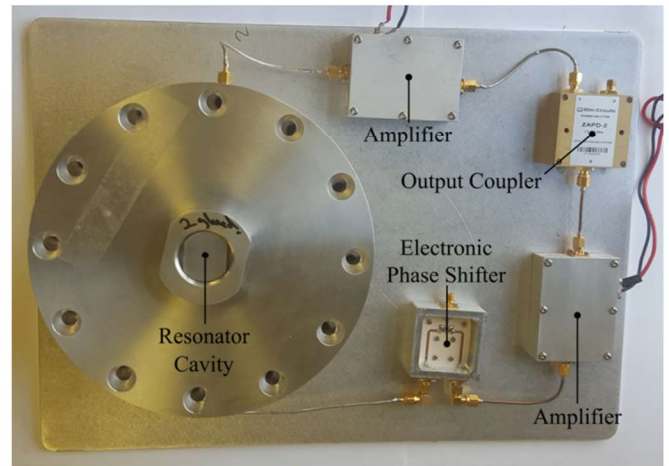


**Figure 4: 1.5 GHz Dielectric Resonator Oscillator.**

### C. Frequency Synthesizer.

Phase locking the DRO to the XO completes the local oscillator, combining the close to carrier phase noise of the XO with the medium and far offset performance of the DRO. Figure 5 shows the phase lock configuration.

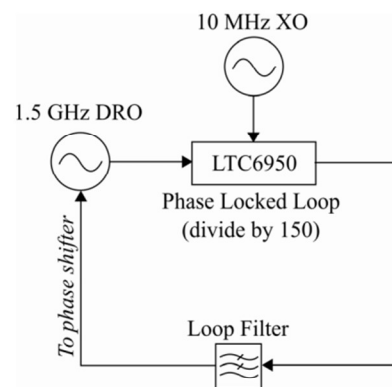


**Figure 5: Block Diagram of PLL configuration.**

A Direct Digital Synthesizer (DDS) chip is clocked by the DRO and used to produce a 17.868 MHz, tuneable signal. A Single Sideband Mixer (SSM) is then used to upconvert the microwave output to 1.517868 GHz, half the hyperfine

splitting frequency of  $^{85}\text{Rb}$ . Figure 6 shows a block diagram of the synthesis chain.

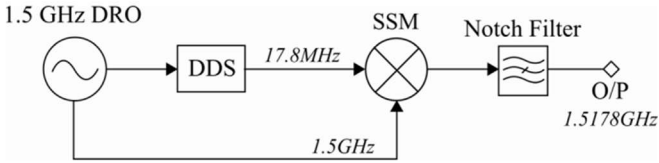


**Figure 6: Synthesis chain block diagram.**

The SSM uses two double balanced mixers. Lumped element and microstrip quadrature dividers were designed, based on the designs in [5], [6], [7]. The two signals are mixed in phase and with  $90^\circ$  phase difference. This resulting output has a high upper sideband (1.5178 GHz), while the lower sideband is suppressed. There is still significant LO (1.5 GHz) feedthrough, since the isolation of the mixers is not perfect. This is further suppressed using a Notch filter, which is based on the design in [8] and incorporates a high-Q ( $\sim 3200$ ) coaxial open circuit stub and microstrip transformer. Figures 7 and 8 show photos of the SSM and Notch filter respectively.

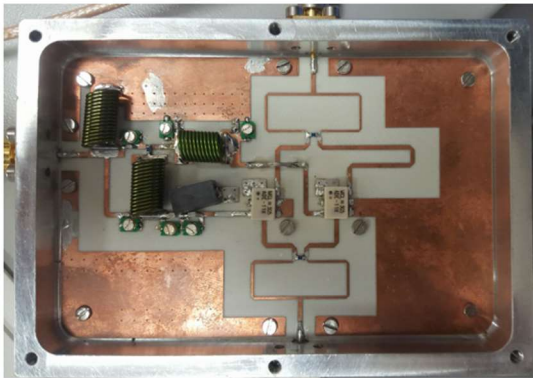


**Figure 7: Single Sideband Mixer.**

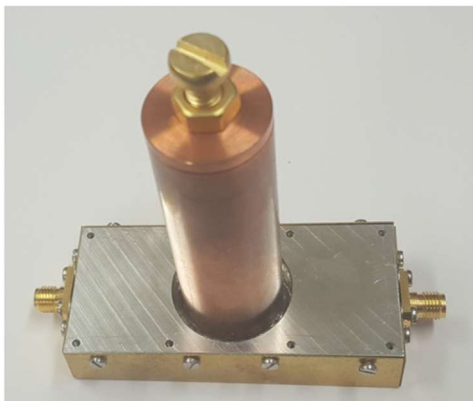


**Figure 8: Coaxial open circuit stub notch filter.**

The filter can be tuned by adjusting the position of the screw. Figure 9 shows the measured frequency response when the notch was tuned to the LO feedthrough frequency. A 30dB notch is achieved with a single filter, while the loss at  $\pm 17$

MHz away from the notch is about 1.5dB. A more compact version of this filter can be built using a ceramic resonator.

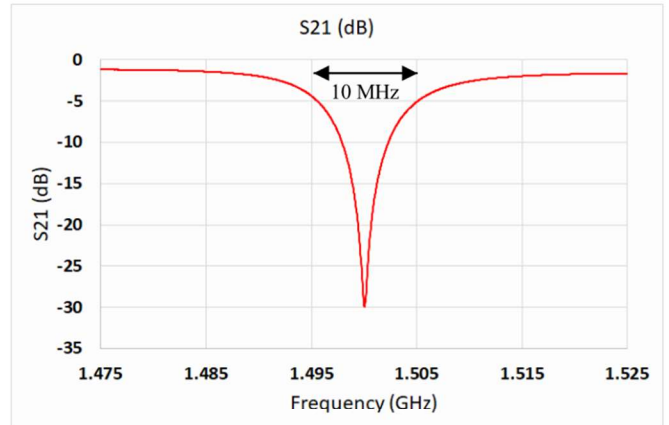


**Figure 9: Notch filter frequency response. (-30dB in the stop band, -1.5dB at  $\pm 15$  MHz)**

### III. PHASE NOISE MEASUREMENTS

The double oven 10 MHz XO phase noise was measured using the Symmetricom 5120A. The performance is shown in Figure 10.

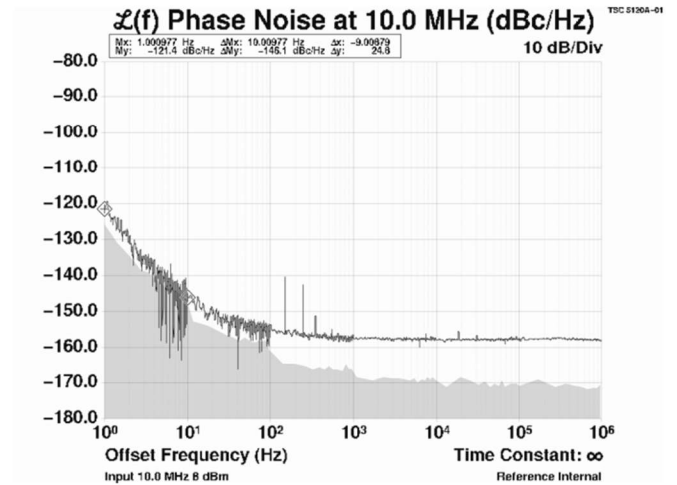


**Figure 10: Double oven XO phase noise.**

The oscillator exhibits a phase noise of -121.4dBc/Hz at 1Hz offset and -145.1dBc/Hz at 10Hz offset.

A preliminary Allan Deviation measurement was also conducted on the oscillator with the double oven stabilization enabled, however the temperature was not exactly set at the inversion point of the crystal. The plot shows an Allan Deviation of  $3 \times 10^{-13}$  at 100ms as presented in Figure 11.

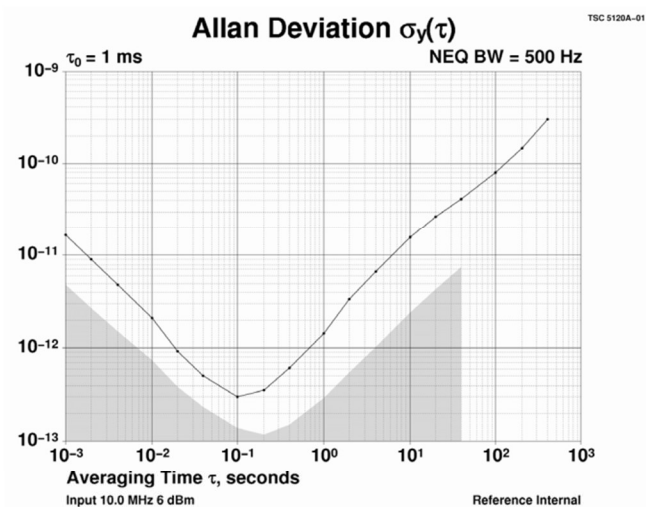


Figure 11: Allan Deviation plot of 10 MHz double oven XO.

The free running DRO was measured by mixing two DROs down to 2.2MHz. The noise floor is set by the measurement system.

The theoretical DRO result is shown in green and based on the following parameters:  $f_0 = 1.5\text{GHz}$ ,  $Q_0 = 43,000$ ,  $Q_L = 21,500$ ,  $P_{AVO} = 200\text{mW}$ , Noise Figure = 11.5dB,  $f_c = 5\text{kHz}$  [3].

The phase locked DRO, shown in blue, was measured directly on an R&S FSWP phase noise analyser. Again, the noise floor is limited by the measurement system.

#### IV. PHASE NOISE PERFORMANCE OF A 1.25GHz DRO

The phase noise performance of a 1.25GHz oscillator measured on a low noise floor single channel HP3048 is shown in Figure 13.

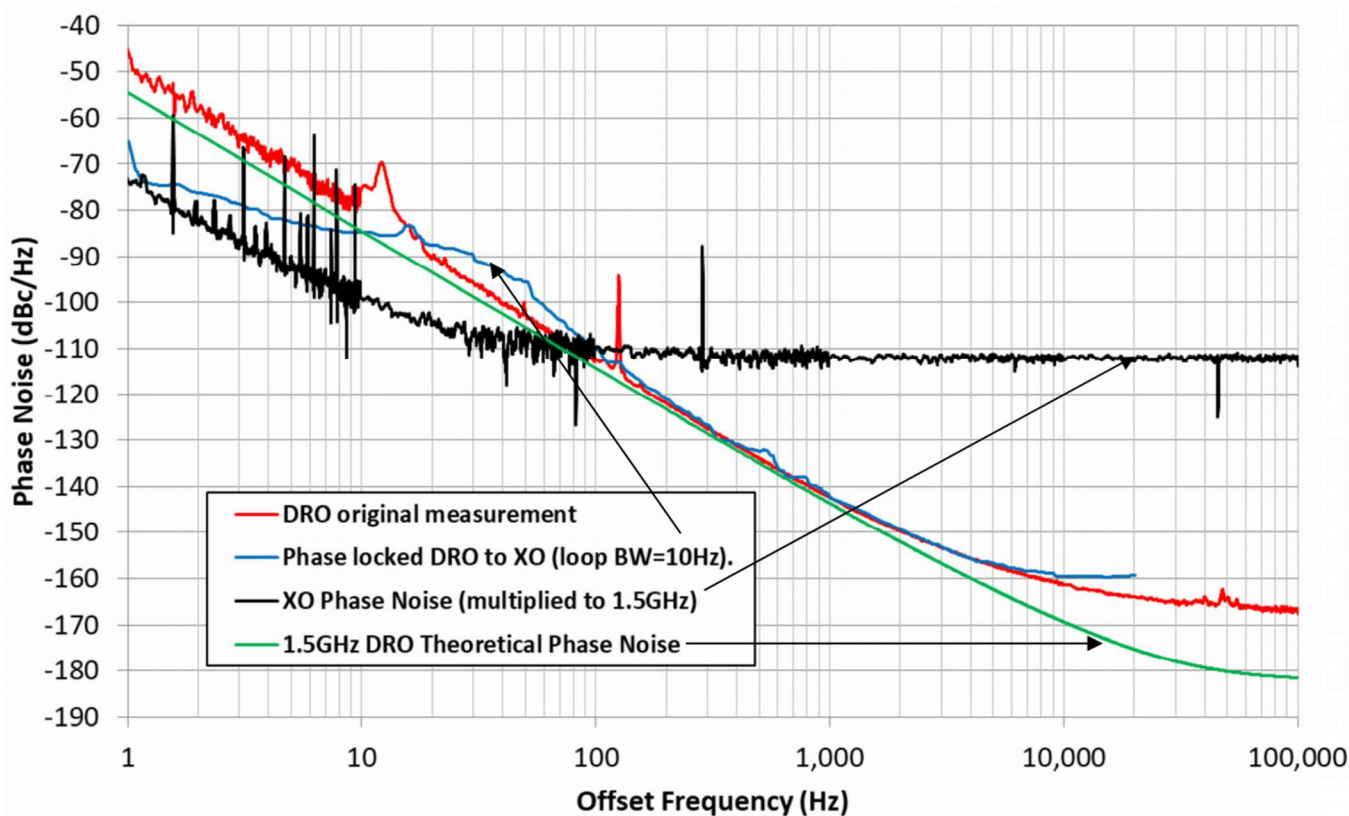


Figure 12: Measured phase noise of free running and phase locked XO and DRO.

Next, the phase locked loop between the XO and DRO was completed and the phase noise of the configuration in Figure 5. This is shown in Figure 12.

The scaled up 10MHz crystal oscillator noise is shown in black.

This demonstrates the low phase noise floor capability of these oscillators. This result is for two oscillators therefore the phase noise performance is -172dBc/Hz at 10kHz offset and < -180dBc/Hz above 50kHz offset.

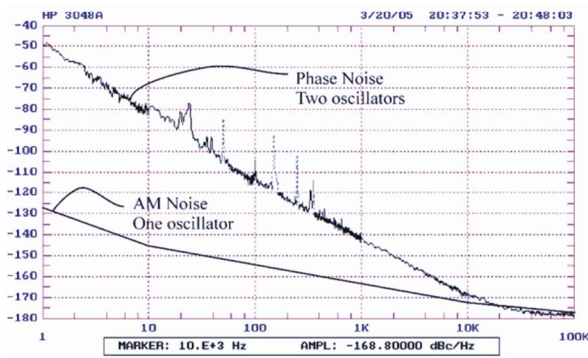


Figure 13: Phase & AM noise for a 1.25GHz DRO

## V. PHYSICS PACKAGE

The physics package consists of a Vertical Cavity Surface Emitting Laser (VCSEL) tuned at the D1 line of  $^{85}\text{Rb}$  atomic transition (795nm), a custom made 25x25 mm vapour cell containing pure  $^{85}\text{Rb}$  and a mixture of buffer gases specified for optimal temperature stability, low noise laser driver electronics and temperature stabilization loops.

A photograph of the AR coated vapour cell with a pair of Helmholtz coils is shown in Figure 14.

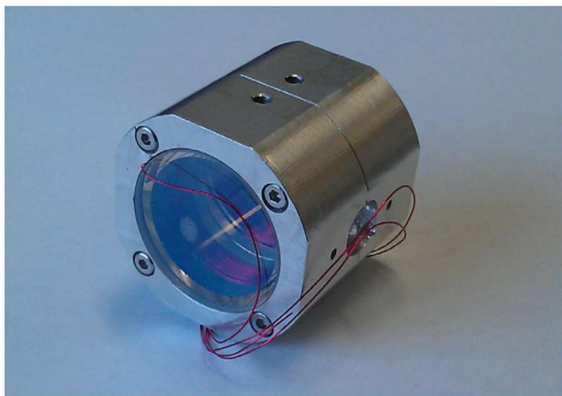


Figure 14: AR coated vapour cell with a pair of Helmholtz coils and optimized Ar/N<sub>2</sub> buffer gas pressures.

Figure 15 shows a photo of the prototype physics package with the optical components and control electronics.

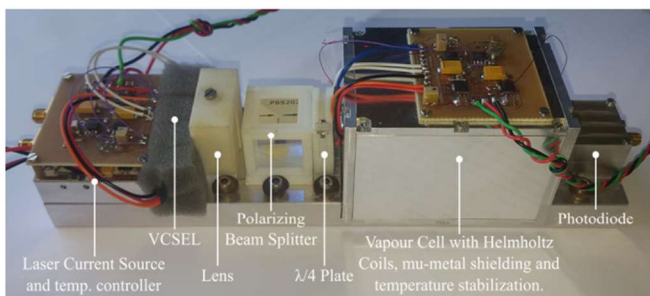


Figure 15: Photo of the  $^{85}\text{Rb}$  physics package.

This prototype was made large to enable ease of alignment. For example, the polarizing beam splitter enables optical measurement of the laser centre frequency and modulation sideband levels using a Fabry-Perot spectrometer. All the mounts, enclosures and control circuits of the physics package were developed from first principles.

## VI. CONCLUSIONS

An ultra-low noise local oscillator and frequency synthesis chain for a Rb CPT atomic clock were designed, incorporating phase locked loops and frequency synthesizer. The local oscillator exhibits excellent phase noise close to carrier, due to the performance of the 10 MHz double oven controlled crystal oscillator. It also exhibits excellent far from carrier phase noise, due to the performance of the 1.5 GHz DRO. By using a direct digital synthesizer, the phase locked microwave signal was upconverted to half of the hyperfine splitting of  $^{85}\text{Rb}$ , which can then be used to detect the CPT resonance. Aspects of the CPT physics package are discussed.

## VII. FURTHER WORK

Future work will be focused on completing the loop, locking the local oscillator to the atomic resonance and performing Allan Deviation and phase noise measurements on the completed system. Measurements will also be conducted using multiple clocks to reduce the noise floor of the measurement. Further optimizations will be performed on the control electronics, phase locked loops and oscillator designs.

## ACKNOWLEDGMENTS

The authors of this paper would like to thank Leonardo MW Ltd. and EPSRC for funding this research, Professor Robert Lamb, Neil Raphael & Stephen Clark at Leonardo MW Ltd for useful discussions and Dr. David Iddles from Filtronic plc. for his help with the dielectric resonators.

## REFERENCES

- [1] Jeremy Everard and Keng Ng, "Ultra-Low Phase Noise Crystal Oscillators", 2007 Joint European Frequency and Time Forum and the IEEE Frequency Control Symposium, Geneva, Switzerland, 29th May to 1st June 2007, pp. 1246-1250.
- [2] Tsvetan Burtichelov, Jeremy Everard, "Low Phase Noise 10MHz Crystal Oscillators", 2016 European Frequency and Time Forum, York, UK, 4th - 7th April 2016
- [3] Jeremy K.A. Everard and Konstantinos Theodoropoulos "Ultra-Low Phase Noise Ceramic based Dielectric Resonator Oscillators", IEEE Frequency Control Symposium, Miami USA, June 2006, pp. 869-874.
- [4] J. Everard, "Fundamentals of RF Circuit Design with Low Noise Oscillators" ISBN 0 47149793 2, Wiley - December 2000, Reprinted October 2002.
- [5] David M. Pozar, "Microwave Engineering", 4th edition, ISBN 978-0-470-63155-3, Wiley - 2012.
- [6] Tadashi Kawai, Hiroyuki Mizuno, Isao Ohta, Akira Enokihara "Lumped-Element Quadrature Wilkinson Power Divider", IEEE, 978-1-4244-2802-1/09, 2009, pp. 1012-1015.
- [7] Fernando Noriega, Pedro J. González, "Designing LC Wilkinson Power Splitters", eefocus.com [Online]. Available: data.eefocus.com/myspace/0/2194/bbs/1190602131/84dbcb80.pdf [Accessed: April 18, 2017]
- [8] J.K.A. Everard, J. Bitterling "Low Phase Noise Highly Power Efficient Oscillators", IEEE, International Frequency Control Symposium, 0-7803-3728-X/97, 1997, pp. 919-924.

# References

- [1] M. A. Lombardi, “The Evolution of Time Measurement, Part 3: Atomic Clocks,” *IEEE Instrumentation & Measurement Magazine*, pp. 46-49, December 2011.
- [2] NPL, “60 years of the atomic clock,” 2015. [Online]. Available: <http://www.npl.co.uk/60-years-of-the-atomic-clock/>. [Accessed 19 July 2017].
- [3] NIST, “The NIST Reference of Constants, units and Uncertainty, International System of Units (SI),” [Online]. Available: <http://physics.nist.gov/cuu/Units/second.html>. [Accessed 18 December 2014].
- [4] Microsemi, “Quantum™ SA.45s CSAC,” 2017. [Online]. Available: [https://www.microsemi.com/document-portal/doc\\_download/133305-quantum-sa-45s-csac](https://www.microsemi.com/document-portal/doc_download/133305-quantum-sa-45s-csac). [Accessed 19 July 2017].
- [5] NIST, “NIST Debuts Dual Atomic Clock — and a New Stability Record,” 28 November 2016. [Online]. Available: <https://www.nist.gov/news-events/news/2016/11/nist-debuts-dual-atomic-clock-and-new-stability-record>. [Accessed 19 July 2017].
- [6] “Model PRS10 Rubidium Frequency Standard Operation and Service Manual,” 21 December 2015. [Online]. Available: <http://www.thinksrs.com/downloads/PDFs/Manuals/PRS10m.pdf>. [Accessed 19 July 2017].
- [7] P. L. Bender, “Atomic Frequency Standards and Clocks,” [Online]. Available: <http://tf.nist.gov/general/pdf/1663.pdf>. [Accessed 18 December 2014].
- [8] “d.i.y. 10MHz Atomic Clock Frequency Standard Using Surplus Rubidium Oscillator,” [Online]. Available: <http://www.diyphysics.com/2012/02/14/d-i-y-10->

mhz-atomic-clock-frequency-standard-using-surplus-rubidium-oscillator/. [Accessed 18 December 2014].

- [9] Sumanta Khan, Molahalli Panidhara Kumar, Vineet Bharti, Vasant Natarajan, “Coherent population trapping (CPT) versus electromagnetically induced transparency (EIT),” *European Physical Journal D*, vol. 71, 2017.
- [10] Shigeyoshi Goka, Taisuke Okura, Munetake Moroyama, Yasuaki Watanabe, “Low Power 85Rb CPT Atomic Clock,” in *IEEE International Frequency Control Symposium*, Honolulu, 2008.
- [11] C. Schori, G. Mileti, B. Leuenbeger, P. Rochat, “CPT Atomic Clock based on Rubidium 85,” in *EFTF-2010 24th European Frequency and Time Forum*, Noordwijk, 2010.
- [12] S. Bize, Y. Sortais, M. S. Santos, C. Mandache, A. Clairon, C. Solomon, “High-accuracy measurement of the 87Rb ground-state hyperfine splitting in an atomic fountain,” *Europhysics Letters*, vol. 45, no. 5, pp. 558-564, 1999.
- [13] Alexander D. Cronin, Jörg Schmiedmayer, David E. Pritchard, “Optics and interferometry with atoms and molecules,” *Reviews of Modern Physics*, vol. 81, pp. 1051-1029, 2009.
- [14] R. Wynands, S. Weyers, “Atomic fountain clocks,” *Metrologia*, vol. 42, pp. S64-S79, 2005.
- [15] Xinliang Wang, Jun Ruan, Hui Zhang, Rui Lin, Dandan Liu, Jiang Chen, Yong Guan, Fengxiang Yu, Junru Shi, Shougang Zhang, “The Optical System of the fountain clock,” in *Frequency Control Symposium (FCS)*, Taipei, 2014.
- [16] Masao Takamoto, Ichiro Ushijima, Manoj Das, Nils Nemitz, Takuya Ohkubo, Kazuhiro Yamanaka, Noriaki Ohmae, Tetsushi Takano, Tomoya Akatsuka, Atsushi Yamaguchi, Hidetoshi Katori, “Frequency ratios of Sr, Yb and Hg based optical lattice clocks and their applications,” 13 May 2015. [Online]. Available:

<https://arxiv.org/abs/1505.03207>. [Accessed 21 July 2017].

- [17] B. J. Bloom, T. L. Nicholson, J. R. Williams, S. L. Campbell, M. Bishof, X. Zhang, W. Zhang, S. L. Bromley & J. Ye, “An optical lattice clock with accuracy and stability at the 10<sup>-18</sup> level,” *Nature*, vol. 506, pp. 71-75, 2014.
- [18] F. Riehle, “Towards a Re-definition of the Second Based on Optical Atomic Clocks,” 28 January 2015. [Online]. Available: <https://arxiv.org/abs/1501.02068>. [Accessed 11 December 2017].
- [19] W. J. Riley, “Techniques for Frequency Stability Analysis,” 4 May 2003. [Online]. Available: <http://www.wiley.com/Techniques.pdf>. [Accessed 11 December 2017].
- [20] D. F. Ramian, “Time Domain Oscillator Stability Measurement Allan variance,” April 2015. [Online]. Available: [https://cdn.rohde-schwarz.com/pws/dl\\_downloads/dl\\_application/application\\_notes/1ef69/1EF69\\_4e\\_TD\\_Osc\\_Stability\\_Allan.pdf](https://cdn.rohde-schwarz.com/pws/dl_downloads/dl_application/application_notes/1ef69/1EF69_4e_TD_Osc_Stability_Allan.pdf). [Accessed 11 December 2017].
- [21] J. Everard, “Low Phase Noise Ceramic Resonator Oscillators,” in *European Frequency and Time Forum*, Toulouse, 2008.
- [22] Jeremy Everard, Konstantinos Theodoropoulos, “Ultra-Low Phase Noise Ceramic based Dielectric Resonator,” in *International Frequency Control Symposium and Exposition*, Miami, 2006.
- [23] Pratik D. Deshpande, Jeremy Everard, “Compact Low Phase Noise 3.8 GHz Oscillator,” in *European Frequency and Time Forum*, Neuchatel, 2014.
- [24] Jeremy Everard, Keng Ng, “Ultra-Low Phase Noise Crystal Oscillators,” in *International Frequency Control Symposium Joint with the 21st European Frequency and Time Forum*, Geneva, 2007.
- [25] C. J. Foot, *Atomic Physics*, Oxford: Oxford University Press, 2005.

- [26] D. A. Steck, “Rubidium 85 D Line Data (revision 2.1.6),” 30 September 2013. [Online]. Available: [http:// http://steck.us/alkalidata](http://steck.us/alkalidata). [Accessed 18 December 2014].
- [27] University of Toronto Physics, “Zeeman effect,” [Online]. Available: <https://www.physics.utoronto.ca/~phy225h/experiments/zeeman-effect/zeeman-effect.pdf>. [Accessed 22 July 2017].
- [28] Y.-Y. Jau, E. Miron, A. B. Post, N. N. Kuzma, and W. Happer, “Push-Pull Optical Pumping of Pure Superposition States,” *Physical Review Letters*, vol. 93, no. 16, 2004.
- [29] Peter Yun, Sinda Mejri, Francois Tricot, Moustafa Abdel Hafiz, Rodolphe Boudot, Emeric de Clercq, Stephane Guerandel, “Double-modulation CPT cesium compact clock,” *Journal of Physics: Conference Series*, vol. 723, 2015.
- [30] RP Photonics, “Vertical Cavity Surface-emitting Lasers,” [Online]. Available: [https://www.rp-photonics.com/vertical\\_cavity\\_surface\\_emitting\\_lasers.html](https://www.rp-photonics.com/vertical_cavity_surface_emitting_lasers.html). [Accessed 11 December 2017].
- [31] Liron Stern, Boris Desiatov, Ilya Goykhman, Uriel Levy, “Nanoscale light–matter interactions in atomic cladding waveguides,” *Nature Communications*, vol. 4, 2013.
- [32] Durham University, “Doppler-free saturated absorption spectroscopy: laser spectroscopy,” [Online]. Available: [http://massey.dur.ac.uk/resources/grad\\_skills/LaserSpectroscopy.pdf](http://massey.dur.ac.uk/resources/grad_skills/LaserSpectroscopy.pdf). [Accessed 24 July 2017].
- [33] D. Miletic, “Light-shift and temperature–shift studies in atomic clocks based on Coherent Population Trapping,” Université de Neuchâtel – Laboratoire Temps - Fréquence, Neuchâtel, 2013.
- [34] Edmund Optics, “Understanding waveplates,” [Online]. Available: <http://www.edmundoptics.com/technical-resources-center/optics/understanding->

waveplates. [Accessed 18 December 2014].

- [35] D. F. Ramian, "Time Domain Oscillator Stability Measurement Allan variance," February 2009. [Online]. Available: <http://www.crya.unam.mx/radiolab/recursos/Allan/RS.pdf>. [Accessed 24 July 2017].
- [36] D. F. Ramian, "Time Domain Oscillator Stability Measurement Allan variance," [Online]. Available: [http://cdn.rohde-schwarz.com/pws/dl\\_downloads/dl\\_application/application\\_notes/1ef69/1EF69\\_E3.pdf](http://cdn.rohde-schwarz.com/pws/dl_downloads/dl_application/application_notes/1ef69/1EF69_E3.pdf). [Accessed 18 December 2014].
- [37] D. Howe, "Time Domain Representation of Oscillator Performance," in *European Frequency and Time Seminar*, Besançon, 2014.
- [38] Runbing Li, Lin Zhou, Jin Wang, Mingsheng Zhan, "Measurement of the quadratic Zeeman shift of 85Rb hyperfine sublevels using stimulated Raman transitions," 1 December 2008. [Online]. Available: <https://arxiv.org/abs/0812.0231>. [Accessed 11 December 2017].
- [39] D. Miletic, C. Affolderbach, M. Hasegawa, R. Boudot, C. Gorecki, G. Mileti, "AC Stark-shift in CPT-based Cs miniature atomic clocks," *Applied Physics B Laser and Optics*, vol. 109, no. 1, pp. 89-97, 2012.
- [40] R. Boudot, P. Dziuban, M. Hasegawa, R. K. Chutani, S. Galliou, V. Giordano, and C. Gorecki, "Coherent population trapping resonances in Cs-Ne vapor microcells for miniature clocks applications," *Journal of Applied Physics*, vol. 109, 2011.
- [41] Qu Su-Ping, Zhang Yi and Gu Si-Hong, "Dependence of the 85Rb coherent population trapping resonance characteristic on the pressure of N2 buffer gas," *Chinese Physics B*, vol. 22, no. 9, 2013.
- [42] G. Mileti, "Physics of Atomic Clocks," in *European Frequency and Time Seminar*, Besançon, 2014.

- [43] Danijela Miletic, Thejesh Bandi, Christoph Affolderbach and Gaetano Mileti, “ac Stark shift in double resonance and coherent population trapping in a wall-coated cell for compact Rb atomic clocks,” *Physica Scripta*, 2012.
- [44] Peter Yun, Francois Tricot, Claudio Eligio Calosso, Salvatore Micalizio, Bruno Francois, Rodolphe Boudot, Stephane Guerandel and Emeric de Clercq, “High-performance coherent population trapping clock with polarization modulation,” *Phys. Rev. Applied*, vol. 7, no. 1, 2017.
- [45] J. K. A. Everard, *Fundamentals of RF Circuit Design*, Wiley, 2001.
- [46] D. B. Leeson, “A Simple Model of Feedback Oscillator Noise Theory,” *IEEE Proceedings Letters*, vol. 54, pp. 329-330, 1966.
- [47] Analog Devices, “Audio Dual Matched NPN Transistor SSM2210,” [Online]. Available: <http://pdf1.alldatasheet.com/datasheet-pdf/view/49083/AD/SSM2210.html>. [Accessed 27 July 2017].
- [48] J. Everard, “Low Noise Power Efficient Oscillators: Theory and Design,” *Proceedings of the IEE*, vol. 133, no. 4, pp. 172-180, 1986.
- [49] D. M. Pozar, *Microwave Engineering*, Wiley, 2012.
- [50] Arthur B. Williams, Fred J. Taylor, *Electronic Filter Design Handbook*, McGRAW-HILL, 2006.
- [51] Microsemi, “5120A High-Performance Phase Noise and Allan Deviation Test Set with Ultra Low Noise Floor,” 2014. [Online]. Available: [https://www.microsemi.com/document-portal/doc\\_view/133388-5120a](https://www.microsemi.com/document-portal/doc_view/133388-5120a). [Accessed 28 July 2017].
- [52] A. H. a. D. A. H. Craig W. Nelson, “Cross-spectral Collapse from Anti-correlated Thermal Noise in Power Splitters,” in *European Frequency and Time Forum*

(EFTF), York, 2016.

- [53] Craig W. Nelson, Archita Hati, David. A. Howe, “A collapse of the cross-spectral function in phase noise metrology,” *Review of Scientific Instruments*, vol. 85, no. 2, 2014.
- [54] Vratislav Michal, Christophe Premont, Gaël Pillonet, Nacer Abouchi, “Single Active Element PID Controllers,” in *20th International Conference Radioelektronika*, Brno, 2010.
- [55] K. Ogata, *Modern Control Engineering*, Pearson Education, 2010.
- [56] KEMET, “High Temperature 150°C, Ultra-Stable X8R Dielectric,” 9 January 2017. [Online]. Available: [http://www.kemet.com/Lists/ProductCatalog/Attachments/9/KEM\\_C1007\\_X8R\\_ULTRA\\_150C\\_SMD.pdf](http://www.kemet.com/Lists/ProductCatalog/Attachments/9/KEM_C1007_X8R_ULTRA_150C_SMD.pdf). [Accessed 28 July 2017].
- [57] Pascall Electronics, “OCXO series & OCXOF series,” 2017. [Online]. Available: [http://www.pascall.co.uk/oscillators\\_products\\_article.aspx?page=S635144040796327285&ArchiveID=22&CategoryID=-1&ItemID=226&src=](http://www.pascall.co.uk/oscillators_products_article.aspx?page=S635144040796327285&ArchiveID=22&CategoryID=-1&ItemID=226&src=). [Accessed 29 July 2017].
- [58] Wenzel Associates Inc., “VHF ULN II,” Wenzel Associates Inc., 2017. [Online]. Available: <http://www.wenzel.com/model/vhf-uln-ii/>. [Accessed 29 July 2017].
- [59] NEL Frequency Controls, Inc., “O-CEX-XXXXXXXXX-X Very Low Phase Noise Precision SC-cut HF OCXO in 36x27mm “Europack”,” NEL Frequency Controls, Inc., 2017. [Online]. Available: <http://www.nelfc.com/pdf/1029c.pdf>. [Accessed 29 July 2017].
- [60] Simberian Elettromagnetic Solutions, “Minimal-reflection bends in micro-strip lines,” May 2008. [Online]. Available: [http://www.simberian.com/AppNotes/BendsOptimization\\_2008\\_05.pdf](http://www.simberian.com/AppNotes/BendsOptimization_2008_05.pdf). [Accessed

30 July 2017].

- [61] Linear Technology, “1.4GHz Low Phase Noise, Low Jitter PLL with Clock Distribution,” 2014. [Online]. Available: <http://cds.linear.com/docs/en/datasheet/6950f.pdf>. [Accessed 31 July 2017].
- [62] Analog Devices, “1 GSPS Direct Digital Synthesizer with 14-Bit DAC,” 2010. [Online]. Available: <http://www.analog.com/media/en/technical-documentation/data-sheets/AD9912.pdf>. [Accessed 1 August 2017].
- [63] Bert C. Henderson, James A. Cook, “Image-Reject and Single-Sideband Mixers,” June 1985. [Online]. Available: [http://www.rfcafe.com/references/articles/wj-tech-notes/ImageRej\\_n\\_SSB\\_mixers.pdf](http://www.rfcafe.com/references/articles/wj-tech-notes/ImageRej_n_SSB_mixers.pdf). [Accessed 1 August 2017].
- [64] Tadashi Kawai, Hiroyuki Mizuno, Isao Ohta, Akira Enokihara, “Lumped-element quadrature wilkinson power divider,” in *Microwave Conference, APMC 2009. Asia Pacific*, Singapore, 2009.
- [65] Fernando Noriega, Pedro J. González, “Designing LC Wilkinson Power Splitters,” August 2002. [Online]. Available: <http://data.eefocus.com/myspace/0/2194/bbs/1190602131/84dbcb80.pdf>. [Accessed 1 August 2017].
- [66] G. Matthaei, L. Young, E. M. T. Jones, *Microwave Filters, Impedance-Matching Networks, and Coupling Structures*, Artech House Inc., McGraw-Hill Book Company, 1980.
- [67] Jeremy K.A. Everard, J. Bitterling, “Low Phase Noise Highly Power Efficient Oscillators,” in *IEEE, International Frequency Control Symposium*, Orlando, 1997.
- [68] T. Burtichelov, “Design and Construction of a Rubidium Atomic Clock - BEng project report,” University of York, 2012.

- [69] K. G. Libbrecht, J. L. Hall, "A low-noise high-speed diode laser current controller," *Rev. Sci. Instrum.*, vol. 64, no. 8, pp. 1233-1235, 1993.
- [70] Texas Instruments, "Noise Analysis in Operational Amplifier Circuits - Application Report," 2007. [Online]. Available: <http://www.ti.com/lit/an/slva043b/slva043b.pdf>. [Accessed 3 August 2017].
- [71] P. J. Fish, *Electronic Noise and Low Noise Design*, McGraw-Hill Companies, 1993.
- [72] P. H. Schimpf, "A Detailed Explanation of Solenoid Force," *Int. J. on Recent Trends in Engineering and Technology*, vol. 8, no. 2, pp. 7-14, 2013.
- [73] R. Boudot, D. Miletic, P. Dziuban, C. Affolderbach, P. Knapkiewicz, J. Dziuban, G. Mileti, V. Girodano, C. Gorecki, "First-order cancellation of the Cs clock frequency temperature-dependence in Ne-Ar buffer gas mixture.," *Optics Express*, vol. 19, pp. 3106-3114, 2011.
- [74] J. Vanier, R. Kunski, N. Cyr, J. Y. Savard, M. Tetu, "On hyperfine frequency shifts caused by buffer gases: Application to the optically pumped passive rubidium frequency standard," *Journal of Applied Physics*, vol. 53, 1982.
- [75] Olga Kozlova, St'ephane Gu'erandel, and Emeric de Clercq, "Temperature and pressure shift of the Cs clock transition in the presence of buffer gases: Ne, N<sub>2</sub>, Ar," *Physical Review A*, vol. 83, 2011.
- [76] M. Arditi and T. R. Carver, "Pressure, Light, and Temperature Shifts in Optical Detection of 0-0 Hyperfine Resonance of Alkali Metals," *Physical Review*, vol. 124, no. 3, 1961.
- [77] J. Vanier, R. Kunski, A. Brisson, P. Paulin,, "Progress and Prospects in Rubidium Frequency Standards," *Journal de Physique Colloques*, vol. 42, 1981.
- [78] Gilles Missout, Jacques Vanier,, "Pressure and Temperature Coefficients of the

More Commonly Used Buffer Gases in Rubidium Vapor Frequency Standards,”  
*IEEE Transactions on Instrumentation and Measurement*, vol. 24, no. 2, 1975.

- [79] Paul L. Stubbs, Advisor: Irina Novikova, “Laser Locking with Doppler-free Saturated Absorption Spectroscopy,” W&M Quantum Optics Group, 2010.
- [80] “Measuring the Hyperfine Levels of Rubidium Using Saturated Absorption Spectroscopy,” [Online]. Available: <http://advancedlab.physics.gatech.edu/labs/SaturationSpectroscopy/SatSpecManual.pdf>. [Accessed 18 December 2014].
- [81] Changmin Leea, G. Z. Iwataa, E. Corsini, J. M. Higbie, S. Knappe, M. P. Ledbetter and D. Budkerd, “Small-sized Dichroic Atomic Vapor Laser Lock (DAVLL),” *Rev. Sci. Instrum.*, vol. 82, pp. 1-14, 2011.
- [82] Z Kristan L. Corwin, Zheng-Tian Lu, Carter F. Hand, Ryan J. Epstein, and Carl E. Wieman, “Frequency-stabilized diode laser with the Zeeman shift in an atomic vapour,” Optical Society of America, 1998.